Characterisation of a novel mouse model of mitochondrial disease – a hypomorphic *Wars2* ENU-induced allele

Thomas Agnew

DPhil Candidate

Department of Biochemistry,
Wolfson College, University of Oxford

Genetics of Type 2 Diabetes,
MRC Mammalian Genetics Unit, Harwell

Characterisation of a novel mouse model of mitochondrial disease – a hypomorphic *Wars2* ENU-induced allele

Thomas Agnew
Department of Biochemistry, Wolfson College, University of Oxford
Genetics of Type 2 Diabetes, MRC Mammalian Genetics Unit, Harwell
A thesis presented for the degree of Doctor of Philosophy, Trinity Term, 2016

Abstract

Mitochondrial aminoacyl-tRNA synthetases (mtRS) are vital for mitochondrial translation. mtRSs catalyse the aminoacylation of mitochondrial tRNA with their cognate amino acid. Mutations in mtRS genes are associated with distinct clinical pathologies in humans. Studying mtRS mutations in model organisms is difficult because mtRS knock-out alleles are haplosufficient and cause embryonic lethality in their homozygous state. In this study, we phenotypically and mechanistically characterised a hypomorphic, ENU-induced *Wars2* allele (*Wars2*-V117L) in mouse with the aim to determine the cause of the tissue-specific penetrance of mtRS mutant alleles.

The *Wars2*-V117L allele caused tissue-specific pathology in mice. *Wars2*$^{V117L/V117L}$ mice developed hypertrophic cardiomyopathy, sensorineural hearing loss, reduced adiposity, increased glucose tolerance and systemic changes in metabolism. Furthermore, we showed that the *Wars2*-V117L allele causes abnormal adipose tissue pathology as shown by 'browning' of WAT depots and lipid accumulation in BAT in *Wars2*$^{V117L/V117L}$ mice.

The *Wars2*-V117L allele disrupts *Wars2* mRNA splicing, resulting in reduced full-length *Wars2* (*Wars2*-FL) mRNA in *Wars2*$^{V117L/V117L}$ tissues and cells. Reduced *Wars2*-FL mRNA caused tissue-specific reductions in mt-TrpRS protein and mitochondrial OXPHOS deficiencies in *Wars2*$^{V117L/V117L}$ mice *in vivo*. OXPHOS deficiencies lead to activation of the Integrated Stress Response (ISR) in *Wars2*$^{V117L/V117L}$ heart and liver. Activation of the ISR in *Wars2*$^{V117L/V117L}$ heart caused up-regulation of *Fgf21* mRNA and increased plasma FGF21, leading to systemic changes in metabolism. Finally, we showed that up-regulation of *Pgc1a* and mitochondrial biogenesis prevented inhibition of mitochondrial translation in *Wars2*$^{V117L/V117L}$ skeletal muscle and mouse embryonic fibroblasts.

Overall, we have characterised the first mouse model of mitochondrial disease caused by a global, hypomorphic, mutation in an mtRS gene. We showed that the tissue-specific pathology observed in *Wars2*$^{V117L/V117L}$ mice was due to activation of tissue-specific stress response mechanisms that either lead to disease pathology, such as activation of the ISR

in the heart, or protection against inhibition of mitochondrial translation, such as up-regulation of *Pgc1a* in iWAT and MEFs. This study provides some evidence that up-regulation of mitochondrial biogenesis could be utilised as a therapeutic strategy to treat human patients with mtRS mutations in the future.

Acknowledgements

First and foremost, I would like to express my sincere gratitude to my supervisor Professor Roger Cox for his mentorship throughout my DPhil. I am especially grateful for the opportunities that Roger has given me over the last 4 years to expand my knowledge and experience in the wider scientific community at conferences and training courses. I would also like to extend my thanks to Dr Michelle Goldworthy for her guidance and her intellectual and technical expertise that has proven invaluable to me over the last 4 years. I would also like to acknowledge everybody in the Type 2 Diabetes Group both past and present in particular Ms Samantha Laber, Dr Liz Bentley, Dr Lee Moir and Dr Alison Hough, for their willingness to help whenever asked, their companionship and for putting up with me, I am truly grateful. Finally, I would also like to thank everybody at MRC Harwell for making the past four years such an enjoyable, stimulating and rewarding experience.

Throughout my DPhil, I have been given the opportunity to foster collaborations with several experts within the field of mitochondrial research. In particular, I would like to thank Professor Joanne Poulton, Professor Karl Morten and Professor Robert Taylor for their mentorship and consideration. Their knowledge and expertise has been vital to the success of this project. I would also like to acknowledge Dr Kyle Thompson for hosting me in Newcastle.

I would like to thank everybody from MRC Harwell that has contributed to the work presented in this thesis. In particular, I would like to acknowledge: Professor Steve Brown, Dr Mike Bowl and Mr Carlos Aguilar from the Deafness Group; Dr Paul Potter and the DMAT group; Marie Hutchinson, Rosie Hillier, Gemma Law from Ward 3; Lucie Vizor and Tamzin Osbourne from Ward 4; Sarah Wells and Heather Cater from the MLC; the Bioinformatics group; the GEMS team; the Clinical Chemistry team; the Necropsy and Histology team and finally the Proteomics and Imaging core facilities. Without the collaborative work of all of these people, it would not have been possible to perform this study and for this I am truly thankful.

I dedicate this thesis to my parents and grandparents. Without their love, support and guidance I would not be where I am today. I owe everything to them and I am eternally grateful.

Table of Contents

Table of Figures

Table of Tables

Abbreviations

AAR	Amino acid response pathway
AARS2	Alanyl-tRNA Synthetase 2, Mitochondrial
αACB	α-anticodon-binding
ABR	Auditory-evoked brainstem response
Acaca	Acetyl-CoA Carboxylase Alpha
Acacb	Acetyl-CoA Carboxylase Beta
Acadl	Acyl-Coenzyme A dehydrogenase, long-chain
Acadm	Acyl-CoA Dehydrogenase, C-4 To C-12 Straight Chain
APR	adenosine 5' phosphosulfate
ARSAL	Autosomal recessive spastic ataxia with leukoencephalopathy
ATF4	Activating Transcription Factor 4
ATF5	Activating Transcription Factor 5
ATF6	Activating Transcription Factor 6
ATP5A	ATP Synthase, H+ Transporting, Mitochondrial F1 Complex, Alpha Subunit 1
BAT	Brown adipose tissue
BC	Back-crossed
BMI	Body mass index
BSA	Bovine Serum Albumin
CI	Complex I, NADH-dehydrogenase
CII	Complex II, Succinate dehydrogenase
CIII	Complex III, ubiquinone-cytochrome c oxidoreductase
CIV	Complex IV, Cytochrome oxidase
CV	Complex V, ATP synthase
C4orf14	Chromosome 4 open reading frame 14 Nitric Oxide Associated 1
C7orf30	Chromosome 7 Open Reading Frame 30
CAGSSS	Cataracts, growth hormone deficiency with short stature, partial sensorineural deafness and peripheral neuropathy
CARS2	Cysteinyl-tRNA Synthetase 2, Mitochondrial
CB	Click box
CD	Cardiovascular Disease
CELF	CUGBP and ETR-3-like factors
Chop	C/EBP-Homologous Protein 10
Cidea	Cell Death-Inducing DFFA-Like Effector A
CLAMS	Comprehensive lab animal monitoring system
CLPP	Caseinolytic Mitochondrial Matrix Peptidase Proteolytic Subunit
CO	Cardiac ouput
CO_2	Carbon Dioxide

Cox7a1	Cytochrome C Oxidase Subunit 7A1
Cox8b	Cytochrome C Oxidase Subunit 8B
Cpt1a	Carnitine palmitoyltransferase 1a
Cpt1b	Carnitine palmitoyltransferase 1b
Cyt c	Cytochrome c
DARS2	Aspartyl-tRNA Synthetase 2, Mitochondrial
DHOD	Dihydroortate reductase
Dio2	Deiodinase, Iodothyronine, Type II
DPBS	Dulbecco's phosphate-buffered saline
EARS2	Glutamyl-tRNA Synthetase 2, Mitochondrial
ECAR	Extracellular acidification rate
EE	Energy expenditure
EF	Ejection fraction
EFTu	Mitochondrial Elongation Factor Tu
EFTs	Mitochondrial Elongation Factor Ts
EFG1	G Elongation Factor, Mitochondrial 1
eIF2A	Eukaryotic Translation Initiation Factor 2A
Eif4a2	Eukaryotic Translation Initiation Factor 4A2
ENU	N-ethyl-N-nitrosourea
ERAL1	Era-like 12S mitochondrial rRNA chaperone 1
ETC	Electron transport chain
FACS	Fluorescence-activated cell sorting
FARS2	Phenylalanyl-tRNA Synthetase 2, Mitochondrial
FCCP	Carbonyl cyanide-4-(trifluoromethoxy)phenylhydrazone
FFA	Free fatty acids
FGF21	Fibroblast growth factor 21
fMet-tRNA^{Met}	Formylmethionine-tRNA^{Met}
FS	Fraction shortening
G1	1st generation
G2	2nd generation
G3	3rd generation
GAPDH	Glyceraldehyde-3-Phosphate Dehydrogenase
GARS	Glycyl-tRNA Synthetase
GCN2	General control nonderepressible 2
GDP	Guanosine diphosphate
GLT	Germ-line transmission
GTP	Guanosine-5'-triphosphate
gWAT	Gonadal white adipose tissue
HARS2	Histidyl-tRNA Synthetase 2, Mitochondrial
HAS	Harwell ageing screen

hGatCAB	Human homolog of the Glu-tRNA(Gln) amidotransferase
HR	Heart rate
HRI	Haem-regulated inhibitor
HRP	Horseradish peroxidase
HSD17B4	Hydroxysteroid (17-Beta) Dehydrogenase 4
HSP	Hereditary spastic paraplegia
HSP60	Heat Shock Protein Family D (Hsp60) Member 1
HSP70	Heat Shock Protein Family A (Hsp70) Member 9
HUPRA	Hyperuricemia, pulmonary hypertension, renal failure, and alkalosis
IARS2	Isoleucyl-tRNA Synthetase 2, Mitochondrial
IMPC	International Mouse Phenotyping Consortium
IMS	Intermembrane space
IP	Immunoprecipitation
IPGTT	Intraperitoneal Glucose Tolerance Test
ISR	Integrated stress response
iWAT	Inguinal white adipose tissue
KARS	Lysyl-tRNA Synthetase
KB	Ketone bodies
KOMP	Knockout Mouse Phenotyping Program
LARS2	Leucyl-tRNA Synthetase 2, Mitochondrial
LBSL	Leukoencephalopathy with brain stem and spinal cord involvement and lactate elevation
LC3	Microtubule Associated Protein 1 Light Chain 3 Alpha
LONP1	Lon Peptidase 1, Mitochondrial
LTBL	Leukoencephalopathy with thalamus and brain stem involvement and high lactate
LV	Left ventricle
LVAW	Left Ventricle Anterior Wall diameter
LVID	Left Ventricle Interior Diameter
MARS2	Methionyl-tRNA Synthetase 2, Mitochondrial
MELAS	Mitochondrial encephalomyopathy, lactic acidosis, and stroke-like episodes
MIDD	Maternally inherited diabetes and deafness
MIM	Mitochondrial inner membrane
MLASA	Myopathy, lactic acidosis, and sideroblastic anemia
MPC-151	Mutant-Pedigree-Cohort-151
MRPS16	Mitochondrial Ribosomal Protein S16
MRPS22	Mitochondrial Ribosomal Protein S22
MRI	Magnetic resonance imaging
mtRRF	Mitochondrial Ribosome Recycling Factor
mtEFG2	Mitochondrial Elongation Factor G2

mt-AlaRS	Mitochondrial alanyl-tRNA synthetase
mt-ArgRS	Mitochondrial arginyl-tRNA synthetase
mt-AsnRS	Mitochondrial asparaginyl-tRNA synthetase
mt-AspRS	Mitochondrial aspartyl-tRNA synthetase
mtCOI	Mitochondrially Encoded Cytochrome C Oxidase I
mt-CysRS	Mitochondrial cysteinyl-tRNA synthetase
mtDNA	Mitochondrial genome
MTFMT	Mitochondrial Methionyl-tRNA Formyltransferase
MTG1	Mitochondrial ribosomal associated GTPase 1
mt-GluRS	Mitochondrial glutamyl-tRNA synthetase
Mthfd2	Methylenetetrahydrofolate Dehydrogenase (NADP+ Dependent) 2, Methenyltetrahydrofolate Cyclohydrolase
mt-HisRS	Mitochondrial histidyl-tRNA synthetase
mtIF2	Mitochondrial translation initiation factor 3
mtIF3	Mitochondrial translation initiation factor 3
mt-IsoRS	Mitochondrial isoleucyl-tRNA synthetase
mt-LeuRS	Mitochondrial leucyl-tRNA synthetase
mt-MetRS	Mitochondrial methionyl-tRNA synthetase
MTO1	Mitochondrial tRNA Translation Optimization 1
mt-PheRS	Mitochondrial phenylalanyl-tRNA synthetase
mt-ProRS	Mitochondrial prolyl-tRNA synthetase
mt-rRNA	Mitochondrial ribosomal RNA
mtRS	Mitochondrial aminoacyl-tRNA synthetase
mt-SerRS	Mitochondrial seryl-tRNA synthetase
mt-ThrRS	Mitochondrial threonyl-tRNA synthetase
mt-tRNA	Mitochondrial tRNA
mt-tRNA^{Trp}	Mitochondrial-tRNA^{Trp}
mt-TrpRS	Mitochondrial trytophanyl-tRNA synthetase
mt-TyrRS	Mitochondrial tyrosyl-tRNA synthetase
MTU1	tRNA 5-Methylaminomethyl-2-Thiouridylate Methyltransferase
mt-ValRS	Mitochondrial valyl-tRNA synthetase
NAFLD	Non-alcoholic Fatty Liver Disease
NARS2	Asparaginyl-tRNA Synthetase, Mitochondrial
nDNA	Nuclear genome
NDUFB8	NADH:Ubiquinone Oxidoreductase Subunit B8
NMR	Nuclear magnetic resonance
O_2	Oxygen
OBGH1	Mitochondrial Ribosome Associated GTPase 2
OCR	Oxygen consumption rate
OXPHOS	Oxidative phosphorylation

PARS2	Prolyl-tRNA Synthetase 2, Mitochondrial
PCH6	Pontocerebellar hypoplasia type 6
PCR	Polymerase chain reaction
PEHO	Progressive Encephalopathy with oedema, Hypsarrhythmia and Optic atrophy
PERK	PKR-like ER kinase
PGC1a	PPARG Coactivator 1 Alpha
PKR	Double stranded RNA-activated protein kinase
PPA2	Pyrophosphatase 2
Pparα	Peroxisome Proliferator Activated Receptor Alpha
Pparγ	Peroxisome Proliferator Activated Receptor Gamma
PPi	Pyrophosphate
PTB	Polypyrimidine tract-binding protein
PUS1	Pseudouridylate Synthase 1
RARS2	Arginyl-tRNA Synthetase 2, Mitochondrial
RER	Respiratory exchange ratio
RNaseP	Ribonuclease P
RNase Z	Ribonuclease Z
ROS	Reactive oxygen species
RRF	Ragged red fibres
rRNA	Ribosomal RNA
RS	aminoacyl-tRNA synthetase
SARS2	Seryl-tRNA Synthetase 2, Mitochondrial
SD	Standard deviation
SDHA	Succinate Dehydrogenase Complex Flavoprotein Subunit A
SEM	Standard error mean
SIRT1	Sirtuin 1
SNP	Single nucleotide polymorphism
SNV	Single nucleotide variants
SOD2	Superoxide Dismutase 2, Mitochondrial
SV	Stroke volume
TAG	Triglycerides
TARS2	Threonyl-tRNA Synthetase 2, Mitochondrial
TCHH	Trichohyalin
T2D	Type 2 Diabetes
TFAM	Transcription Factor A, Mitochondrial
TFB1M	Transcription Factor B1, Mitochondrial
TFB2M	Transcription Factor B2, Mitochondrial
UCP1	Uncoupling Protein 1
UPR^{er}	Endoplasmic reticulum unfolded protein response
UPR^{mt}	Mitochondrial unfolded protein response

UQCRC2	Ubiquinol-Cytochrome C Reductase Core Protein II
VARS2	Valyl-tRNA Synthetase 2, Mitochondrial
VCO_2	CO_2 production
VO_2	Oxygen consumption
WARS2	Tryptophanyl tRNA Synthetase 2, Mitochondrial
Wars2-KO	*Wars2*$^{tm1.1(KOMP)Vlcg}$
WAT	White adipose tissue
WGS	Whole genome sequencing
WT	Wild-type
XBP1	X-box binding protein 1
YARS2	Tyrosyl-tRNA Synthetase, Mitochondrial

1 Introduction

1.1 Mitochondrial Disease

The United Mitochondrial Disease Foundation define mitochondrial diseases as follows *'Mitochondrial diseases are the result of either inherited or spontaneous mutations in mtDNA or nDNA which lead to altered functions of the proteins or RNA molecules that normally reside in mitochondria'.* This definition successfully describes the cause of mitochondrial disease, i.e. genetic mutation. It also alludes to the many 'functions' of mitochondria that extend beyond the oxidative phosphorylation (OXPHOS) pathway such as intracellular calcium signalling, heme biosynthesis, intracellular reactive oxygen species (ROS) homeostasis, pyrimidine biosynthesis and steroid synthesis. To label a patient as having 'mitochondrial disease' therefore gives little insight into the clinical pathology or genetic cause of the individual's disease state. Here I review the pathways required for expression of the mitochondrial genome and review examples of reported patients with mitochondrial diseases caused by mutations in genes required specifically for mitochondrial translation.

1.1.1 The mitochondrial genome

The mitochondrial genome is highly conserved in human and mouse (Bibb, Van Etten, Wright, Walberg, & Clayton, 1981). The mitochondrial genome (mtDNA) is a small ~16kb circular chromosome containing 37 genes encoding 13 mRNAs, 2 ribosomal RNAs (rRNA) and 22 tRNAs that is located in the mitochondrial matrix (Anderson et al., 1981) (**Figure 1.1**). mtDNA is made up of two circular strands of DNA. There is an uneven distribution of GC nucleotide content on each of the circular strands resulting in so called 'heavy' and 'light' strands. The mtDNA is compact with no introns and few non-coding nucleotides between genes. mtDNA differs from nDNA in that it is maternally inherited and there are multiple copies per cell. mtDNA copy number varies in a tissue / cell specific manner

dependent upon metabolic requirements (Taylor & Turnbull, 2005). As such, inheritance of mtDNA mutations is not Mendelian but rather dependent on population genetics or heteroplasmy.

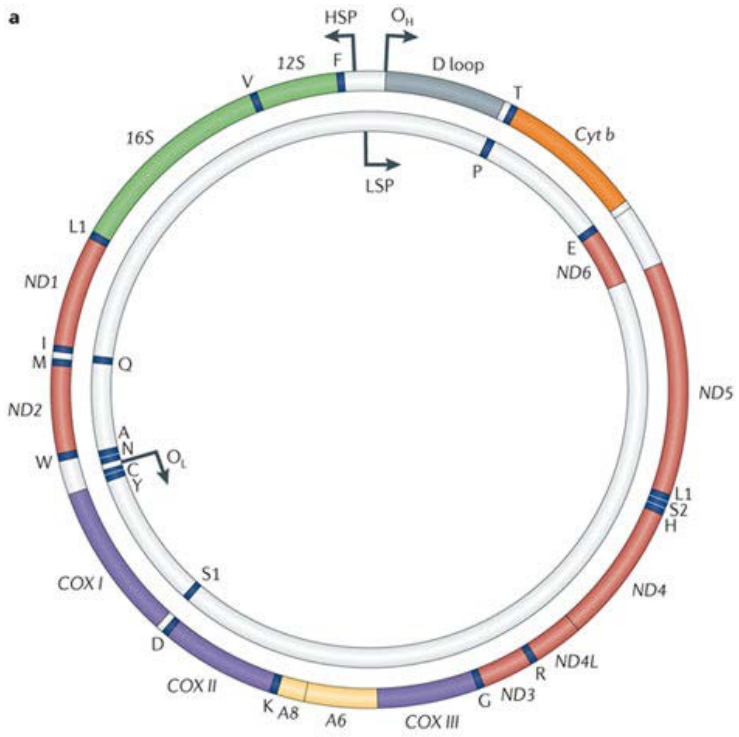

Figure 1.1 – The human mitochondrial genome.
Schematic diagram of the mitochondrial genome. The locations of the 37 genes encoded by the mtDNA are shown including two ribosomal rRNAs (green), 22 tRNAs (blue) and 13 mRNAs. The 13 mRNAs encode subunits of the OXPHOS pathway including 7 subunits of CI (red), one subunit of CIII (orange), 3 subunits of CIV (purple) and two subunits of CV (yellow). Also shown are the promoters of transcription on the heavy (HSP) and light (LSP) strands and the origins of replication on the heavy (O_H) and light strand (O_L). Figure from Schon et al. 2012.

The 13 mRNAs encoded by mtDNA encode subunits of the mitochondrial oxidative phosphorylation (OXPHOS) pathway (Anderson et al., 1981) (**Figure 1.2**). These include: seven subunits of complex I (CI, NADH-dehydrogenase) ND1, ND2, ND3, ND4, ND4L, ND5 and ND6; one subunit of complex III (CIII, cytochrome c reductase) Cyt b, three subunits of complex IV (CIV, cytochrome c oxidase) mtCOI, mtCOII and mtCOIII; and two subunits of complex V (CV, ATP synthase) ATP6 and ATP8 (Anderson et al., 1981). The remaining OXPHOS protein subunits are encoded by the nuclear genome (nDNA) along with over 50

proteins required for OXPHOS assembly and function are synthesized in the cytoplasm and are imported into mitochondria (Herrmann & Neupert, 2004).

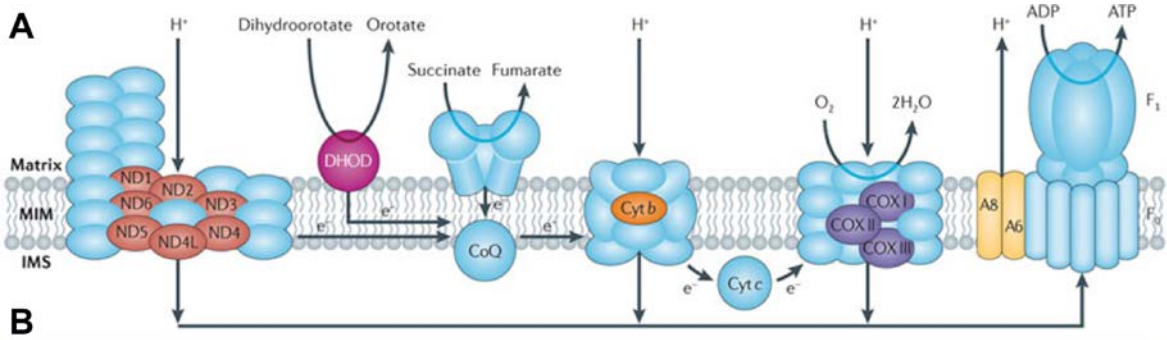

Polypeptides	Complex I	Complex II	Complex III	Complex IV	Complex V
mtDNA-encoded subunits	7	0	1	3	2
nDNA-encoded subunits	~39	4	10	10	~14
Assembly proteins	~11	~2	~9	~30	~3

Figure 1.2 – The mitochondrial oxidative phosphorylation (OXPHOS) pathway.
A) Schematic diagram of the OXPHOS pathway. The mitochondrial OXPHOS pathway couples ATP synthesis with oxygen consumption. The OXPHOS pathway is made up of 5 complexes: NADH dehydrogenases (CI) succinate dehydrogenase (CII), ubiquinone-cyt c oxidoreductase (CIII), cytochrome c oxidase (CIV) and ATP synthase (CV) and two electron carriers coenzyme Q (ubiquinone/coQ) and cytochrome c (Cyt c). Complexes I-IV make up the electron transport chain (ETC). The ETC functions to pump H^+ ions, derived from NADH and $FADH_2$, from the mitochondrial matrix across the mitochondrial inner membrane (MIM) and into the intermembrane space (IMS) creating a proton gradient. This process is facilitated by the transfer of electrons, from CI or CII to CIV, to molecular oxygen producing water. The proton gradient creates the mitochondrial transmembrane potential that drives ATP synthase that generate ATP from ADP by dissipating the mitochondrial transmembrane potential. mtDNA encoded OXPHOS subunits are in colors corresponding to figure 1 and nuclear encoded OXPOS subunits are coloured light blue. CoQ can also derive electrons from dihydroorotate dehydrogenase (DHOD, coloured in pink). B) Table listing the number of nDNA and mtDNA encoded genes encoding OXPHOS complex subunits and assembly factors. Figure adapted from Schon et al. 2012.

1.1.2 mtDNA mutations

Epidemiological studies report that the minimum prevalence of pathogenic mtDNA mutations is 1 in 5000 in the population with pathogenic mtDNA alleles being present in 1 in 200 live births (Chinnery et al., 2000; Elliott, Samuels, Eden, Relton, & Chinnery, 2008; Schaefer et al., 2008). To date, over 300 disease causing mtDNA mutations have been documented (Brandon et al., 2005). Interestingly over half of the reported mtDNA mutations are located within mitochondrial tRNA (mt-tRNA) genes which, given that mt-tRNA genes

comprise ~10% of mtDNA sequence, is unexpected. mtDNA mutations are thought to be caused by OXPHOS-derived reactive oxygen species (ROS). It has been proposed that the increased susceptibility of mtDNA to damage is a result of its proximity to the OXPHOS pathway (Brown, George, & Wilson, 1979).

As mentioned previously, multiple copies of mtDNA are present in every cell meaning that mtDNA mutations often exist alongside wild-type alleles in a state of heteroplasmy. mtDNA mutations may not cause disease pathology until a 'threshold' level' of mutant mtDNA has been achieved. The threshold level for any given mtDNA mutation varies dependent upon the nature of the mutation. For instance, the threshold for deletion mutations are often 50-60% whereas for some point mutations in mt-tRNA genes the threshold is >90%. Additionally, the clinical outcome for mtDNA mutation may vary dependent upon the mutant load. An example of this is seen with the m8993T>G mutation in the mtDNA encoded *ATP6* gene. Patients with a mutant load of >90% present with maternally inherited Leigh's syndrome whereas patients with a mutant load of 70-90% have neuropathy, ataxia and retinitis pigmentosa (Holt, Harding, Petty, & Morgan-Hughes, 1990; Santorelli, Shanske, Macaya, DeVivo, & DiMauro, 1993).

Mutant mtDNA load and the mutation classification are both factors in disease pathology. Disease pathology is however unexpectedly variable in mtDNA patients. As mentioned previously, mtDNA genes encode functional elements required for mitochondrial translation, such as rRNA and tRNAs, and OXPHOS subunits. Mitochondria are found in all cells within the body except erythrocytes and mtDNA copy number is dependent upon cellular bioenergetic demand. Therefore, one might expect that loss-of-function mutations in mtDNA genes ultimately lead to OXPHOS deficiencies in cell/tissues with high energetic demand such as brain, heart and muscle. However, in reality the clinical pathology of mtDNA patients is highly variable. A comprehensive list of clinical pathologies associated with mtDNA mutations can be found at MITOMAP (Brandon et al., 2005). Clinical

pathologies commonly associated with mtDNA mutations include: myopathy, deafness, diabetes mellitus, encephalopathy, MELAS, MERRF and CPEO.

Although the overarching clinical pathology associated with mtDNA mutations is highly varied, there are biochemical and morphological commonalities. The first of these is OXPHOS deficiencies. Given that the mitochondrial genome encodes genes required for translation of OXPHOS subunits and for OXPHOS subunits themselves, this is not unexpected. That being said, no subunits of succinate dehydrogenase (SDH, CII) are mtDNA encoded. Therefore, mtDNA mutations typically cause combined OXPHOS deficiencies in CI, CIII, CIV and CV, with CII remaining normal or as in some cases being elevated. Secondly, as a result of OXPHOS deficiencies, elevated lactate levels are often observed in blood and cerebral spinal fluid of mtDNA patients (DiMauro & Schon, 2003). Finally ragged red fibres (RRF) are also a feature of mtDNA patients. RRF are observed in skeletal and are the result of compensatory proliferation of OXPHOS-defective mitochondria (Mita, Schmidt, Schon, DiMauro, & Bonilla, 1989). These can be visualized histologically through modified gomori-trichome or COX-SDH staining.

1.1.2.1 *MT-TW* mutations

As an example I will now briefly summarize known pathological mutations found within the mtDNA gene *MT-TW*. *MT-TW* encodes mitochondrial-tRNA^{Trp} (mt-tRNA^{Trp}). To date 15 pathological mutations in *MT-TW* have been reported (**Table 1.1**). As you can see from the table the ascribed clinical pathologies associated with MT-TW mutations is varied including encephalopathy, deafness, myopathy, hypertrophic cardiomyopathy and gastrointestinal syndrome. Equally the age of onset is variable from neonatal to adulthood. Encephalopathy was observed in the majority of *MT-TW* mutant patients including A5514G, T5523G, G5532A, A5537insT, G5540A, C5541T, G5549A, G5556A, and A5559G. The mutant load of *MT-TW* patients with encephalopathy varied from ~30 – 100% and shows no correlation

with age of onset indicating that the pathological mutant load is genotype specific. In the remaining *MT-TW* patients, encephalopathy was either not reported (C5545T and G556A) or was not a clinical feature (G5521A, T5543C, T5567C AND A5568G). With respect to the G5521A, T5543C and T5567C mutations, late onset myopathy was observed with mutant loads ranging from 98% to 30%.

Pos.	Locus	Disease	Age of Onset	Allele	Mutant mtDNA load	Ref
5514	MT-TW	Encephalopathy	Neonatal	A5514G	100% - homoplasmic	(Del Mar O'Callaghan et al., 2012)
5521	MT-TW	Mitochondrial myopathy	Adulthood	G5521A	98% - heteroplasmic	(Silvestri et al., 1998)
5523	MT-TW	Leigh Syndrome (deafness)	Infancy	T5523G	63% - heteroplasmic	(Mkaouar-Rebai et al., 2009)
5532	MT-TW	Gastrointestinal syndrome, encephalopathy, deafness	Infancy	G5532A	92% - heteroplasmic	(Maniura-Weber et al., 2004)
5537	MT-TW	Leigh Syndrome	Infancy	A5537insT	>92% - heteroplasmic	(Santorelli et al., 1997)
5540	MT-TW	Encephalomyopathy & deafness	Childhood	G5540A	98% - heteroplasmic	(Silvestri et al., 2000)
5541	MT-TW	MELAS	N/A	C5541T	84-87% - heteroplasmic	(Blakely et al., 2013)
5543	MT-TW	Mitochondrial myopathy	Adult onset	T5543C	Variable, 95% in muscle	(Anitori et al., 2005)
5545	MT-TW	Hypertrophic cardiomyopathy, severe multisystem disorder	Childhood	C5545T	<25% heteroplasmic	(Sacconi et al., 2008)
5549	MT-TW	Encephalopathy, dementia, deafness, chorea	Adulthood	G5549A	Variable 40-93% - heteroplasmic	(Nelson et al., 1995)
5556	MT-TW	Mitochondrial encephalomyopathy	Adulthood	G5556C	70% - heteroplasmic	(Sanaker, Nakkestad, Downham, & Bindoff, 2010)
5556	MT-TW	Progressive multisystem disorder	Infancy	G5556A	92-93% - heteroplasmic	(Smits et al., 2010)
5559	MT-TW	Leigh Syndrome	Childhood	A5559G	43% - heteroplasmic	(Mkaouar-Rebai et al., 2009)
5567	MT-TW	Myopathy	Adulthood	T5567C	30-50% - heteroplasmic	(Valente et al., 2009)
5568	MT-TW	Maternally inherited deafness	N/A	A5568G	N/A	(Jacobs et al., 2005)

Table 1.1 – Summary of pathological mutations in mtDNA encoded $tRNA^{Trp}$.

Table of all known pathological mutations in mtDNA encoded tRNA-tryptophan (MT-TW) in humans indicating the mutation location along with associated clinical pathology, age of onset and mutant load.

The location of pathological *MT-TW* mutations is shown in **Figure 1.3**. 8 out of 9 *MT-TW* mutations associated with encephalopathy are located within double stranded 'stem' regions and thus more likely to alter mt-tRNA^{Trp} secondary structure. In contrast with this, three out of four MT-TW mutations associated with late-onset myopathy are located within 'loop' regions of mt-tRNA^{Trp} and are less likely to alter mt-tRNA^{Trp} secondary structure.

One particularly interesting *MT-TW* mutation is the C5545T mutation located within the central base within the anticodon triplet. The C5545T mutation caused hypertrophic cardiomyopathy and multisystem disorder in childhood (Sacconi et al., 2008). This mutation is exceptional as a <25% mutant load was detected in patient samples making is a 'dominant-like' allele. This is the first identified mtDNA mutation to behave in a 'dominant-like' manner and is likely due to its location within the anticodon triplet. The C5545T mutation is located within the central nucleotide of the TCA anticodon which is decoded by the UGA codon for tryptophan. In the case of the C5545T mutant, the TCA tryptophan anticodon is converted to TTA. The reciprocal codon for TTA is UAA which does not decode an amino acid but represents a stop codon. It is possible therefore that the C5545T mutation has a dominant negative effect by disrupting termination of mitochondrial protein synthesis, preventing dissociation ribosomal machinery and release of newly synthesis mtDNA encoded peptides.

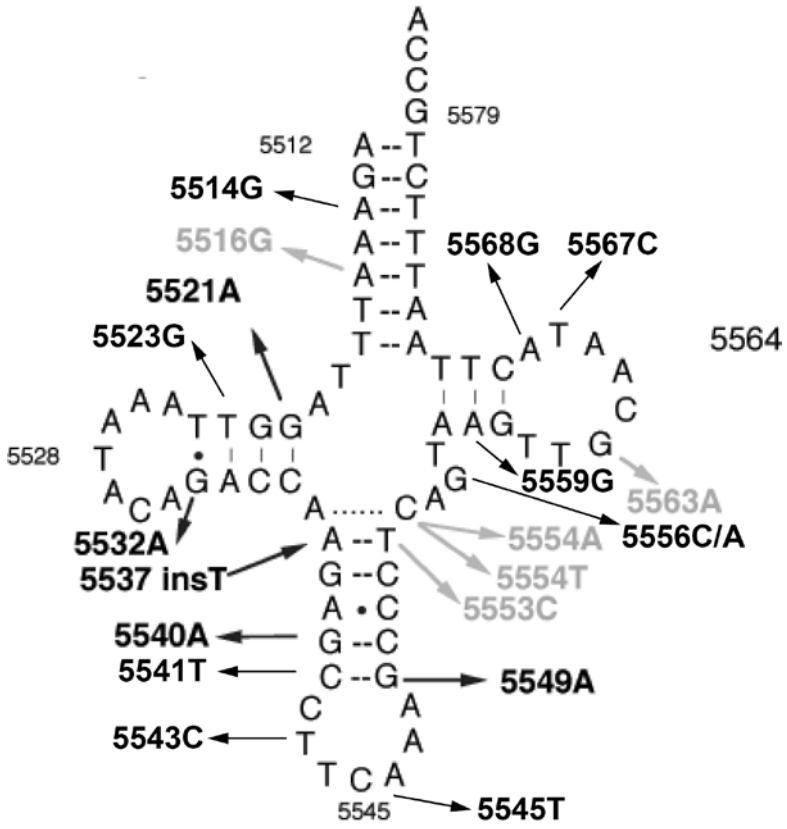

Figure 1.3 – Location of pathological mutations in MT-TW within the secondary structure of mt-tRNA^{Trp}.
Schematic diagram of the secondary structure of mt-tRNA^{Trp}. The locations of pathological mutations are in black and other known polymorphisms are in grey. Figure updated from (Pütz, Dupuis, Sissler, & Florentz, 2007).

1.1.3 Mitochondrial Transcription

The mtDNA heavy and light strands each have a predominant promoter for transcription, HSP and LSP respectively. mtDNA transcription from HSP and LSP is bidirectional however transcription predominantly occurs in the direction indicated (**Figure 1.1**) allowing transcription of mtDNA in both directions simultaneously (Chang, Hixson, & Clayton, 1986). Mitochondrial transcription is performed by mitochondrial RNA polymerase and requires the transcription factors TFAM, TFB1M and TFB2M (Falkenberg et al., 2002; R. P. Fisher & Clayton, 1985). TFAM is a bidirectional mitochondrial transcription factor that associates with upstream binding sites of HSP and LSP promoters and is essential for mitochondrial transcription (Robert P. Fisher, Topper, & Clayton, 1987). TFAM is also required for packaging mtDNA into nucleoids a process that is involved in mtDNA copy number control

(Ekstrand et al., 2004). mtDNA genes are arranged end-to-end with few non-coding nucleotides between genes and therefore mtDNA genes are transcribed in long polycistronic transcripts containing multiple gene sequences that are cleaved into individual gene transcripts prior to mitochondrial translation (Anderson et al., 1981). Open reading frame sequences are cleaved from polycistronic transcripts in order to obtain mRNA transcripts. During this process, the 3' stop codon of mRNA transcripts is truncated and requires subsequent adenylation in order to achieve mature mRNA transcripts that can be translated (Nagaike, Suzuki, Katoh, & Ueda, 2005).

1.1.4 Mitochondrial translation

Mitochondrial protein translation is required for the synthesis of the 13 OXPHOS subunits encoded by the mtDNA. The machinery required for mitochondrial translation is encoded by both mtDNA and nDNA. mtDNA encodes ribosomal RNA (mt-rRNA) subunits 12S and 16S, and 22 mt-tRNAs as mentioned previously. All of the other functional apparatus required for mitochondrial translation is encoded by nDNA such as ribosomal assembly proteins, aminoacyl-tRNA synthetases, tRNA modifying enzymes, initiation factors, elongation factors, termination factors and ribosomal recycling factors.

Several characteristics of mitochondrial translation make it unique and are not observed in prokaryotic or eukaryotic cytoplasmic translation. First of all, the genetic code of mtDNA, whilst similar to the universal coding sequence of mammalian nDNA, has some differences. In nDNA, AUG is the only codon for the initiator methionine. In mtDNA, AUA and AUG code for initiator methionine. AUU can also code for methionine during initiation but codes for isoleucine during mitochondrial elongation. UGA encodes a stop codon in nDNA but encodes tryptophan in mtDNA. Finally AGA and AGG codons encode arginine in nDNA but are not recognized by any mt-tRNAs (Osawa, Jukes, Watanabe, & Muto, 1992) (**Table 1.2**).

Amino Acid	nDNA	mtDNA	Amino Acid	nDNA	mtDNA
Phe	UUU	UUU	**Tyr**	UAU	UAU

	UUC	UUC		UAC	UAC
Leu	UUA	UUA	**Stop**	UAA	UAA
	UUG	UUG		UAG	UAG
	CUU	CUU		UGA	
	CUC	CUC	**His**	CAU	CAU
	CUA	CUA		CAC	CAC
	CUG	CUG	**Gln**	CAA	CAA
Ile	AUU	AUU		CAG	CAG
	AUC	AUC	**Asn**	AAU	AAU
	AUA			AAC	AAC
Met	AUG	AUA	**Lys**	AAA	AAA
		AUG		AAG	AAG
Val	GUU	GUU	**Asp**	GAU	GAU
	GUC	GUC		GAC	GAC
	GUA	GUA	**Glu**	GAA	GAA
	GUG	GUG		GAG	GAG
Ser	UCU	UCU	**Cys**	UGU	UGU
	UCC	UCC		UGC	UGC
	UCA	UCA	**Trp**	UGG	UGA
	UCG	UCG			UGG
Pro	CCU	CCU	**Arg**	CGU	CGU
	CCC	CCC		CGC	CGC
	CCA	CCA		CGA	CGA
	CCG	CCG		CGG	CGG
Thr	ACU	ACU		AGA	~~AGA~~
	ACC	ACC		AGG	~~AGG~~
	ACA	ACA	**Ser**	AGU	AGU
	ACG	ACG		AGC	AGC
Ala	GCU	GCU	**Gly**	GGU	GGU
	GCC	GCC		GGC	GGC
	GCA	GCA		GGA	GGA
	GCG	GCG		GGG	GGG

Table 1.2 – Comparison of mtDNA and nDNA codons.
Summary of codons in human nDNA and mtDNA. Codons that differ between genomes are highlighted in red. AGA and AGG are not used in mtDNA (line through). AUU (blue) can code for isoleucine of methionine in mtDNA.

Mitochondrial mRNAs are distinct from nDNA encoded mRNA sequences as they have either no or few 5'untranslated nucleotides, are uncapped and the poly(A) tail either immediately follows the stop codon or forms part of the stop codon (K. Grohmann, F.

Amalric, S. Crews, 2013; Montoya, Ojala, & Attardi, 1981). A further difference of mitochondrial translation in seen in the small 28S mitochondrial ribosomal subunits where mRNA binding is sequence independent and does not require initiation factor binding or initiation tRNA (H. X. Liao & Spremulli, 1989).

Prior to mitochondrial translation, several other processes are required such as tRNA maturation, tRNA modification and ribosomal assembly. mt-tRNAs are transcribed as part of long polycistronic transcripts containing rRNA, tRNA and mRNA transcripts. tRNAs are located between mRNA and rRNA sequences and must be separated from rRNA and mRNA sequences. This process is performed by 5' and 3' endonucleases, RNaseP and RNase Z respectively to form mature mt-tRNAs (Dubrovsky, Dubrovskaya, Levinger, Schiffer, & Marchfelder, 2004; Vilardo et al., 2012). Following this process, mt-tRNAs are post-transcriptionally modified. Post-transcriptional modifications are required for mt-tRNA stability and function. Several types of modifications have been identified in mt-tRNAs such as pseudouridylation by PUS1 (Bykhovskaya, Casas, Mengesha, Inbal, & Fischel-Ghodsian, 2004), 5-carboxymethylaminomethylation by MTO1 (Tischner et al., 2015), thiolation by MTU1 (Sasarman, Antonicka, Horvath, & Shoubridge, 2011) and formylation by MTFMT (Tucker et al., 2011). Finally, mt-tRNAs must be 'charged' with their cognate amino acid. This is performed by aminoacyl-tRNA synthetases that catalyse the aminoacylation of mt-tRNA with their cognate amino acid (**see section 1.1.6**)

Mitochondrial ribosome assembly is required for mitochondrial protein translation. Mitochondrial ribosomes interact with the inner mitochondrial membrane to allow insertion of newly synthesized OXPHOS subunits into the inner mitochondrial membrane (H. X. Liao & Spremulli, 1989). Like OXPHOS complexes, the mitochondrial ribosome contains multiple subunits and requires multiple assembly factors. Human mitochondrial ribosomes are made up of small 28S and large 39S ribosome subunits and mt-tRNAs. The 28S subunit is assembled from 30 proteins and the mtDNA encoded 12S rRNA (E C Koc et al., 2000).

The 39S subunit is assembled from 48 proteins and the mtDNA encoded 16S rRNA (Emine Cavdar Koc et al., 2001). To date little is known about mitochondrial ribosome assembly however it is known that ERAL1 and C4orf14 are required for assembly of the 28S subunit (Dennerlein, Rozanska, Wydro, Chrzanowska-Lightowlers, & Lightowlers, 2010; He et al., 2012) and MTG1, OBGH1 and C7orf30 are required for assembly of the 39S subunit in humans (Kotani, Akabane, Takeyasu, Ueda, & Takeuchi, 2013; Rorbach, Gammage, & Minczuk, 2012).

The process of mitochondrial translation can be divided into four stages: initiation, elongation, termination and ribosome recycling. The exact mechanism of mitochondrial protein synthesis is poorly understood however the current working model of mitochondrial protein synthesis is based upon the bacterial model of protein synthesis along with some additional studies performed using mitochondria (L. Van Den Heuvel, Smits, & Smeitink, 2010).

1.1.4.1 Initiation

The exact mechanism of mitochondrial translation initiation is poorly understood. What is known is that in mammals two mitochondrial initiation factors have been identified, mtIF2 and mtIF3, and are required for this process. Based upon the most current model of initiation, mitochondrial initiation translation factor 3 (mtIF3) aids dissociation of mitochondrial 55S ribosomes into its two component subunits by binding the 28S subunit (E C Koc & Spremulli, 2003) (**Figure 1.4, step 1**). Subunit dissociation stimulates formation of the initiation complex and makes the 28S subunit interface accessible for N-formylmethionine-$tRNA^{Met}$ (fMet-$tRNA^{Met}$) (**Figure 1.4, step 2**). As mentioned previously, mitochondrial mRNAs are uncapped and have limited 5'UTR. It is therefore not yet known how mitochondrial ribosomes bind mRNAs or how they are directed to start codons. mtIF3 is thought to aid the mRNA ribosome binding process and to ensure that the start codon is positioned correctly within the ribosomal peptidyl (P) site. Mitochondrial initiation translation

factor 2 (mtIF2) then facilitates fMet-tRNA^{Met} binding to the 28S subunit in the presence of mRNA, a process that is enhanced by GTP binding (Hua Xin Liao & Spremulli, 1990; Ma & Spremulli, 1995) (**Figure 1.4, step 3**). The 39S subunit then binds to the 28S subunit (**Figure 1.4, step 4)**. It is thought that through doing so mtIF3 dissociates (**Figure 1.4, step 5**) (Haque, Grasso, & Spremulli, 2008). Finally, 39S binding also triggers GTP hydrolysis of mtIF2 causing mtIF2 dissociation (**Figure 1.4, step 6**) completing the translation in initiation phase.

1.1.4.2 Elongation

Mitochondrial translation elongation requires three elongation factors EFTu, EFTs and EFG1. EFTu binds 'charged' mt-tRNAs and GTP to form a ternary mt-tRNA-EFTu-GTP complex (**Figure 1.4, step 7**). EFTu is thought to be vital for ensuring mischarged tRNAs are not incorporated in mitochondrial translation (Nagao, Suzuki, & Suzuki, 2007). EFTu protects the aminoacyl-tRNAs from hydrolysis and directs the aminoacyl-tRNAs to the mitochondrial ribosomal acceptor (A) site located in the 28S subunit (**Figure 1.4, step 10**). At the A site, mitochondrial mRNA is decoded through codon-anticodon interactions with the aminoacyl-tRNA. The mitochondrial ribosome stimulates GTP hydrolysis on EFTu-GTP and EFTu-GDP dissociates from the ribosome (**Figure 1.4, step 8**). EFTu-GDP is recycled by the nucleotide exchange protein EFTs, regenerating active EFTu-GTP (**Figure 1.4, step 9**). After EFTu-GDP is released from the ribosome, the 3' end of the aminoacyl-tRNA moves into the peptidyl transfer centre of the 39S ribosome subunit catalysing a peptide bond between the peptide growing peptide sequence and the amino group of the aminoacyl-tRNA (**Figure 1.4, step 11**). The ribosome then advances one codon along the mRNA in a translocation step. This involves EFG1-GTP, which catalyses the translocation step though hydrolysis of GTP. In the translocation step the tRNAs located in P and A sites are shifted into the P and 'exit' (E) sites respectively as the mitoribosome advances one codon along the mRNA (**Figure 1.4, step 12**). The tRNA located in the E site then dissociates from the

ribosome (**Figure 1.4, step 13**). The elongation process is then complete and is repeated until the mRNA stop codon is reached (**Figure 1.4, step 14**).

1.1.4.3 Termination

Mitochondrial translation termination involves mitochondrial release factors RFa/RF1L. Mitochondrial translation termination occurs in humans when either of the mRNA stop codons, UAG or UAA, enters the ribosomal A site. RF1a/RF1L recognizes the mRNA stop codon (**Figure 1.4, step 15**) and catalysis the hydrolysis of the ester bond between the P site tRNA and the newly synthesized peptide, a process that requires GTP hydrolysis. The newly synthesized peptide and RF1a/RF1L then dissociate from the ribosome (**Figure 1.4, step 16**) completing the mitochondrial translation termination step.

1.1.4.4 Ribosomal Recycling

Following mitochondrial translation termination, the mitochondrial ribosomal machinery is then recycled. This process is performed by mtRRF and mtEFG2-GTP. Together mtRRF and mtEFG2-GTP facilitate dissociation of the mitochondrial ribosomal subunits, tRNA and mRNA (**Figure 1.4, step 17**). Following dissociation of the ribosomal machinery, GTP hydrolysis of mtEFG2-GTP is required to allow dissociation from the 39S ribosomal subunit (**Figure 1.4, step 18**) (Bhargava, Templeton, & Spremulli, 2004). Ribosomal recycling allows the process of mitochondrial translation to begin again.

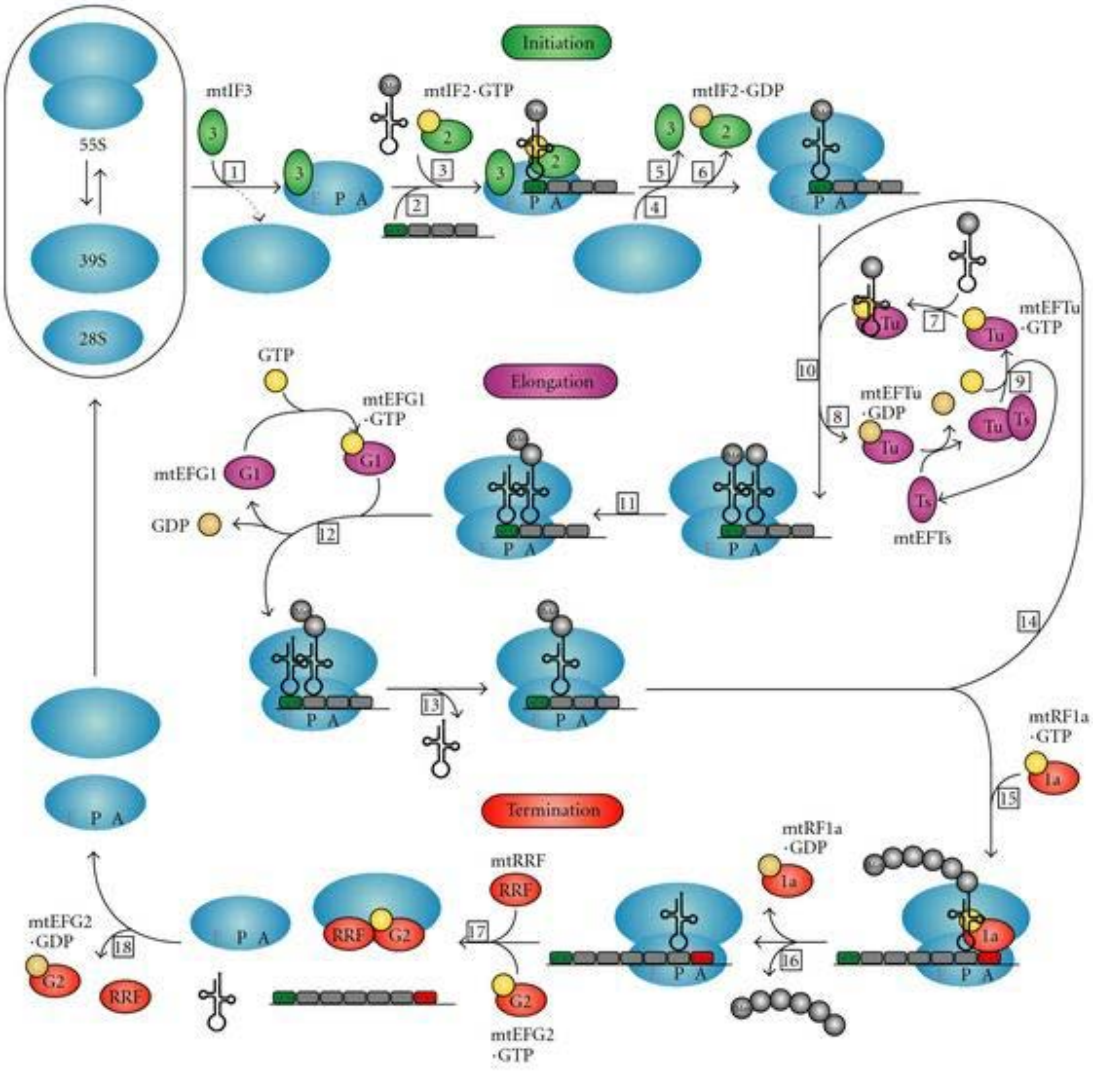

Figure 1.4 – Human mitochondrial protein synthesis mechanism.
See text for description. Figure from Van Den Heuvel et al. 2010.

1.1.5 Mutations in mitochondrial translation genes

As mentioned previously over 300 mutant variants have been identified in mtDNA. Loss of function mutations in mtDNA encoded mt-tRNAs and mt-rRNAs cause dysfunction to mitochondrial translation. However, the vast majority of the mitochondrial translation apparatus is encoded by nDNA. Several patients have been identified with mutations in nDNA genes required for mitochondrial protein synthesis including genes encoding the mitochondrial elongation factors EFG1 (*GFM1*), EFTu (*TFSM*) and EFTs (*TUFM*) and genes encoding the mitochondrial ribosomal subunits such as *MRPS16* and *MRPS22*. However, the clinical pathology associated with loss-of-function mutations in genes

required for mitochondrial translation is highly variable. For instance, EFG1 mutations have been associated with hepatoencephalopathy (L. P. Van Den Heuvel, Ph, Shoubridge, & Ph, 2004) whilst MRPS16 mutations have been reported to cause cardiomyopathy and tubulopathy (Saada et al., 2007). Here mutations in different elements of the mitochondrial translation pathway cause differing clinical pathologies.

Another example of this is the varied clinical pathologies associated with mutations in the mitochondrial tRNA synthetase (mtRS) genes. 17 mtRS genes have been identified: *AARS2*, *CARS2*, *DARS2*, *EARS2*, *FARS2*, *HARS2*, *IARS2*, *LARS2*, *MARS2*, *NARS2*, *PARS2*, *RARS2*, *SARS2*, *TARS2*, *VARS2*, *WARS2* and *YARS2*. Two cytoplasmic aminoacyl tRNA synthetases also function in mitochondria: glycyl-tRNA synthetase (*GARS*) and KARS lysyl-tRNA (*KARS*). There are 22 mt-tRNA genes one for each of the 20 amino acids required for mitochondrial protein synthesis with two mt-tRNA^{Ser} and mt-tRNA^{Leu} genes. To date no mitochondrial homolog of glutaminyl-tRNA synthetase has been identified (what would be called *QARS2*). mt-tRNA^{Gln} is aminoacylated via an indirect pathway where mitochondrial glutamyl-tRNA synthetase first misaminoacylates mt-tRNA^{Gln} with glutamate forming mt-Glu-tRNA^{Gln}. It is thought that misaminoacylated mt-Glu-tRNA^{Gln} is subsequently transamidated to form mt-Gln-tRNA^{Gln}, a process that requires the hGatCAB heterotrimer (Nagao, Suzuki, Katoh, Sakaguchi, & Suzuki, 2009). To date, patients with mutations in all of the mtRS genes, including GARS and KARS, have been identified except for mitochondrial tryptophanyl-tRNA synthetase (*WARS2*, the subject of this thesis). Here I review the reported patients identified with mutations in mtRS genes and associated clinical pathologies as this is the primary focus of this thesis.

1.1.5.1 AARS2

AARS2 encodes mitochondrial alanyl-tRNA synthetase (mt-AlaRS). Mt-AlaRS as well as containing a catalytic aminoacylation domain is unique in having an additional editing domain. The mt-AlaRS catalytic domain is accessible to not only alanine but also serine

and glycine. The editing domain is required to deacetylate mischarged mt-tRNA^{Ala} and prevent mistranslation of serine or glycine for alanine during mitochondrial translation of mitochondrial encoded transcripts (Guo et al., 2009).

In 2011 Götz *et al* reported three patients from two families with early-onset hypertrophic cardiomyopathy and lactic acidosis caused by mutation(s) in *AARS2*. The first patient was homozygous for the Arg<592>Trp mt-Ala-RS mutation and the other two patients were siblings compound heterozygous for the Arg<592>Trp and Leu<155>Arg mt-Ala-RS mutations. The patient homozygous for the Arg<592>Trp mutation died at 10 months of age whilst the siblings with compound heterozygous mt-AlaRS mutations died perinatally or *in utero* each with severe hypertrophic cardiomyopathy and lactic acidosis. The Arg<592>Trp mutation is located at the surface of the mt-AlaRS editing domain and is predicted to effect the binding or recognition of mischarged mt-tRNA^{Ala}. The Leu<155>Arg is located in the mt-AlaRS catalytic domain and is predicted to be a total loss-of-function allele likely explaining the increased severity of the compound heterozygous siblings' disease. Post-mortem autopsy identified OXPHOS deficiencies in the heart, brain and muscle of the described patients with obvious hypertrophic cardiomyopathy. In all cases brain and muscle morphology was normal. Interestingly, cultured fibroblast or myoblasts from patients did not harbour OXPHOS defects. Given that all three patients reported by Götz *et al*, carried at least one copy of the Arg<592>Trp allele it was speculated that the observed hypertrophic cardiomyopathy pathology associated with AARS2 mutations is resultant of mitochondrial mistranslation rather than inhibition of mitochondrial translation (Götz et al., 2011).

Later in 2014, Dallabona *et al* reported 6 patients with *AARS2* mutations with progressive leukoencephalopathy and ovarian failure in females. The age of onset for these 6 patients ranged from 3 to 40 years of age. No evidence of hypertrophic cardiomyopathy or lactic acidosis were reported in any of the 6 patients. 5 out the 6 patients were female and had

amenorrhea due to ovarian failure. Only two patients were extensively investigated for mitochondrial defects. Both patients had COX negative skeletal muscle fibres and reduced CIV activity and steady state levels in skeletal muscle homogenates. Fibroblasts from one patient were cultured and had normal OXPHOS complex levels and mitochondrial respiration showing no evidence of mitochondrial dysfunction. All 6 patients' mutations had *AARS2* mutations and 5 out 6 patients had mutations in both catalytic and editing domains. Functional studies were performed in yeast for 3 mutations, Phe<50>Cys missense, Arg521* nonsense and Leu<155>Arg missense, and all were shown to be loss-of-function alleles (Dallabona et al., 2014).

The clinical associations with *AARS2* mutations reported by these two studies suggest that mutations in *AARS2* can manifest in at least two distinct pathologies. The question is what dictates the clinical outcome of a patient with mutant *AARS2*? It was suggested by Götz *et al* that *AARS2* mutations in the mt-AlaRS editing domain will cause mitochondrial mistranslation and that this is the explanation for cardiac specific association. However, Dallabona *et al* also identified mutations within the mt-AlaRS editing domain that were associated with brain and ovarian abnormalities independent of cardiac phenotypes. A clear difference between the patients observed in both studies is the age-of-onset. The patients with leukoencephalopathy did not have cardiac dysfunction and had varied age of onset from 3 to 40 years of age. The patients with cardiac phenotypes all died within 10 months of age. What we do not know is whether the mutations that caused the cardiac phenotypes would also cause leukoencephalopathy if life were prolonged beyond 10 months of age. In order to address this question brain and heart specific mouse models would have to be utilized.

1.1.5.2 CARS2

CARS2 encodes mitochondrial cysteinyl-tRNA synthase (mt-CysRS). The first patients identified with mutations in *CARS2* were reported in 2014 by Hallmann *et al*. Hallmann *et*

al report two patients with childhood onset myoclonic and generalized tonic-clonic seizures, progressive tetraparesis, visual and hearing impairment and cognitive decline. Both patients died prematurely, one died at 28 years of age and the other died at 18 years of age. MRI scans showed non-specific white matter lesions in both patients. One patient had slightly elevated blood lactate levels. Patient muscle biopsies or fibroblasts were not taken. The siblings were homozygous for an Ala<219>Thr *CARS2* mutation. The Ala<219>Thr codon is split between *CARS2* exon 6 and exon 7 with the mutated nucleotide being located in the last nucleotide of exon 6. Subsequent studies showed that the Ala<219>Thr mutation causes a splicing defect resulting in skipping of exon 6 and a frame shift deletion of 28 residues from Gly191_Pro218. This deletion is located within a conserved motif predicted to be required for tRNA stabilization (Hallmann et al., 2014).

A third patient was identified with a mutation in *CARS2*, born from unrelated parents, in 2015 by Coughlin *et al*. The patient had epileptic encephalopathy and complex movement disorder. Symptoms were first reported at 5 weeks of age. Brain MRI scans showed progressive atrophy of white matter and the cortex. The patient had CI, CIII and CIV OXPHOS deficiencies in liver with a non-significant trend for reduced CI and CIV activity in muscle. Interestingly mtDNA:nDNA content in patient skeletal muscle was over 3-fold increased compared to age matched controls suggesting a compensatory increased in mitochondrial biogenesis in skeletal muscle possibly explaining the non-significantly different OXPHOS complex activities observed in skeletal muscle. Incomplete assembly of CV was reported in both patient skeletal muscle and cultured fibroblasts. The patient was found to be compound heterozygous for *CARS2* mutations Glu<217>del and Pro<251>Leu. Both mutations were highly conserved amino acid residues located within the *CARS2* aminoacylation catalytic domain (Coughlin et al., 2015).

In all three patients reported with *CARS2* mutations, symptoms of complex and progressive epileptic disorders with abnormal brain pathology were reported. There is a clear difference

again in the age of onset of patients from the two different families that may be explained by the severity of the reported 'loss-of-function' mutations. Coughlin *et al* reported that the patient had combined OXPHOS deficiencies in the liver and reduced blood albumin levels suggesting liver dysfunction may also be associated with *CARS2* loss-of-function alleles. No data regarding liver function or OXPHOS levels were reported from the patients identified in the Hallmann *et al* paper making it impossible to validate this observation. Most interesting of all may be the increased mtDNA:nDNA copy number observed in the skeletal muscle of the Coughlin patient, suggesting that skeletal muscle may compensate for loss of *CARS2* function through up-regulation of mitochondrial biogenesis preventing significant OXPHOS deficiency.

1.1.5.3 DARS2

DARS2 encodes mitochondrial aspartyl-tRNA synthetase (mt-AspRS). Since 2007, 9 reports have identified patients with *DARS2* mutations. The original study was performed by Scheper *et al* identifying mutations in *DARS2* as the cause of leukoencephalopathy with brain stem and spinal cord involvement and lactate elevation (LBSL) in individuals from 30 unrelated families. Additional clinical observations reported were cerebellar ataxia, spasticity and variable degrees of cognitive impairment. The age of onset varied from childhood to adulthood. Elevated lactate was observed in affected white matter but not CSF or whole blood. Muscle biopsies and cultured myoblast or fibroblast from patients showed no OXPHOS deficiencies. In almost all LBSL patients identified in this study had one copy of a common splice site mutation as well as an additional missense allele. The common splice site mutation was shown to affect splicing of exon 3 leading to a frameshift and protein truncation. The common splice site mutation is thought to be 'leaky' allowing a proportion of mtAspRS to remain whilst the associated missense mutations were thought to be loss-of-function (Scheper et al., 2007). Studies from Isohanni *et al* and Martikainen *et al* have also identified LBSL patients with compound heterozygous for *DARS2* mutations

and in both cases, patients carried one copy of the common splice site allele with an additional missense allele (Isohanni et al., 2010; Martikainen, Ellfolk, & Majamaa, 2013).

Several additional reports have documented compound heterozygous LBSL patients with one copy of the splice site mutation with varied clinical presentations. Lin *et al* and Tzoulis *et al* have identified compound heterozygous *DARS2* patients with leukoencephalopathy with brainstem and spinal cord involvement with normal lactate (Lin et al., 2010; Tzoulis et al., 2012). Labauge *et al* reported an adult, compound heterozygous *DARS2* patient with the MRI profile of LBSL that was clinically asymptomatic (Labauge, Dorboz, Eymard-Pierre, Dereeper, & Boespflug-Tanguy, 2011).

To date 3 studies have documented LBSL patients homozygous for *DARS2* mutations with varying degrees of disease severity. Reports from Synofzik *et al* and Kohler *et al* identified LBSL patients with homozygous DARS2 missense mutations that presented with a relatively benign disease course (Synofzik et al. 2011; Kohler et al. 2015). Miyake *et el* identified 3 LBSL patients homozygous for the common DARS2 splice site mutation that presented with severe forms of LBSL associated with profound cognitive impairments (Miyake et al., 2011).

Since Scheper *et al*'s first study where all LBSL patients had *DARS2* mutations, there has been a bias in identifying *DARS2* patients dependent upon fulfilling the LBSL profile. Subsequent reports have identified patients with *DARS2* mutations that fulfil some but not all of the original LBSL criteria such as variable brain pathology, age or onset, normal white matter lactate and varied additional associated symptoms. That being said there is clearly an association between *DARS2* mutations and brain dysfunction with specific white matter involvement. Van Berge *et al* attempted to explain this association by studying the common intron *DARS2* splice site mutant in neuronal and non-neuronal cell lines showing that a greater proportion exon 3 skipping occurred in mutant neuronal cell lines than mutant cell

lines from other origins (van Berge et al., 2012). However subsequent identification of LBSL patients with homozygous DARS2 missense mutations (that do not influence splicing) indicates that tissue specific regulation of *DARS2* splicing is not the cause of the white matter penetrance of all *DARS2* mutations.

1.1.5.4 EARS2

EARS2 encodes mitochondrial glutamyl-tRNA sythetase (mt-GluRS). The first patient with mutations in *EARS2* presented with distinct brain MRI alterations notably leukoencephalopathy with thalamus and brain stem involvement and high lactate (LTBL). A further 11 patients from unrelated families with similar MRI phenotype were also found to be compound heterozygous for deleterious *EARS2* mutations. In these cases, the brain phenotypes were distinct with asymmetric abnormalities of cerebellar white matter, thalamus, midbrain, pons, medulla oblongata and cerebral white matter. In all patients, blood lactate levels were elevated and CI, CIII and CIV OXPHOS defects were observed in both skeletal muscle biopsies and fibroblast cultures. The progression of the disease in these patients could be separated out into two groups 'mild' and 'severe'. All patients had infantile onset with rapid progression of the disease. 'Mild' patients showed partial recovery by regaining milestones from 2 years of age including MRI improvement and lowered blood lactate levels. 'Severe' patients however showed clinical stagnation, brain atrophy and progressively increased lactate levels. Of these 11 patients, 15 different *EARS2* mutations were identified, all of which were predicted to be deleterious. 6 of these patients carried one copy of the Arg<108>Trp low frequency allele found in 3 out of 13500 cases within the wider population (Steenweg et al., 2012).

Since this initial report further patients with *EARS2* mutations have been reported. In 2016 Sahin *et al* identified two novel *EARS2* mutation in two siblings with 'mild' LTBL (Şahin et al., 2016). Again in 2016, Taskin *et al* identified a patient homozygous for the low frequency *EARS2* Arg<108>Trp allele with early-onset mild type LTBL (Taskin et al., 2016). Talim *et*

al identified a patient with a homozygous *EARS2* missense mutation causing the most severe reported cases of LTBL to date with combined severe infantile multisystem disease involving brain and liver and premature death at 3 months of age (Talim et al., 2013).

Taken together these reports indicate that mutations in *EARS2* cause a distinct clinical pathology namely LTBL to differing degrees of severity in humans. However again it must be taken into account that patients are first being identified with LTBL before whole-exome sequencing meaning that identification of clinical pathologies associated with *EARS2* mutations is biased by prior diagnosis. Nevertheless, given the sheer number of different mutations identified within differing *EARS2* functional domains, (mitochondrial targeting sequence, anticodon binding domain and catalytic domain) is further evidence that there is a strong association between loss-of-function *EARS2* mutations and the distinct clinical pathology LTBL.

1.1.5.5 FARS2

FARS2 encodes mitochondrial phenylalanyl-tRNA synthetase (mt-PheRS). Multiple studies have reported patients with *FARS2* mutations. In 2012 Elo *et al* reported two patients with fatal epileptic mitochondrial encephalopathy reminiscent of Alper's Syndrome caused by compound heterozygous Iso<329>Thr and Asp<391>Val missense mutations in *FARS2*. Muscle biopsy was taken from one patient showing reduced CIV activity (Elo et al., 2012). Shamseldin *et al* identified 3 siblings from consanguineous parents homozygous for the Tyr<144>Cys missense mutation again with severe mitochondrial encephalopathy (Shamseldin et al., 2012). Patients from both studies died before 2 years of age. Elo *et al* also performed functional studies for a Tyr<144>Cys FARS2 variant previously reported by Shamseldin *et al* showing that this mutation was likely pathogenic.

Almalki *et al* identified a patient with novel *FARS2* mutations causing early-onset epilepsy and isolated CIV deficiency in muscle. The CIV deficiencies were maintained in patient

myoblast but not fibroblast cultures. The patient was compound heterozygous for a 88kb genomic deletion variant resulting in partial deletion of LYRM4 and FARS2 and an Asp<325>Tyr FARS2 missense variant (Almalki et al., 2014). LYRM4 encodes a protein required for mitochondrial iron-sulphur protein biosynthesis and has been identified in patients with combined OXPHOS deficiencies (Lim et al., 2013). It is therefore not possible to know whether identified patient has combined OXPHOS deficiency due to loss of FARS2 and/or LYRM4 function.

In 2015, Yang *et al* reported 4 patients from a Chinese consanguineous family with a homozygous Asp<124>Tyr FARS2 missense mutation causing hereditary spastic paraplegia (HSP). All 4 reported patients had 'pure' HSP with symptoms including progressive lower limb spasticity, pyramidal weakness with hyperreflexia, extensor plantar responses and scissors gaits(Yang et al., 2016).

Finally, in 2016 Walker *et al* identified a patient with juvenile onset refractory epilepsy and progressive myoclonus caused by compound heterozygous Phe<85>Ala and His<135>Asp *FARS2* missense mutations. Clinical and neuropathological symptoms for this patient closely resemble those reported by Elo *et al* and Almalki *et al* with observations of progressive myoclonus, cortical necrosis. However, in this patient the disease progressed slower and the patient died at 15 years of age (Walker et al., 2016).

These reports demonstrate a relatively specific association between *FARS2* mutations and phenotypes associated with central nervous system. However, there appears to be some variability in the presentation of *FARS2* patients with regard to neurological pathophysiology and age of onset. Yang *et al* showed increased mt-PheRS protein in Purkinje cells of the rat cerebellum suggesting that loss of Purkinje cells may be the cause of HSP disorders (Yang et al., 2016).

1.1.5.6 HARS2

HARS2 encodes mitochondrial histidyl-tRNA synthetase (mt-HisRS). There is only one reported family affected by *HARS2* mutations and it was shown to be causal for Perrault Syndrome. Perrault syndrome is characterized by ovarian dysgenesis in females and sensorineural hearing loss is both males and females. Perrault syndrome is a heterogeneous recessive disorder that has previously been shown to be caused by mutations *HSD17B4*, *CLPP* and *LARS2* (Jenkinson et al., 2013; Sarah B. Pierce et al., 2010, 2013; Solda et al., 2015). In 2011, Peirce *et al* reported 5 out of 11 siblings with Perrault syndrome each compound heterozygous for two missense mutations Leu<200>Val and Val<368Leu in highly conserved amino acids of *HARS2*. The former mutation also caused missplicing resulting in deletion of 12 codons. Both mutations showed reduced *HARS2* aminoacylation activity. No skeletal muscle biopsies or fibroblasts were cultures in these patients (S B Pierce et al., 2011).

This is the only reported case of *HARS2* mutations causing Perrault syndrome. Further identification of *HARS2* mutations causing Perrault syndrome are required to confirm the tissue specific association. It was suggested by Pierce *et al* that the tissue specificity of the reported *HARS2* mutations may be due differences in tissue specific splicing efficiency however this was purely speculation.

1.1.5.7 IARS2

IARS2 encodes isoleucyl-tRNA sythetase (mt-IsoRS). In 2014, Schwartzentruber *et al* reported 3 patients with cataracts, growth hormone deficiency with short stature, partial sensorineural deafness and peripheral neuropathy (CAGSSS). Patients were homozygous for a Pro<909>Leu missense mutation in *IARS2* located in a highly conserved amino acid found in the *IARS2* anticodon RNA-binding domain. Cultured fibroblasts from patients showed reduced IARS2 protein however no mitochondrial OXPHOS deficiencies were observed and mitochondrial translation was normal compared to controls. No skeletal

muscle biopsies were taken in any of the patients (Schwartzentruber et al., 2014). Further identification of patients with *IARS2* mutations is required to confirm the association with CAGSSS.

1.1.5.8 LARS2

LARS2 encodes mitochondrial leucyl-tRNA synthetase (mt-LeuRS). Mutations in *LARS2*, similarly to *HARS2*, are associated with Perrault Syndrome. In 2013, Pierce *et al* identified four patients with Perrault syndrome caused by *LARS2* mutations. Three patients were siblings from a consanguineous Palestinian family and were homozygous for Thr<522>Asn *LARS2* mutation, a highly conserved amino acid residue located within the catalytic domain. The fourth patient was compound heterozygous for a c.1077delT mutation and c.1886C>T missense mutation causing a Thr<629>Met amino acid change. The c.1077delT mutation causes a frame shift and was shown to be a loss of function allele. The Thr<629>Met amino acid substitution is located within the *LARS2* 'leucine-specific domain' found adjacent to the catalytic loop. This mutation was found to be loss of function in yeast studies. No skeletal muscle biopsies or fibroblast cultures were taken from patients (Sarah B. Pierce et al., 2013).

The association between *LARS2* and Perrault syndrome was further validated in an independent study performed by Solda *et al* in 2015. Solda *et al* identified two siblings with Perrault Syndrome both of whom were heterozygous for novel missense mutations in *LARS2*. Again no functional analysis was performed using primary tissue or cells from patients (Solda et al., 2015).

1.1.5.9 MARS2

MARS2 encodes mitochondrial methionyl-tRNA synthetase (mt-MetRS). Mutations in *MARS2* were found to be associated with autosomal recessive spastic ataxia with leukoencephalopathy (ARSAL) a condition found in 54 patients from 38 French-Canadian families (Bayat et al., 2012; Thiffault et al., 2006). Brain MRI showed cerebellar atrophy and

in some cases cortical atrophy, leukoencephalopathy and corpus callosum thinning were also observed. Complex *MARS2* genomic rearrangements were identified in ARSAL patients including homozygous duplication or compound heterozygous duplication-deletion alleles. Whilst increased *MARS2* mRNA expression was observed in patient cells, reduced mt-MetRS and CI deficiency was also noted. The age of onset in patients varied from 2 to 59 years of age. Patients with duplication-deletion *MARS2* alleles had earlier onset disease compared to those with only duplication alleles.

Webb *et al* identified additional patients with *MARS2* mutations in 2015 that presented with clinical features distinct form ARSAL patients. Two siblings with developmental delay, poor growth and sensorineural hearing loss were identified with compound heterozygous *MARS2* mutations. Brain MRI in the two patients noted quadriventricular dilation, white matter change, cerebral atrophy and high arched, posteriorly thin corpus callosum. Both patients had one copy of nonsense Gln<184* and missense Arg<142>Trp *MARS2* variants. Patient fibroblasts showed CI and CIV deficiencies (Webb et al., 2015).

There appears to be genotype-phenotype relationship in *MARS2* patients. Patients with complex duplication/deletion *MARS2* alleles present with ARSAL and have CI deficiencies in cell cultures. The siblings with the compound heterozygous MARS2 missense & nonsense alleles have developmental delay, poor growth, sensorineural hearing loss, neuropathology and CI & CIV deficiencies in cell cultures. There is a clear association between the *MARS2* duplication alleles and ARSAL. However, it is not completely clear whether the complex duplication/deletion alleles are gain or loss-of-function. Further identification of patients with loss-of-function *MARS2* alleles is required to confirm the association.

1.1.5.10 NARS2

NARS2 encodes mitochondrial asparaginyl-tRNA synthetase (mt-AsnRS). Several reports in recent years have identified mutations in *NARS2* as causal for various human pathologies. In 2014 Sofou *et al* identified a patient with Alper's syndrome caused by a homozygous Pro<214>Leu missense mutation in *NARS2*. Alper's syndrome is progressive neurodegenerative disorder characterized by diffuse degeneration of cerebral grey matter. Several additional symptoms were reported including: generalized seizures of multiple types, renal dysfunction, increase blood lactate levels and cortical visual impairments causing blindness. Generalized reductions in OXPHOS enzyme activities were shown in skeletal muscle homogenates but the steady state protein levels of OXPHOS subunits were within the normal range (Sofou et al., 2015).

In 2015, Vanlander *et al* identified two consanguineous patients with a homozygous missense mutation in *NARS2* that caused disrupted exon splicing leading to complete exon skipping of exon 7 and part of exon 8 in *NARS2* mRNA. The two siblings presented with different phenotypes, one with mild intellectual disabilities and childhood epilepsy and one with severe myopathy (Vanlander et al., 2015).

Finally, in 2015, Simon *et al* identified *NARS2* variants in two unrelated families associated with non-syndromic deafness (homozygous Val<213>Phe missense) and Leigh syndrome (compound heterozygous: Tyr323* + Asn<381>Ser). Leigh syndrome is a neurodegenerative disorder with characteristic symmetric, bilateral lesions located in the basal ganglia, thalamus and brain stem. Simon *et al* showed reduced mt-tRNA^{Asn} steady state levels and reduced oxygen consumption rates in fibroblast isolated from one of the two Leigh syndrome patients. Additionally general reductions in OXPHOS enzyme activities were observed in whole muscle lysates from the same patient (Simon et al., 2015).

Taken together these studies demonstrate some diversity in clinical pathologies associated with mutations in *NARS2*. That being said, neurological dysfunction was reported in all three studies suggesting that the there is an association between NARS2 mutations and neuronal dysfunction.

1.1.5.11 PARS2

PARS2 encodes mitochondrial prolyl-tRNA synthetase (mt-proRS). A single patient has been identified with compound heterozygous mutations in *PARS2* causing Alpers syndrome. The patient was compound heterozygous for a one base insertion c.1130dupC, K<378fs*1 premature stop codon allele and a missense Ser<279>Leu amino acid change allele located in a conserved motif of unknown function in *PARS2*. As well as Alpers syndrome the patient was reported as having reduced height and dilated cardiomyopathy with left ventricular hypertrophic cardiomyopathy resulting in death at 2 years of age due to heart failure. OXPHOS enzyme activity assays were performed using the patients skeletal muscle biopsy showing reduced CI and CIV activity. Further identification of patients with mutations in PARS2 are required in order to confirm the association between *PARS2* and Alpers Syndrome (Sofou et al., 2015).

1.1.5.12 RARS2

RARS2 encodes mitochondrial arginyl-tRNA synthetase (mt-ArgRS). Edvardson *et al* reported the first patients with *RARS2* mutations in 2007. 3 siblings born from consanguineous Sephardic Jewish parents presented with severe infantile encephalopathy associated with pontocerebellar hypoplasia type 6 (PCH6) and multiple mitochondrial OXPHOS defects in skeletal muscle homogenates and fibroblast cultures were observed. Brain MRI showed progressive atrophy in cerebellum, pons, cerebral cortex and white matter. All three patients died before the achieving 2 years of age. The patients were homozygous for a splice site mutation in *RARS2* intron 2 causing skipping of exon 2 and a frame shift (Edvardson et al., 2007).

In 2010, Rankin *et al* reported a patient with PCH6 without the associated muscle OXPHOS defects that was compound heterozygous for *RARS2* mutations. Additionally oedema and other PEHO-like symptoms were reported (Rankin et al., 2010). A further five patients with PCH6 from three unrelated families were identified by Cassandrini *et al* with compound heterozygous mutations in *RARS2*. Whilst their neurological pathology was consistent with previously documented cases, OXPHOS deficiencies were not observed in muscle of fibroblasts from two patients (Cassandrini et al., 2013). Glamuzina *et al* document another PCH6 patient with compound heterozygous *RARS2* mutations again with only mild CIV deficiencies observed in skeletal muscle (Glamuzina et al., 2012).

More varied phenotypes have been reported in *RARS2* patients. Kastrissianakis *et al* reported two siblings with compound heterozygous *RARS2* mutations that displayed typical clinical features of PCH6 that however had distinct neurological pathology including marked supratententorial atrophy, bilateral subdural effusions, decelerating head growth and lack of early pontocerebellar hypoplasia (Kastrissianakis et al., 2013). Nishri *et al* describe two compound heterozygous patients with *RARS2* mutations that again did not have pontocerebellar hypoplasia or muscle OPHOS deficiencies but rather early onset epileptic encephalopathy, postnatal microcephaly and progressive cerebral atrophy (Nishri et al., 2016). Lax *et al* documented the most severe PCH6 patients with additional cardiomyopathy and hydrops fetalis. The siblings were compound heterozygous for *RARS2* mutations and died within two weeks of birth (N.Z. et al., 2015). Finally Li *et al*, identified two siblings with PCH6 caused by homozygous mutations in the *RARS2* promoter causing reduced *RARS2* mRNA (Li et al., 2015).

The association between homozygous and compound heterozygous RARS2 mutations with neuropathology resulting in early death is clear. In most cases *RARS2* mutations are associated with pontocerebellar hypoplasia and early death. In some cases, skeletal muscle OXHOS deficiencies were also observed. The sheer amount and varied nature of

the *RARS2* mutations identified as causing PCH6 shows that this association is not genotype specific and is most likely caused by reduced mt-AspRS function rather than an alternate mechanism.

1.1.5.13 SARS2

SARS2 encodes mitochondrial seryl-tRNA synthetase (mt-SerRS). Mt-SerRS catalyses the esterification of two mitochondrial tRNA isoacceptors: $tRNA^{Ser(AGY)}$ and $tRNA^{Ser(UCN)}$. In 2011, Belostotsky *et al* reported three patients homozygous for an Asp<390>Gly mutation in *SARS2* with a multisystem disorder characterized by prematurity, progressive renal failure leading to electrolyte imbalances, metabolic alkalosis and pulmonary hypertension called HUPRA syndrome (Hyperuricemia, pulmonary hypertension, renal failure and alkalosis). The described mutation was shown to likely impact the acylation of $tRNA^{Ser(AGY)}$ but not $tRNA^{Ser(UCN)}$. All three patients died within 13 months of age and were reported as having additional phenotypes including hypertrophic cardiomyopathy, elevated blood lactate and diabetes mellitus. Skeletal muscle biopsies were attained for two patients showing OXPHOS deficiencies in both cases (Belostotsky et al., 2011). A second report from Rivera *et al* identified a novel *SARS2* mutation in two siblings with HUPRA syndrome. The siblings were homozygous for a Arg<420>His missense mutation proximal to the previously identified mutation. Again hypertrophic cardiomyopathy was observed in both patients that died at around 2 years of age (Rivera et al., 2013).

Taken together these studies demonstrate a convincing link between *SARS2* mutations and HUPRA syndrome. In all of the patients additional to HUPRA symptoms hypertrophic cardiomyopathy was observed equally suggesting a causal link with *SARS2*.

1.1.5.14 TARS2

TARS2 encodes mitochondrial threonyl-tRNA synthetase (mt-ThrRS). In 2014 Diodato *et al* identified two siblings with axial hypotonia and limb hypertonia, psychomotor delay and elevated blood lactate levels. In one patient brain MRI showed a thin corpus callosum and

hyperintense lesions of the globi pallidi at 5 months of age. Both patients died within a few months of birth. Whole-exome-sequencing was used to show that the patients were compound heterozygous for two *TARS2* mutations: a Pro<282>Leu missense mutation and an intronic variant c.695+3A>G predicted to effect *TARS2* mRNA splicing (Diodato et al., 2014). Diodato *et al* reported reduced maximal respiratory rates and reduced mt-ThrRS protein levels in isolated patient fibroblasts compared to controls. Combined reductions in CI, CIII, CIV and CV activities were reported in skeletal muscle homogenates. No additional information about patient symptoms were reported.

Diodato *et al* show that compound heterozygous *TARS2* mutations are causal for encephalopathy in two human patients. Further identification of additional *TARS2* mutations is required to confirm the association between *TARS2* and brain specific pathology.

1.1.5.15 VARS2

VARS2 encodes mitochondrial valyl-tRNA synthetase (mt-ValRS). In 2014 Diodata *et al* identified a patient with microcephaly and epilepsy caused by a homozygous Thr<367>Ile missense *VARS2* mutation located within a conserved amino acid. Additional phenotypes were reported as psychomotor delay, facial dimorphisms and microcephaly. Brain MRI showed hyperintense lesions in periventricular regions, the insulae and frontotemporal right cortex. No abnormalities were detected in skeletal muscle biopsy however maximal respiration levels were decreased in patient fibroblast cultures (Diodato et al., 2014). An additional patient with multiple mitochondrial respiratory chain complex deficiency was identified with possible pathogenic mutations in *VARS2* in a study performed by Taylor *et al*. The identified patient was compound heterozygous for two missense mutations in *VARS2*: Ala<379>Thr and Ala<626>Asp. The patient presented with muscle weakness and hypotonia at 1 year of age but developed central neurological disease including progressive external ophthalmoplegia, ptosis and ataxia. CI and CIV deficiencies were reported in patient cells and muscle biopsy showed mosaic COX-positive fibres. Further functional

studies were not performed for this patient meaning that it is not possible to confirm the pathogenicity of the *VARS2* mutations (Taylor et al., 2014).

There is some evidence that loss-of-function *VARS2* mutations are associated with encephalopathy in humans however further identification of additional patients with novel *VARS2* mutations is required to confirm this association.

1.1.5.16 YARS2

YARS2 encodes mitochondrial tyrosyl-tRNA synthetase (mt-TyrRS). Several patients with different mutations in *YARS2* have been identified. In 2010 Riley *et al* reported 3 patients from 2 unrelated consanguineous families of Lebanese origin with myopathy, lactic acidosis, and sideroblastic anaemia (MLASA). All three patients were homozygous for a Phe<52>Leu *YARS2* missense mutation located within the mt-TyrRS catalytic domain. All three patients had reduced CI and CIV activities in skeletal muscle homogenates; CIII activity was tested in just one patient and was reduced. Citrate synthase and CII activities were above the normal range in two out of 3 patients indicating compensatory up-regulation of mitochondrial biogenesis. Fibroblasts were taken from one patient that showed normal OXPHOS activities. Hypertrophic cardiomyopathy was also observed in one patient (Riley et al., 2010). Later in 2013, Shahni *et al* reported another Lebanese MLASA patient with the same Phe<52>Leu YARS2 missense mutation. The patient showed remarkably similar clinical symptoms including additional hypertrophic cardiomyopathy as previously observed in one patient from Riley *et al* (Shahni et al., 2013).

In 2012, Sasarman reported a patient with adult onset MLASA with a novel Gly<46>Asp missense mutation in *YARS2* located in the of mt-TyrRS catalytic domain. Again the patient had combined respiratory chain deficiencies in skeletal muscle homogenates. Cultured myoblasts whilst showing mitochondrial translation defects did not have resultant OXPHOS deficiencies (Sasarman, Nishimura, Thiffault, & Shoubridge, 2012).

In 2013, Riley *et al* performed a genetic screen of patients with mitochondrial respiratory chain disorders with associated anaemia and 3 out of 12 patients were identified with *YARS2* mutations. Two patients were homozygous for the previously identified Phe<52>Leu *YARS2* missense mutation and the third was compound heterozygous for two novel *YARS2* mutations a Gly<191>Asp missense mutation and an Arg360X nonsense mutation. Of the patients with the Phe<52>Leu *YARS2* mutation, one was severely and one mildly effected. An additional clinical feature of the severely affected patient was cardiomyopathy. The variability in disease severity between the two patients was suggested to be due to differing mtDNA haplotypes. In all three patients severe CI, CIII and CIV deficiencies were observed in myoblast but not fibroblast cultures. Increased PGC1a and TFAM protein levels were observed in skeletal muscle homogenates again indicating compensatory up-regulation of mitochondrial biogenesis (Riley et al., 2013).

In 2014, Nakajima *et al* identified two Turkish siblings homozygous for a novel Ser<435>Gly *YARS2* missense mutation located within the ribosomal protein S4-like domain. The patients had severe MLASA with early onset and both patients died within 3 months of age (Nakajima et al., 2014).

Finally, in 2015, Ardissone *et al* reported two Italian siblings with a homozygous Asp<311>Glu missense mutation in *YARS2* located within the α-anticodon-binding (αACB) domain. The αACB domain is required for interaction with the anticodon of the cognate mt-tRNA^{Tyr}. Both patients presented with anaemia and lactic acidosis but showed no signs of muscle involvement. However, in one patient, mild myopathic features were observed in patient skeletal muscle biopsies and CI, CIII and CIV defects were observed in muscle homogenates but not fibroblasts (Ardissone et al. 2015)

In all 11 *YARS2* patients identified, anaemia and lactic acidosis were observed. Myopathy was also a feature in 9 patients. 6 different *YARS2* mutations were identified in these patients including four within the catalytic domain, one in the αACB domain and one in the S-4 like domain. The age-of-onset varied from 1 month of age to 31 years of age. The clinical outcomes of patients were equally variable with one patient dying at 3 months of age and the oldest surviving patient being over 34 years of age. Clear justification for the range of severity in phenotypes observed is difficult given that there is a degree of disease heterogeneity even between the six identified patients with the Phe<52>Leu mutation with anaemia being identified as early as 2 months and as late as 23 years in different patients. This may suggest that unidentified polygenic modifiers determine clinical outcomes as eluded to by Riley *et al* in 2013.

1.1.5.17 Summary of mtRS patients

As stated previously, pathological mutations in all of the mtRS genes have been identified except for *WARS2*. In most cases there is an association between the mtRS gene and tissue specific pathology. Clinical pathologies were observed in many different tissues of mtRS patients including brain, heart, kidney, skeletal muscle, the auditory system and ovary (**Figure 1.5**). A summary of all known mtRS mutations and associated clinical observations can be seen in **Table 1.3**.

The most commonly affected organ is the brain with mutations in *AARS2*, *CARS2*, *DARS2*, *EARS2*, *IARS2*, *FARS2*, *MARS2*, *NARS2*, *PARS2*, *RARS2*, *TARS2* and *VARS2* all causing abnormal brain pathology in human patients. In some cases, there is even a distinct brain pathology associated with mutations in certain mtRS genes. For example, *RARS2* mutations are associated with PCH6, *DARS2* mutations are associated LBSL and EARS2 mutations are associated with LTBL. Whereas *NARS2* mutations appear to be associated with more generalized and varied brain pathologies. On the other hand, mutations in several other mtRS genes were not associated with any brain specific pathology at all. No abnormal

brain pathology was reported in any of the patients reported with HARS2, LARS2 or SARS2 mutations. Therefore, the question is: what determines the tissue or brain specific pathologies associated with mtRS mutations?

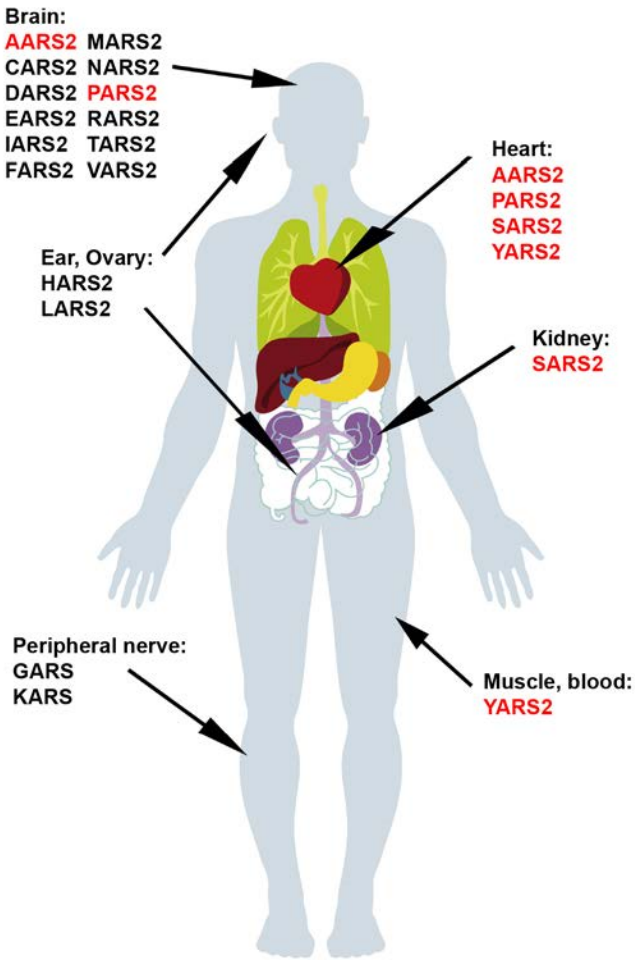

Figure 1.5 – Tissue specific pathology associated with mutations in mitochondrial aminoacyl-tRNA synthetase genes.
Schematic diagram showing the main tissue(s) affected by mutations in mtRS genes. Genes highlighted in red show associated pathology with more than one tissue. Figure adapted from Konovalova & Tyynismaa 2013.

With regard to brain specific pathologies, it must be acknowledged that patients that present with LBSL, LBTL or PCH6 are subsequently genotyped for known causal mutations in mtRS

genes. Therefore, there is a selection bias for identifying the phenotypes previously found to be associated mtRS mutations and patients with phenotypes that do not fit the known criteria associated with a gene will go unidentified. That being said, the large number of patients and known causal mutations in *RARS2*, *DARS2* and *EARS2* suggest that the association between gene and phenotype is real and independent of genotype. In other cases, this may not be true. For instance, the association between *MARS2* and ARSAL may be dependent upon genotype as subsequent studies identified novel loss-of-function alleles that did not present with the same brain pathology.

Logically one might expect that mtRS genes are transcriptionally co-regulated given that their co-ordinated function is required for efficient mitochondrial translation. Furthermore, one might also expect that mtRS gene expression correlates with the rate of mitochondrial translation i.e. high mtRS gene expression in tissues with high rates of mitochondrial translation and low expression in tissues with low levels of mitochondrial translation. However, the pattern of expression of mtRS genes in human tissues differs from one mtRS gene to another (**Figure 1.6**). For example, LARS2 (**Figure 1.6H**) and VARS2 (**Figure 1.6N**) are highly expressed in the brain relative to other tissues, whereas DARS2 (**Figure 1.6C**), FARS2 (**Figure 1.6E**), IARS2 (**Figure 1.6G**), RARS2 (**Figure 1.6L**) and WARS2 (**Figure 1.6O**) are lowly expressed in brain relative to other tissues. This indicates that mtRS are differentially regulated at a transcriptional level from one another and in a tissue specific manner. This observation may provide an explanation for the tissue specific pathologies associated with mtRS genes. If disease pathology is observed in tissues with high mtRS gene expression, then different tissue specific pathologies would be expected because mtRS genes are highly expressed in different tissues.

For some mtRS genes this hypothesis may hold true. For instance, *HARS2* is highly expressed in the ovary relative to other tissues, only being expressed higher in the spleen (**Figure 1.6A**). *HARS2* was shown to be associated with Perrault syndrome characterized

as sensorineural hearing loss and ovarian dysgenesis in female patients. Here an expression-phenotype relationship is observed and may explain the associated clinical pathology. However, there are many more examples where no expression-phenotype relationship is present. For instance, *LARS2*, also associated with Perrault syndrome, is more highly expressed in the brain than the ovary and yet no brain specific pathology was observed in patients with LARS2 mutations (**Figure 1.6H**). In this circumstance the association between *LARS2* mutations and ovarian dysgenesis appears to be independent of tissue specific expression levels. Equally many of the mtRS genes associated with brain specific pathology are not highly expressed in the brain relative to other tissues. An example of this is *RARS2*, which is associated with PCH6, is expressed more highly in heart, kidney, liver and many other tissues than the brain (**Figure 1.6L**). The association between mtRS mutations and clinical pathology appears to be independent of mRNA expression levels.

Perhaps what may be more interesting is the pattern of mtRS gene expression within the brain (**Figure 1.7**). *AARS2* (**Figure 1.7A**), *CARS2* (**Figure 1.7B**), *HARS2* (**Figure 1.7F**), *RARS2* (**Figure 1.7L**) and *VARS2* (**Figure 1.7N**) all show greatly increased mRNA expression levels in the cerebellar hemisphere and cerebellum relative to other regions of the brain such as the cortex, hippocampus, hypothalamus, spinal cord and amygdala. This peak in expression in the cerebellum is not observed for the remaining mtRS genes. Independent of a direct association between mtRS expression and brain specific pathology, these results are intriguing and suggest that mtRS genes are differentially regulated in the cerebellum compared to other regions of the brain. In the case of *RARS2*, the increased expression observed in the cerebellar hemisphere and cerebellum may explain the associated brain pathologies as cerebellar atrophy was observed in all reported patients. However again, mRNA expression levels do not appear to correlate with brain specific pathology in other circumstances. *DARS2* is associated with LBSL, yet *DARS2* mRNA expression levels appear to be expressed at comparable levels in different region of the brain and are in fact expressed at the lowest levels in the spinal cord relative to other

measure brain regions (**Figure 1.7C**). The question remains, what dictates the tissue specific penetrance of mtRS mutations?

Gene	Mutation state	Main Clinical Pathology	Age of onset	Additional clinical observations	Brain Pathology	Elevated Lactate	OXPHOS deficiencies		Number of patients	Ref
							Tissues	Cells		
AARS2	Hom & C. Het	Hypertrophic cardiomyopathy	Neonatal - Infancy	Lactic acidosis, early death	Normal	Blood	CI & CIV - Heart, brain, muscle	Normal	3	Gotz et al
	C. Het	(ovario)leukoencephalopathy	Childhood - Adulthood	cognitive & motor deterioration, dysarthria, dystonia, ataxia, spasticicity	Abnormalities in periventricular, frontal and pariental white matter	Normal	CIV - skeletal muscle	Normal	6	Dallabona et al
CARS2	Hom	MERRF syndrome	Childhood	severe myoclonic epilepsy, static tetraparesis, vision & hearing impairment, cognitive decline	Non-specific white matter lesions	Blood	N/A	N/A	2	Hallmann et al
	C. Het	Epileptic encephalopathy and complex movement disorder	Infancy	Reduced albumin	Atrophy of white matter and cortex	Blood and CSF	CI, CII & CIV - Liver	Incomplete CV assembly - myoblasts and fibroblasts	1	Coughlin II et al
DARS2	C. Het	LBSL	Childhood - Adulthood	Cerebellar ataxia, spasticity, variable cognitive impairment	Abnormalities in cerebral white matter, brain stem and spinal cord tracts	White matter	Normal	Normal	38, 3, 8	Scheper et al, Martikainen et al, Isohanni et al
		LBSL with normal lactate				Normal	N/A	N/A	1, 2	Lin et al and Tzoulis et al
		LBSL, asymptomatic	Childhood	One patient -spastic paraparesis, mixed proprioceptive and cerebellar ataxia and intension tremor in both limbs, one patient asymptomatic		White matter			2	Laubauge et al
	Hom	mild LBSL	Adulthood	exercise induced paroxysmal gait ataxia, areflexia, cerebellar ataxia		Elevated blood lactate, normal is CSF			1	Synofzik et al
		Early-onset leukoencephalopathy	Infancy	Severe neurological deterioration following respiratory tract infection (9 months of age) followed by almost complete remission of symptoms, asymmetrical sensorineural deafness)	Diffuse symmetrical abnormalities of white matter. No abnormalities in basal ganglia, thalamus, brainstem or cerebellum.	Normal			1	Kohler et al
		severe LBSL with normal lactate	Infancy - Childhood	Cerebellar ataxia, spasticity, variable cognitive impairment	Abnormalities in cerebral white matter, brain stem and spinal cord tracts with additional diffuse involvement of cerebellum white matter and central tegmental tracts	Normal CSF and blood lactate			3	Miyake et al, Yamashita et al
EARS2	C. Het	mild' / 'severe' LTBL	Infancy	mild' - >2 years of age regain milestones, MRI improvement & lowered blood lactate. 'severe' - >2 years of age clinical stagnation, brain atrophy, increased blood lactate.	asymmetric abnormalities of cerebellar white matter, thalamus, midbrain, pons, medulla oblongata and cerebral white matter.	Blood	CI, CIII & CIV - Skeletal muscle	CI, CIII & CIV - Fibroblasts	12	Steenweg et al
	Hom	early onset 'mild' LTBL	Infancy				N/A	N/A	1	Taskin et al
	C. Het	mild' LTBL	Infancy	hypotonia and delayed developmental milestones or seizures and spasticity in lower extremities			N/A	N/A	2	Sahin et al
	Hom	severe' LTBL	Perinatal	Severe infantile multisystem disease involving brain and liver. Hypospadias, hypotonia, failure to gain weight. Died at 3 months.			CIV - liver, CI & CIV - Skeletal muscle	N/A	1	Talim et al
FARS2	C. Het	Fatal infantile mitochondrial Alper's encephalopathy / Alpers-Huttenlocher disease	Perinatal	Microcephaly, epilepsy. In one patient: liver disease	Laminar cortical necrosis and severe cortical atrophy	Elevated CSF and blood lactate	Sk. Muscle: CIV deficiency brain: CI and CIV deficiency	ND in fibroblasts	2	Elo et al

	Hom	Fatal infantile mitochondrial Alper's encephalopathy	Infancy	Epilepsy, developmental delay, no liver disease		Elevated blood lactate	N/A	N/A	3	Shamseldin et al
	C. Het	Early onset epilepsy	Infancy	No visual awareness, small, round anteriorly rotated ears and broad nasal root.	Symmetrical white matter lesions, thinning of anterior and genu of the corpus callosum	N/A	Sk. Muscle: CIV deficiency	Normal in fibroblasts; CIV in myoblasts	1	Almalki et al
	Hom	Hereditary spastic paraplegia (HSP)	N/A	Progressive lower limb spasticity, pyramidal weakness with hyperreflexia, extensor plantar responses and scissors gaits	N/A	N/A	N/A	N/A	4	Yang et al
	C. Het	Juvenile onset refractory epilepsy and progressive myoclonus	Childhood	Developmental milestones, cortical necrosis	T2 hyperintensity in left caudate and left medial temporal lobe and the right occipital lobe along the superior bank of the right calcarine sulcus with encephalomalacia of the calcaravis	Transient elevation in blood lactate	Normal in sk. Muscle	N/A	1	Walker et al
HARS2	C. Het	Perrault Syndrome	Varied	Progressive sensorineural hearing loss and ovarian dysgenesis in females	N/A	N/A	N/A	N/A	5	Pierce et al
IARS2	Hom	CAGSSS	Infancy	Delayed developmental milestones, dysmorphic facial features, hand joints, spine and knee. No cognitive defects.	Atrophy of the pituitary adenohypophysis and a small neurohypophysis	N/A	N/A	Normal OXPHOS and mitochondrial translation in fibroblasts	3	Schwartzentruber et al
LARS2	3 x Hom, 1 x C.Het	Perrault Syndrome	Childhood - Adulthood	Progressive sensorineural hearing loss and ovarian dysgenesis in females	N/A	N/A	N/A	N/A	4	Pierce et al
	C.Het				Normal neurological and cognitive function reported	N/A	N/A	N/A	2	Solda et al
MARS2	Hom, C. Het	ARSAL	Childhood - Adulthood	All cases: ataxia, spasticity and hyperreflexia; variable symptoms: dysarthria, dysmetria, nystagmus, dystonia, scoliosis, urinary urgency leukodystrophy and cerebellar atrophy	Cerebral atrophy and is some cases cortical atrophy, leukoencephalopathy and corpus callosum thinning	N/A	N/A	Lymphoblasts: reduced CI activity and reduced mitochondrial protein synthesis	54	Thiffault et al, Bayat et al
	C. Het	Developmental delay, poor growth and sensorineural hearing loss	Perinatal	Dysmorphic features	Quadriventricular dilation, white matter changes, cerebral atrophy and high arched, posteriorly thin corpus callosum	Occasional mild elevation of lactate in one patient	N/A	Fibroblast: C and CIV deficiencies	2	Webb et al
NARS2	Hom	Alpers Syndrome	Infancy	Generalised seizures of multiple types, cortical visual impairments and renal dysfunction	Profound supratentional atrophy of the cerebral cortex, complete agenesis of the corpus callosum and hypomyelination of the white matter	Blood	Sk. Muscle: General decrease in OXPHOS enzyme activities but no enzyme deficiency	Reduced mt-AspRS in fibroblasts	1	Sofou et al
	Hom	Variable	Childhood	Mild intellectual disabilities and childhood epilepsy in one patient, severe myopathy in the other	Normal cerebral MRI reports in both patients	Normal	Sk. Muscle: CI & CIV deficiency	Reduced charged mt-tRNA-Asn in lymphoblasts	2	Valander et al
	Hom	Leigh syndrome	Childhood	Epilepsy and sensorineural hearing loss	Cortical atrophy, with laminar necrosis, atrophy of the corpus callosum, white matter oligodendroglial loss, neural grey matter loss, symmetrical lesions in the brainstem and thalamus	Elevated CSF lactate, normal blood lactate	Sk. Muscle: CI and CIV deficiencies	Fibroblasts: reduced oxygen consumption and reduced mt-tRNAAsn levels	2	Simon et al
PARS2	C. Het	Alpers Syndrome	Infancy	Reduced height, dilated cardiomyopathy and left ventricular hypertrophic cardiomyopathy, generalised seizures, hypotonia,	Generalised cerebral cortical atrophy	Elevated lactate in blood and CSF	Sk. Muscle: Reduced CI and CIV activity	N/A	1	Sofou et al

				dystonia, progressive microcephaly, severe mental retardation, cortical visual impairment.						
RARS2	Hom	Severe infantile encephalopathy associated with pontocerebellar hypoplasia (PCH6)	Infancy	generalised hypotonia, intractable seizures, microcephaly	Progressive atrophy in cerebellum, pons, cerebral cortex and white matter	Variable and mild elevation in blood and CSF lactate	Sk. Muscle: Reduced CI, CIII & CIV activity	Fibroblasts: Reduced CI activity	3	Edvardson et al
	C. Het		Perinatal	Oedema and additional symptoms of a PEHO-like phenotype and microcephaly	Generalised cerebral atrophy, thinning of the pons and gross atrophy and flattening of cerebellar hemispheres		Normal sk. Muscle	N/A	1	Rankin et al
	C. Het		Neonatal - Infancy	Epileptic encephalopathy, poor psychomotor development, progressive microcephaly	Progressive and cerebral cortical atrophy		Normal in skeletal muscle	Normal in fibroblasts	5	Cassandrini et al
	C. Het			Microcephaly, complex epilepsy, severe dystonia, optic atrophy and suggested sensorineural hearing loss	Progressive cerebellar and cerebral atrophy		Mild CIV deficiency in sk. Muscle	N/A	1	Glamuzina et al
	C. Het	Clinical features of PCH6 with distinct brain MRI	Perinatal	Microcephaly, spastic quadriplegia, delayed developmental milestones, generalised seizures	Marked supratentorial atrophy, bilateral subdural effusions, cerebellar atrophy, no pontocerebellar hypoplasia		N/A	N/A	2	Kastrissianakis et al
	C. Het	Early onset epileptic encephalopathy, microcephaly and progressive cerebral atrophy	Perinatal	profound global developmental delay	Diffuse brain atrophy, more pronounced in frontal regions, cerebellar atrophy, no pontocerebellar hypoplasia		Normal sk. Muscle OXPHOS	N/A	2	Nishri et al
	C. Het	severe PCH6	Perinatal	cardiomyopathy, hydrops, pulmonary hypoplasia and death a 2 weeks	Marked cerebellar hypoplasia., gyral immaturity, punctate lesions in cerebral white matter and unfused deep cerebral grey matter		Sk. Muscle & Cardiac muscle: Reduced CI, CIII & CIV activity	N/A	2	Nichola et al
	Hom	PCH6	Infancy	hypotonia, seizures, developmental delay, microcephaly, progressive vision loss	Progressive cerebellar and cerebral atrophy	Normal CSF and blood lactate	N/A	N/A	2	Li et al
SARS2	Hom	Tubulopathy (Hyperuricemia, metabolic alkosis) hypertension and progressive renal failure in infancy - HUPRA syndrome	Perinatal	Hypertrophic cardiomyopathy, diabetes mellitus, developmental delay, premature death	Normal brain ultrasound	Elevated CSF and blood lactate	Sk. Muscle: Mild reduction in CI, CIII and CIV activity	N/A	3	Belostotsky et al
	Hom				N/A	Normal blood lactate	Normal OXPHOS activities in sk. Muscle	Mild CI & CIV deficiency in fibroblasts	2	Revera et al
TARS2	C. Het	Axial hypotonia and severe psychomotor delay	Perinatal	Premature death	Thin corpus callosum and hyperintense lesions of the globi pallidi in one patient	Elevated blood lactate	Sk. Muscle: reduced CI, CIII & CIV activity	Reduced oxygen consumption in fibroblasts	2	Diodata et al
VARS2	Hom	Microcephaly and epilepsy	Perinatal	psychomotor delay, facial dysmorphisms	Hyperintense lesions in the periventricular regions, the insulae and the frontotemporal right cortex	Lacate peak in white matter	Sk. Muscle: reduced CI activity	No enzyme defects in fibroblasts	1	Diodata et al
	C. Het	Central neurological disease including progressive external opthalmoplegia, ptosis and ataxia	Childhood	muscle weakness and hypotonia	N/A	N/A	Sk. Muscle: mosaic COX +ve fibres.	CI & CIV deficiencies	1	Taylor et al
YARS2	Hom	Myopathy, lactic acidosis and sideroblastic anaemia (MLASA)	Infancy	Hypertrophic cardiomyopathy in one patient	N/A	Elevated blood lactate	Sk. Muscle: reduced CI, CIII & CIV activity	Normal OXHOS activities in fibroblasts	3	Riley et al (2010)
		Myopathy, lactic acidosis and sideroblastic anaemia (MLASA)	Infancy	Hypertrophic cardiomyopathy	N/A		N/A	N/A	1	Shahni et al

	Hom	MLASA	Adulthood	N/A	Normal brain pathology		Sk. Muscle: Reduced CI, CIII and CIV activity and steady state levels	Reduced mitochondrial translation but normal OXPHOS levels in myoblast	1	Sasarman et al
	Hom; C. Het	Variable MLASA	Infancy - Adulthood	Myopathy was only observed in two patients, hypertrophic cardiomyopathy was observed in one patient and caused premature death at 3 months of age	N/A		Data from one patient showed reduced CI, CIII and CIV activity in sk. muscle but not in liver	Fibroblasts and myoblast (one patient): Ci and CIV deficiencies	3	Riley et al (2013)
	Hom	Severe MLASA	Perinatal	Hypertrophic cardiomyopathy and premature death within 3 months of age, ketosis, hypoammonemia, axial hypotonia	Thinning of corpus callosum with normal progress of myelination		N/A	N/A	2	Nakajima et al
	Hom	Anaemia and lactic acidosis	Infancy	No signs of myopathy or hypertrophic cardiomyopathy	Mild hyperintensity in the pallida, small abnormal signals in pontine tegmentum		Sk. Muscle (one patient): CI, CIII and CIV	Normal in fibroblasts (one patient)	2	Ardissone et al

Table 1.3 – Summary of all known pathological mutations in mitochondrial aminoacyl-tRNA synthetase genes.
N/A – data not available, Hom – homozygous, C. het – compound heterozygous.

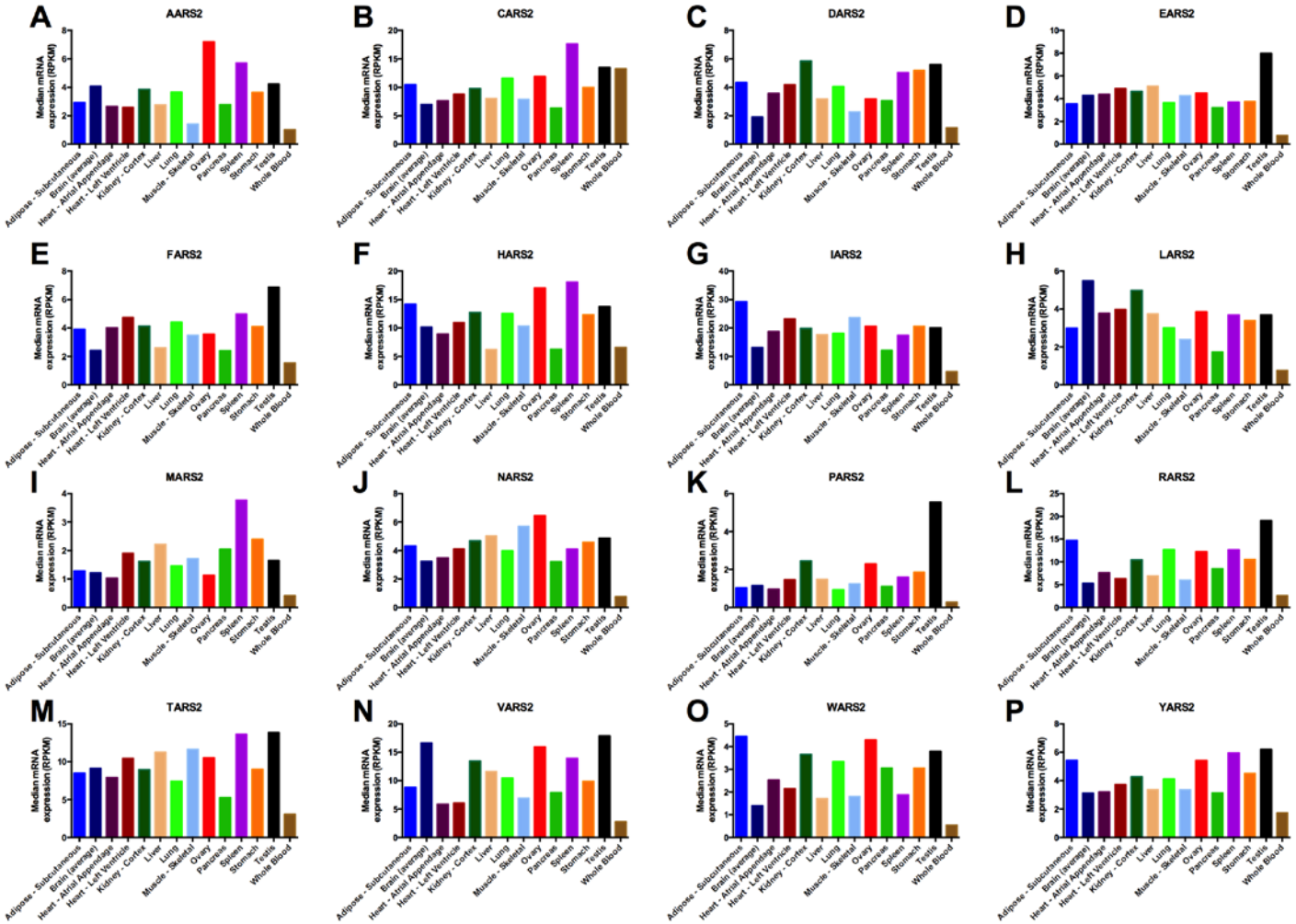

Figure 1.6 – Tissue specific expression of mtRS genes.
Tissue specific mRNA transcript levels of A) AARS2, B) CARS2, C) DARS2, E) FARS2, F) HARS2, G)IARS2, H) LARS2, I) MARS2, J) NARS2, K) PARS2, L) RARS2, M) TARS2, N) VARS2, O) WARS2 and P) YARS2. The data generated in this figure were obtained from the GTEx Portal

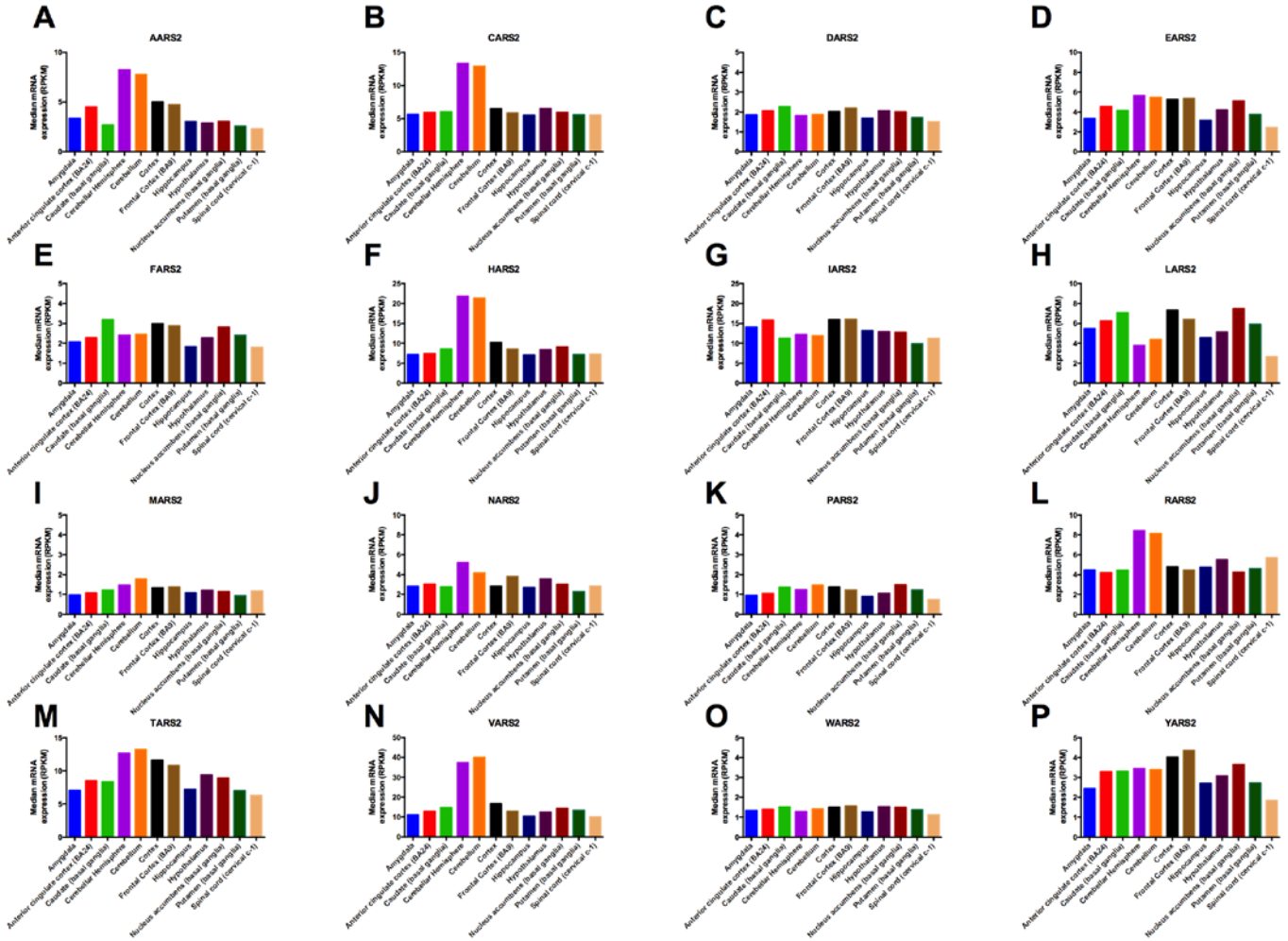

(http://www.gtexportal.org). No data was available for SARS2. Data shown as median transcript levels. RPMK – reads per kilobase per million mapped reads.

Figure 1.7 – Brain specific expression of mtRS genes.

mRNA transcript levels of A) AARS2, B) CARS2, C) DARS2, E) FARS2, F) HARS2, G)IARS2, H) LARS2, I) MARS2, J) NARS2, K) PARS2, L) RARS2, M) TARS2, N) VARS2, O) WARS2 and P) YARS2 in different regions of the brain. The data generated in this figure were obtained from the GTEx Portal

(http://www.gtexportal.org). No data was available for SARS2. Data shown as median transcript levels. RPMK – reads per kilobase per million mapped reads.

1.2 Mitochondrial dysfunction in common disease

As well as patients with defined mitochondrial diseases, mitochondrial dysfunction has been implicated in the pathogenesis of many common diseases not typically classified as mitochondrial disorders. These include cardiovascular disease (CVD), type 2 diabetes (T2D), obesity and non-alcoholic fatty liver disease (NAFLD). For example, Corral-Debrinski *et al* showed that in normal human cardiac tissue, mtDNA deletions appear after 40 years of age. However, mtDNA deletions were 7-220-fold increased in cardiac tissue collected from patients with coronary heart disease relative to age matched controls. (Corral-Debrinski, Shoffner, Lott, & Wallace, 1992). A comparable increase in mtDNA deletions were observed in human ischemic heart tissue (Corral-Debrinski et al., 1991). Together these studies provide some evidence that respiratory stress and mtDNA damage are linked within the context of CVD.

There is also evidence within the literature linking mitochondrial dysfunction with T2D and obesity. Ritov *et al* showed that skeletal muscle subsarcolemmmal and intermyofibrillar mitochondrial fractions from obese and T2D humans had reduced OXPHOS enzyme activities compared to lean controls (Ritov et al., 2005). Kelley *et al* performed rotenone sensitive NADH:O_2 oxidoreductase activity assays using isolated mitochondrial from skeletal muscle of lean, obese, diabetic and non-diabetic individuals to access mitochondrial OXPHOS function between groups. They showed reduced OXPHOS activity in skeletal muscle from individuals with T2D and obese compared to non-diabetic and lean controls. Additional mitochondrial morphology analysis showed that mitochondria were also smaller in size (reduced total mitochondrial area) in skeletal muscle from T2D and obese subjects compared to lean controls (Kelley, He, Menshikova, & Ritov, 2002). Together these data show differences in mitochondrial function and structure in type-2-diabetic and obese skeletal muscle (Kelley et al., 2002; Ritov et al., 2005). Fleischman *et al* showed

reduced mitochondrial function in skeletal muscle was associated with insulin resistance in overweight and normal-weight children (Fleischman, Kron, Systrom, Hrovat, & Grinspoon, 2009). Furthermore, microarray analysis of skeletal muscle from humans with T2D identified a sub-set of nuclear encoded OXPHOS genes were down-regulated and that these genes were transcriptionally co-regulated by PGC1a that was also down-regulated (Mootha, Lindgren, & Eriksson, 2003). These data offer a possible explanation for the reduction in mitochondrial function observed in T2D skeletal muscle that was shown in other studies. However, the role of mitochondrial dysfunction in the pathogenesis of T2D, obesity and insulin resistance remains to be determined.

Mitochondrial dysfunction has also been described as a feature of NAFLD. NAFLD includes hepatic steatosis, non-alcoholic steatohepatitis (NASH), fibrosis and cirrhosis. Pérez-Carreras *et al* showed that hepatic mitochondrial OXPHOS enzyme activities were substantially reduced in the NASH patients compared to matched controls (Pérez-Carreras et al., 2003). Furthermore, mitochondrial morphology analysis using TEM showed reduced mitochondrial cristae and intramitochondrial crystalline inclusions in the liver of NASH patients (Caldwell et al., 1999; Sanyal et al., 2001). Finally, drugs that induce steatohepatitis, such as 4,4'-Diethylaminoethoxyhexestrol, have been show to accumulate within rat mitochondria where they inhibit beta-oxidation and mitochondrial respiration causing decreased ATP and increased ROS production (Berson et al., 1998). Together these studies implicate abnormal mitochondrial morphology and function in NAFLD pathogenesis. But again it is unclear whether mitochondrial dysfunction is a cause or consequence of NAFLD.

Overall, there is an abundance of evidence that mitochondrial dysfunction is not only a feature of mitochondrial diseases but also likely plays a role in the pathogenesis of common disease such as CVD, T2D, obesity and NAFLD. However, these associations and observations require further insight and examination to determine their relevance. By

studying models of mitochondrial dysfunction and disease, such as the *Wars2*-V117L mouse model described in this thesis, it may be possible to gain valuable insight into the pathophysiology of not only mitochondrial disease but also common diseases where mitochondrial dysfunction is a feature.

1.3 Thesis aims

Modelling mitochondrial disease, or more specifically patients with mtRS mutations, in model organisms has some difficulties. The main challenge is the nature of the identified mtRS mutations. All mutant mtRS alleles identified in humans to date are recessively inherited. It is thought that no patients with homozygous null mtRS alleles have been identified. This is supported by data from the International Mouse Phenotyping Consortium (mtRS) that has generated global knock-out mouse strains for *AARS2*, *DARS2*, *RARS2* and *WARS2*, in each case knock-out alleles were embryonic lethal in their homozygous state. In fact, global knock-out *WARS2* was shown to embryonic lethal prior to embryonic day 9.5 demonstrating the fundamental requirement for mtRS activity during embryonic development. It is therefore believed that some residual mtRS activity is required to sustain life with patients being either homozygous for hypomorphic mtRS alleles or compound heterozygous for null and/or hypomorphic mtRS alleles.

In order to model human mtRS patients in mouse, hypomorphic mtRS alleles must be used. One method of generating hypomorphic mtRS alleles would be to use recently developed CRISPR-cas9 single nucleotide editing to directly mimic human mtRS mutations in mice. Alternatively, random mutagenesis methods can be used such as ENU mutagenesis.

In this thesis I present a novel ENU-induced mouse model of mitochondrial disease with a hypomorphic *Wars2* allele associated with hypertrophic cardiomyopathy, sensorineural hearing loss and reduced adiposity.

The aims of this this thesis were:

- To determine the tissue specific pathology associated with the *Wars2*-V117L allele in mouse (Chapter 3)
- To determine the nature of the *Wars2*-V117L allele *in situ*, *in vitro* and *in vivo* (Chapter 4)
- To investigate tissue specific response mechanisms in *Wars2*$^{V117L/17L}$ mice (Chapter 5)

The overarching goal of this study was to determine cause of the tissue specific penetrance of the *Wars2*-V117L allele. Through doing we aimed to gain insight that will allow us to answer the question, what determines the tissue specific pathologies associated with mtRS mutations in humans?

2 Materials and Methods

2.1 Mouse Methods

2.1.1 Animal Husbandry

Mouse studies were performed under the Home Office Licenses 30/3070 and 30/2642. Mice were housed in controlled conditions: light - 12hr light / dark cycle, temperature - 21°C ± 2°C and humidity – 55 % ± 10 %, in accordance with UK Home Office welfare guidelines. Mice were fed ad libitum commercially available diet (SDS maintenance chow, RM3, 3.6 kcal/g) and had free access to water (25 ppm chlorine).

2.1.2 Mouse phenotyping

2.1.2.1 Body Composition

Body mass was measured monthly on scales calibrated to 0.01 g. Body composition was measured monthly using Echo-MRI (Echo-MRI-100, Echo-MRI, Texas, U.S.A.). Through using EchoMRI it was possible to measure: fat mass, lean mass and free water in live, non-anaesthetised mice. Echo-MRI utilizes Nuclear Magnetic Resonance (NMR) Relaxometry to create contrast between soft tissues by taking advantage of differences in the relaxation times of hydrogen proton spins in different environments such as between fat and muscle tissue. Radio pulses cause proton spins to process and emit radio signals that are then received and analysed. The amplitude, duration, and spatial distribution of these signals are related to properties of the material scanned. Specially composed radio pulse sequences are used to further enhance the contrast between tissue types allowing accurate quantification of different tissue masses.

2.1.2.2 Click box

Mice were tested using the click box protocol as previously described (Hardisty-Hughes, Parker, & Brown, 2010). Briefly, mice were placed on the operator's palm and hearing was

tested using a purpose built frequency calibrated click box (CB) that emits a 90dB SPL tone at 20kHz (CB apparatus was obtained from MRC Institute of Hearing Research, Nottingham, UK). The CB emits a tone that elicits a Preyer reflex from the mouse as seen by a visible flick of the pinna or a startle response if the mouse can hear. The presence or absence of a Preyer reflex is then scored as follows: 2 – normal startle response, 1 – reduced startle, 0 – no startle. CB testing was performed blinded and away from the home cage to prevent littermates from becoming attenuated to the CB tone.

2.1.2.3 Auditory-evoked brainstem response

Auditory-evoked brainstem response (ABR) testing was performed as previously described (Hardisty-Hughes et al., 2010). Briefly, mice were anaesthetized via administration of an intra-peritoneal (IP) injection of anaesthetic (1 ml Ketamine, 0.5mL Xylasine, 8.5mL sterile H2O) at a rate of 0.1mL/10 grams of body mass. Once unconscious, the mouse was placed on a heated mat in a sound proof booth. Electrodes were then placed sub-dermally below the right pinna (ground), into the muscle mass below the left ear (reference) and on the midline of the skull (active). Mice were placed with their auditory canal 1.5cm from the speaker and were being exposed to tones at 8, 12, 20 and 26Hz followed by a click tone. The electrodes recorded the auditory brainstem responses to the tones. The recorded data was calibrated, generated and processed using the Tucker Davies Technology system III. Following the ABR testing an IP injection of Antipamezole (0.1ml in 9.9ml of sterile water) at a rate of 0.1mL <50g or 0.2mL >50 total body mass to reverse the anaesthetic. Mice were placed in a recovery cage until they had recovered from the anaesthetic before being placed back in their home cage.

2.1.2.4 Retro-orbital bleed

Food was withdrawn and mice were fasted at 8:00 AM. 4hrs later, mice were culled by administration of an over-dose of anaesthetic (0.2 mL of pentobarbitone) via intra-peritoneal injection in accordance with home office procedures. Once the mouse is fully anaesthetized a glass capillary is inserted into the anterior corner of the mouse eye to puncture the

membrane of the retro-orbital sinus. Blood was collected from the capillary in Lithium-Heparin microvette tubes (CB30, Sarstedr, Numbrecht, Germany). Once enough blood was collected mice were then dissected and tissues were taken for further analysis.

2.1.2.5 Plasma Biochemistry

Blood samples were collected via retro-orbital bleeding using Lithium-Heparin coated tubes and were kept on ice until they were processed. Samples were centrifuged for 10 mins at 8000 x g at 8°C. The supernatant blood plasma was removed and analysed on a board Beckman Coulter AU680 clinical chemistry analyser using reagents and settings recommended by the manufacturer.

2.1.2.6 Echocardiogram

Mice were placed under general anaesthetic using 4 % isoflurane using an anaesthetic chamber. Once unconscious the mouse is placed on an ECG platform (Visualsonics heat pad / ECG platform) and mouse limbs are taped to ECG probes to allow heart rate monitoring. Anaesthesia was maintained using a nose cone and 1.5 % (or as appropriate to maintain a heart rate <400bpm) isoflurane. Hair is removed from the mouse chest using hair clippers followed by hair removal cream. A rectal thermometer is inserted and used to monitor core body temperature throughout the procedure. Contact gel is applied to the shaven mouse chest and a 707B probe is lowered to the mouse chest locating the mouse heart left ventricle until contractions of the left ventricle could be monitored on the Visualsonics Vevo 770 high resolution *in vivo* micro imaging system. Several images of mouse heart were taken making sure that images were not distorted by mouse inhalations. Following successful data capture, the rectal probe, contact gel and limb tape was removed and the mouse was placed in a heat box to recover from the anaesthetic.

2.1.2.7 Intra-Peritoneal Glucose Tolerance Test

Mice were fasted overnight (up to 18 hrs) and IPGTT were performed the following morning. Mice were weighed in the morning and a local anaesthetic was administered to the mouse

tail (EMLA cream, Eutectic mixture of Local Anaesthetics Lidocaine / Prilocaine, AstraZeneca, UK). A blood sample was collected from the mouse tail at time point zero in Lithium-Heparin microvette tubes (CB30, Sarstedr, Numbrecht, Germany) to establish a baseline blood glucose level. Mice were then administered an intra-peritoneal injection of 2 g glucose / kg body weight (20 % glucose in 0.9 % NaCl). Blood samples were then taken 60 and 120 mins post-injection. At each time point, blood glucose levels were measured using the handheld Alphatrak (Abbott) glucose monitor with a fresh Alphatrak strip (Abbott) being used for every reading.

2.1.2.8 Comprehensive Lab Animal Monitoring System

The Comprehensive lab animal monitoring system (CLAMS) was used to simultaneously measure individual mice energy expenditure, activity, feeding and drinking at 'thermoneutrality' (28°C) and at the home cage temperature (22°C) according to standard protocols. Briefly mice were placed in individual cages for a total of 72 hours. Measurements of oxygen (O_2) and carbon-dioxide (CO_2) in-flow and out-flow concentrations were automatically monitored and recorded along with food consumption and water intake throughout the 72 hour period. Mice were weighed and EchoMRI body composition analysis was performed before and after being placed in the CLAMS system. Data from the first 24 hours was removed from the analysis as this period was used to allow the mice to acclimatise to their new environment. Data collected from the second 24 hour period was used for all subsequent analysis. O_2 and CO_2 concentration measurements were used to calculate oxygen consumption (VO_2), CO_2 production (VCO_2), respiratory exchange ratio (RER) and heat production. These were calculated as follows:

$VO_2 = ViO_2i - VoO_2o$

$VCO_2 = ViCO_2i - VoCO_2o$

$RER = VCO_2 / VO_2$

Heat = CV x VO_2 (where CV = Calorific value = 3.815 + 1.232 x RER)

o = outflow, i = inflow

In order to normalise data, adjustments were made for variations in lean mass using multiple linear regression analysis (ANCOVA). VO_2, VCO_2 and EE were adjusted for lean mass as previously described (McMurray et al., 2013).

2.1.2.9 Grip Strength

Maximum combined forelimb and hindlimb grip strength measurements were measured using grip strength apparatus (Bioseb). To do this, mice were lowered onto the grid platform so that both front paws and hind paws grip the grid. The mouse is then pulled across the grid making sure to keep the torso parallel until the grip is releases down the complete length of the grid. Grip strength readings were taken four times for each animal and average grip strength was calculated, normalizing values to total mouse body weight.

2.1.3 Tissue Collection & organ weights

Mice were culled at various time points and tissues were collected for subsequent analysis. Following confirmation of death: heart, liver, kidney, inguinal white adipose tissue, gonadal which adipose tissue, brown adipose tissue and skeletal muscle were dissected. For subsequent protein, RNA and DNA analysis tissues were placed in cryotubes (Nunc, Thermo Fisher Scientific-Heraeus) and snap frozen in liquid nitrogen. Tissue samples were stored long-term at -70 °C.

2.2 DNA Methods

2.2.1 General

2.2.1.1 DNA Extraction

Unless otherwise stated total DNA was extracted from mouse ear tissue using the DNeasy Blood & Tissue Kit (Qiagen) according to the manufacturer's instructions. Briefly, mouse

ear tissues were lysed in 180 µL of tissue lysis buffer (ATL) supplemented with 20 µL of proteinase K (600 mAU/ml solution) at 56°C until completely lysed (4 – 24 hours). DNA was precipitated in 200 µL of buffer AL supplemented with 200 µl of 100% ethanol. Lysate was passed through a silica-based DNA purification spin column to bind precipitant DNA to the column. Precipitant DNA was washed twice with two wash buffers (AW1 and AW2). Precipitant DNA was dissolved and eluted from the column in 30 – 100 µL of H2O or AE buffer.

2.2.1.2 Nucleic Acid Quantification

The concentrations of purified DNA and RNA were quantified using the Epoch Microplate Spectrophotometer (BioTek). 1 - 1.5 µL of DNA or RNA solution was placed on the Take3 Micro Volume Plate (BioTek) and the absorbance of UV-light for DNA (260nm/280nm) or RNA (260nm / 280nm / 230nm) was measured. The concentrations of DNA and RNA were calculated from the measured absorbance at 260nm using the Beer Lambert Law. DNA or RNA purity was assessed using the 260nm / 280nm ratio; a 260nm/280nm ratio value of ~1.8 or ~2.0 was accepted as 'pure' DNA or RNA respectively. The purity of RNA was additionally accessed using the 260 nm / 230 nm ratio; a 260 nm / 230 nm ratio value of 2.0 – 2.2 being accepted as 'pure'.

2.2.1.3 Gel electrophoresis

Gel electrophoresis was performed to ensure that PCR amplification was successful, to validate the size of the PCR amplicon or to separate DNA amplicons by size. To do this 1 - 4 % (w/v) agarose, 1X TAE (40 mM Tris, 20mM acetic acid; 1mM EDTA) gels containing 0.4µg/mL ethidium bromide were cast. An aliquot (5-50µL) of PCR products were mixed with 10% (w/v) DNA loading buffer and loaded onto the agarose gel. 10µL of 100bp DNA ladder (Invitrogen) was also loaded to allow subsequent size determination. Electrophoresis was then performed. Following electrophoresis, PCR amplicons were

imaged using a UV transilluminator (Molecular Imager Gel Doc XR System, Biorad, Hertfordshire, U.K.).

2.2.1.4 PCR Purification

PCR product purification was performed using the QIAquick PCR purification kit according to manufacturer's instructions (Qiagen).

2.2.1.5 Gel extraction

PCR products separated by size by gel electrophoresis were visualised over a UV transilluminator and excised from the agarose gel using a scalpel blade. Excised PCR products were purified from the agarose using QIAquick Gel Extraction Kit (Qiagen) according to the manufacturer's instructions.

2.2.1.6 Sanger Sequencing

Sanger sequencing was performed by Source BioScience (Source BioScience, Nottingham, UK). Samples were sent to Source BioScience along with 10 μM sequencing primers. Sequencing results were analysed using DNASTAR Lasergene SeqMan software (DNASTAR Inc, Wisconsin, USA).

2.2.2 Identification and validation of candidate ENU-induced mutations

2.2.2.1 DNA extraction

DNA for whole-genome sequencing (WGS) or SNP mapping was extracted from G3 MPC-151 mice ear biopsies using the Nucleon BACC2 Genomic DNA extraction System (GE Healthcare Life Sciences) according to the manufacturers protocol.

2.2.2.2 SNP Mapping

SNP mapping was performed as previously described (Potter et al., 2016). Individual mutations were mapped using the Illumina GoldenGate Mouse Medium Density Linkage

Panel (Gen-Probe Life Sciences Ltd, UK) that utilizes over 900 single-nucleotide polymorphisms (SNPs) for the C3H.Pde6b+ and C57BL/6J strains. The genotypes of G3 'affected' (elevated ABR thresholds) MPC-151 mice were compared to 'non-affected' ('normal' ABR thresholds) littermate controls. This allowed us to identify a 75Mb region within which all 'affected' MPC-151 mice were homozygous for C57BL/6J SNPs and 'non-affected' MPC-151 littermates were either heterozygous or homozygous for C3H.Pde6b+ SNPs.

2.2.2.3 Whole-genome sequencing

To identify candidate causal ENU-induced mutations within the mapped region, WGS was performed using DNA from an 'affected' G3 MPC-151 mouse. WGS was performed as previously described (Potter et al., 2016). Briefly, following DNA extraction a library was generated and a single lane or paired-end sequencing (100nt) was performed using the Illumina HiSeq platform (Oxford Genomics Centre, Wellcome Trust Centre for Human Genetics). The 100nt paired-end reads were aligned to the reference mouse genome (NCBIM38/mm10) using Burrows-Wheeler Aligner software (Li, H. & Durbin, R. Fast and accurate short read alignment with Burrows-Wheeler transform (Bioinformatics 25, 1754–1760 (2009)). Single-nucleotide variants (SNVs) were identified for each alignment using the unified GenotypeCaller tool in the Genome Analysis Toolkit (GATK) as previously described (Potter et al., 2016). Here the mouse dbSNP version 137 was used as the background SNP set using default parameters. Identified SNVs were then given a quality score (Phred scaled quality score, -10 x log(1-p), p is the probability of a SNV being called incorrectly). SNVs with a quality score of <100 or with a read depth of <3 reads were removed from all further analysis. All remaining SNVs were termed 'high-confidence' mutations and were compared to previously identified SNPs from 17 inbred strains from the Mouse Genome Project (Keane et al., 2011) as well as an in-house library of SNVs. Any overlapping sites were removed leaving the final list of novel ENU-induced SNVs for the 'affected' MPC-151 G3 mouse. SNVs were annotated using NGS-SNP to give an indication

of the nature of the SNV (e.g. Missense, splice-site variant or intronic). 3 high-confidence, ENU-induced, missense mutations were identified for the MPC-151 G3 'affected' mouse that were located within the 75Mb mapped region as previously identified. We then proceeded to validate these mutations as follows.

2.2.2.4 Validation of candidate ENU-induced mutations

WGS of an 'affected' MCP-151 G3 mouse identified 3 high-confidence ENU-induced candidate mutations: *Tchh*-D<1105>V, *Wars2*-V<117>L and *Ppa2*-Y<123>F. To validate these mutations primers were designed to amplify the mutation containing regions. Primers were designed using Primer3Plus (http://www.bioinformatics.nl/cgi-bin/primer3plus/primer3plus.cgi), see below.

Primer	**Sequence**
Wars2 Forward	5'-GGAGAGCGAGTGTTTTCTGG-3'
Wars2 Reverse	5'-GCTGCCTGGAGTACAGGGTA-3'
Ppa2 Forward	5'-ATTCCCAGATTGCCACAGAG-3'
Ppa2 Reverse	5'-GTTCCCAGCACTCACAAGGT-3'
Tchh Forward	
Tchh Reverse	

Following optimisation of the annealing temperature, PCR reactions were performed using DNA extracted from C3H.Pde6b+, C57BL/6J and MPC-151 G3 'affected' mice according to the following protocol:

Component	**Volume (µL)**
Taq PCR Master Mix	25
Forward Primer (5ng/µl)	1.0
Reverse Primer (5ng/µl)	1.0

DNA (10µg/µl)	5
ddH2O	17
Total Reaction Volume	50

PCR thermocyling was carried out using the following program:

Initial denaturation at 94°C for 5mins

34 cycles of: Denaturation at 94°C for 1min

Annealing at 60°C for 45s

Extension at 72°C for 1min

Final extension at 72°C for 10mins

Gel electrophoresis was performed using 10 µL of PCR products to ensure that successful PCR amplification and confirm PCR amplicon size. The remaining 40µL of PCR products were purified and sent for Sanger sequencing. Sequencing results were analysed using DNASTAR Lasergene SeqMan software.

2.2.3 Genotyping assays

2.2.3.1 Pyrosequencing Assays

Mice were assayed for the presence or absence of ENU-induced mutations: *Ppa2*^{A398T} and *Wars2*^{G380T} via pyrosequencing. PCR primers were designed to amplify the regions of interest using a biotinylated primer for the Pyrosequencing template strand. PCR products the regions of interest were amplified as follows:

Component	**Volume (µL)**
Hotshot Diamond Master Mix	5
Forward Primer (10µM)	0.2
Reverse Primer (10µM)	0.2
DNA (5ng/µL)	2

ddH2O	2.6
Total	10

Primer	**Sequence**
Ppa2^{A398T} Forward (Biotin)	5'-CTCAATCCCATTAAGCAAGATAT-3'
Ppa2^{A398T} Reverse	5'-GGTTTCTGTAGAAGGCATAAAAG-3'
Ppa2^{A398T} Reverse (Sequencing)	5'-GGGAAGATGTTCGGTG-3'
Wars2^{G380T} Forward	5'-GGTCACCTTTCTTTCTCTCC-3'
Wars2^{G380T} Reverse (Biotin)	5'-CAGGTGAGGATCCAACTTAA-3'
Wars2^{G380T} Forward (Sequencing)	5'-TTTCTCTCCTTCCTTTTAG-3'

PCR thermocycling was performed on a Tetrad 2 Peltier Thermal Cycler (BioRad) using the following conditions:

Initial denaturation at 94°C for 3 min

43 cycles of: Denaturation at 95°C for 30sec

Annealing at 60°C for 30 sec

Extension at 72°C for 30 sec

Final extension at 72°C for 4min

Following PCR amplification pyrosequencing was carried out using the PSA HS96 according to the manufacturer's instructions. Briefly the PCR amplicon was denatured and the single-stranded biotinylated template was isolated using Streptavidin Sepharose Beads (Qiagen). The purified template strand was hybridized with its respective 'Sequencing' Primer. Following this, the hybridized template strand was incubated with: DNA polymerase, ATP sulfurylase, luciferase, apyrase, adenosine 5' phosphosulfate (APS) and luciferin and placed within the pyrosequencer before being placed in the pyrosequencer machine. Within the sequencer, PCR was performed one nucleotide at a time with individual

dNTPs being added sequentially to determine the sequence of the template strand. If the dNTP was complimentary to the template strand, DNA polymerase catalysed the addition of the dNTP to the sequencing primer, releasing pyrophosphate (PPi). PPi, in the presence of APS, was converted to ATP by ATP sulfurylase. The newly generated ATP triggered the conversion of luciferin to oxyluciferin and light was emitted. This light was detected by a charge coupled device camera and was quantified to generate a light peak. The size of the peak was proportional to the number of nucleotides incorporated. Apyrase degraded any unincorporated dNTPs and ATP. Following degradation of unincorporated dNTPs or ATP, the next dNTP was added and the process was repeated until the sequence of the template strand was determined.

2.2.3.2 *Wars2*$^{V117L/-}$ genotyping strategy

A combination of two genotyping strategies were used to genotype the *Wars2* compound heterozygous mice generated from *Wars2*$^{V117L/-}$ x *Wars2*$^{+/-}$ mattings.

To genotype the *Wars2*-V117L ENU-induced allele the Idaho Technology LightScanner System (Idaho Technology Inc, Utah, USA) was used in accordance with the manufacturers standard protocols. Briefly, PCR was performed in the presence of a double stranded DNA binding dye LCGreen. PCR amplicons were then heated and the fluorescence emitted by bound LCGreen was monitored. As the double stranded PCR amplicons became denatured, LCGreen was released and the fluorescence level decreased allowing the DNA melting temperature to be calculated. This technology was utilised to quantitatively determine the *Wars2*-V117L allele frequency. Asymmetric exhaustive PCR was performed using primer pairs to amplify the SNP region in the presence of a 3'blocked lunaProbe designed to directly bind to the mutant SNP allele. This generated two PCR products a full-length PCR product and another product where the lunaProbe was bound to the opposite strand. When these two products were melted, the lunaProbe melted at a different

temperature in mutant and wild-type alleles due to differing binding affinities. PCR reactions were prepared as follows:

Primer	**Sequence**
Wars2V117L Forward	5'-TCAGCCTATCCCTGTTGTCTA-3'
Wars2V117L Reverse	5'-TGGTGTAAATGCTGCAATCG-3'
Wars2V117L Probe	5'-CCTTCCTTTTAGTTGTCTGAACACACTCAG-3'

Component	**Volume (µL)**
HotShot master mix	5
LCGreen	1
Forward Primer (20ng/µL)	0.1
Reverse Primer (20ng/µL)	0.5
LunaProbe (20ng/µL)	0.5
DNA (5ng/µL)	2
ddH2O	0.9
Total	10

PCR program:

Initial denaturation at 95°C for 2 min

55 cycles of: Denaturation at 95°C for 30sec

Annealing at 60°C for 30 sec

Extension at 72°C for 30 sec

Hybridisation: 95°C for 30 sec

25°C for 30 sec

15°C for 30 sec

To determine the frequency of the *Wars2*-KO allele a LacZ qRT-PCR copy number assay was performed using FAM-labelled taqman probes. LacZ is the reporter for the *Wars2*-KO construct and presence of LacZ indicated presence of *Wars2*-KO allele. Assays were performed using FAM-labelled taqman probes for LacZ and *Wars2*-WT DNA sequences. Each assay was performed along with an additional VIC-labelled taqman probe designed to Dot1l that acted as an internal control.

The genotyping assay was performed as follows:

Primer	**Sequence**
Wars2-WT Forward	5'-GCCCAGCACTTGGGATGT-3'
Wars2-WT Reverse	5'-GCAGCCAGCTCACCAATG-3'
Wars2-WT Probe (FAM)	5'-TCCCTTCACTTTCCTGTCTCCGTTTC-3'
Wars2-LacZ Forward	5'-CTCGCCACTTCAACATCAAC-3'
Wars2-LacZ Reverse	5'-TTATCAGCCGGAAAACCTACC-3'
Wars2-LacZ Probe (FAM)	5'-TCGCCATTTGACCACTACCATCAATCC-3'
Dot1l Forward	5'-GCCCCAGCACGACCATT-3'
Dot1l Reverse	5'-TAGTTGGCATCCTTATGCTTCATC-3'
Dot1l Probe (VIC)	5'-CCAGCTCTCAAGTCG-3'

Component	**Volume (µL)**
ABI GTX Taqman master mix	5
Dot1l Forward (20µM)	0.225
Dot1l Reverse (20µM)	0.225
Dot1l Probe (5µM)	0.2
FAM assay primers*	0.2
ddH2O	1.55
DNA (5ng/µL)	2.5
Total	10

* FAM assay primers - 5μM of Probe and 15μM or primers.

2.2.4 Mitochondrial DNA copy number assay

The ratio of mitochondrial DNA (mtDNA) to genomic DNA (nDNA) was assayed as follows. Primers were designed to amplify a genomic gene (GAPDH) and a mitochondrial gene (mtND1) using Primer3Plus online software (http://www.bioinformatics.nl/cgi-bin/primer3plus/primer3plus.cgi). Total DNA, including both nDNA and mtDNA, were extracted from tissues using the DNeasy Blood and Tissue Kit (Qiagen) as described previously. qRT-PCR was performed using the Fast SYBR Green (Applied Biosystems) system on the ABIPRISM 7500 Fast Real-Time PCR System (Applied Biosystems) using the standard Fast PCR program. Primer concentrations were optimized in order to determine the lowest primer concentrations that achieve the lowest CT value whilst minimizing non-specific amplification. To do this a matrix of primer concentrations was used ranging from 50 – 900 nM for each primer pair. Once optimal primer concentrations had been established a melting curve was performed post PCR to ensure the presence of a single amplicon per primer pair. PCR products were then run on a 2% agarose gel in order to ensure that the size of the amplicon was as predicted. The optimized assay was performed using technical triplicates as follows:

Primer	**Sequence**
mtND1 Forward Primer	5'-CCCATTCGCGTTATTCTT-3'
mtND1 Reverse Primer	5'-AAGTTGATCGTAACGGAAGC-3'
GAPDH Forward Primer	5'-CAAGGAGTAAGAAACCCTGGACC-3'
GAPDH Reverse Primer	5'-CGAGTTGGGATAGGGCCTCT-3'

Component	**Volume (μL)**
Fast SYBR Green Master Mix (2X)	10
mtND1 Forward Primer (5μM)	1.2

mtND1 Reverse Primer (5μM)	1.2
DNA (5ng/μL)	2
ddH2O	5.6
Total	20

Component	**Volume (μL)**
Fast SYBR Green Master Mix (2X)	10
GAPDH Forward Primer (5μM)	0.2
GAPDH Reverse Primer (5μM)	0.2
DNA (5ng/μL)	2
ddH2O	7.6
Total	20

2.3 RNA Methods

2.3.1 General

2.3.1.1 Standard RNA Extraction

The following protocol was performed to extract RNA from non-fibrous and non-fatty tissues e.g. Liver or kidney. RNA was isolated from mouse tissues using the RNeasy Mini Kit according to the manufacturer's instructions (Qiagen). Briefly, 20 - 30 mg of tissue was homogenized in 600μL of Buffer RLT Plus supplemented with β-Mercapoethanol using ceramic beads (Precellys) in a Precellys-24 automated homogenizer (Precellys). Homogenates were centrifuged at 13,000 RPM at 4°C for 3 mins to pellet cell debris and collect the supernatant. 70% ethanol was added to the supernatant to precipitant RNA before passing it through the RNeasy spin column to bind precipitant RNA to the column. Precipitant RNA was washed once with Buffer AW1. Contaminant DNA was removed by

performing on-column DNase I (1500 Kunitz units) digestion. Following this, precipitant RNA was washed once with Buffer RW1 and twice with Buffer RPE before eluting in 30 – 100 µL of RNase-free water. Isolated RNA was quantified as previously described (see nucleic acid quantification).

2.3.1.2 RNA Extraction - 'fatty' tissues

The following protocol has been adapted for RNA extraction from tissues with a high fat content in particular: White Adipose Tissue, Brown Adipose Tissue and Brain. 1ml of TRIzol Reagent (ThermoFisher Scientific) was added to 50-100 mg of tissue and homogenized using ceramic beads (Precellys) in a Precellys-24 automated homogenizer (Precellys). Homogenates are incubated for 5 mins at room temperature before adding 200 µL of Chloroform. Samples were shaken vigorously for 15 secs, incubated at room temperature for 3 mins and centrifuged at 13,000rpm for 15 mins at 4°C. Following centrifugation, the upper colourless phase, containing soluble RNA, was transferred to a new tube before addition of an equal volume of 70% ethanol, the sample was vortexed to precipitate the RNA. The sample was applied to an RNeasy spin column before completing the rest RNA extraction as described in 'Standard RNA Extraction.

2.3.1.3 RNA Extraction – Fibrous Tissues

The following protocol was adapted for isolation of RNA from fibrous tissues including heart and skeletal muscle. The protocol was performing as described in 'Standard RNA Extraction' with the following amendment. Following homogenization, proteinase K (Qiagen) was added to the homogenate and incubated at 55 °C for 10 mins before proceeding the with the protocol as described above.

2.3.1.4 cDNA Synthesis

Following the quantification of RNA, samples were diluted to an appropriate working concentration (200 ng/µL) before setting up reverse transcription reactions using Super

Script III reverse transcriptase (Invitrogen), following the manufacturer's standard protocol. When generating cDNA typically 2µg of RNA was used in each 20µL reaction.

2.3.1.5 Real-Time PCR

cDNA was analysed using quantitative real-time PCR real time fluorescence detection. TaqMan Gene Expression Assay (**Table 2.1**) reagents and TaqMan FAM dye-labelled probes (Applied Biosystems, Invitrogen, U.S.A.) were used to set up appropriate reactions according to the manufacturers protocol. RT-PCR reactions were then analysed using an ABIPRISM 7500 Fast Real-Time PCR System (Applied Biosystems). Data was normalized to house-keeping genes specific to the tissue / cell line being used. In order to determine the most suitable house-keeping gene to use, GeNORM analysis of 12 house-keeping genes was performed. Data were analysed using the comparative ΔΔCT method in order to determine the difference in sample groups relative to control samples.

Gene	Gene name	Taqman assay ID
Tryptophanyl tRNA Synthetase 2, Mitochondrial	*Wars2 (Exon 2-3)*	Mm04208965_m1
Tryptophanyl tRNA Synthetase 2, Mitochondrial	*Wars2 (Exon 4-5)*	Mm04208967_m1
Tryptophanyl tRNA Synthetase 2, Mitochondrial	*Wars2 (Exon 5-6)*	Mm00840490_m1
Peroxisome Proliferator-Activated Receptor Gamma, Coactivator 1 Alpha	*Pgc1α*	Mm01208835_m1
Activating Transcription Factor 4	*Atf4*	Mm00515324_m1
Activating Transcription Factor 5	*Atf5*	Mm00459515_m1
DNA Damage Inducible Transcript 3	*Ddit3 (Chop)*	Mm01135937_g1
Methylenetetrahydrofolate Dehydrogenase (NADP+ Dependent) 2, Methenyltetrahydrofolate Cyclohydrolase	*Mthfd2*	Mm00485276_m1

Fibroblast Growth Factor 21	*Fgf21*	Mm00840165_g1
Sirtuin 1	*Sirt1*	Mm00490758_m1
Transcription Factor A, Mitochondrial	*Tfam*	Mm00447485_m1
Peroxisome Proliferator Activated Receptor Alpha	*Pparα*	Mm00440939_m1
Acetyl-CoA Carboxylase Alpha	*Acaca*	Mm01304257_m1
Acetyl-CoA Carboxylase Beta	*Acacb*	Mm01204671_m1
Acyl-CoA Dehydrogenase, C-4 To C-12 Straight Chain	*Acadm*	Mm01323360_g1
Acyl-Coenzyme A dehydrogenase, long-chain	*Acadl*	Mm00599660_m1
Carnitine palmitoyltransferase 1a	*Cpt1a*	Mm00550438_m1
Carnitine palmitoyltransferase 1b	*Cpt1b*	Mm00487200_m1
Uncoupling Protein 1	*Ucp1*	Mm01244861_m1
Deiodinase, Iodothyronine, Type II	*Dio2*	Mm00515664_m1
Cell Death-Inducing DFFA-Like Effector A	*Cidea*	Mm00432554_m1
Peroxisome Proliferator Activated Receptor Gamma	*Pparγ*	Mm00440945_m1
Cytochrome C Oxidase Subunit 7A1	*Cox7a1*	Mm00438297_g1
Cytochrome C Oxidase Subunit 8B	*Cox8b*	Mm00432648_m1
Glyceraldehyde-3-Phosphate Dehydrogenase	*Gapdh*	4352932-1211040
Eukaryotic Translation Initiation Factor 4A2	*Eif4a2*	Mm01730183_gH
ATP Synthase, H+ Transporting, Mitochondrial F1 Complex, Alpha Subunit 1, Cardiac Muscle	*Atp5a1*	Mm00431960_m1

Table 2.1 – Table of taqman gene expression assays.

2.3.2 Identification of *Wars2* transcripts

To determine the effect of the *Wars2*-V117L ENU-induced mutation on splicing we amplified all *Wars2* mRNA transcripts using PCR. Total MEFs RNA was isolated and cDNA was generated as previously described. Primers were designed to *Wars2* 'start' to 'stop' codons using Primer3Plus software and the primer annealing temperatures were optimised. 50µL PCR reactions were set up using the Taq PCR Master Mix kit (Qiagen) as follows:

Primer	Sequence
Wars2 Forward Primer	5’-GTGGGAAGCTTGATGGCGCTGTT-3’
Wars2 Reverse Primer	5’-GTGTGGAATTCCCAGAATCCCCA-3’

Component	Volume (µL)
Taq PCR Master mix (2X)	25
Forward Primer (10µM)	2.5
Reverse Primer (10µM)	2.5
cDNA (50ng/µL)	10
ddH2O	10
Total	50

PCR thermocyling was carried out using the following program:

Initial denaturation at 95°C for 5mins

34 cycles of: Denaturation at 95°C for 45secs

Annealing at 53 for 45secs

Extension at 72°C for 60secs

Final extension at 72°C for 10mins

50µL PCR products were separated by size using electrophoresis, bands were identified and cut from the gel, as previously described before being purified and sent for Sanger sequencing.

2.3.3 *Xbp1* Splicing Assay

Total, spliced and unspliced *Xbp1* mRNA transcript levels were quantified as previously described (Oslowski & Urano, 2011). Briefly, total RNA was extracted from mouse hearts and total cDNA was generated. *Xbp1* mRNA transcripts were analysed using the SYBR green qRT-PCR fluorescence detection system using *Xbp1* transcript specific primers (Oslowski & Urano, 2011):

Primer	**Sequence**	**Conc.**
Total XBP1 Forward	5'-TGGCCGGGTCTGCTGAGTCCG-3'	0.1μM
Total XBP1 Reverse	5'-GTCCATGGGAAGATGTTCTGG-3'	0.1μM
Spliced XBP1 Forward	5'-CTGAGTCCGAATCAGGTGCAG-3'	0.6μM
Spliced XBP1 Reverse	5'-GTCCATGGGAAGATGTTCTGG-3'	0.1μM
Unspliced XBP1 Forward	5-'CAGCACTCAGACTATGTGCA-3'	0.6μM
Unspliced XBP1 Reverse	5'-GTCCATGGGAAGATGTTCTGG-3'	0.1μM

For each sample, PCR reactions were prepared for all three primer pairs in triplicate. Reactions were prepared as follows:

Component	**Volume (μL)**
Fast SYBR Green Master Mix (2✕)	10
Forward Primer (10μM)	Variable
Reverse Primer (10μM)	Variable
cDNA (4ng/μL)	5
RNase free H2O	Variable
Total	20

qRT-PCR reactions were then analysed using an ABIPRISM 7500 Fast Real-Time PCR System and were analysed using methods previously described.

2.4 Protein Methods

2.4.1 Protein Extraction

Snap frozen mouse tissues were homogenized in 2 ml Precelly tubes containing ceramic beads with a Precelly-24 automated homogenizer (Bertin Technologies). Soft tissues such as: liver, kidney and adipose tissues were homogenized in Precelly CK14 2 mL tubes and fibrous tissue such as muscle and heart were homogenized in Precelly CK28 2 mL tubes (Bertin Technologies). Tissues were homogenised in pre-prepared lysis buffer CelLyic MT Mammalian Tissue Lysis / Extraction Reagent (Sigma- Aldrich) freshly supplemented with 1 X complete protease inhibitor cocktail (1 µL / 100 µL lysis buffer, Sigma- Aldrich) and 1 X PhosStop phosphatase inhibitor cocktail (1 µL / 100 µL lysis buffer, Sigma Aldrich). Following homogenization, lysates were centrifuged at 13,000 rpm for 15 mins at 4 °C to pellet cell debris and non-homogenised tissue / cells. The supernatant was removed and placed in 1.5 mL Eppendorf tube making sure that minimal lipid was carried over. Lysates were placed on ice for immediate use or frozen in aliquots and stored at -70 °C for long-term storage.

2.4.2 Protein Concentration Assay

The protein concentrations of tissue protein lysates were determined using the BCA (bicinchoninic acid) Protein Assay Reagent (BioRad) according to the manufacturer's instructions. Briefly, 5 µL of sample / standard were pipetted into a 96 well flat-bottomed optical plate. 25 µL of Reagent A (supplemented with 20 µL / mL of Reagent S) and 200 µL of Reagent B were added to each sample / standard. The plate was covered in aluminium foil and placed on a plate shaker (STR9 orbital shaker, Stuart Scientific) at 300 rpm for 15 – 30 mins. The absorbance was then measured at 750 nm on a Spectra Max 190 spectrometer (MDS Analytical Technologies Ltd, Berkshire, U.K.). Standards were prepared from a pre-prepared solution of 10 µg/µL Bovine Serum Albumin (BSA). A serial dilution of BSA in ddH2O was used to generate a standard curve from 0.16 – 2.5 µg / µL.

Samples were diluted in ddH2O as appropriate (typically a 1 in 10 / 20 dilution of sample in ddH2O) in order to achieve an absorbance that was within the linear range of the standard curve.

2.4.3 Immunoblotting

Protein electrophoresis and immunoblotting was performed using the NuPAGE Electrophoresis System (Invitrogen). Samples were diluted to 4 µg / µL in lysis buffer. Sample were then prepared as follows:

Component	**Volume (µL)**
NuPAGE LDS Sample Buffer (4X)	2.5
NuPage Reducing Agent (10X)	1
ddH2O	1.5
Protein Sample (4µg / µL)	5
Total	10

Samples were denatured by heating at 70 °C for 10 mins before being placed on ice. Protein samples were separated using 4-12 % linear gradient Bis-Tris ready polyacrylamide gels with 1 X MOPS electrophoresis running buffer (Invitrogen) using the XCell Surelock Mini Cell tanks (Invitrogen). The inner chamber of tank was supplemented with 500 µL of NuPage Antioxidant (Invitrogen) to prevent oxidation of samples during electrophoresis. 10 µL of sample / protein ladder were loaded per lane. Precision Plus Protein Standard (Invitrogen) was used as a protein ladder allowing an estimation of protein molecular weights to be later determined. Gels were run at 200 V for 50 mins to allow sufficient separation of protein samples.

Following electrophoresis, protein samples were electrotransferred from the gel onto PVDF membrane (Hybond – P, GE Healthcare Amersham) using a XCell II Blot Module

(Invitrogen), PVDF membranes were cut and charged by immersion in 100 % methanol for 1 min before assembly and transferred in NuPage Transfer Buffer (Invitrogen) with 10 % Methanol for 1 hr at 30 V. Following immunoblotting membranes were placed in 50 mL Falcon Tubes and all subsequent blocking, washing and antibody incubation steps were performed on a benchtop roller. Membranes were blocked in 10 mL of either 5 % non-fat milk TBST (non-phospho antibodies) or 5 % Bovine Serum Albumin TBST (phosphor-antibodies) at room temperature for an hour or overnight at 4°C. Primary antibodies were diluted to optimized concentrations in either 5 % non-fat milk TBST or 5 % Bovine Serum Albumin TBST (**Table 2.2**). Membranes were incubated with primary antibodies overnight at 4 °C. The following day membranes were washed 3-5 times in TBST for 10 mins at room temperature. Secondary antibodies were diluted in 5 % non-fat milk TBST. Membranes were incubated with species-specific secondary horseradish peroxidase (HRP) conjugated antibodies for 4 hrs at room-temperature. Membranes were washed 5 X 10 mins in TBST.

Following washing, membranes were placed on cling film and 1ml of Enhanced Chemiluminesence Plus (ECL plus; Amersham, GE Healthcare) was pipetted onto the membrane surface and incubated for 5 mins in the dark according to the manufacturer's instructions. Excess ECL was removed from the membrane and membranes were wrapped in cling film before imaging. Membranes were imaged using the ChemiDoc UV chemiluminescent imager. Exposure times were optimized in order to obtain optimal signal from the membranes.

Following imaging, blots were washed briefly in TBST to remove remnant ECL before being probed with an appropriate control antibody raised to an appropriate house-keeping protein. The process was then repeated in order to quantify the house keeping protein of interest.

Bands were analysed and quantified using ImageJ. Quantified bands for the protein of interest were normalized to the housekeeping protein in order to control for loading.

Protein Abbreviation	Protein Name	Supplier	Catalogue Number
mt-TrpRS (WARS2)	Mitochondrial tryptopanyl-tRNA synthetase	Custom	N/A
NDUFB8	NADH:Ubiquinone Oxidoreductase Subunit B8	Abcam	ab110242
SDHA	Succinate Dehydrogenase Complex Flavoprotein Subunit A	Abcam	ab14715
UQCRC2	Ubiquinol-Cytochrome C Reductase Core Protein II	Abcam	ab14745
mtCOI	mtDNA Encoded Cytochrome C Oxidase I	Abcam	ab147705
ATP5A	ATP Synthase, H+ Transporting, Mitochondrial F1 Complex, Alpha Subunit 1	Abcam	ab14748
eIF2A (Total)	Eukaryotic Translation Initiation Factor 2A	Cell Signalling	#5324
pS51-eIF2A	Eukaryotic Translation Initiation Factor 2A	Epitomics	#1090-1
ATF4	Activating Transcription Factor 4	Santa Cruz	sc-22800
LONP1	Lon Peptidase 1, Mitochondrial	Abcam	ab103809
CLPP	Caseinolytic Mitochondrial Matrix Peptidase Proteolytic Subunit	Abcam	ab124822
HSP60	Heat Shock Protein Family D (Hsp60) Member 1	Abcam	ab46798
HSP70	Heat Shock Protein Family A (Hsp70) Member 9	Abcam	ab2799

phospho-PERK	Phospho-PERK (Thr980) (16F8) Rabbit mAb	Cell Signalling	#3179
PERK (Total)	PERK (C33E10) Rabbit mAb	Cell Signalling	#3192
ATF6	Activating Transcription Factor 6	Abcam	ab37149
SOD2	Superoxide Dismutase 2, Mitochondrial	Abcam	ab13533
PGC1a	Peroxisome Proliferator-Activated Receptor Gamma, Coactivator 1 Alpha	Santa Cruz	sc-13067
PGC1a UCP1	Peroxisome Proliferator-Activated Receptor Gamma, Coactivator 1 Alpha Uncoupling Protein 1	Source Bioscience	SBS1314
		Santa Cruz	sc-6539
LC3	Microtubule Associated Protein 1 Light Chain 3 Alpha	Cell Signalling	#3868
Actin	Alpha-actin-1	Millipore	MAB1501
Tubulin	Tubulin Alpha-3 Chain	Cell signalling	#2144
GAPDH	Glyceraldehyde-3-Phosphate Dehydrogenase	Abcam	ab8245

Table 2.2 – Table of antibodies.

2.4.4 Generation and validation of custom mt-TrpRS antibody

2.4.4.1 Antibody Generation

Due to the lack of commercially available mt-TrpRS antibodies, a custom mt-TrpRS antibody was generated (Covalab). To do this, two mt-TrpRS peptides C-

KGPAATLAPQKESGERVFSGIQ-coNH2 and C-KKVKSLRDPSSKMSKSDPDKL-coNH2 were synthesised and used to immunize rabbits (Covalab). Two rabbits were injected with both synthesized mt-TrpRS peptides at days 0, 21, 41 and 54 before being bled at day 88. Rabbit antisera were affinity purified on Sulfolink coupling gel (Pierce) before antibody characterization.

2.4.4.2 Immunoprecipitation & Mass Spectrometry

To validate the custom mt-TrpRS antibody, immunoprecipitation followed by mass spectrometry was performed to determine the specificity of the identified 37kDa band. Liver protein lysates were prepared as previously described. Lysates were pre-incubated with protein G sepharose beads (Sigma) twice for 2-3 hours at 4°C with gentle agitation to reduce non-specific binding. The beads were removed and discarded following incubations. Lysates were then incubated with the mt-TrpRS antibody for 3 hours before the addition of protein G sepharose beads and incubation over-night at 4°C with gentle agitation. The following day, lysates were centrifuged at 100 rpm to pellet the beads and the supernatant protein lysate was removed. The beads were washed 3 times with fresh lysis buffer and placed in a clean Eppendorf tube to remove remnant protein lysate. NuPAGE LDS sample buffer (1X) and NuPAGE Reducing Agent (1X) were added to the beads and bead-bound-proteins were then denatured by heating the bead solution to 70°C for 10mins (beads were gently agitated every 2 mins to prevent sedimentation). Denatured bead suspensions were then centrifuged to pellet the beads and the supernatant, containing immunoprecipitant proteins, was removed and protein electrophoresis was performed using a 4-12% polyacrylamide gel as previously described. Following gel electrophoresis, the polyacrylamide gel was incubated with SimplyBlue Coomassie protein stain (ThermoFisher Scientific) to visualise immunoprecipitant protein bands. The gel was washed three times with ddH_2O for 3 hours to remove excess stain and to reduce background staining. Bands at 37kDa were observed and cut from the gel. Protein gel bands were sent for mass-spectrometry to identify the isolated protein band. Mass spectrometry was performed at the

Functional Genomics, Proteomics and Metabolomics Facility, University of Birmingham, UK.

2.4.5 FGF21 ELISA

Plasma FGF21 levels were assayed using Quantikine ELISA Mouse / Rat FGF-21 Immunoassays (Quantikine) according to manufacturer's instructions. Briefly, 50µL of Assay Diluent RD1-41 was added to each well of the Mouse / Rat FGF-21 antibody pre-coated ELISA plate followed by 50 µL of standard / control / sample. The plate was incubated for 2 hours at room temperature to allow sample FGF21 to bind to the Mouse / Rat FGF21 antibody. Wells were washed five times with Wash Buffer to remove unbound substrate. 100 µL of Mouse / Rat FGF-21 Conjugate was added to each well, covered and incubated for 2 hours at room temperature. The Mouse / Rat FGF-21 conjugate solution contains an enzyme-linked polyclonal antibody specific to Mouse / Rat FGF-21. The plate was washed 5 times with wash buffer. 100uL of substrate solution was added to each well and the plate was incubated at room temperature for 30 mins in the dark. 100 µL of Stop Solution was added to each well and the absorbance was measured at 450 nm. Samples FGF21 concentrations were quantified using a standard curve generated from a serial dilution of Mouse / Rat FGF-21 Standard (20,000 pg / mL) ranging from 31.3 – 2000 pg / mL. The lower limit of detection for the assay described is 13.4pg/mL with <0.5% cross-reactivity with available related molecules. All sample measurements were performed in triplicate and calculated FGF21 sample values were obtained within the linear range of the standard curve and were above the lower sensitivity limit. The coefficient of variance for the FGF21 ELISA assay is < 5%.

2.4.6 OxyBlot

Reactive oxygen species can damage proteins by introducing carbonyl groups. Carbonylated proteins can be quantified using the OxyBlot Protein Detection Kit (Merck

Millipore). Total carbonylated protein content was assessed in mouse heart samples according to the manufacturer's instructions.

2.5 Mammalian cell culture methods

2.5.1 Mouse embryonic fibroblast isolation and culture

2.5.1.1 Embryo Collection

In order to generate primary mouse fibroblast cell cultures, timed matings were set up between *Wars2*$^{+/V117L}$ x *Wars2*$^{+/V117L}$ and females were plug checked daily. Females were sacrificed at 12.5 - 14.5 days post coitum (dpc) and embryos were collected. Individual embryos were dissected. The head, liver and any blood clots were removed. The liver was kept for DNA extraction and subsequent genotyping. Embryos were then placed in individual wells of a six well plate and suspended in Dulbecco's phosphate-buffered saline (DPBS). DPBS was then removed and 1.5mL of dissociation reagent (0.25% Trypsin (1X), 25050-014). Embryos were minced using dissection scissors and incubated at 37°C for 5mins. To further homogenise the tissue samples were passed through a 21 gauge x1.5' needle (microlance, Becton Dickinson, New Jersey, U.S.A.) on a 1mL syringe 10 times. 5mL of MEFs media (DMEM (31966-021) 1 X NEAA (Sigma-Aldrich M7145) 1 X Penicillin/Streptomycin (15070-063) 50 µM 2-mercaptoethanol (31350-010) 10 % FBS (10500-064)) was added to each well. MEFs were incubated at 37°C until confluent before being split into T25 flasks. Following this MEFs were split every 2-3days or when confluent.

2.5.1.2 Mouse Embryonic Fibroblast Isolation

In order to generate MEFs, timed matings were set up and mice were plug checked daily to determine the date of conception. Females were sacrificed at 12.5-14.5 days post coitum and embryos were collected. Individual embryos were dissected. The head, liver and any blood clots were removed. The liver was kept for DNA extraction and subsequent genotyping. Embryos were then placed in individual wells of a six well plate and suspended

in Dulbecco's phosphate-buffered saline (DPBS). DPBS was then removed and 1.5mL of dissociation reagent (0.25% Trypsin (1X), 25050-014). Embryos were minced using dissection scissors and incubated at 37°C for 5mins. To further homogenise the tissue samples were passed through a 21 gauge x1.5' needle (microlance, Becton Dickinson, New Jersey, U.S.A.) on a 1mL syringe 10 times. 5mL of MEFs media (DMEM (31966-021) 1 X NEAA (Sigma-Aldrich M7145) 1 X Penicillin/Streptomycin (15070-063) 50 μM 2-mercaptoethanol (31350-010) 10 % FBS (10500-064)) was added to each well. MEFs were incubated at 37°C until confluent before being split into T25 flasks. Following this MEFs were split every 2-3 days or when confluent.

2.5.2 Seahorse Extracellular Flux Analysis

The Seahorse XF24 flux analyser (Seahorse Bioscience) measures changed in pH and oxygen levels in the media of cells seeded on a 24-well plate. Oxygen consumption rate (OCR) and extracellular acidification rate (ECAR) is measured by monitoring the changes in dissolved oxygen and H^+ ions, respectively, in the media above the cell monolayer using solid state sensor probes. OCR is a measure of mitochondrial oxidative phosphorylation and ECAR is an indirect measurement of lactate production from cellular anaerobic glycolysis.

MEFs were counted and plated on to seahorse 24 well plates, 20000 cells were seeded per well in 100μL of MEFs media and left to adhere overnight. The seahorse XF-24 instrument cartridge was loaded with seahorse calibrant and placed in CO2 free incubator at 37°C overnight.

On the day of the assay MEFs media was replaced with XF Assay Media, L-glutamine 2 mM, sodium pyruvate 2 mM, and glucose 10 mM (pH was measured and adjusted to pH 7.4 at 37 °C). The cell plate was then incubated for at least 1 hour at 37°C in a CO2 free

incubator to allow CO2 to diffuse out of solution. The seahorse XF-24 analyser cartridge was then loaded with compounds as follows.

Port A: Oligomycin

Port B: FCCP

Port C: Rotenone and Antimycin

The XF-24 instrument cartridge was calibrated before running the assay.

Basal OCR is the amount of oxygen that is being consumed by the cell when oxygen consumption is coupled with ATP synthetase activity and conditions are optimal for cell growth and propagation. Basal OCR is measured by the XF-24 analyser before Port A has been added to each well. Maximal OCR is determined after the proton gradient been uncoupled from ATP synthetase. This is achieved first though inhibition of ATP synthetase using oligomycin and secondly through treatment with the protonophore Carbonyl cyanide-4-(trifluoromethoxy)phenylhydrazone (FCCP). Protonophores such as FCCP can facilitate the transport of protons across lipid membranes. In this case FCCP catalyses the transport of protons from the intermembrane space into the inner matrix of mitochondria. Through doing so the proton gradient is uncoupled from ATP synthesis allowing the electron transport chain to reach its maximal rate and hence the rate of oxygen consumption is maximal. The Seahorse XF-24 analyser measures maximal OCR after Port A and Port B have been added to each well.

2.5.2.1 Live Dead Cell Staining

Following the seahorse assay, data was normalized to the relative number of live cells in each well of the 24 well seahorse cell plate. Seahorse assay medium was removed and cells were washed twice with DPBS. Cells were then treated with live/dead stain [(Invitrogen) 2 µM Calcein AM and 4 µM EthD-1] and incubated at room temperature for

15mins, protected from light. The plate was read on an Optima Plate reader (BMG labtech, Offenburg, Germany), with filters for Live (calcein) excitation 485-12nm and emission 520-10nm and Dead (EthD-1) excitation 520-10nm and emission 650-10nm.

2.5.3 Mitochondrial translation assay

MEFs were seeded in T75 flasks and cultured in DMEM, high glucose, GlutaMAX (Sigma 10566016), 10% BSA for two days prior to the assay. Complete DMEM media was removed and cells were washed twice with PBS. The cells were incubated with pre-warmed methionine / cysteine free DMEM (Sigma D0422) at 37°C for 10mins before discarding the medium. This step was repeated once more. Medium was removed and replaced with methionine / cysteine free DMEM supplemented with 10% dialysed PCS and 100µg/mL emetine dihydrochloride; cells were incubated for 10mins at 37°C. Emetine dihydrochloride inhibits cytoplasmic protein synthesis. 20µL/mL of [35S]-methionine/cysteine mix (PerkinElmer EasyTag express protein labelling mix NEG-772, 73% L-met, 22% L-cyc) was added to each flask and cells were incubated at 37°C for 30mins. Medium was removed, cells were washed twice and harvested in chilled 1mM EDTA/PBS. Cells were pelleted by centrifugation at 250 x g for 4mins. The cell pellet was washed 3 times with cold PBS and resuspended in 30-100µL ice cold PBS supplemented with Roche EDTA protease inhibitor cocktail and 1mM PMSF. Cell-suspensions were snap frozen in liquid nitrogen and stored at -80°C overnight. The next day, samples were defrosted on ice. Once defrosted total protein was quantified using a Bradford assay and 10µL aliquots of samples at 5µg/µL were prepared. 2x dissociation buffer (20% glycerol, 4% SDS (Sigma L4509), 250mM Tri-HCL pH 6.8, 100mM DTT) and 0.5µL Benzonase nuclease were added to each sample before incubating at room temperature for 1hour. Samples were loaded on to a 15% SDS-PAGE gels. Electrophoresis was performed at 20mA for 1.5hours. The gel was then fixed overnight (3% glycerol, 10% acetic acid, 30% methanol) with gentle agitation. The following day the gel was removed from the fixative and dried under a vacuum at 65°C for 2-4 hours.

The dried gel was then visualised using the PhosphorImager / Image Quant software (Molecular Dynamics GE Healthcare).

2.6 Histology & Histochemistry Methods

2.6.1 H & E staining

Mice were culled by cervical dislocation and tissues were dissected as described previously. Liver, kidney, liver, skeletal muscle, iWAT, gWAT and BAT were dissected completely and tissues were weighed. Tissues were fixed in neutral buffered 4 % formaldehyde for at least 24 hours at room temperature. Tissues were paraffin embedded and 6 µm and stained with haematoxylin and eosin according to standard protocols (perform by the Histology Department, MRC Harwell). Stained sections were imaged using the Hamamatsu NaoZoomer slide scanner and NDP 2 serve software was used to export the images at appropriate magnifications.

2.6.2 Luxol Fast Blue and Cresyl Violet Brain Staining

Whole brains were dissected and were placed in moulds, submerged in cryoprotectant OCT and frozen in an isopentane ice bath according to standard protocol. Briefly, a flask of isopentane is placed in liquid nitrogen until frozen. The flask is then removed from liquid nitrogen and placed on dry ice. Once the isopentane has melted, the brain mould is placed in the isopenane bath until the OCT has become opaque and completely frozen. Frozen brains were cut in a standard brain matrix in order to obtain comparable sections between samples. 10 µm frozen sections were cut using a cryostat sections and brains were stained with luxol fast blue and cresyl violet. The Histology Team at MRC Harwell performed the processes of brain dissection, freezing and staining.

2.7 Statistical analysis

Results are shown as mean ± standard deviation (SD) or standard error mean (SEM). Statistical analysis was performed using GraphPad Prism software.

Statistical analysis of data where two variables were present, e.g. total body weight over time, was performed using repeated measures two-way ANOVA with Bonferroni's post hoc test to correct for multiple comparisons. If the data sets were incomplete, then repeated measures were not performed and data was analysed with ANOVA followed by Bonferroni's post hoc test. ABR data was analysed using one-way ANOVA with Tukey's post hoc test to adjust for multiple comparisons. The Student's t-test was used to analyse the difference between the means of two groups e.g. *Wars2*$^{+/+}$ and *Wars2*$^{V117L/V117L}$. One-way ANOVA was used to analyse the difference between the means of or more genotype groups e.g. *Wars2*$^{+/+}$, *Wars2*$^{+/-}$, *Wars2*$^{+/V117L}$ and *Wars2*$^{V117L/-}$. Significance was assigned to results if the probability was >5%, ($P<0.05$). Significance levels are indicated above each figure with asterisks: *$P<0.05$, **$P<0.01$, ***$P<0.001$.

3 Identification and phenotypic characterization *Wars2*-V117L allele in mice

3.1 Introduction

In an ageing population, the prominence of age related disease is greater than ever. Many diseases are associated with ageing including: diabetes, cancer, kidney disease, cardiovascular disease and neurodegenerative disease (Niccoli & Partridge, 2012). The requirement to determine genetic variants predisposing individuals to age related disorders are vital to further our understanding of the pathogenesis of age-related disorders, to develop novel therapeutic strategies to combat age-related disorders and relinquish the growing financial burden of an ageing society.

The Harwell Ageing Screen (HAS) is an on-going N-ethyl-N-nitrosourea (ENU) mutagenesis program founded to identify novel genomic modifiers of age related disorders. Founder C57BL/6J male mice were treated with ENU and following a period of sterility mated to C3H/C3PDE (wild type) females to generate 1st generation (G1) progeny. G1 male mice were mated to wild-type (WT) C3H/C3PDE females generating a 2nd generation (G2) progeny. Finally, G1 males were mated with G2 females to generate third generation (G3) cohorts (**Figure 3.1**). G3 cohorts entered a phenotype driven recessive screen, with mice being aged to 18 months to identify phenotypes associated with age (**Table 3.1**).

The principle of the screen was to use ENU to induce random point mutations in the murine genome (**Figure 3.1**). Offspring of mutagenized mice were extensively phenotyped over a period of 18 months with the aim of identifying phenodeviants particularly in 'aged' mice (**Table 3.1**). Phenodeviants were identified within cohorts, dependent upon 3 or more mice

producing a value of 2 standard deviations higher or lower than the calculated reference range for a given phenotyping test. Establishing the percentile positions from the entire data set generated the calculated reference range for each phenotyping test allowing outliers to be identified. SNP mapping and next generation sequencing were then used to identify the causal ENU-induced mutation for the phenotypes identified.

Figure 3.1 - Schematic diagram of The Harwell Ageing Screen mutagenesis breeding program.

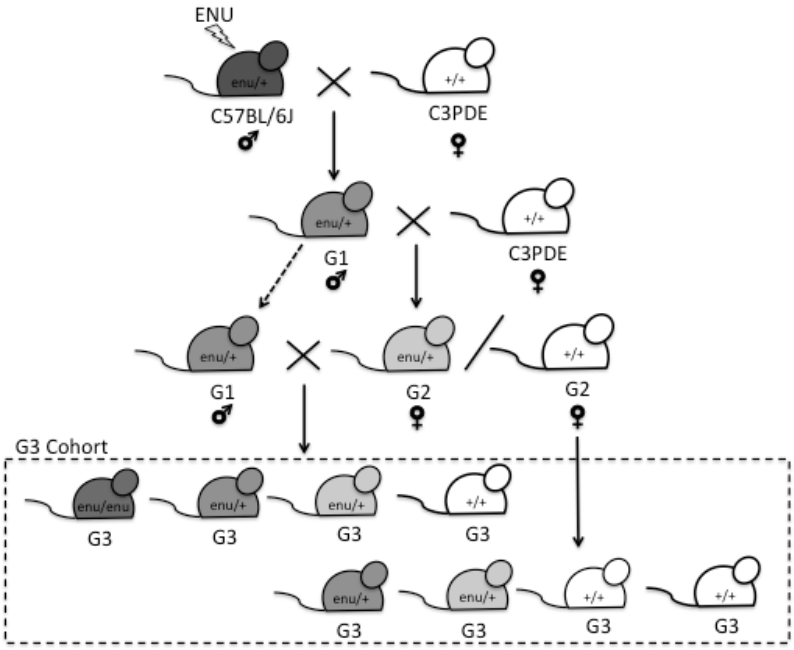

The colour of the mice illustrates that mice generated in the HAS are mixed genetic background, with 'dark grey' mice being C57BL/6J inbred mice, 'white' mice being C3PDE inbred mice and their offspring are coloured shades of grey to represent differing proportions of both C57BL/6J and C3PDE background strains.

Mutant-Pedigree-Cohort-151 (MPC-151) was generated from the HAS. A subset of mice within MPC-151 were identified as having progressive hearing loss and reduced adiposity phenotypes. Here I present work performed to identify the causal mutation for these linked phenotypes followed by further phenotypic characterization of the causal ENU-induced mutant allele.

In this chapter I present compelling evidence that the causal mutation for the aforementioned phenotypes is located within the mitochondrial tryptophanyl-tRNA synthetase (*Wars2*) gene. As mentioned in my previous chapter, mutations within mtRS

genes cause varied and unexplained tissue specific clinical pathologies in humans. To date, little is known about the tissue specific disease mechanisms associated with mtRS mutations and current treatments target patient symptoms rather than their mechanistic underpinning. Following the identification of this ENU-induced *Wars2* mutation, we were excited to be given the opportunity to characterize the tissue-specific, disease causing mechanisms in this mouse model and with the overarching goal of providing insight that may lead to novel therapeutic strategies for mutant-mtRS patients in the future.

Test	Phenotypic Area	Age (Weeks)
Electrocardiogram (ECG)	Cardiac	12
SHIRPA	Neurological	13, 66
Grip Strength	Musculoskeletal/Neurological	13, 66
Slit Lamp/ophthalmoscope	Vision	15, 49, 65, (73)
Optokinetic Drum	Vision/Neurological	15, 49, 65, (73)
Click Box	Hearing	14, 26, 39, 50
Auditory Brainstem Response + click stimulus	Hearing	14, 39
Echo-MRI	Growth/Body composition	16, 27, 51, 71
Dual Energy X ray Analysis (DEXA)	Musculoskeletal/Body composition	16, 51,
X ray	Musculoskeletal	16, 51, 74
Pupilometry	Vision/Neurobehavioral	18, 68
Sleep tracking	Neurobehavioral	18, 68
Clinical Chemistry	Pathology	28, 53, 80
Fasted Bleed	Diabetes/Metabolism	17, 28, 52, 80
Fasted Insulin	Diabetes/Metabolism	33, 57, 72
Intraperitoneal Glucose Tolerance Test (IPGTT)	Diabetes/Metabolism	33, 57, 72

Table 3.1 - The Harwell Ageing Screen phenotyping pipeline.
Summary of phenotyping tests employed during the Harwell Ageing Screen with scheduled time points for each test.

3.2 Results

3.2.1 Mutant-Pedigree-Cohort-151 Phenotyping

Mutant-Pedigree-Cohort-151 (MPC-151) was generated from 'The Harwell Ageing Screen' (HAS). As part of the HAS phenotyping pipeline, MPC-151 mice ability to hear was tested using Click Box stimulation (CB) and Auditory Brainstem Response (ABR) threshold analysis at various time-points. Normal click-box (CB) responses were recorded at 3 months of age for all MPC-151 mice. At 6 months of age 2 mice within the cohort failed to respond to CB stimuli. At 9 and 12 months of age, 7 and 5 mice within the cohort had abnormal CB responses respectively (**Table 3.2**). CB and ABR data were not available at 12 months of age for two affected mice due to procedural termination in keeping with HAS phenotyping pipeline. Auditory brainstem response thresholds at 9 months of age demonstrated that the same 5 mice with absent CB responses had elevated ABR thresholds across all frequencies indicative of sensorineural hearing loss. ABR thresholds for these 5 mice were further elevated at 12 months of age indicating that the sensorineural hearing loss phenotype observed in these mice is progressive with age (**Figure 3.2A**).

	CLICK BOX RESPONSE			
Mouse ID	3 MONTHS	6 MONTHS	9 MONTHS	12 MONTHS
MPC-151/2.1F	2	2	0.5	0
MPC-151/2.1K	2	2	0.5	N/A
MPC-151/2.8E	2	1	0	0
MPC-151/2.9H	2	2	0	0
MPC-151/2.11C	2	2	0	0
MPC-151/2.10G	2	2	1	N/A
MPC-151/2.10J	2	0	0	0
MPC-151/2.8D	2	2	2	2
MPC-151/2.11D	2	2	2	2
MPC-151/2.10F	2	2	2	2

Table 3.2 – Summary of click box responses in MPC-151.
MPC-151 CB responses were scored at 3, 6, 9 and 12 months of age. Score: 2 = normal startle, 1 = reduced startle and 0 = no startle. Mice with abnormal CB responses are highlighted in red. These data were collected by the Deafness Group, MRC Harwell.

Mice with sensorineural hearing loss also had reduced total body mass from 7 months of age (**Figure 3.2B**). EchoMRI body composition analysis at 15 months showed that the reduction in total body mass was due to significantly reduced fat mass in MPC-151 mice with progressive hearing loss (**Figure 3.2C**). All mice with abnormal CBR also had elevated ABR thresholds, reduced total body mass and reduced adiposity indicating that these phenotypes were co-inherited and likely caused by the same ENU-induced mutant allele.

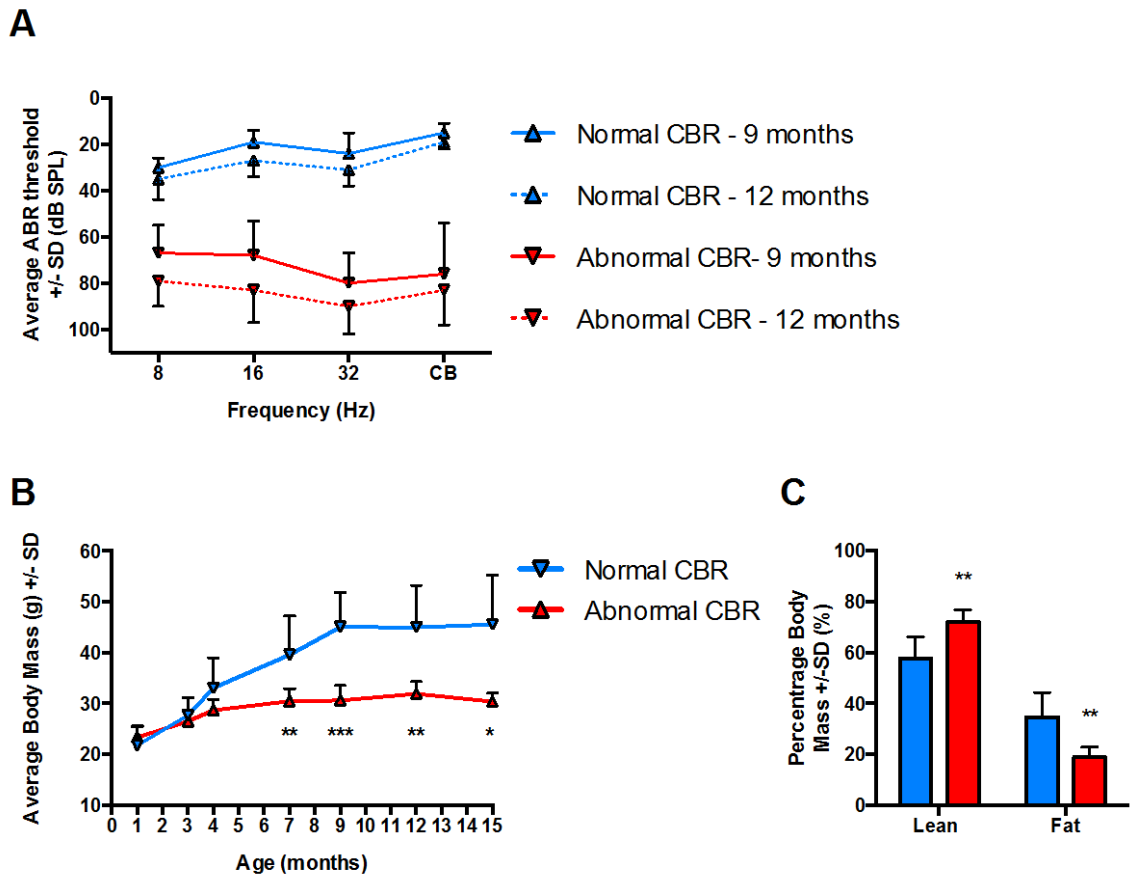

Figure 3.2 – MPC-151 auditory brainstem response thresholds and body composition analysis.
MPC-151 mice with: normal CB response = blue and abnormal CB response = red. A) Auditory brainstem response thresholds were recorded at single frequencies: 8, 16 and 32Hz, and mixed frequencies (CB), solid line = 9 months of age, dotted line = 12 months of age. Data analyzed using one-way ANOVA with Tukey's multiple comparisons test. B) Average total body mass over time. Data analyzed using two-way ANOVA with bonferroni post-hoc test. C) EchoMRI body composition analysis at 15 months of age: percentage lean mass and percentage fat mass. Data analyzed using student's t-test. All data shown as mean ± SD. * P<0.05, ** P<0.01, *** P<0.001. ABR data was collected by the Deafness Group, MRC Harwell.

3.2.2 MPC-151 Mapping and Next Generation Sequencing

In order to determine the causal ENU-induced mutation(s) for the hearing loss and reduced adiposity phenotypes observed in the MPC-151 cohort, single nucleotide polymorphism (SNP) mapping was performed. DNA from 7 ‘affected’ and 7 ‘non-affected’ MPC-151 mice were sent for SNP analysis of 1422 SNPs at a density of approximately 1 SNP per 1.8Mb. SNP analysis was performed against reference SNPs from C57BL/6J and C3H/C3PDE mice. SNP mapping identified a 73 Mb region on chromosome 3 (Chr3: 70015850 – 143057879; GRCm38 genome assembly) from rs6198234 to rs6407142 within which all MPC-151 mice with hearing loss were homozygous or heterozygous C57BL/6J and MPC-151 mice with normal hearing were either heterozygous or homozygous C3H/C3PDE (**Figure 3.3**).

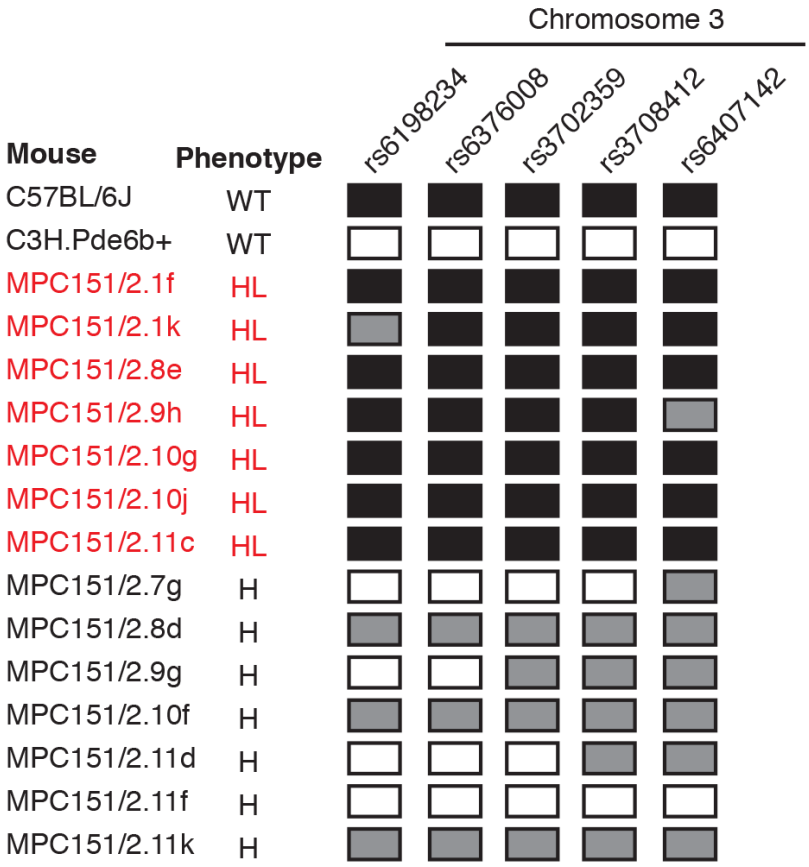

Figure 3.3 - MPC-151 SNP mapping Chr 3.
Schematic diagram of hearing loss / reduced adiposity 73Mb SNP mapping region on Chromosome 3 (Chr3: 70015850 – 143057879; GRCm38 genome assembly) from rs6198234 to rs6407142. SNP mapping was performed using the Illumina Medium Density SNP mapping panel which is informative for >900 SNPs for C57BL/6J and C3H/C3PDE reference strains. Red text = MPC-151 mice with hearing loss (n=7), black text = MPC-151 mice with normal hearing (n=7). Black box = homozygous for C57BL/6J SNP reference allele, white box = homozygous for C3H/C3PDE SNP reference allele and grey box = heterozygous for C57BL/6J &C3H/C3PDE SNP reference alleles. SNP mapping analysis was performed by the Bioinformatics Group, MRC Harwell.

Whole genome sequencing of an 'affected' G3 mouse identified 540 ENU-induced mutations within this region to varying degrees of confidence. Of these 540 mutations, 3 high-confidence missense mutations were identified (**Table 3.3**). To confirm that these mutations were not genome sequencing errors, DNA from the G1 founder male and an MPC-151 'affected' mouse were extracted and the genomic regions of interest were amplified using polymerase chain reaction (PCR). PCR products were sequenced using Sanger Sequencing and all 3 missense mutations were validated as shown by the presence of the mutant allele in the MPC-151 founder G1 (heterozygous for mutant allele) and MPC-151 'affected' G3 (homozygous for mutant allele) (**Figure 3.4**).

GENE	LOCATION	CLASSIFICATION	MUTATION	AMINO ACID CHANGE
Tchh	3:93250490	MISSENSE	A➔T	D1105V
Wars2	3:99008459	MISSENSE	G➔T	V117L
Ppa2	3:132993418	MISSENSE	A➔T	Y123F

Table 3.3 – Missense mutations identified on Chr 3 from whole mouse sequencing of MPC-151 'affected' G3 mouse.
Three missense mutations were identified within the SNP mapping region on Chr 3; *Tchh*-D<1105>V, *Wars2*-V<117>L and *Ppa2*-Y<123>F. D = aspartic acid, V = Valine, L = Leucine, Y = Tyrosine and F = Phenylalanine. Sequence obtained from NCBIM37/mm9.

Tchh encodes Trichohyalin, the function of which has been studied at length. Trichohyalin is an intermediate filament-associated protein that associates with keratin intermediate filaments found in inner root sheath cells of hair follicles and the granular layer of the epidermis (O'Keefe, Hamilton, Lee, & Steinert, 1993). *Tchh* has been shown to be expressed exclusively in these cell-types making the *Tchh*-D1105V ENU-induced mutation an unlikely candidate for hearing loss or reduced adiposity.

Ppa2 encodes pyrophosphatase 2 (PPase-2), the function of which has yet to be characterized at length. It is known the PPase-2 has an N-terminal mitochondrial import signalling peptide that targets the protein to the mitochondrial matrix and *Ppa2* shares signature sequences found in other pyrophosphatases and therefore is speculated to play a role in cellular phosphate metabolism (Curbo et al., 2006). The yeast homolog of PPase-2 has been shown to be required for mitochondrial DNA maintenance (Lundin, Baltscheffsky, & Ronne, 1991). Given how little is known about this gene, it is possible that the *Ppa2*-Y123F ENU-induced mutation could be causal for hearing loss or reduced adiposity in the MPC-151 cohort.

Wars2 encodes mitochondrial tryptophanyl tRNA sythetase (mtTrpRS) (Borglum et al., 1996). mtTrpRS is vital for mitochondrial protein synthesis as it catalyses the aminoacylation of mtDNA encoded $tRNA^{Trp}$ with tryptophan to form Trp-$tRNA^{Trp}$. Once $tRNA^{Trp}$ has been 'charged', tryptophan can then be incorporated in newly synthesized peptides during mitochondrial protein translation. As mentioned previously no human patients with *WARS2* mutations have been identified. However, mutations in several other mtRS genes have been shown to be associated with hearing loss in humans including: *LARS2*, *HARS2,* and *NARS2* (S B Pierce et al., 2011; Sarah B. Pierce et al., 2013; Simon et al., 2015). Based upon this we thought that the *Wars2*-V117L ENU-induced mutation was a good candidate for the sensorineural hearing loss phenotype observed in MPC-151 mice. There was also evidence to indicate that *Wars2*-V117L was causal for reduced adiposity. Wolny *et al.* performed a retrospective study looking at body mass index (BMI) in children with mitochondrial disease. In this study they showed that children with mitochondrial disease have low BMI that progressively decreases with age (Wolny, McFarland, Chinnery, & Cheetham, 2009). It is possible therefore that the *Wars2*-V117L was causal for the hearing loss and reduced adiposity observed in MPC-151 mice with exciting implications for the study of the *Wars2*-V117L ENU-induced mutation to model human mitochondrial disease in the mouse.

In order to determine the causal ENU-induced mutation for the phenotypes observed in the original MPC-151 cohort, new cohorts of MPC-151 mice were re-derived via *in vitro* fertilization of C3H/C3PDE females using MPC-151 G1 founder male sperm. Mice were backcrossed (BC) 3 times to C3H/C3PDE. Mice were genotyped for the three ENU-induced missense mutations after each BC in order segregate candidate mutations. Segregation of the *Ppa2*-Y123F ENU-induced mutation was achieved at BC2. Segregation of the in *Tchh*-D1105V and *Wars2*-V117L ENU-induced mutations was not achieved due to their close proximity. Two cohorts of mice, namely: MPC-151-*Ppa2* and MPC-151-*Wars2*/*Tchh*, were

bred and phenotyped in order determine whether the hearing loss and lean phenotypes could be recapitulated in either cohort.

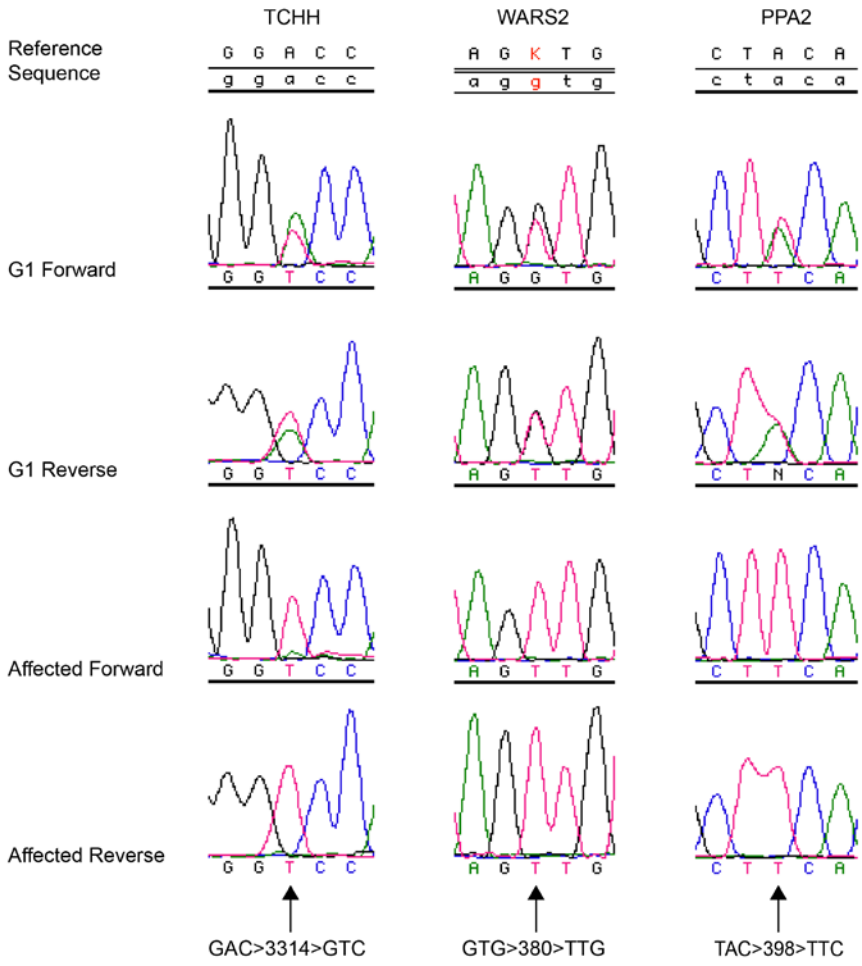

Figure 3.4 – Validation of ENU-induced missense mutations identified in G3 'affected' mouse by Next Generation Sequencing.
Sanger sequencing of MPC-151 G1 founder and MPC-151 'affected' G3 at the shown locations corresponding to the three identified ENU-induced missense mutations on Chr 3: *Tchh*-GAC>3314>GTC, *Wars2*-GTG>380>TTG and *Ppa2*-TAC>398>TTC. The MPC-151 G1 founder is heterozygous for all 3 missense mutations. The MPC-151 'affected' G3 is homozygous for the three missense mutations.

3.2.3 MPC-151-*Ppa2* Phenotyping

A cohort of MPC-151-*Ppa2* mice were generated by mating MPC-151-*Ppa2*$^{+/Y123F}$ male with MPC-151-*Ppa2*$^{+/Y123F}$ females. MPC-151-*Ppa2*$^{Y123F/Y123F}$ (*Ppa2*$^{Y123F/Y123F}$) mice were phenotyped in order to determine whether the *Ppa2*-Y123F ENU-induced mutation was causal for the phenotypes observed in the original MPC-151 cohort. *Ppa2*$^{Y123F/Y123F}$ mice were weighed monthly from 2 months of age. Both male (**Figure 3.5A**) and female (**Figure**

3.5B) *Ppa2*$^{Y123F/Y123F}$ and *Ppa2*$^{+/Y123F}$ mice showed no significant differences in total body mass compared to *Ppa2*$^{+/+}$ littermates at any time point. EchoMRI body composition analysis at 3, 5 and 6 months equally showed no significant differences in percentage lean mass and percentage fat mass between *Ppa2*$^{Y123F/Y123F}$ and *Ppa2*$^{+/Y123F}$ male (**Figure 3.5C+E**) and female (**Figure 3.5D+F**) mice compared to *Ppa2*$^{+/+}$ littermate controls.

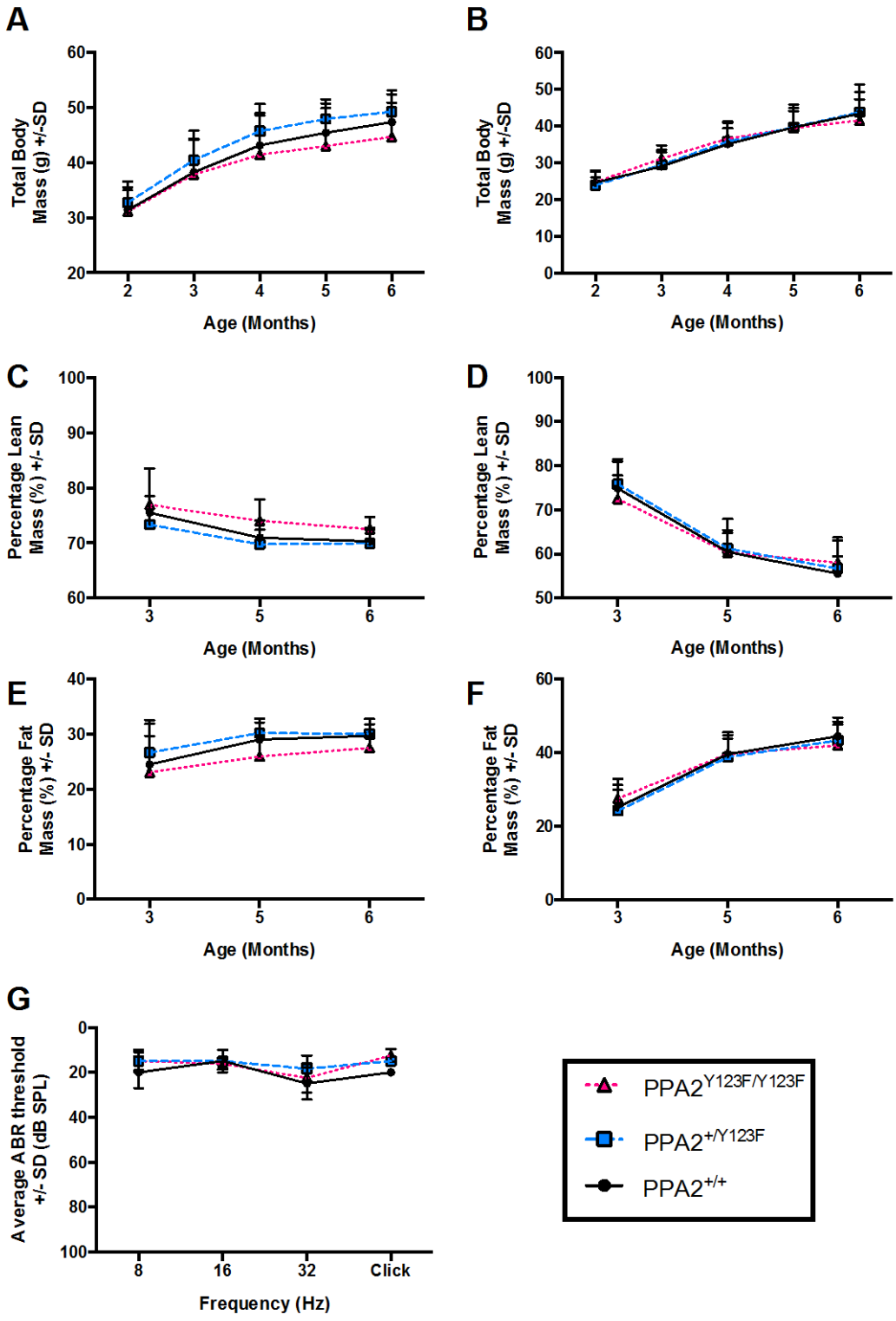

Figure 3.5 – *Ppa2*$^{Y123F/Y123F}$ phenotyping data.
A) Male total body mass. B) Female total body mass. C) Male percentage lean mass. D) Female percentage lean mass. E) Male percentage fat mass. F) Female percentage fat mass. Males; *Ppa2*$^{+/+}$ n=7, *Ppa2*$^{+/Y123F}$ n=12, *Ppa2*$^{Y123F/Y123F}$ n=6. Females; *Ppa2*$^{+/+}$ n=4, *Ppa2*$^{+/Y123F}$ n=12, *Ppa2*$^{Y123F/Y123F}$ n=5. Time course data were analyzed using two-way ANOVA with bonferroni post-hoc test: ***** P<0.05, ****** P<0.01, ******* P<0.001 G) Auditory brainstem response thresholds were recorded at single frequencies: 8, 16 and 32Hz, and mixed frequencies (CB) at 6 months of age. *Ppa2*$^{+/+}$ n=2, *Ppa2*$^{+/Y123F}$ n=3, *Ppa2*$^{Y123F/Y123F}$ n=4. Data shown as mean ± SD. ABR data analyzed using one-way ANOVA with Tukey's multiple comparisons test: ***** P<0.05, ****** P<0.01, ******* P<0.001.

Mice hearing ability was tested at 6 months of age and ABR analysis showed no significant differences in ABR thresholds between *Ppa2*$^{Y123F/Y123F}$, *Ppa2*$^{+/Y123F}$ and *Ppa2*$^{+/+}$ mice at any measured frequency (**Figure 3.5G**). Given that neither the hearing loss or reduced adiposity phenotypes were observed in *Ppa2*$^{Y123F/Y123F}$ mice we concluded that the *Ppa2*-Y123F ENU-induced mutation was not the causal mutation for the phenotypes previously observed in the original MPC-151 cohort.

3.2.4 MPC-151-*Wars2* Phenotyping

In order to determine whether the *Wars2*-V117L or *Tchh*-D1105V ENU-induced mutations were causal for the phenotypes observed in the original MPC-151 cohort, MPC-151-*Wars2*$^{V117L/V117L}$ mice were generated and phenotyped. We were unable to develop a reliable genotyping assay for the *Tchh*-D1105V ENU-induced mutation due to the mutation being located within a region of serial repeats. Mice were therefore genotyped only for the *Wars2*-V117L ENU-induced mutation. MPC-151-*Wars2*$^{V117L/V117L}$ will be referred to as *Wars2*$^{V117L/V117L}$ mice from now on. It is worth bearing in mind that these mice likely still retain the *Tchh*-D1105V allele.

Wars2$^{V117L/V117L}$ mice were generated from crossing *Wars2*$^{+/V117L}$ males with *Wars2*$^{+/V117L}$ females. Mice were weighed monthly from 1 month of age and body composition analysis was performed monthly using EchoMRI from 2 months age. No significant differences in total body mass were observed in male and female *Wars2*$^{V117L/V117L}$, *Wars2*$^{+/V117L}$ and *Wars2*$^{+/+}$ mice at 1 month of age. However, from 2 (male) and 3 (females) months of age *Wars2*$^{V117L/V117L}$ mice had significantly reduced total body mass compared to *Wars2*$^{+/+}$ littermate controls (**Figure 3.6A + B**). Male and female *Wars2*$^{V117L/V117L}$ mice showed no significant differences in percentage lean or fat mass at 2 months of age compare to littermate controls. However, both *Wars2*$^{V117L/V117L}$ male and females had significantly decreased percentage fat mass from 3 months of age compared to littermate controls

(**Figure 3.6C – F**). Heterozygous *Wars2*$^{+/V117L}$ male and female mice showed no significant differences in total body mass, percentage fat mass or percentage lean mass compared to *Wars2*$^{+/+}$ littermate controls at any time point.

Wars2$^{V117L/V117L}$ ABR thresholds were measured at 4 and 6 months of age. *Wars2*$^{V117L/V117L}$ ABR thresholds were significantly elevated at all measured frequencies compared to *Wars2*$^{+/+}$ littermate controls at both time points (**Figure 3.6G + H**). *Wars2*$^{+/V117L}$ ABR thresholds showed no significant differences compared *Wars2*$^{+/+}$ littermate controls at any frequency and at either time point.

In conclusion, both the hearing loss and reduced adiposity phenotypes observed in the original MPC-151 cohort were recapitulated in the *Wars2*$^{V117L/V117L}$ mice suggesting that either the *Wars2*-V117L or *Tchh*-D1105V ENU-induced mutations were causal.

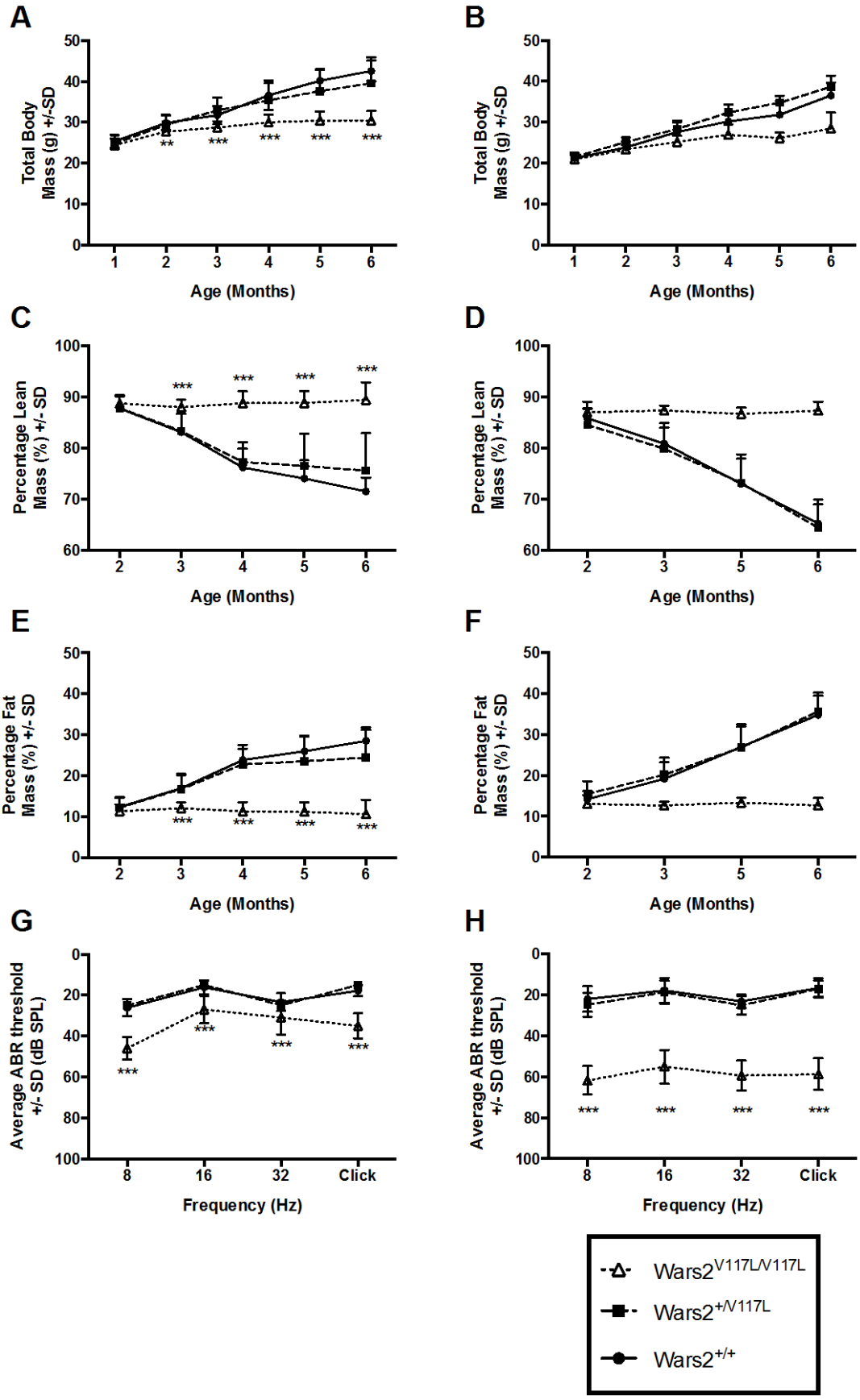
A
Total Body Mass (g) +/-SD
Age (Months)
B
Total Body Mass (g) +/-SD
Age (Months)
C
Percentage Lean Mass (%) +/- SD
Age (Months)
D
Percentage Lean Mass (%) +/- SD
Age (Months)
E
Percentage Fat Mass (%) +/- SD
Age (Months)
F
Percentage Fat Mass (%) +/- SD
Age (Months)
G
Average ABR threshold +/- SD (dB SPL)
Frequency (Hz)
8
16
32
Click
H
Average ABR threshold +/- SD (dB SPL)
Frequency (Hz)
Wars2V117L/V117L
Wars2+/V117L
Wars2+/+

Figure 3.6 – *Wars2*$^{V117L/V117L}$ phenotyping data
A) Male total body mass. B) Female total body mass. C) Male percentage lean mass. D) Female percentage lean mass. E) Male percentage fat mass. F) Female percentage fat mass. Males; *Wars2*$^{+/+}$ n=13, *Wars2*$^{+/V117L}$ n=19, *Wars2*$^{V117L/V117L}$ n=11. Females; *Wars2*$^{+/+}$ n=18, *Wars2*$^{+/V117L}$ n=19, *Wars2*$^{V117L/V117L}$ n=10. Time course data were analyzed using two-way ANOVA with bonferroni post-hoc test: ***** P<0.05, ****** P<0.01, ******* P<0.001. Auditory brainstem response thresholds at G) 4 months H) 6 months were recorded at single frequencies: 8, 16 and 32Hz, and mixed frequencies (CB). *Wars2*$^{+/+}$ n=13, *Wars2*$^{+/V117L}$ n=18, *Wars2*$^{V117L/V117L}$ n=15. Data shown as mean ± SD. ABR data analyzed using one-way ANOVA with Tukey's multiple comparisons test: ***** P<0.05, ****** P<0.01, ******* P<0.001.

3.2.5 Complementation Test

Given that we were unable to segregate the *Wars2*-V117L and *Tchh*-D1105V alleles, it was not possible for us determine which ENU-induced mutation(s) were causal for the hearing loss or lean phenotypes. In order to determine whether the *Wars2*-V117L ENU-induced mutation was causal we performed a complementation test by crossing *Wars2*$^{+/V117L}$ males with *Wars2*$^{+/-}$ females generating compound heterozygote *Wars2*$^{V117L/-}$ mice. Through doing so we were asked the question: does the *Wars2*-V117L ENU-induced allele compliment the *Wars2*-KO? We hypothesised that the *Wars2*-V117L allele does not compliment the *Wars2*-KO allele and will lead to a similar or probably more severe / faster progressing phenotypes as identified in the *Wars2*$^{V117L/V117L}$ mice.

Wars2$^{tm1.1(KOMP)Vlcg}$ (*Wars2*-KO) mice were generated by The Jackson Laboratory as part of the Knockout Mouse Phenotyping Program (KOMP). *Wars2*-KO mice were generated using a promoter-driven targeting cassette to delete a critical region in *Wars2* and introduce a premature stop codon (**Figure 3.7**).

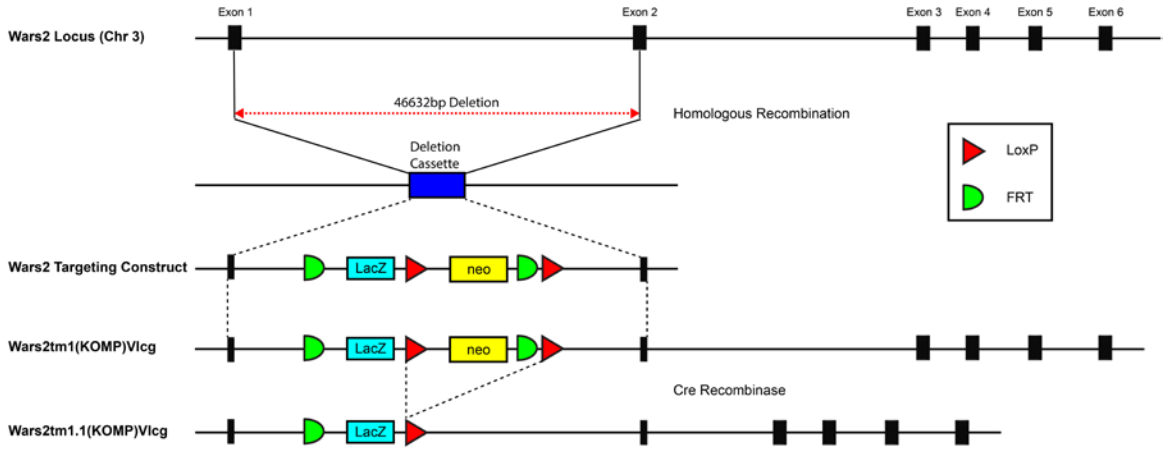

Figure 3.7 – Schematic diagram illustrating the generation of KOMP *Wars2*-KO allele. C57BL/6N embryonic stem cells were transfected with the *Wars2*$^{tm1(KOMP)Vlcg}$ construct. Once transfected the promoter-driven targeting cassette integrated into the ES cell genome via homologous recombination deleting 46632bp in *Wars2* including critical regions of both *Wars2*-Exon1 and *Wars2*-Exon2. Through doing so, a premature stop codon was also introduced. *Wars2*$^{tm1(KOMP)Vlcg}$ ES cells were micro-injected into C57BL/6N blastocysts generating mosaic C57BL/6N-*Wars2*$^{tm1(KOMP)Vlcg}$ offspring. Germ-line transmission (GLT) of the *Wars2*$^{tm1(KOMP)Vlcg}$ construct was determined by genotyping C57BL/6N-*Wars2*$^{tm1(KOMP)Vlcg}$ x C57BL/6N offspring for the neomycin selection cassette. Once GLT was achieved C57BL/6N-*Wars2*$^{tm1(KOMP)Vlcg}$ mice were crossed with cre-recombinase expressing mice to remove the neomycin selection cassette.

First we determined whether compound heterozygous *Wars2*$^{V117L/-}$ mice had reduced adiposity. Compound heterozygous male *Wars2*$^{V117L/-}$ mice had significantly reduced average total body mass from 1 month of age compared to *Wars2*$^{+/+}$ littermate controls (**Figure 3.8A**). *Wars2*$^{V117L/-}$ males had significantly reduced percentage fat mass from 2 months of age compared to *Wars2*$^{+/+}$ littermates (**Figure 3.8B + C**). No significant differences in total mass, percentage lean mass or percentage fat mass were observed in single heterozygous *Wars2*$^{+/V117L}$ or *Wars2*$^{+/-}$ male mice compared to *Wars2*$^{+/+}$ littermate controls at any time point.

We then tested whether compound heterozygous *Wars2*$^{V117L/-}$ mice had hearing loss. At 4 months of age *Wars2*$^{V117L/-}$ mice had elevated ABR thresholds at all measured frequencies compared to *Wars2*$^{+/+}$ littermate controls (**Figure 3.8D**). No significant differences in ABR thresholds were observed in single heterozygous *Wars2*$^{+/V117L}$ and *Wars2*$^{+/-}$ mice compared to *Wars2*$^{+/+}$ littermates at any measure frequency.

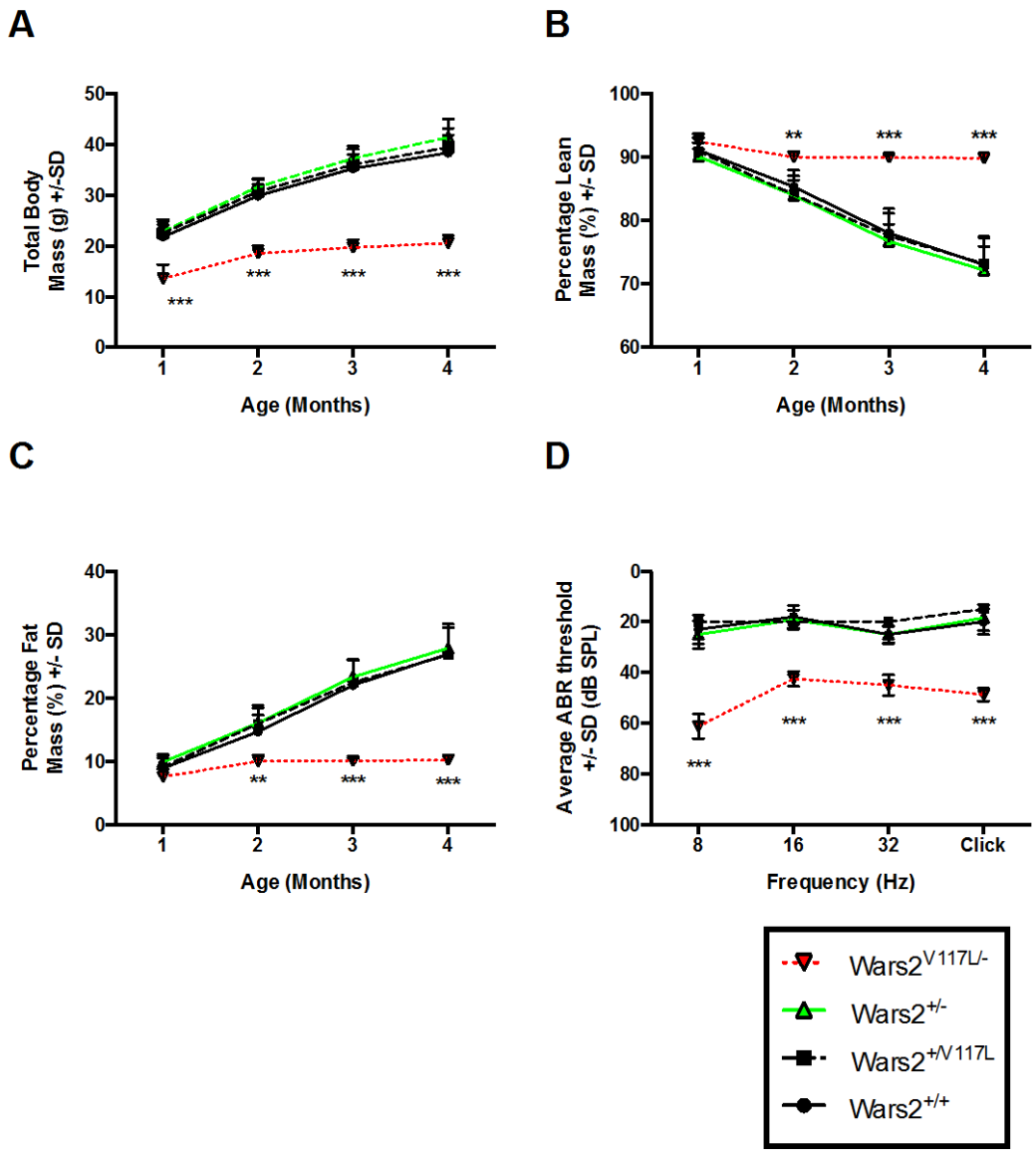

Figure 3.8 – *Wars2*$^{V117L/-}$ phenotyping data.
Male A) total body mass, B) percentage lean mass and C) percentage fat mass over time. Males; *Wars2*$^{+/+}$ n=8, *Wars2*$^{+/V117L}$ n=13, *Wars2*$^{+/-}$ n=9, *Wars2*$^{V117L/-}$ n=6. Time course data were analyzed using two-way ANOVA with bonferroni post-hoc test: ***** P<0.05, ****** P<0.01, ******* P<0.001 D) Auditory brainstem response thresholds at 4 were recorded at single frequencies: 8, 16 and 32Hz, and mixed frequencies (CB). Males; *Wars2*$^{+/+}$ n=5, *Wars2*$^{+/V117L}$ n=1, *Wars2*$^{+/-}$ n=6, *Wars2*$^{V117L/-}$ n=4. Data shown as mean ± SD. ***** P<0.05, ****** P<0.01, ******* P<0.001. ABR data analysed using one-way ANOVA with Tukey's multiple comparisons test: ***** P<0.05, ****** P<0.01, ******* P<0.001.

These data show that *Wars2*$^{V117L/-}$ mice have reduced adiposity and sensorineural hearing loss. By crossing the *Wars2*-V117L allele with the *Wars2*-KO allele we recapitulated the phenotypes observed in the *Wars2*$^{V117L/V117L}$ mice and showed that the *Wars2*-V117L ENU-induced allele does not complement the *Wars2*-KO allele. Also this indicates that the

Wars2-V117L allele, and not the *Tchh*-D1105V allele or any other mutation carried within the pedigree, is causal for the phenotypes observed in the *Wars2*$^{V117L/V117L}$ mice. Furthermore, as the *Wars2*-V117L allele does not compliment the complete loss-of-function *Wars2*-KO allele then this shows that the *Wars2*-V117L allele is also a loss-of-function allele. As mentioned in my introduction, homozygous null mtRS alleles cause embryonic lethality in mice. However, we were able to generate homozygous *Wars2*$^{V117L/V117L}$ mice. This tells us that the *Wars2*-V117L ENU-induced mutation is a partial loss-of-function, hypomorphic allele rather than a complete loss-of-function, null allele.

3.2.6 Embryonic Lethality

In order to address whether the *Wars2*-V117L allele affects mice viability, I analysed the genotype ratios of mice generated during this study. To do this we compared the observed number of mice born per genotype and compared it with the expected number of mice born per genotype (as predicted by Mendelian patterns of inheritance).

As mentioned previously, homozygous null mtRS mutations cause embryonic lethality in mice (**Figure 3.9A**). As part of the International Mouse Phenotyping Consortium (IMPC), *Wars2*$^{+/-}$ x *Wars2*$^{+/-}$ matings were set up with the aim of generating *Wars2*$^{-/-}$ mice. The expected genotype inheritance ratios for mice born from *Wars2*$^{+/-}$ x *Wars2*$^{+/-}$ matings is 0.25:0.5:0.25 (*Wars2*$^{+/+}$:*Wars2*$^{+/-}$:*Wars2*$^{-/-}$). However, the observed genotype inheritance ratios from *Wars2*$^{+/-}$ x *Wars2*$^{+/-}$ matings was 0.3:0.7:0.0 respectively (**Figure 3.9A**). These data show that inheritance of the *Wars2*-KO allele does not follow the Mendelian inheritance patterns and Chi-squared analysis calculated a p-value of <0.0001 indicating that this was statically highly unlikely to happen by chance. As no *Wars2*$^{-/-}$ mice were born, this indicates that the *Wars2*$^{-/-}$ allele causes embryonic lethality. Further genotype analysis of embryos generated from *Wars2*$^{+/-}$ x *Wars2*$^{+/-}$ matings was performed by the IMPC. The IMPC was unable to observe a single *Wars2*$^{-/-}$ embryo at E12.5 or E9.5 indicating that the *Wars2*$^{-/-}$ allele causes embryonic lethality prior to organogenesis.

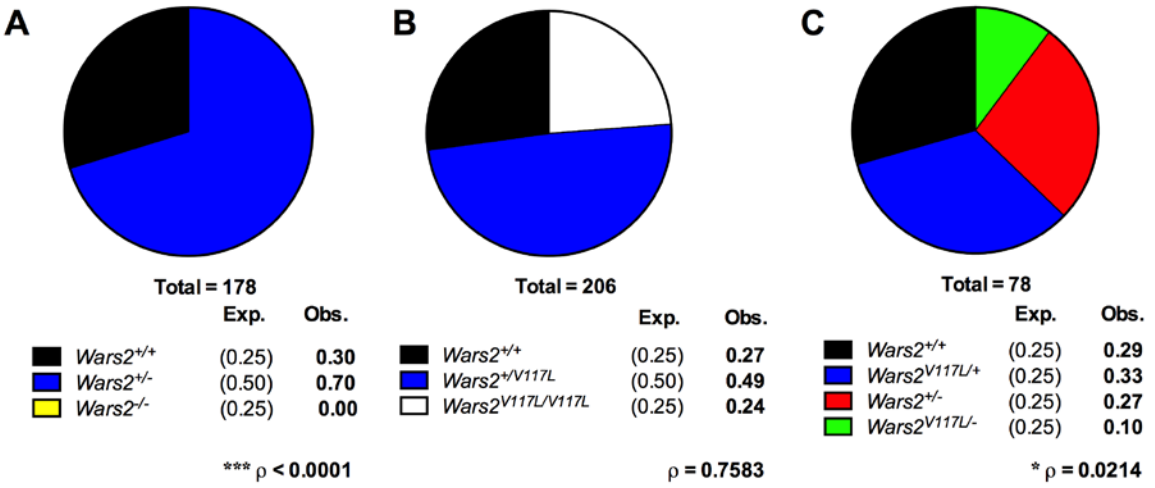

Figure 3.9 – Embryonic lethality.
Pie graphs showing the percentage of mice born per genotype from: A) *Wars2*$^{+/-}$ x *Wars2*$^{+/-}$, B) *Wars2*$^{+/V117L}$ x *Wars2*$^{+/V117L}$ and C) *Wars2*$^{+/V117L}$ x *Wars2*$^{+/-}$ matings. Data shown here is percentage mice born per genotype. Exp. (expected) & Obs. (observed) percentage of mice born per genotype. Data were analysed using Chi-squared test: ***** P<0.05, ****** P<0.01, ******* P<0.001.

Based upon the *Wars2*-KO data from the IMPC we asked the question: is the *Wars2*-V117L allele inherited according to Mendelian patterns of inheritance. We first analysed the number of mice per genotype from *Wars2*$^{+/V117L}$ x *Wars2*$^{+/V117L}$ matings. The expected ratio of mice per genotype from *Wars2*$^{+/V117L}$ x *Wars2*$^{+/V117L}$ matings is 0.25:0.5:0.25 (*Wars2*$^{+/+}$:*Wars2*$^{+/V117L}$:*Wars2*$^{V117L/V117L}$). The observed ratios of mice per genotype was 0.27:0.49:0.24 respectively and was comparable to the expected ratios (**Figure 3.9B**).

Finally, we investigated whether the *Wars2*$^{V117L/-}$ allele is inherited in according to Mendelian patterns of inheritance. The expected inheritance ratios of mice born from *Wars2*$^{+/V117L}$ x *Wars2*$^{+/-}$ matings is 0.25:0.25:0.25:0.25 (*Wars2*$^{+/+}$:*Wars2*$^{+/V117L}$:*Wars2*$^{+/-}$:*Wars2*$^{V117L/-}$) however the observed ratio was 0.29:0.33:0.27:0.10 respectively. Only 10% of mice born from the *Wars2*$^{+/V117L}$ x *Wars2*$^{+/-}$ matings were *Wars2*$^{V117L/-}$, 15 percentage points lower than expected. Chi-squared analysis calculated a p-value of 0.024 indicating that it is unlikely that this occurred by chance. These data indicate that the inheritance of the *Wars2*$^{V117L/-}$

allele is not Mendelian and that the *Wars2*$^{V117L/-}$ allele causes sub-viability in mice (**Figure 3.9C**).

As shown here, the homozygous *Wars2*-KO null allele causes embryonic lethality. However, compound heterozygous *Wars2*$^{V117L/-}$ mice are sub-viable. These data provide further evidence that the *Wars2*-V117L ENU-induced mutation is a partial loss-of-function, hypomorphic allele and is not a complete loss-of-function allele.

3.2.7 *Wars2*$^{V117L/V117L}$ Additional Phenotyping

Following the confirmation that the *Wars2*-V117L ENU-induced mutation was causal for the phenotypes observed in the original MPC-151 cohort, several cohorts of *Wars2*$^{V117L/V117L}$ mice were generated and phenotyped according to the following pipeline (**Table 3.4**). The aim of this pipeline was fully characterize phenotypes previously identified as well as identify any additional phenotypes previously unidentified in the original HAS. mtRS mutations have been shown to effect several different tissues including brain, heart, the auditory system, skeletal muscle and the kidney. By further phenotyping these mice we aimed to fully phenotypically characterise the *Wars2*-V117L allele and determine the tissue-specific penetrance of this ENU-induced mutation.

Test	Phenotype Area	Age (Months)
EchoMRI	Metabolism	Monthly
Intraperitoneal Glucose Tolerance Test (IPGTT)	Metabolism	3, 6
Complete Lab Animal Monitoring System	Metabolism	
Terminal Fasted Bleed	Metabolism	12
Clinical Chemistry	Metabolism	
Echocardiogram	Cardiac	2, 5
Auditory Brain Response	Hearing	1, 3, 4, 6, 9 ,12

Grip Strength	Musculoskeletal/Neurological	
Histology	All	3, 9
Organ Weights	All	

Table 3.4 – *Wars2*$^{V117L/V117L}$ additional phenotyping pipeline.
Summary of additional phenotyping tests performed on *Wars2*$^{V117L/V117L}$ mice.

3.2.8 Metabolic Phenotyping

As we had previously identified that *Wars2*$^{V117L/V117L}$ mice had reduced adiposity, we planned several additional metabolic phenotyping tests with the aim of determining the cause of the reduced adiposity phenotype. These included: IPGTT, CLAMS and plasma clinical chemistry.

3.2.8.1 IPGTT

Whilst diabetes mellitus is not a common clinical feature of mtRS mutant patients, some other mitochondrial genes have been found to cause diabetes such as the A<3243>G mt-tRNA^{Leu} mutation (Maassen et al., 2004). In order to assess the effect of the *Wars2*-V117L allele on glucose tolerance, intraperitoneal glucose tolerance tests (IPGTT) were performed at 3 and 6 months of age. At 3 months of age there was no difference in *Wars2*$^{V117L/V117L}$ fasted blood glucose concentrations (time point - 0 minutes) compared to *Wars2*$^{+/+}$ littermate controls. However, *Wars2*$^{V117L/V117L}$ mice had significantly lower blood glucose concentrations 60 and 120 minutes after IP glucose injection compared to *Wars2*$^{+/+}$ littermate controls (**Figure 3.10A**). At 6 months of age *Wars2*$^{V117L/V117L}$ mice had significantly reduced blood glucose concentrations at 0, 60 and 120 minutes after IP glucose injection compared to *Wars2*$^{+/+}$ littermates (**Figure 3.10B**). *Wars2*$^{+/V117L}$ mice showed no significant differences in blood glucose concentrations compared to *Wars2*$^{+/+}$ littermate controls at both 3 and 6 months of age. These data show that *Wars2*$^{V117L/V117L}$ mice were more efficient at normalizing their blood glucose concentrations that littermate controls. In fact, at both 3 and 6 months of age, *Wars2*$^{V117L/V117L}$ mice were able to return blood glucose concentrations to fasting levels (time point 0 minutes) within 120 minutes following IP glucose injection.

These data show that the *Wars2*$^{V117L/V117L}$ mice have increased glucose tolerance compared to littermate controls, unlike the patients with the A<3243>G mt-tRNA^{Leu} mutation that develop glucose intolerance.

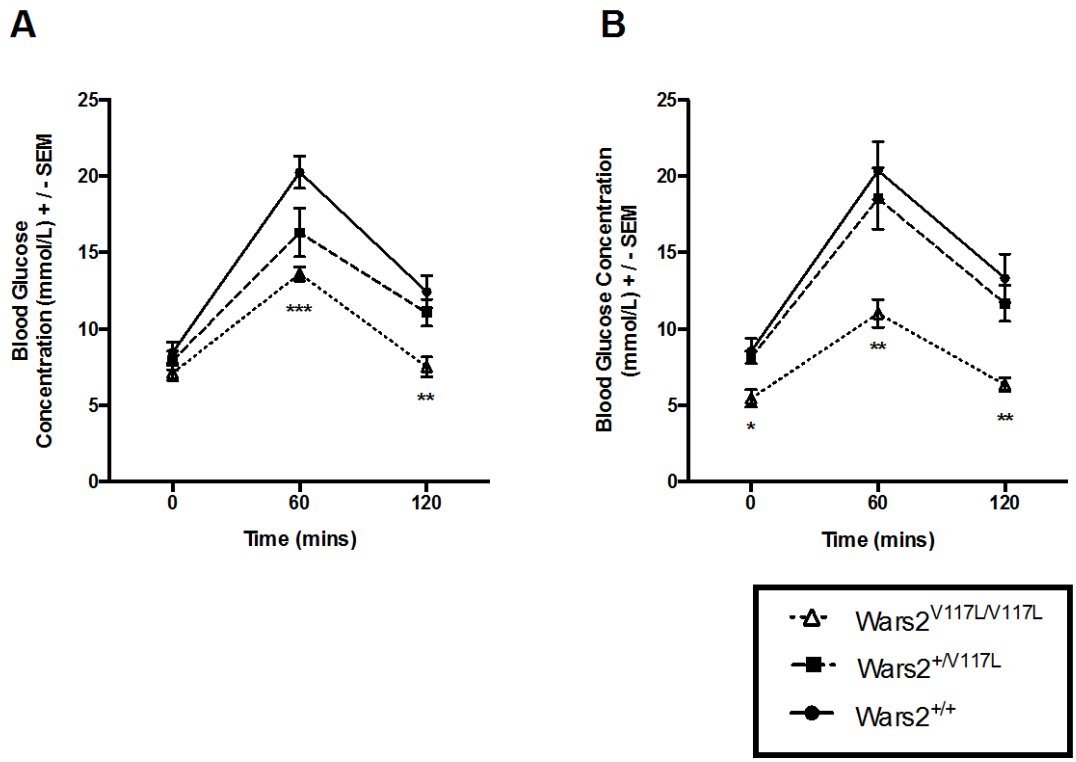

Figure 3.10 – *Wars2*$^{V117L/V117L}$ intraperitoneal glucose tolerance tests.
IPGTT were performed first thing in the morning following over-night fasting at A) 3 months B) 6 months of age. Male; *Wars2*$^{+/+}$ n=9, *Wars2*$^{+/V117L}$ n=12, *Wars2*$^{V117L/V117L}$ n=6 Data shown here is mean blood glucose concentrations ± SEM: 0, 60 and 120 minutes after an intraperitoneal glucose injection. Data analyzed using two-way ANOVA with bonferroni post-hoc test: ***** P<0.05, ****** P<0.01, ******* P<0.001.

3.2.8.2 Clinical Chemistry

In order to determine whether *Wars2*$^{V117L/V117L}$ mice have global changes in metabolism plasma clinical chemistry analysis of circulating metabolites was performed. Terminal blood samples were collected from the retro-orbital sinus at 12 months of age following 4hour fasting. Plasma was isolated from blood samples and key plasma metabolites were measured (**Table 3.5**). There were no significant differences observed in plasma: total cholesterol, HDL, LDL, glycerol or CK in *Wars2*$^{V117L/V117L}$ and *Wars2*$^{+/+}$ mice. *Wars2*$^{V117L/V117L}$ fasted plasma glucose concentrations were significantly lower than *Wars2*$^{+/+}$ littermate controls consistent with IPGTT data previously shown. *Wars2*$^{V117L/V117L}$ mice also had

significantly decreased plasma triglycerides (TAG) and increased free fatty acids (FFA) compared to *Wars2*$^{+/+}$ controls indicative of increased lipolysis. These data are consistent with the reduced adiposity phenotype observed previously and indicates that reduced adiposity may be caused by increased lipid breakdown. Unexpectedly and most significantly, plasma ketone bodies were 3-fold higher in *Wars2*$^{V117L/V117L}$ mice compared to *Wars2*$^{+/+}$ mice.

	***Wars2*$^{+/+}$**	***Wars2*$^{V117L/V117L}$**	**ρ value**
Total Cholesterol (mmol/L)	4.23 ± 0.80	3.91 ± 0.55	0.27
HDL (mmol/L)	3.02 ± 0.65	2.82 ± 0.48	0.41
LDL (mmol/L)	0.96 ± 0.35	0.78 ± 0.20	0.13
Glucose (mmol/L)	13.97 ± 1.59	12.22 ± 2.40 *****	0.04
Triglycerides (mmol/L)	0.92 ± 0.38	0.61 ± 0.29 *****	0.03
Glycerol (µmol/L)	211.69 ± 56.37	190.18 ± 33.32	0.27
Free Fatty Acids (mmol/L)	0.36 ± 0.06	0.42 ± 0.10	0.05
CK (U/L)	117.92 ± 115.4	65.00 ± 23.0	0.15
Ketone Bodies (mmol/L)	0.28 ± 0.13	0.86 ± 0.23 *******	0.0000001

Table 3.5 – *Wars2*$^{V117L/V117L}$ plasma biochemistry parameters.
Mice were fasted for 6-8 hours. Retro-orbital blood samples were collected and plasma was isolated at 12 months of age. Plasma metabolites were measured and are shown here. *Wars2*$^{+/+}$ n=13 and *Wars2*$^{V117L/V117L}$ n=11. Data shown here is mean ± SD. Data analysed using student's t-test: ***** P<0.05, ****** P<0.01, ******* P<0.001.

3.2.8.3 Comprehensive Lab Animal Monitoring System

As previously shown, *Wars2*$^{V117L/V117L}$ mice have reduced adiposity, increased glucose tolerance and altered plasma metabolite concentrations. In order to understand the body weight differences and changes in adipose tissue mass further, we analysed global metabolism *in vivo* using the Comprehensive Lab Animal Monitoring System (CLAMS). We hypothesised that *Wars2*$^{V117L/V117L}$ mice have increased global energy expenditure compared to *Wars2*$^{+/+}$ as this would explain the reduced adiposity phenotype also observed in these mice.

Within the CLAMS system several parameters were measured including: VO_2 consumption, VCO_2 production, food & water intake and activity. Mice were placed in the CLAMS for 72 hours. Data shown here was taken between 24 and 48 hours after mice were placed in the CLAMS system to allow the mice to familiarize themselves with their new surroundings prior to experimental data collection. Data was collected throughout this 24 hour period and was analysed as two distinct 12 hour periods 'dark' (7:00PM-7:00AM) and 'light' (7:00AM-7:00PM). Mice are nocturnal animals and therefore are more active, have increased respiration and feed more during the 'dark' period.

CLAMS analysis was performed using two different cage temperatures: 28°C (~thermoneutrality) and 22°C (home-cage temperatures). At MRC Harwell, mice are housed at 22°C under normal conditions and are therefore exposed to mild cold stress 24hours a day. Mice must therefore thermoregulate in order to maintain core body temperatures. By performing CLAMS analysis at 22°C and thermoneutrality (~28°C) we asked an additional question: does environmental temperature influence global metabolism in *Wars2*$^{V117L/V117L}$ mice?

At 28°C *Wars2*$^{V117L/V117L}$ mice had significantly increased VO_2 consumption (**Figure 3.11A**) and VCO_2 production (**Figure 3.11B**) during the dark period compared with *Wars2*$^{+/+}$ littermate controls; no significant differences in VO_2 consumption or VCO_2 production were observed in *Wars2*$^{V117L/V117L}$ and *Wars2*$^{+/+}$ mice during the light period. Similarly, *Wars2*$^{V117L/V117L}$ Respiratory Exchange Ratio (RER) was significantly increased during the dark period at 28°C compared to *Wars2*$^{+/+}$ controls but were comparable to controls during to the light period at the same temperature (**Figure 3.11D**). Equally no significant differences in RER were observed in *Wars2*$^{V117L/V117L}$ and *Wars2*$^{+/+}$ mice during either period at 22°C.

No significant difference in Energy Expenditure (EE) was observed in *Wars2*$^{V117L/V117L}$ and *Wars2*$^{+/+}$ mice during the light or dark period at 28°C. However, at 22°C, *Wars2*$^{V117L/V117L}$ mice had significantly reduced EE compared to *Wars2*$^{+/+}$ littermates in both dark and light periods (**Figure 3.11C**). This data shows that *Wars2*$^{+/+}$ mice at 22°C increase their total energy expenditure, relative to that at 28°C, to compensate for the lower temperature. However, when *Wars2*$^{V117L/V117L}$ mice are placed at 22°C, total EE is does not increase to the same extent as *Wars2*$^{+/+}$ mice suggesting that *Wars2*$^{V117L/V117L}$ mice cannot compensate for the 'mild' cold stress that they are constantly exposed to in their home cages. This data show that *Wars2*$^{V117L/V117L}$ have reduced thermogenic capacity compared to *Wars2*$^{+/+}$ littermate controls.

No significant differences in food intake were observed in *Wars2*$^{V117L/V117L}$ and *Wars2*$^{+/+}$ mice at 28°C. At 22°C, food intake was non-significantly different between *Wars2*$^{V117L/V117L}$ and *Wars2*$^{+/+}$ mice during the dark period but was significantly reduced in *Wars2*$^{V117L/V117L}$ mice during the light period at 22°C. Interestingly, at 28°C, average food intake during light and dark periods were comparable. However, at 22°C, both *Wars2*$^{+/+}$ and *Wars2*$^{V117L/V117L}$ average food intake is much greater during the dark period (**Figure 3.11E**).

Mice were weighed before and after being placed in the CLAMS. Interestingly *Wars2*$^{V117L/V117L}$ mice total body mass increased approximately 5% over the 72 hour period that they were housed at 28°C. *Wars2*$^{+/+}$ total body mass did not change during the same period. At 22°C both *Wars2*$^{V117L/V117L}$ and *Wars2*$^{+/+}$ body mass decreased but there was no significant difference between genotypes (**Figure 3.11F**). These data suggest that environmental temperature may influence *Wars2*$^{V117L/V117L}$ adiposity.

In summary, *Wars2*$^{V117L/V117L}$ mice housed at 22°C had reduced EE compared to *Wars2*$^{+/+}$ indicating that the reduced adiposity phenotype observed in these mice is independent of EE and via an alternate mechanism, contrary to our hypothesis. Under the same conditions

no difference in RER or substantial differences in food intake were observed suggesting that the reduced adiposity phenotype is also independent of substrate utilisation or calorific intake. Perhaps the most telling result was observed at thermoneutrality (28°C) as *Wars2*$^{V117L/V117L}$ total body mass dramatically increased over a period of 72 hours. This observation suggests that the reduced adiposity phenotype observed in the *Wars2*$^{V117L/V117L}$ mice is dependent upon them being housed at 22°C.

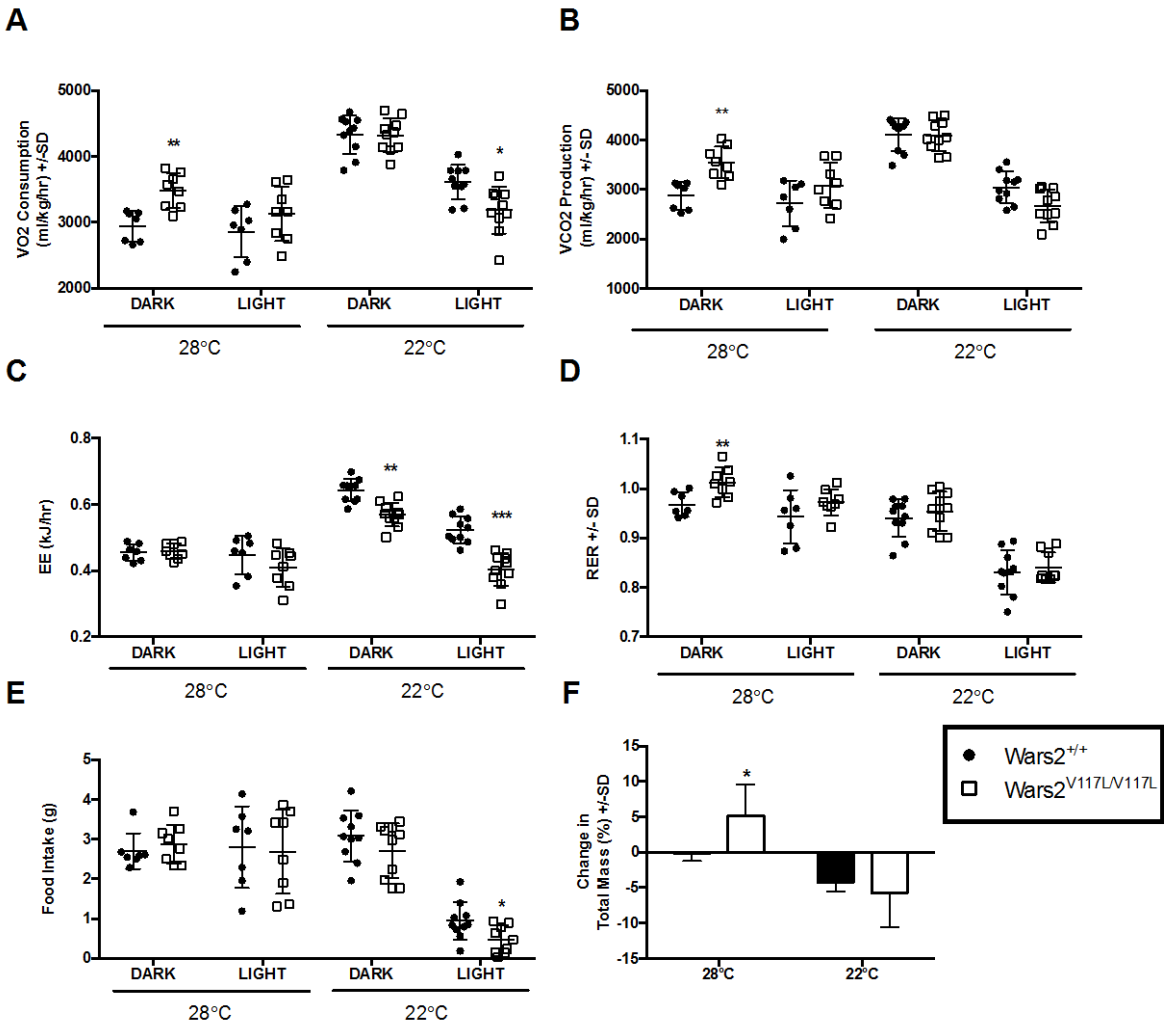

Figure 3.11 – *Wars2*$^{V117L/V117L}$ Comprehensive laboratory monitoring system data. Mice were housed individually in the CLAMS for a total of 72 hours at two temperatures: 22 and 28°C. Several parameters were measured including: A) VO_2 consumption, B) VCO_2 production, and E) food intake. C) Energy expenditure (EE) and D) respiratory exchange ratios (RER) were calculated from VO_2 and VCO_2 measurements. VO_2, VCO_2 and EE data have normalized to lean mass by multiple linear regression (ANCOVA). Data in A-E shown as mean ± SD with individual data points. Mice were weighed before and after entering CLAMS, F) shows mean change in total mass after being housed in CLAMS for 72 hours at 28 and 22°C ± SD. 28°C; *Wars2*$^{+/+}$ n=7 and *Wars2*$^{V117L/V117L}$ n=8. 22°C; *Wars2*$^{+/+}$ n=10 and *Wars2*$^{V117L/V117L}$ n=10. The p-values in A – E were calculated using a Welch *t*-test of the null hypothesis. The p-value in F were generated using a student t-test. In A-F ***** p<0.05, ****** p<0.01, ******* p<0.001.

3.2.9 Histology

3.2.9.1 White Adipose Tissue

Having shown that the *Wars2*-V117L ENU-induced mutation causes changes in global adiposity in *Wars2*$^{V117L/V117L}$ mice we performed histological analysis of adipose depots in order to identify abnormal pathology. In order to analyse adipose tissue morphology visceral (gWAT) and subcutaneous (iWAT) white adipose tissue depots were taken at 3 months of age, were fixed and stained with H&E. *Wars2*$^{V117L/V117L}$ gWAT and iWAT H&E sections showed reduced adipocyte size compared to *Wars2*$^{+/+}$ mice at both 3 months of age consistent with reduced adiposity (**Figure 3.12A + B**). Interestingly, not only were *Wars2*$^{V117L/V117L}$ adipocytes smaller size but there are also differences in the adipocyte morphology. *Wars2*$^{+/+}$ WAT adipocytes are large, containing a single, large lipid droplet as is typical of mature white adipocytes. However, in both gWAT and iWAT *Wars2*$^{V117L/V117L}$ sections a substantial proportion of adipocytes contained multi-locular lipid droplets at 3 months of age. Multi-locular lipid droplet formation is indicative of white adipocyte 'browning'. Adipocyte 'browning' occurs when there is up-regulation of mitochondrial genes including the mitochondrial uncoupler UCP1 as well as genes involved in lipolysis. The up-regulation of lipolysis genes causes breakdown of adipocyte lipid stores leading to the presence of multi-locular lipid droplets. This evidence suggests that WAT browning may contribute to reduced adiposity in *Wars2*$^{V117L/V117L}$ mice.

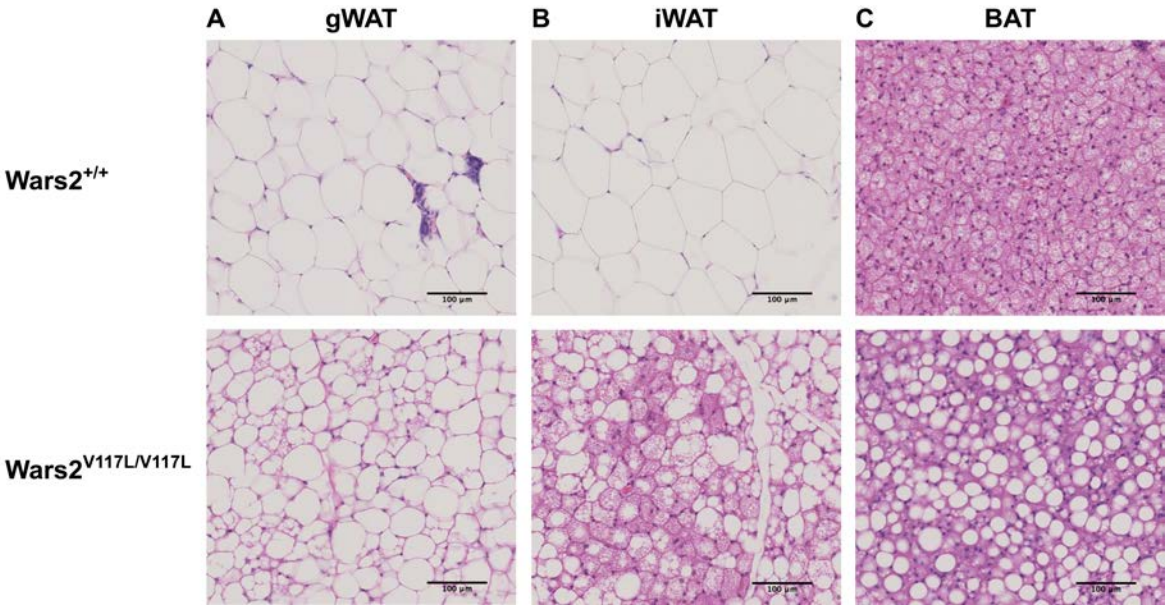

Figure 3.12 – *Wars2*$^{V117L/V117L}$ adipose tissue histology.
Adipose tissues depots were dissected at 3 months of age from female mice. H&E stained sections of A) gonadal white adipose tissue (gWAT), B) inguinal white adipose tissue (iWAT) and C) brown adipose tissue (BAT) of a representative Wars2$^{+/+}$ (n=3) and *Wars2*$^{V117L/V117L}$ (n=3) using x 10 objective. Scale bar = 100µm for each image.

3.2.9.2 Brown Adipose Tissue

Unlike WAT, brown adipose tissue (BAT) primary function is thermoregulation. Brown adipocytes contain large numbers of mitochondria, express the mitochondrial uncoupler UCP1 and have high rates of lipolysis. Previous CLAMS data suggested that *Wars2*$^{V117L/V117L}$ mice have reduced thermogenic ability as they had reduced EE at 22°C. Histological analysis of BAT was performed in order to determine whether dysfunctional BAT causes reduced thermogenic ability in *Wars2*$^{V117L/V117L}$ mice.

In stark contrast with the 'browning' observed in *Wars2*$^{V117L/V117L}$ WAT depots, *Wars2*$^{V117L/V117L}$ BAT showed evidence of 'whitening'. As seen in *Wars2*$^{+/+}$ BAT sections, normal brown adipocytes are smaller than white adipocytes and contain small, multi-locular lipid droplets. However, in *Wars2*$^{V117L/V117L}$ BAT, large unilocular lipid droplets were observed consistent with those typically seen in white adipocytes (**Figure 3.12C**).

BAT is required for rodent thermoregulation where fat is metabolized by uncoupled mitochondria to generate energy in the form heat rather than ATP. The presence of uni-locular lipid droplets in *Wars2*$^{V117L/V117L}$ BAT suggests that lipolysis is inhibited in brown adipocytes leading lipid accumulation. This is consistent with previous data showing that *Wars2*$^{V117L/V117L}$ mice have reduced total EE at 22°C and may suggest that BAT dysfunction is the reason why *Wars2*$^{V117L/V117L}$ mice do not increase their total EE at lower temperatures.

3.2.9.3 Additional Tissues

Given that abnormal pathology has been observed in multiple different tissues in mtRS patients, we performed histological analysis was performed using multiple tissues from *Wars2*$^{V117L/V117L}$ mice in order to identify abnormal pathology. Liver, kidney and skeletal muscle samples were fixed and stained with H&E before being analysed by Professor Cheryl Scudamore, MRC Harwell resident veterinary pathologist. Representative images of *Wars2*$^{V117L/V117L}$, *Wars2*$^{+/V117L}$ or *Wars2*$^{+/+}$ liver **(Figure 3.13A)**, kidney **(Figure 3.13B)** or skeletal muscle **(Figure 3.13D)** sections harvested at 9 months of age. Liver and kidney sections were also scored from 0 – 5 using a non-linear semi-quantitative grading system for the presence of abnormal pathologies, where 0 means no finding in tissue and 5 meaning that the whole tissue was affected (**Table 7.1**, see appendix). Scoring was performed blinded by genotype. For example, the presence of inflammatory cell foci and single cell necrosis in liver samples were scored. Inflammatory cell foci were scored as 1 in all *Wars2*$^{+/+}$, *Wars2*$^{+/V117L}$ and *Wars2*$^{V117L/V117L}$ liver sections (**Table 7.1**, see appendix). A score of 1 meaning that the presence of cell foci was minimal, 'the least change that is visible on a light microscopy at 20x, small, focal or affect <10% of tissue'. Overall, no differences in the histopathology of liver, kidney or skeletal muscle were observed between genotypes. Some abnormal pathology was observed in these tissues such as hepatocellular adenoma however these pathologies were deemed to be consistent with the age and genetic background.

Whole brains were dissected at the same time point and sections were stained with Luxol Fast Blue and Cresyl Violet and were again assessed by Professor Cheryl Scudamore. No abnormal brain pathology was observed in *Wars2*$^{V117L/V117L}$, *Wars2*$^{+/V117L}$ or *Wars2*$^{+/+}$ brains at 9 months of age (data not shown).

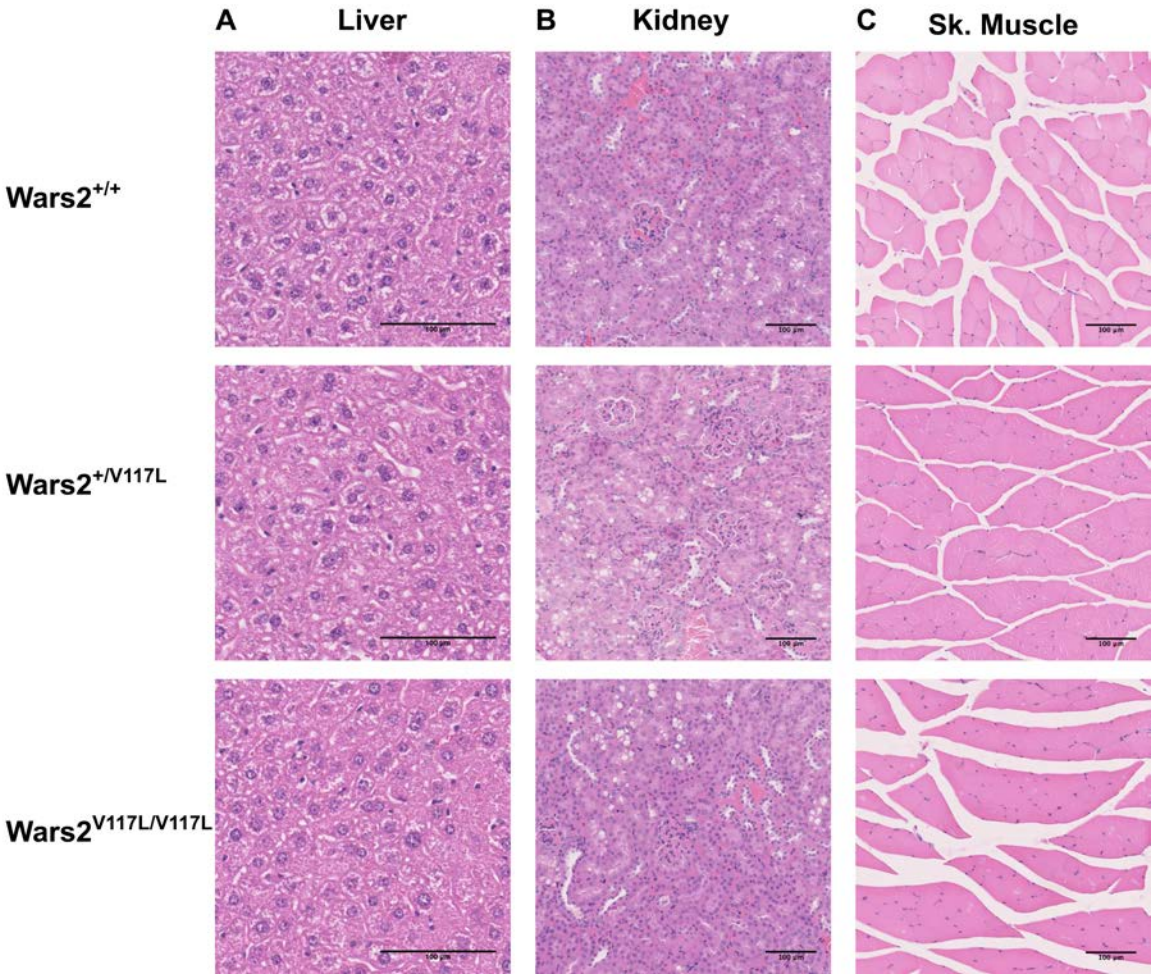

Figure 3.13 – *Wars2*$^{V117L/V117L}$ liver, kidney and skeletal muscle histology.
Liver, kidney and skeletal muscle were dissected at 9 months of age from female mice. Representative images of H&E stained sections of A) liver, B) kidney and C) skeletal muscle from *Wars2*$^{+/+}$ (n=3), *Wars2*$^{+/V117L}$ (n=3) and *Wars2*$^{V117L/V117L}$ (n=3) mice using a 20x objective for liver and a 10 x objective for kidney and skeletal muscle. Scale bar = 100 µm for each image.

3.2.10 Cardiac Phenotyping

In the previous chapter I showed you that several mutations in several mtRS genes are associated with hypertrophic cardiomyopathy in humans including: *AARS2*, *PARS2*, *SARS2* and *YARS2*. In order to assess whether the *Wars2*-V117L ENU-induced mutation influences cardiac function and morphology, Echocardiogram analysis was performed at 5

months of age. Echocardiogram images were taken in by Heather Cater who was blinded to the genotype of the mice throughout the procedure. Echocardiographic images were taken through the left ventricle in motion mode (M-mode) which generates a composite image of the left-ventricle (y-axis) over time (x-axis) (**Figure 3.14 A & B)**. M-mode images were analysed using Visual Sonics Vevo 2100 software which identifies and defines the structural components of the left ventricle such as the walls of the anterior and posterior left ventricular walls and the left ventricle chamber (**Figure 3.14 A & B – highlighted in blue)** allowing measurements of these structures to be taken. From these measurements it is possible to quantitatively analyse several parameters such as Left Ventricle Interior Diameter (LVID), Left Ventricle Anterior Wall diameter (LVAW), Left Ventricle (LV) volume, LV mass, Stroke Volume (SV), Ejection Fraction (EF), Fractional Shortening (FS), Cardiac Output (CO) and Heart Rate (HR) (**Table 3.6**). From the representative M-mode images shown in **Figure 3.14** it is possible to see reduced contractile function of *Wars2*$^{V117L/V117L}$ left ventricle is reduced compared to *Wars2*$^{+/+}$ controls. Furthermore, quantitative analysis showed LVAW diameter and LV Mass were significantly increased in *Wars2*$^{V117L/V117L}$ mice compared to *Wars2*$^{+/+}$ in both diastolic and systolic states indicative of hypertrophic cardiomyopathy. LVID, LV Volume, SV, CO and HR were significantly reduced in *Wars2*$^{V117L/V117L}$ mice compared to *Wars2*$^{+/+}$ littermate controls. Ventricular stiffness is a common secondary effect of cardiac hypertrophy due impaired ventricular relaxation. The reduced LVID, LV Volume, SV and CO observed in *Wars2*$^{V117L/V117L}$ mice are consistent with ventricular stiffness and hypertrophic cardiomyopathy. No significant differences in EF and FS were observed between genotypes. EF and FS are typically preserved in patients with hypertrophic cardiomyopathy. In summary these data show that the *Wars2*-V117L allele causes hypertrophic cardiomyopathy in mice expanding the list phenotypes associated with this ENU-induced *Wars2* mutation (**Table 3.6**).

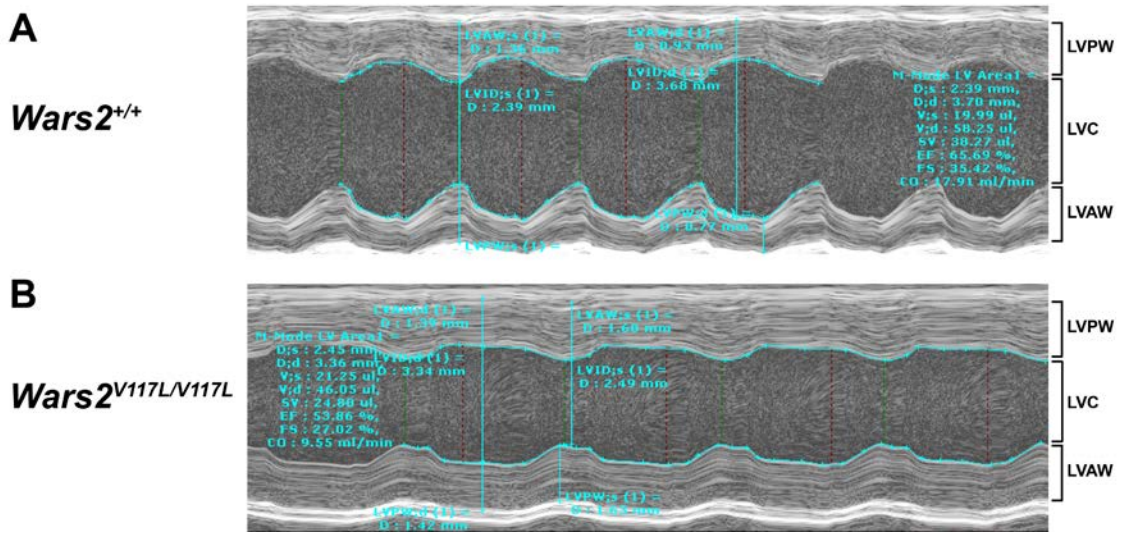

Figure 3.14 – Representative analysis of *Wars2*$^{V117L/V117L}$ Echocardiogram images in M-mode.
Representative echocardiogram images of the left ventricle from A) *Wars2*$^{+/+}$ and B) *Wars2*$^{V117L/V117L}$ mice in M-mode. M-mode imaging generates a composite image of the left ventricle (x-axis) over time (y-axis) allowing diastolic and systolic function to be visualized. Visual Sonics Vevo 2100 software was then used to define structural components of the left ventricle, such as the left ventricular anterior wall, (LVAW), left ventricle posterior wall (LVPW) and left ventricle chamber (LVC) (highlighted in blue), which were used for follow-up analysis.

	Wars2$^{+/+}$	*Wars2*$^{V117L/V117L}$	ρ value
LVID-d (mm)	3.93 ± 0.31	3.53 ± 0.26 *	0.04
LVID-s (mm)	2.72 ± 0.44	2.49 ± 0.53	0.45
LVAW-d (mm)	1.01 ± 0.10	1.34 ± 0.14 **	0.002
LVAW-s (mm)	1.44 ± 0.19	1.76 ± 0.25 *	0.04
LV Vol-d (µL)	67.61 ± 12.26	52.23 ± 8.98 *	0.03
LV Mass (mg)	178.97 ± 23.51	211.84 ± 15.99 *	0.02
Stroke Volume (µL)	39.73 ± 4.90	27.26 ± 2.87 ***	0.0005
Ejection Fraction (%)	58.81 ± 7.54	53.97 ± 13.87	0.50
Fractional Shortening (%)	30.86 ± 5.09	28.07 ± 10.27	0.59
Cardiac Output (ml/min)	17.07 ± 2.85	9.91 ± 1.77 ***	0.0006
Heart Rate (BPM)	429.20 ± 39.21	362.50 ± 43.04 *	0.02

Table 3.6 – *Wars2*$^{V117L/V117L}$ Echo-Cardiogram Analysis.
Echo-Cardiogram images of the left ventricle were captured in *Wars2*$^{V117L/V117L}$ mice at 6 months of age. Functional analysis of Echo-Cardiogram images allowed us to measure several parameters including: Left Ventricle Interior Diameter (LVID), Left Ventricle Anterior Wall diameter (LVAW), Left Ventricle (LV) volume, LV mass, Stroke Volume (SV), Ejection Fraction (EF), Fractional Shortening (FS), Cardiac Output CO and Heart Rate (HR). LVID, LVAW and LV measurements were obtained at both diastolic (-d) and systolic (-s) dimensions. Data shown is mean ± SD from male mice. *Wars2*$^{+/+}$ n=5 and *Wars2*$^{V117L/V117L}$ n=6. Data analysed using student's t-test: * P<0.05, ** P<0.01, *** P<0.001.

3.2.11 Organ Weights

Previously I showed you echocardiographic evidence that the *Wars2*$^{V117L/V117L}$ mice have hypertrophic cardiomyopathy. In order to provide further evidence of a cardiac phenotype mouse tissues were dissected and weighed. Tissue weights have been normalized to total body weight. *Wars2*$^{V117L/V117L}$ mice have significantly increased heart weight at 6 months of age compared to *Wars2*$^{+/+}$ littermate controls (**Figure 3.15A**). This is consistent with echocardiographic evidence of hypertrophic cardiomyopathy in *Wars2*$^{V117L/V117L}$ mice shown previously. In order to determine whether hypertrophy was specific to the heart, liver and kidney weights were also taken. No significant differences in liver or kidney weights were observed in *Wars2*$^{V117L/V117L}$ mice at 6 months of age (**Figure 3.15A**). In order to determine whether the hypertrophic cardiomyopathy phenotype was progressive with age, heart weights were also measured at 12 months of age (**Figure 3.15B**). There was no increased in *Wars2*$^{V117L/V117L}$ heart weight between 6 and 12 months of age indicating that the hypertrophic cardiomyopathy was not progressive with age in *Wars2*$^{V117L/V117L}$ mice.

Previously I showed you that *Wars2*$^{V117L/V117L}$ mice have reduced adiposity and reduced white adipocyte size. In order to further validation of these results, adipose tissue depots were dissected and weighed at 6 months of age. gWAT, iWAT and BAT weights were all significantly reduced in *Wars2*$^{V117L/V117L}$ mice compared to *Wars2*$^{+/+}$ controls at 6 months of age consistent with reduced adiposity as shown previously (**Figure 3.15A**).

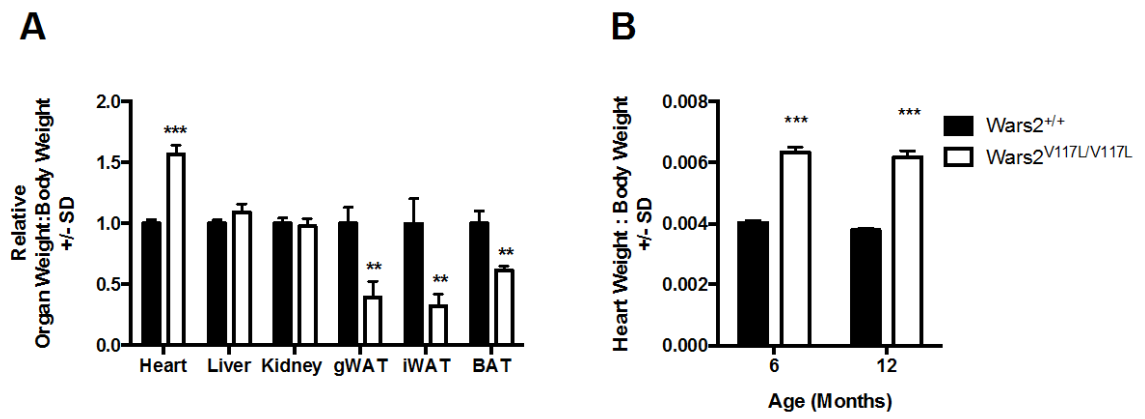

Figure 3.15 – *Wars2*$^{V117L/V117L}$ organ weights.
At 6 months of age *Wars2*$^{V117L/V117L}$ mice were culled, organs were dissected and weighed. A) Relative organ weights normalized to total body mass. B) Heart weights normalized to total body weights at 6 and 12 months of age. *Wars2*$^{+/+}$ n=5 and *Wars2*$^{V117L/V117L}$ n=6. Data shown as mean ± SD. Data analyzed using student's t-test: ***** P<0.05, ****** P<0.01, ******* P<0.001.

3.2.12 Grip Strength

In order to test neuro-muscular function in *Wars2*$^{V117L/V117L}$ mice, grip strength analysis was performed at 5 months of age (**Figure 3.16**). Data was normalized to body weight in accordance with standard practices. Grip strength analysis showed no differences in *Wars2*$^{V117L/V117L}$ *Wars2*$^{+/V117L}$ and *Wars2*$^{+/+}$ combined forelimb and hindlimb grip strength.

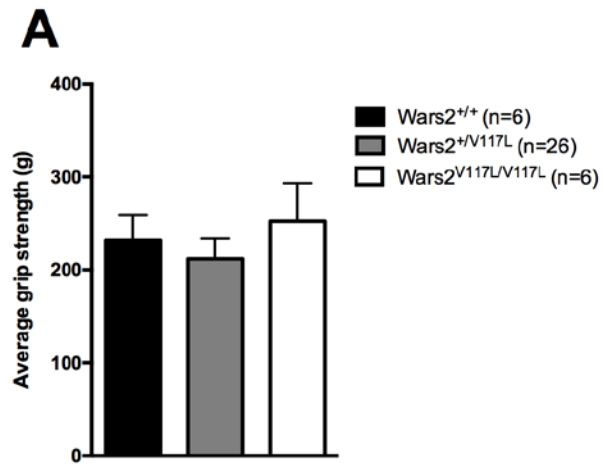

Figure 3.16 - Grip strength analysis.
Grip strength analysis was performed in *Wars2*$^{V117L/V117L}$, *Wars2*$^{+/V117L}$ and *Wars2*$^{+/+}$ mice at 5 months of age. Raw data was normalised to total body weight. Date shown as average ± SD. Data was analyzed using one-way ANOVA with Bonferroni post-host test.

3.3 Discussion

3.3.1 Summary

These data showed that the *Wars2*-V117L allele was the causal mutation for sensorineural hearing loss and reduced adiposity phenotypes identified in the original MPC-151 cohort phenotyped in the HAS. These data also showed that *Wars2*-V117L ENU-induced allele is associated with additional phenotypes in *Wars2*$^{V117L/V117L}$ mice including: global changes in metabolism, increased glucose tolerance, WAT 'browning', BAT dysfunction, ketogenesis and hypertrophic cardiomyopathy. These data showed that loss-of-function alleles in *Wars2* are recessive, as phenotypes were not observed in *Wars2*$^{+/V117L}$ or *Wars2*$^{+/-}$ littermate controls. Finally, these data showed that the *Wars2*-V117L is likely a hypomorphic, partial loss-of-function allele as the homozygous *Wars2*-KO null allele causes embryonic lethality whereas compound heterozygous *Wars2*$^{V117L/-}$ mice are sub-viable.

To date no human patients with *WARS2* mutations have been identified. Based upon the distinct tissue specific pathologies observed in the *Wars2*-V117L mouse model namely: sensorineural hearing loss, reduced adiposity and hypertrophic cardiomyopathy, it may be possible to complete the list of clinical pathologies associated with mutations in mtRS genes in humans.

3.3.2 The *Wars2*-V117L ENU-induced mutation is the causal mutation for the phenotypes identified in MPC-151 mice

MPC-151 was generated as part of the HAS. From a total of 52 mice within the cohort 6 phenodeviants were identified with hearing loss, as shown by absent CB responses and increased ABR thresholds, and reduced adiposity, as shown by EchoMRI body composition analysis. Given that only 6 mice from the cohort were identified with these phenotypes it was likely that the causative allele was recessively inherited based on Mendelian patterns of genetic inheritance. SNP mapping identified a 31-73 Mb region on chromosome 3 where

all ‘affected’ MPC-151 mice were homozygous C57BL/6J and ‘non-affected’ control were heterozygous C3H/C3PDE. This was the only region where all affected mice were homozygous C57BL/6J allowing us to be confident that this was critical region containing the causal ENU-induced mutation because the founder G1 male that was treated with ENU was C57BL/6J. Whole genome sequencing of an affected G3 mouse identified three missense mutations within this causal region: *Ppa2*-Y123F, *Tchh*-D1105V and *Wars2*-V117L. All three mutations were validated by Sanger sequencing and were present in both the G1 founder male (heterozygous) and an affected MPC-151 mouse (homozygous) and were absent in an unaffected MPC-151 mouse. This showed that the mutations were likely ENU-induced and not spontaneous mutations. Based on these findings we went on to determine which of these three ENU-induced mutations were causal for the MPC-151 phenotypes.

In order to test whether the *Ppa2*-Y123F was the causal mutation, we segregated the *Ppa2*-Y123F from the other two candidate ENU-induced mutations and generated $Ppa2^{Y123F/Y123F}$ mice for phenotyping. Neither hearing loss nor reduced adiposity were observed in $Ppa2^{Y123F/Y123F}$ or $Ppa2^{+/Y123F}$ mice. Based on this we were able to rule out the *Ppa2*-Y123F ENU-induced mutation as causal.

In order to determine whether the *Wars2*-V117L ENU-induced mutation was causal $Wars2^{V117L/V117L}$ mice were bred $Wars2^{+/V117L}$ x $Wars2^{+/V117L}$ matings. Both hearing loss and reduced adiposity phenotypes were recapitulated in re-derived cohorts of $Wars2^{V117L/V117L}$ mice consistent with the hypothesis that the *Wars2*-V117L ENU-induced was causal. All $Wars2^{V117L/V117L}$ mice had both hearing loss and reduced adiposity suggesting that a single allele was causal for both phenotypes observed. Hearing loss and reduced adiposity were observed in both male and female $Wars2^{V117L/V117L}$ mice indicating that these phenotypes are independent of sex. $Wars2^{+/V117L}$ mice had non-significantly different ABR thresholds,

total body mass or percentage fat mass compared with *Wars2*$^{+/+}$ controls indicating that the *Wars2*-V117L ENU-induced mutation was a recessive allele.

Whilst this data strongly suggested that the *Wars2*-V117L allele was causal for the phenotypes observed we could not rule out the possibility that the *Tchh*-D1105V ENU-induced mutation or another non-coding ENU-induced mutation proximal to *Wars2* may be causal as they may be co-inherited along with the *Wars2*-V117L allele. To confirm that the *Wars2*-V117L ENU-induced mutation was causal, and to rule out the *Tchh*-D1105V and any other mutations, we performed a complementation test by crossing *Wars2*$^{+/V117L}$ mice with *Wars2*$^{+/-}$ mice generating compound heterozygous *Wars2*$^{V117L/-}$ mice for phenotypic analysis. *Wars2*$^{V117L/-}$ mice had elevated ABR thresholds compared to *Wars2*$^{+/+}$ littermate controls at 4 months of age. *Wars2*$^{V117L/-}$ ABR thresholds were higher than those observed in *Wars2*$^{V117L/V117L}$ mice at the same time point, 4 months of age. Similarly, *Wars2*$^{V117L/-}$ mice had significantly reduced total body mass and reduced adiposity at earlier time-points that were observed in *Wars2*$^{V117L/V117L}$ mice. These data show that the *Wars2*-V117L allele was not complimented by the *Wars2*-KO allele confirming that the *Wars2*-V117L ENU-induced mutation is causal for the observed phenotypes in *Wars2*$^{V117L/V117L}$ mice. The fact that the *Wars2*-V117L allele did not compliment with the *Wars2*-KO null allele shows that the *Wars2*-V117L allele is also a loss-of-function allele. However, the phenotypes observed in *Wars2*$^{V117L/-}$ mice were observed at earlier time points and were more severe than in *Wars2*$^{V117L/V117L}$ mice indicating that the *Wars2*-V117L allele was likely a partial-loss-of function, hypomorphic allele compared with the complete loss-of-function *Wars2*-KO allele.

Mice homozygous for the *Wars2*-KO, null-allele are not viable. Therefore, some degree of *Wars2* (or mt-TrpRS) function is required to sustain life. We showed that the *Wars2*$^{V117L/V117L}$ allele is inherited according to Mendelian ratios. However, only 10% or mice generated from *Wars2*$^{+/V117L}$ x *Wars2*$^{+/-}$ matings were *Wars2*$^{V117L/-}$ indicating that the *Wars2*$^{V117L/-}$ allele is sub-viable. These data suggest that there is a minimum threshold of *Wars2* / mt-TrpRS

activity required for mice to be born and that this threshold activity is likely comparable to that in *Wars2*$^{V117L/-}$ mice. That being said, neither hearing loss or reduced adiposity were observed in *Wars2*$^{+/-}$ and *Wars2*$^{V117L/-}$ mice indicating that loss-of-function *Wars2* mutations are haplosufficient. Given that both *Wars2*$^{V117L/V117L}$ and *Wars2*$^{V117/-}$ mice both develop sensorineural hearing loss and reduced adiposity suggests that *Wars2* loss-of-function alleles cause tissue-specific pathology in mice independent of genotype.

Taken together these data showed that the *Wars2*-V117L ENU-induced mutation was causal for sensorineural hearing loss and reduced adiposity as previously observed in the MPC-151 cohort. This led us to ask the questions: Does the *Wars2*-V117L cause any additional phenotypes in mice? Why are *Wars2*$^{V117L/V117L}$ mice lean? What determines the tissue specific penetrance of the *Wars2*-V117L hypomorphic allele? The first two questions were addressed by performing additional phenotyping tests on the re-derived cohorts of *Wars2*$^{V117L/V117L}$ mice and are discussed below. The final question will be addressed in the next two results chapters.

3.3.3 Does the *Wars2*-V117L cause any additional phenotypes in mice?

In the original HAS, phenodeviants within the MPC-151 cohort were identified as having reduced adiposity and sensorineural hearing loss. We went on to show that these phenotypes were caused by the *Wars2*-V117L ENU-induced allele. *Wars2* is expressed in all cell-types except in erythrocytes that do not contain mitochondria. *Wars2* encodes mt-TrpRS, a protein vital for mitochondrial translation. Following the confirmation that the *Wars2*-V117L allele was causal for the aforementioned phenotypes we hypothesised that other tissues with high mitochondrial content, such as the heart, liver, kidney or skeletal muscle may also be affected by the *Wars2*-V117L allele. Therefore, additional *Wars2*$^{V117L/V117L}$ mice were generated and phenotyped with the aim of determining whether additional phenotypes or pathology were associated with the *Wars2*-V117L allele.

In humans, several gene mutants have been identified that cause 'monogenic' forms of diabetes. Of particular interest and relevance to this project are mutations in mtDNA that cause mitochondrial diabetes also known as 'maternally inherited diabetes and deafness' (MIDD) (van den Ouweland et al., 1992).The most common mutation associated with MIDD is the A<3243>G mutation in the mtDNA gene *MT-TL1* that encoded mt-tRNA^{Leu}. The association between mtDNA mutations and type-1 diabetes mellitus is to some extent unsurprising. Mitochondrial ATP production is a key step in glucose stimulated insulin secretory pathway that occurs in β-cells of pancreatic islets. To assess whether the *Wars2*-V117L mutation influences glucose homeostasis, IPGTT were performed at 3 and 6 months of age. We showed that *Wars2*$^{V117L/V117L}$ mice have increased glucose tolerance illustrated by their ability to normalize their blood glucose concentrations at a higher rate than *Wars2*$^{+/+}$ littermate controls. Increased glucose tolerance is indicative of increased insulin sensitivity suggesting the glucose stimulated insulin secretory pathway is functionally active in *Wars2*$^{V117L/V117L}$ mice. *Wars2*$^{V117L/V117L}$ mice also had significantly lower fasted blood glucose levels compared to *Wars2*$^{+/+}$ littermate controls and in contrast to human MIDD patients that usually have elevated fasting glucose concentrations. Unlike the monogenic mtDNA mutations that cause mitochondrial diabetes, the *Wars2*-V117L ENU-induced mutation appears to have no negative effect on glucose homeostasis. However, whilst it is possible to say that *Wars2*$^{V117L/V117L}$ mice do not have hyperglycemia, it is not possible to say for sure that the mice do not harbour diabetic traits such as insulin resistance or hyper/hypoinsulinemia. In the future, plasma insulin ELISA's could be performed to determine whether mice have hyper/hypoinsulinemia. Furthermore, intraperitoneal insulin tolerance tests could be performed to determine whether *Wars2*$^{V117L/V117L}$ have insulin resistance.

As well as the previously mentioned mutations in mtRS genes, several mutations in other genes required for mitochondrial protein translation have been associated with hypertrophic cardiomyopathy in humans including: *MTO1*, *MRPL3* and *MRPS22* ((Baruffini et al., 2013;

Galmiche et al., 2011; Smits et al., 2011)). In order to investigate whether the *Wars2*-V117L allele influences cardiac function and pathology, Echocardiograms were performed at 5 months of age. *Wars2*$^{V117L/V117L}$ mice had significantly increased LVAW diameter and LV mass compared to *Wars2*$^{+/+}$ mice indicating hypertrophic cardiomyopathy. *Wars2*$^{V117L/V117L}$ cardiac function was impaired as shown by significantly reduced: LVID, stroke volume and cardiac output compared to *Wars2*$^{+/+}$ littermate controls indicative of cardiac stiffness and consistent with hypertrophic cardiomyopathy. Furthermore, total heart weight was approximately 50% increased in *Wars2*$^{V117L/V117L}$ mice compared with *Wars2*$^{+/+}$ littermate controls, again indicating cardiac hypertrophy. Taken together, these data showed that the *Wars2*-V117L ENU-induced mutation is associated with hypertrophic cardiomyopathy in mice.

In order to investigate whether other tissues with high mtDNA copy number were affected by the *Wars2*-V117L allele, organ weight analysis and histological analysis were performed using additional tissues. No significant differences in kidney or liver weights were observed in *Wars2*$^{V117L/V117L}$ and *Wars2*$^{+/+}$ mice indicating that increased organ weight was specific to cardiac tissue in *Wars2*$^{V117L/V117L}$ mice. Furthermore, histological analysis provided no evidence of abnormal pathology in *Wars2*$^{V117L/V117L}$ liver, kidney, skeletal muscle and brain. Finally, forelimb and hindlimb grip-strength analysis was performed to test *Wars2*$^{V117L/V117L}$ neuromuscular function and showed no significant difference between genotypes. Taken together these data show that the *Wars2*-V117L allele does no cause abnormal pathology in several tissues with high mitochondrial content / function in *Wars2*$^{V117L/V117L}$ mice.

Additional phenotyping tests performed on *Wars2*$^{V117L/V117L}$ mice showed that the *Wars2*-V117L ENU-induced mutation is associated with not only sensorineural hearing loss and reduced adiposity but also hypertrophic cardiomyopathy. Equally these data showed that the *Wars2*-V117L allele is not associated with abnormal pathology or function in several other tissues. Again this left us with the question: what determines the tissue specific

penetrance of the *Wars2*-V117L hypomorphic allele? It is known that mt-TrpRS function is required for mitochondria protein translation and in nearly all cell types. Perhaps therefore, the question should be: why aren't all cell types / organs affected by the *Wars2*-V117L allele? These questions will be addressed in the next two chapters.

3.3.4 Why are *Wars2*$^{V117L/V117L}$ mice lean?

During this study I have shown that there are systemic changes in *Wars2*$^{V117L/V117L}$ metabolism. Extensive metabolic phenotype analysis was performed with the aim of identifying the cause of the reduced adiposity phenotype observed in these mice. Based upon the results of these phenotyping tests I will now discuss the potential causal mechanisms for reduced adiposity in *Wars2*$^{V117L/V117L}$ mice.

3.3.4.1 Energy imbalance model

The fundamental causes for changes in body weight are commonly simplified to the relationship between energy intake and energy expenditure. For example: energy intake > energy expenditure = increased body weight, and conversely: energy intake < energy expenditure = reduced body weight. Based upon this model, the reduced adiposity and reduced total body weight phenotypes observed in the *Wars2*$^{V117L/V117L}$ mice must either be due to increased energy expenditure or reduced energy intake.

In order to analyse global metabolism, CLAMS analysis was performed at two difference temperatures. In order to determine why the *Wars2*$^{V117L/V117L}$ mice are lean I will first refer only to the data collected at 22°C as this is the temperature that the mice were kept in for the duration of their lives in their home cage. At 22°C, *Wars2*$^{V117L/V117L}$ mice had reduced energy expenditure compared to *Wars2*$^{+/+}$ mice. Therefore, we can certainly say that increased energy expenditure is not the reason that *Wars2*$^{V117L/V117L}$ mice are lean as in fact the converse is true. Therefore, in order for the energy balance model to still fit, *Wars2*$^{V117L/V117L}$ energy intake would also have to be greatly reduced in order for energy

intake to be less than energy expenditure. During the dark phase, when mice consume the vast majority of their calories, no significant differences in food intake were observed in *Wars2*$^{V117L/V117L}$ and *Wars2*$^{+/+}$ mice at 22°C. During the light phase, *Wars2*$^{V117L/V117L}$ food intake was slightly, albeit, significantly reduced compared to *Wars2*$^{+/+}$ mice. Overall, food intake was comparable in *Wars2*$^{V117L/V117L}$ and *Wars2*$^{+/+}$ mice indicating that reduced food intake is not the cause for the reduced adiposity phenotype observed in *Wars2*$^{V117L/V117L}$ mice.

Taken together these data suggest that energy expenditure is more greatly reduced than food intake meaning that the reasons why the *Wars2*$^{V117L/V117L}$ mice are lean is independent of energy expenditure or food intake. Here a distinction between energy input and food intake must be made. From the data collected in this study, it is not possible to calculate the actual energy intake because not all of the calories eaten by the mice are absorbed in the gut. This leaves the possibility that uptake of calories in the gut of *Wars2*$^{V117L/V117L}$ mice may be reduced which could shift the energy balance so that energy intake < energy expenditure and could explain the reduced adiposity observed in *Wars2*$^{V117L/V117L}$ mice. In order to test this hypothesis, further experiments would need to be performed such as paired-feeding analysis performed alongside faecal calorific analysis to determine actual calorific uptake in *Wars2*$^{V117L/V117L}$ mice digestive system.

3.3.4.2 Impaired thermoregulation

There is evidence to suggest that *Wars2*$^{V117L/V117L}$ mice have impaired thermoregulation as shown by abnormal *Wars2*$^{V117L/V117L}$ BAT pathology and reduced EE at 22°C. Furthermore, when *Wars2*$^{V117L/V117L}$ mice were housed at thermoneutrality, their total body mass increased. These data suggest that environmental temperature may contribute to adiposity in *Wars2*$^{V117L/V117L}$ mice. I will discuss this hypothesis further.

Thermoregulation is a complex process involving multiple systems and organs. In rodents, brown adipose tissue plays an important role in thermoregulation (Harms & Seale, 2013). BAT differs from WAT in several aspects that allow it to function as a thermoregulating organ including: increased mitochondrial mass, increased vasculature, increased lipolysis and vitally UCP1 expression (Bartelt et al., 2011).

In coupled mitochondrial, the electron transport chain pumps H^+ ions from the matrix, across the inner mitochondrial membrane and into the intermembrane space. This generates the mitochondrial membrane potential which is an oxygen consuming process. The mitochondrial membrane potential is required to mechanically drive ATP synthase. The rate of the electron transport chain is limited by ATP synthase, thus oxygen consumption is coupled with ATP synthesis. In BAT, UCP1 uncouples mitochondrial oxygen consumption from ATP synthesis (Fedorenko, Lishko, & Kirichok, 2012). This allows the electron transport chain to function at an increased rate, increasing oxygen consumption and, as a bi-product of this exothermic sequence, generate increased heat. This heat is used to thermoregulate.

In *Wars2*$^{V117L/V117L}$ mice there is evidence of BAT dysfunction and reduced thermogenic ability. Histological analysis of *Wars2*$^{V117L/V117L}$ BAT showed increased uni-locular lipid droplet formation indicative of reduced or inhibited lipolysis. In BAT, lipids are broken down and provide substrate for uncoupled mitochondria and heat production. However, in *Wars2*$^{V117L/V117L}$ BAT, lipolysis appeared to be inhibited resulting in lipid accumulation. This is likely explained by mitochondrial dysfunction in *Wars2*$^{V117L/V117L}$ BAT. Mitochondrial dysfunction in BAT would cause lipid accumulation, impairing *Wars2*$^{V117L/V117L}$ mice ability to thermoregulate and causing reduced EE at 22°C.

Consistent with *Wars2*$^{V117L/V117L}$ mice having impaired thermoregulation is the evidence of brown-like adipocytes in *Wars2*$^{V117L/V117L}$ WAT depots. Histological analysis of

Wars2$^{V117L/V117L}$ WAT showed reduced adipocyte size and multilocular lipid droplet formation. Multilocular lipid droplet formation is indicative of increased lipolysis and up-regulation of 'browning' pathways. Browning of WAT usually occurs in rodents due to cold exposure. Upon cold-exposure, beta-adrenergic stimuli from the brain signal to WAT causing up-regulation of mitochondrial biogenesis, lipolysis genes and UCP1 expression (Murano, Barbatelli, Giordano, & Cinti, 2009). In this circumstance, despite the cold-exposure stimuli being the same (22°C) in both *Wars2*$^{V117L/V11L}$ and *Wars2*$^{+/+}$ mice, *Wars2*$^{V117L/V117L}$ BAT is dysfunctional. Therefore, in *Wars2*$^{V117L/V117L}$ mice, the increased heat energy required to thermoregulate at 22°C cannot not be produced by BAT and required activation of alternate compensatory mechanisms. This could then cause compensatory up-regulation of browning pathways in *Wars2*$^{V117L/V117L}$ WAT. As the process of WAT 'browning' also involves the up-regulation of lipolysis genes, this could also explain the reduced adiposity phenotypes observed in *Wars2*$^{V117L/V117L}$ mice and elevated plasma FFA.

Consistent with this hypothesis is the observation that when *Wars2*$^{V117L/V117L}$ mice were housed at thermoneutrality (~28°C) their total body mass increased on average 5 % in 72 hours. This observation suggests that *Wars2*$^{V117L/V117L}$ mice ability to accumulate body weight is dependent on environmental temperature. In order to confirm that this is the case, a further study could be performed where *Wars2*$^{V117L/V117L}$ mice are housed at thermoneutrality for the duration of their lives in order to test the hypothesis that reduced adiposity in *Wars2*$^{V117L/V117L}$ mice is dependent upon environmental temperature and the requirement to thermoregulate.

If this hypothesis is true in *Wars2*$^{V117L/V117L}$ mice, then it may also be true in human patients with mitochondrial disease. Until recently, substantial BAT depots were only thought to be present in new-born humans. Several papers have now shown that healthy adult humans have significant and metabolically active BAT depots (Cypess et al., 2009; Saito et al., 2009; Virtanen et al., 2009). It has also been shown that BAT function increased during the

winter in adult humans suggesting a role for BAT function in human thermoregulation (Saito et al., 2009). If this hypothesis is true, it is possible that BAT dysfunction may explain the relationship between mitochondrial disease and low BMI observed by Wolny *et al* (Wolny et al., 2009) and opens up the possibility of using thermoregulation as a therapy resolve systemic changes in metabolism observed in mtRS patients and reduce global energy demand.

3.3.4.3 Ketogenesis

Whilst our data suggests that thermoregulation may play a role in the reduced adiposity phenotype observed in *Wars2*$^{V117L/V117L}$ mice, there is an alternate and more likely explanation. Systemic changes in metabolism were observed in *Wars2*$^{V117L/V117L}$ mice including reduced plasma TAG, increased plasma FFA and increased plasma ketone bodies. Taken together these data suggest that fuel is being proportioned differently in *Wars2*$^{V117L/V117L}$ mice away from lipid storage and in favour of ketogenesis, much like the systemic changes in metabolism observed during starvation. It is possible that mitochondrial dysfunction triggered a starvation-like response in *Wars2*$^{V117L/V117L}$ mice resulting in increased ketogenesis and consequently reduced adiposity. I will now discuss this hypothesis further.

Ketone bodies are primarily produced in the liver when glucose is not readily available in a process called ketogenesis. During ketogenesis FFA are liberated from adipose tissue where they are taken up by the liver. FFAs are converted into acetyl-CoA by beta oxidation in liver mitochondria. Acetyl-CoA is then converted into the ketone bodies (KB) acetoacetate (AcAc) and 3-beta-hydroxybutyrate (3HB). KBs are transported into the blood stream where they are metabolized primarily by the brain and heart (Newman & Verdin, 2014). *Wars2*$^{V117L/V117L}$ mice had significantly elevated plasma KBs compared *Wars2*$^{+/+}$ littermate controls. Additionally, plasma FFAs were elevated in *Wars2*$^{V117L/V117L}$ mice and plasma TAG were reduced indicating that lipid breakdown is being favoured over storage.

This is consistent with the hypothesis that in *Wars2*$^{V117L/V117L}$ mice, lipid is being liberated from adipose tissue in order to generate ketone bodies and, as a consequence of this, causing reduced adiposity.

Ketogenesis can be stimulated by insufficient glucose stores, which most commonly occurs during starvation, or insulin insufficiency, such as in patients with diabetic ketoacidosis (Newman & Verdin, 2014; Perilli, Saraceni, Daniels, & Ahmad, 2013). This led us to ask the question: what causes ketogenesis in *Wars2*$^{V117L/V117L}$ mice? Data collected during the CLAMS analysis showed that *Wars2*$^{V117L/V117L}$ food intake was comparable to *Wars2*$^{+/+}$, ruling out starvation as the cause. IPGTT data showed demonstrated that *Wars2*$^{V117L/V117L}$ mice have increased glucose tolerance suggesting that the glucose stimulated insulin secretory pathway was functional in *Wars2*$^{V117L/V117L}$ mice allowing us to rule out diabetic ketoacidosis as the cause. Taken together this suggests that ketogenesis is stimulated via an alternate pathway in *Wars2*$^{V117L/V117L}$ mice.

A possible explanation for activation of a starvation-like response in *Wars2*$^{V117L/V117L}$ mice is increased plasma FGF21. FGF21 is an endocrine hormone that has been shown to stimulate lipolysis in white adipose tissue and hepatic ketogenesis in a fed state in mice (Inagaki et al., 2007). Furthermore, elevated plasma FGF21 has been shown to be a biomarker or mitochondrial disease in humans (Davis et al., 2013). This led us to the hypothesis that FGF21 may contribute to systemic changes in metabolism observed in *Wars2*$^{V117L/V117L}$ mice including ketogenesis, increased glucose tolerance and increased WAT lipolysis. This hypothesis will be explored further in my final results chapter.

4 Characterization of the *Wars2*-V117L allele

4.1 Introduction

4.1.1 Mitochondrial tryptophanyl-tRNA synthetase – structure and function

Mitochondrial aminoacyl-tRNA synthetases (mtRSs) catalyse the aminoacylation of mtDNA encoded tRNA with their cognate amino acid. There are 17 known mtRSs, one for each amino acid required for mitochondrial protein synthesis, the exceptions being *GARS* and *KARS* that function in both the cytoplasm and mitochondria. mtRS genes, such *Wars2*, are found in nDNA and encode proteins that are synthesized in the cytoplasm. Newly synthesized mtRS proteins are transported from the cytoplasm to the mitochondrial matrix, a process that requires a mitochondrial targeting peptide sequence. All mtRS proteins have an N-terminal mitochondrial targeting peptide sequences that vary in length from 18 to 54 amino acids. Mitochondrial targeting peptides contain multiple positively charged residues and form an amphiphilic α-helix required to traffic mtRS to outer-mitochondrial membrane (Hammen & Weiner, 1998). mtRS proteins are imported to the mitochondrial matrix. Upon mitochondrial import, the mitochondrial targeting peptide is cleaved in a two-step reaction by the mitochondrial processing protease and the mitochondrial intermediate peptidase (Tyynismaa, 2013).

All aminoacyl-tRNA synthetases, cytoplasmic and mitochondrial, can be separated into two classes based on the presence of the following motifs. Class I aminoacyl-tRNA synthetases (RS) contain two sequence motifs: HIGH and KMSKS, indicative of the presence of a Rossman Fold required for ATP binding (Schmitt, Panvert, Blanquet, & Mechulam, 1995). Class II RSs share an anti-parallel beta-sheet fold flanked by alpha helixes and have three

distinct motifs: motif 1 – gΦxxΦxxPΦΦ; motif 2 - (F/Y/H)Rx(E/D) followed 4 to 12 aa away by (R/H)xxxFxxx(D/E); motif 3 - λxΦgΦgΦeRΦΦΦΦΦ (λ – small aa, Φ hydrophobic aa, x – any aa, small letters are used for aa conserved in 11 out of 17 sequences used). In type II RSs, motif I and motif 2 are usually separated by 40 to 80 amino acid residues however the distance between motif 2 and motif 3 is more variable and can be between 70 and 300 amino acids apart. Type I RSs tend to be monomeric whereas type II RSs tend to be dimeric or polymeric. Class I and Class II RS also functionally differ. Class I RSs bind the aminoacyl group to the 2'hydroxyl group of the tRNA whereas Class II RSs bind at the 3'-hydroxyl group (Eriani, Delarue, Poch, Gangloff, & Moras, 1990).

Wars2 encodes mitochondrial-Tryptophanyl-tRNA-Synthetase (mt-TrpRS). Human mt-TrpRS was identified and characterized in 2000 by Jorgensen R *et al* (Jorgensen, Søgaard, Rossing, Martensen, & Justesen, 2000). mt-TrpRS is 360 amino acids in length with a predicted weight of 40kDa. The amino acid sequence of human mt-TrpRS is highly conserved in amniota vertebrates. The peptide sequence of human mt-TrpRS shares 99.72% homology with mouse mt-TrpRS (**Figure 4.1A**).

mt-TrpRS has a short mitochondrial signalling peptide sequence that is 18 amino acids in length and is required to localize the protein to the mitochondrial matrix. Jorgensen R *et al* performed immunoblot assays for mt-TrpRS, observing a band at ~35kDa consistent with cleavage of the mitochondrial signalling peptide (Jorgensen et al., 2000). mt-TrpRS is a Class I mtRS illustrated by the conservation of both HIGH (Exon 2) and KMSKS (Exon 6) motifs required for ATP binding. Protein sequence analysis predicts that the mt-TrpRS catalytic core domain is based on a Rossman fold and requires amino acids from position 36 to 312 (encoded by Exons 2-6). The mt-TrpRS catalytic core domain was predicted based upon the conservation of 25 key amino acid residues also found in the peptide sequences of cytoplasmic-Trptophanyl-tRNA-synthetase (cyt-TrpRS) in various different organisms (**Figure 4.1B**). cyt-TrpRS is encoded by the *Wars* gene.

A

	1:	2:	3:	4:	5:	6:	7:	8:	9:	10:	11:
1: Wars2-V117L	100.00										
2: Mouse	99.72	100.00									
3: Rat	94.44	94.72	100.00								
4: Human	86.11	86.39	84.17	100.00							
5: Gorilla	85.83	86.11	84.44	99.72	100.00						
6: Cow	85.83	86.11	85.28	89.44	89.17	100.00					
7: Dog	84.72	85.00	84.72	86.94	86.67	88.33	100.00				
8: Platypus	68.06	68.33	68.89	70.00	69.72	70.56	71.39	100.00			
9: Chicken	66.67	66.96	66.08	67.54	67.25	67.54	67.25	68.13	100.00		
10: Zebrafish	62.01	62.29	62.85	62.01	62.29	60.34	61.17	60.89	62.46	100.00	
11: Anole	67.46	67.75	67.16	68.64	68.34	68.05	68.93	67.16	73.67	61.42	100.00

B

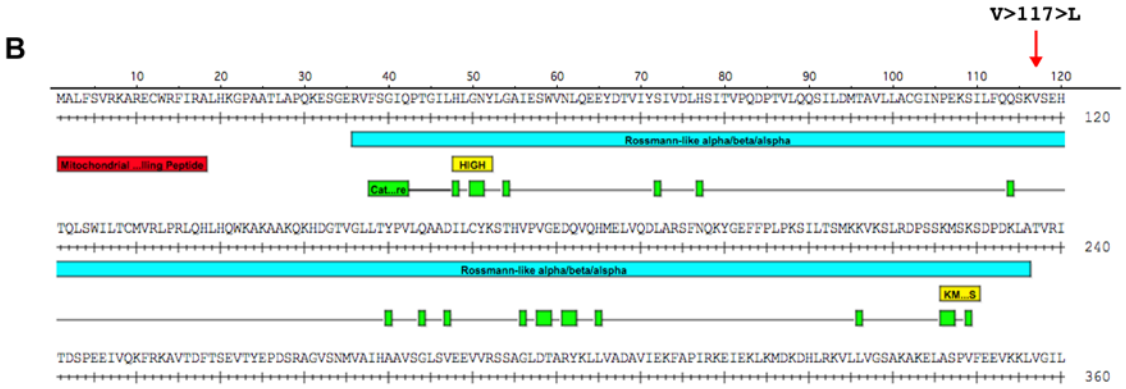

Figure 4.1 - mt-Trp-RS sequence conservation and functional domains.
A) mt-Trp-RS amino acid sequence conservation in amniota vertebrates (Herrero et al., 2016). B) Schematic diagram of predicted mt-Trp-RS functional domains. Red – mitochondrial signaling peptide (1 – 18); blue – Rossman fold (36 – 312); yellow – HIGH / KMSKS mtRS type I motifs (48-52 and 223-228 respectively); green –cyt-Trp-RS and mt-Trp-RS conserved residues.

4.1.2 Chapter aims

In the previous chapter, I presented evidence the *Wars2-V117L* allele caused hypertrophic cardiomyopathy, sensorineural hearing loss and reduced adiposity in mice. I also presented evidence indicating that the *Wars2*-V117L allele is a hypomorphic, partial loss-of-function allele. The aims of this chapter are to characterize the nature of the *Wars2*-V117L allele *in silico*, *in vitro* and *in vivo.*

The ENU-induced c.349G>T *Wars2* mutation encodes a Valine (GTG)117>Leucine (TTG) amino acid substitution in a highly conserved amino acid. However, the c.349G>T nucleotide is also located within the first codon of exon 3 in *Wars2*. Given the proximity of

the c.349G>T nucleotide substitution to the intron 2 – exon 3 boundary, we hypothesized that the *Wars2*-V117L allele would disrupt splicing of the third exon in *Wars2* resulting in reduced mt-TrpRS steady state protein levels, inhibition of mitochondrial translation and mitochondrial OXPHOS deficiency.

4.2 Results

4.2.1 Characterization of *Wars2*-V117L ENU-induced mutation *in silico*

The previously described c.349G>T ENU-induced mutation in *Wars2* encodes a Valine to Leucine amino acid substitution in mt-TrpRS at position 117. mt-TrpRS Valine-117 is conserved in all amniota vertebrates (**Figure 4.2A**). In order to predict the functional effects of the *Wars2*-V117L missense mutation on mtTrpRS protein function, SNAP2, SIFT and EASE-MM analysis was performed. SNAP2, SIFT and EASE-MM are publically available online programs used to predict the functional effects of missense mutations.

SNAP2 analysis integrates: evolutionary conservation, predicted secondary structures, solvent accessibility and functionally annotated regions to generate a predictive score of whether an amino acid substitution within a given protein sequence will have a negative effect on protein function (Bromberg & Rost, 2007). The SNAP2 scoring system ranges from -100 to 100, where -100 means that there is strong signal for neutral effect and a score of 100 predicts that there is a strong signal for a functional effect. The SNAP2 score for the mt-TrpRS Val<117>Leu amino acid substitution was -1 meaning that there was not strong evidence that amino acid substitution will have a negative or a neutral effect on mt-TrpRS function. By comparison, SNAP2 analysis predicted that substituting mt-TrpRS Valine-117 with any other amino acid, excluding leucine and isoleucine, would have a negative effect on mt-TrpRS function (SNAP2 score of >50) (**Figure 4.2B**).

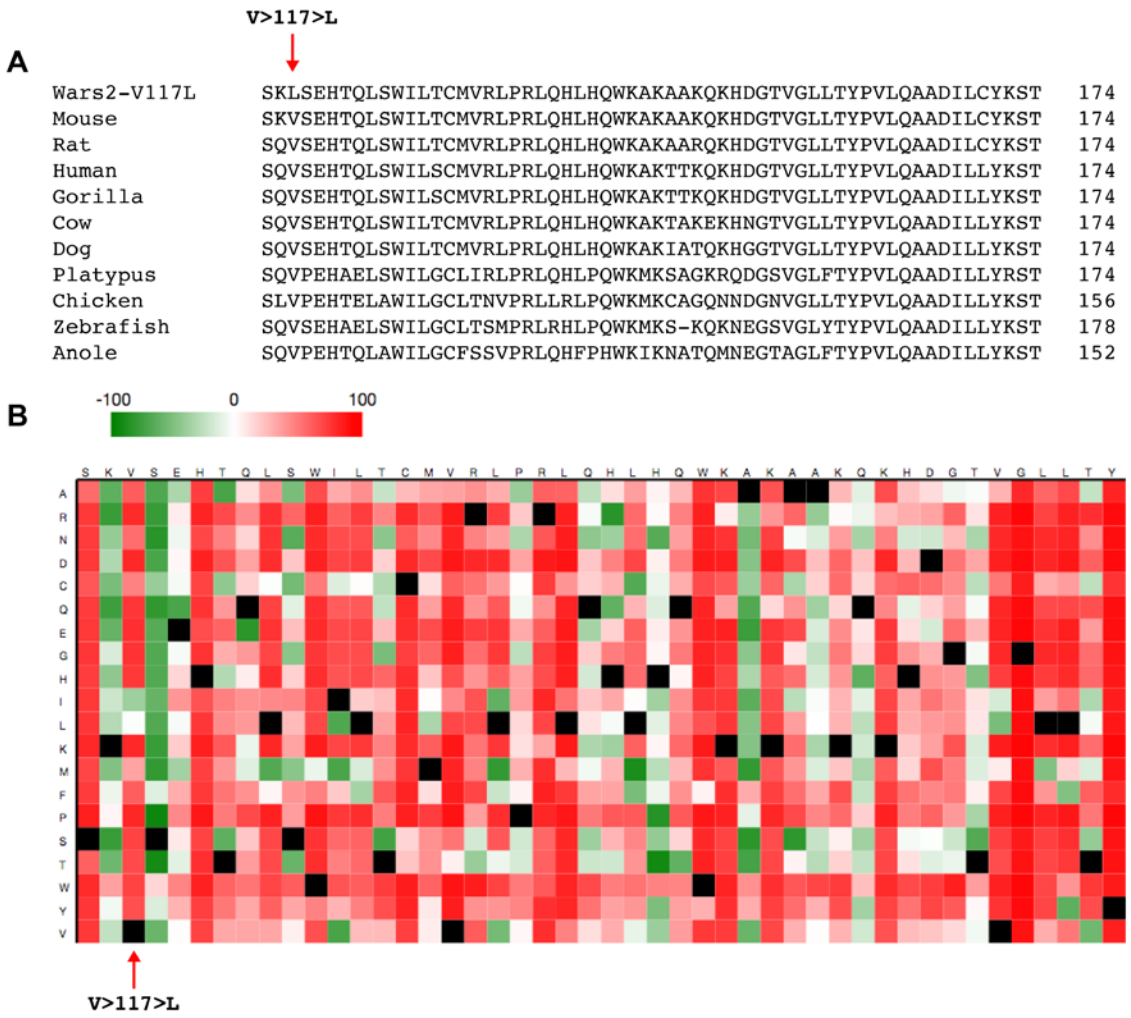

Figure 4.2 – *In silico* analysis of the functional effects of mt-Trp-RS Val<117>Leu substitution.
A) Conservation of mt-Trp-RS-Valine-117 in amniota vertebrates. B) SNAP2 analysis of mt-Trp-RS amino acid substitutions predicted to effect protein function. Data shown as heat map (adapted from www.predictprotein.org) illustrating predictive scores for amino acid substitutions. Dark red = strong signal for effect (score >50), white = weak signals (-50<score<50) and green = strong signal for neutral effect (score <-50).

SIFT analysis predicted that the V<117>L substitution will have a deleterious effect on mt-TrpRS, however it could only make this prediction with low confidence. The reason for the low confidence prediction in this circumstance was because there was not enough diversity in the aligned sequences used for the analysis and therefore the negative effect predicted by the SIFT program was based upon high sequence conservation alone (Kumar, Henikoff, & Ng, 2009).

Finally, EASE-MM analysis was performed. EASE-MM (Evolutionary, Structural, and Amino acid Encodings with Multiple Models) is a machine based learning method that predicts the effects of amino acid substitutions on protein stability by generating the a real value of the stability change denoted as ΔΔG (Folkman, Stantic, Sattar, & Zhou, 2016). Here the ΔΔG value defines the stability change as the difference in the Gibbs free energies of unfolding between the mutated and wild-type proteins (ΔΔG = ΔG (mutated) – ΔG(wild-type). If ΔΔG < 0 then the mutation is predicted to destabilise the protein (ΔΔG > -1 = destabilising; -1 < ΔΔG < -0.5 = likely destabilising; -0.5 < ΔΔG < 0.5 = neutral; 0.5 < ΔΔG < 1 = stabilising; ΔΔG > 1 = stabilising). ΔΔG values were calculated for substitutions of mt-TrpRS Valine 117 with every amino acid. Using EASE-MM analysis, all amino acid substitutions for mt-TrpRS Valine 117 were predicted to be destabilising apart from Isoleucine that was predicted to be likely destabilising. Substitution of mt-TrpRS Valine 117 with Leucine was predicted to be destabilising and the ΔΔG was -1.0776. However, substitution of mt-TrpRS Valine with any other amino acid, except Isoleucine, was predicted to be more destabilising that the mt-TrpRS Valine 117 Leucine substitution (**Table 4.1**).

#seq_name	mutation	ddG	ddG_class
mt_Trp_RS	V117G	-3.2042	destabilising
mt_Trp_RS	V117S	-2.4272	destabilising
mt_Trp_RS	V117D	-2.3177	destabilising
mt_Trp_RS	V117A	-2.127	destabilising
mt_Trp_RS	V117P	-1.9977	destabilising
mt_Trp_RS	V117N	-1.8972	destabilising
mt_Trp_RS	V117H	-1.8848	destabilising
mt_Trp_RS	V117R	-1.8771	destabilising
mt_Trp_RS	V117E	-1.8706	destabilising
mt_Trp_RS	V117K	-1.8444	destabilising
mt_Trp_RS	V117T	-1.695	destabilising
mt_Trp_RS	V117Q	-1.6846	destabilising
mt_Trp_RS	V117C	-1.6049	destabilising
mt_Trp_RS	V117W	-1.5848	destabilising
mt_Trp_RS	V117Y	-1.5178	destabilising
mt_Trp_RS	V117M	-1.365	destabilising
mt_Trp_RS	V117F	-1.3308	destabilising
mt_Trp_RS	V117L	-1.0776	destabilising
mt_Trp_RS	V117I	-0.6434	likely_destabilising

Table 4.1 – EASE-MM analysis of stability changes caused by mt-TrpRS valine<117>leucine substitution.

Taken together, *in silico* analysis has provided no compelling evidence that the Valine<117>Leucine amino acid substitution is deleterious to mt-TrpRS structure, function or stability. Online protein prediction programmes can predict the effects of amino acid substitutions to high degrees of confidence when the 3D-structure of the protein is known. To date, mt-TrpRS has not been crystallised so its 3D structure is yet unknown meaning that I could not use these programmes to analyse the mt-TrpRS valine 117 leucine substitution. The programmes used in this study are machine based learning programmes that predict the effect of an amino acid substitution on protein function based upon several factors including evolutionary conservation, structural predictions and solvent accessibility. These programmes use this information to predict the effects of amino-acid substitutions that have previously been characterised empirically. The programme is then modified and the process is repeated until the programme predicts the same outcome that was empirically shown. The value of the predicted results from the machine based learning programmes used in this study must be treated as predictions and require experimental confirmation. That being said, mt-TrpRS Valine 117 is highly conserved throughout evolution. This fact alone suggests that Valine 117 is vital for mt-TrpRS function however as yet there is no empirical evidence to support this.

4.2.2 Characterization of *Wars2*-V117L ENU-induced mutation *in vitro*

4.2.2.1 *Wars2* mRNA splicing in *Wars2*$^{V117L/V117L}$ MEFs

Given the proximity of the Val (GTG) < 117 > Leu (TTG) ENU-induced mutation to the *Wars2* Intron 2 / Exon 3 boundary we investigated the effect on *Wars2* mRNA splicing. To do this all *Wars2* mRNA transcripts were amplified by PCR using RNA isolated from *Wars2*$^{+/+}$ and *Wars2*$^{V117L/V117L}$ cultured primary mouse embryonic fibroblast cells (MEFs).

PCR amplicons were separated by size using gel electrophoresis. Following size separation, detectable bands were purified and sequenced by Sanger sequencing. In both *Wars2*$^{+/+}$ and *Wars2*$^{V117L/V117L}$ MEFs, multiple transcripts were identified (**Table 4.2**). *Wars2*-FL (full length) mRNA transcripts were identified in both *Wars2*$^{+/+}$ and *Wars2*$^{V117L/V117L}$ MEFs containing all 6 *Wars2* Exons. Two additional transcripts were identified in *Wars2*$^{+/+}$ MEFs: *Wars2*-TR2 and *Wars2*-TR3, where *Wars2*-Exon2 and *Wars2*-Exon3 were skipped in phase as shown by the presence of *Wars2*-Exon1/Exon3 and *Wars2*-Exon2/Exon4 boundaries respectively (**Figure 4.3A**). *Wars2*-TR2 was not observed in *Wars2*$^{V117L/V117L}$ MEFs (**Figure 4.3A**). *Wars2*-TR3 was also observed in *Wars2*$^{V117L/V117L}$ MEFs. However, an additional *Wars2* transcript was identified in *Wars2*$^{V117L/V117L}$ MEFs: *Wars2*-2+3; in which both *Wars2*-Exon2 and *Wars2*-Exon3 were skipped in phase as shown by the presence of the *Wars2*-Exon1/Exon4 boundary (**Figure 4.3A**).

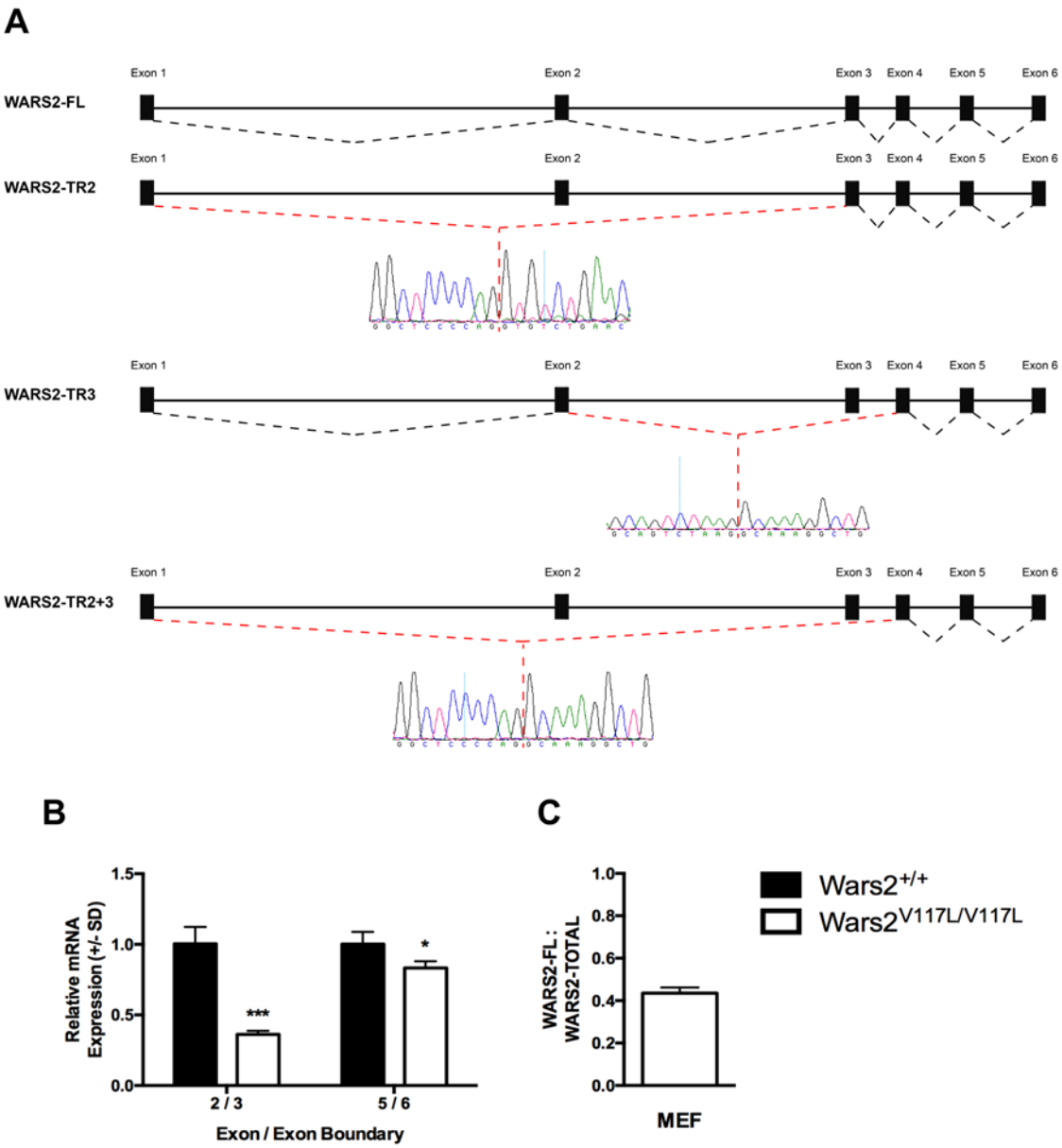

Figure 4.3 – Identification and quantification of *Wars2* mRNA transcripts.
A) Diagram of identified *Wars2* mRNA transcripts with Sanger sequencing data for novel *Wars2* mRNA transcripts that have in-phase exon-skipping. B) Relative expression levels of *Wars2*-Exon2/3 (*Wars2*-FL) and *Wars2*-Exon5/6 (*Wars2*-Total) mRNA in MEF. $Wars2^{+/+}$ (n=3) and $Wars2^{V117L/V117L}$ (n=3). Data shown as mean 2□ddCT ± SD. Data analyzed using student's t-test: ***** P<0.05, ****** P<0.01, ******* P<0.001.

Transcript	Exon 1	Exon 2	Exon 3	Exon 4	Exon 5	Exon 6	MEF
***Wars2*-FL**	☐	☐	☐	☐	☐	☐	***Wars2*$^{+/+}$ & *Wars2*$^{V117L/V117L}$**
***Wars2*-TR2**	☐	☐	☐	☐	☐	☐	***Wars2*$^{+/+}$**
***Wars2*-TR3**	☐	☐	☐	☐	☐	☐	***Wars2*$^{+/+}$ & *Wars2*$^{V117L/V117L}$**
***Wars2*-2+3**	☐	☐	☐	☐	☐	☐	***Wars2*$^{V117L/V117L}$**

Table 4.2 – Summary *Wars2* transcripts identified in *Wars2*$^{+/+}$ and *Wars2*$^{V117L/V117L}$ MEFs.

In order to quantify *Wars2* exon-skipping in *Wars2*$^{+/+}$ and *Wars2*$^{V117L/V117L}$ MEFs, qRT-PCR was performed using probes targeted to different *Wars2*-Exon/Exon boundaries: *Wars2*-Exon5/Exon6 and *Wars2*-Exon2/Exon3. The *Wars2*-Exon5/Exon6 boundary was present in all *Wars2* mRNA transcripts identified (*Wars2*-FL, *Wars2*-TR2, *Wars2*-TR3 and *Wars2*-TR2+3) allowing us to quantify *Wars2*-Total mRNA (**Table 4.2**). The *Wars2*-Exon2/Exon3 boundary was only present in *Wars2*-FL mRNA and absent in *Wars2*-TR2, *Wars2*-TR3 and *Wars2*-2+3 transcripts (**Table 4.2**). By quantifying the presence of *Wars2*-Exon2/Exon3 boundary we were able to quantify *Wars2*-FL mRNA transcripts. By comparing the relative levels of *Wars2*-FL mRNA to *Wars2*-Total mRNA we were able to quantify the amount of exon-skipping in *Wars2*$^{+/+}$ and *Wars2*$^{V117L/V117L}$ MEFs.

Wars2-Total mRNA was 17% reduced in *Wars2*$^{V117L/V117L}$ MEFs compared to *Wars2*$^{+/+}$. *Wars2*-FL mRNA transcripts (retaining Exon 2 and Exon 3) were 64% reduced in *Wars2*$^{V117L/V117L}$ MEFs relative to *Wars2*$^{+/+}$ (**Figure 4.3B**). By calculating the ratio of *Wars2*-FL : *Wars2*-Total mRNA (*Wars2*-Exon2/Exon3 : *Wars2*-Exon5/Exon6) we determined the proportion of *Wars2*-Total mRNA that is full-length. The *Wars2*-FL : *Wars2*-Total ratio in

Wars2$^{V117L/V117L}$ MEFs is 0.43 meaning that 43% of *Wars2*-Total mRNA is *Wars2*-FL in *Wars2*$^{V117L/V117L}$ MEFs (**Figure 4.3C**). By inference therefore 57% of *Wars2*-Total mRNA is not *Wars2*-FL and is miss-spliced in *Wars2*$^{V117L/V117L}$ MEFs.

These data show that there is increased exon-skipping of Exon 2 and/or Exon 3 in *Wars2*$^{V117L/V117L}$ MEFs compared to *Wars2*$^{+/+}$ resulting in a reduction in *Wars2*-FL mRNA. These data were consistent with our hypothesis that the *Wars2*-V117L allele disrupts *Wars2* exon splicing and leads to reduced levels of full-length *Wars2* mRNA. Based upon these data we predicted that reduced *Wars2*-FL mRNA would result in a reduction in mt-TrpRS protein and cause inhibition of mitochondrial protein synthesis, OXPHOS deficiency and mitochondrial dysfunction in MEFs. At the time, we did not have an mt-TrpRS antibody so we were unable to quantify mt-TrpRS steady state protein levels in MEFs. We therefore looked further down the pathway and investigated mitochondrial translation and mitochondrial function in *Wars2*$^{V117L/V117L}$ MEFs.

4.2.2.2 Mitochondrial translation in *Wars2*$^{V117L/V117L}$ MEFs

In order to determine the functional effects of the *Wars2*-V117L ENU-induced mutation on mitochondrial protein synthesis in MEFs, [^{35}S]-methionine / cysteine mitochondrial protein translation assays were performed (**Figure 4.4A+B**). There was no detectable difference in the amount of [^{35}S]-methionine / cysteine incorporated into mitochondrial subunits in *Wars2*$^{V117L/V117L}$ MEFs compared to *Wars2*$^{+/+}$ MEFs (**Figure 4.4A**). These data indicate that mitochondrial protein synthesis is not inhibited in *Wars2*$^{V117L/V117L}$ MEFs under these experimental conditions.

To confirm this result we quantified the steady state protein levels of mitochondrial OXPHOS subunits CI (NDUFB8) and CIV (mtCOI) in MEFs by immunoblot analysis (**Figure 4.4C**). No detectable differences in CI or CIV were observed in *Wars2*$^{V117L/V117L}$ MEFs compared with *Wars2*$^{+/+}$ MEFs consistent with data from the mitochondrial translation assay

(**Figure 4.4C**). Taken together, these data show that the *Wars2*-V117L ENU-induced mutation does cause mitochondrial protein synthesis inhibition in MEFs.

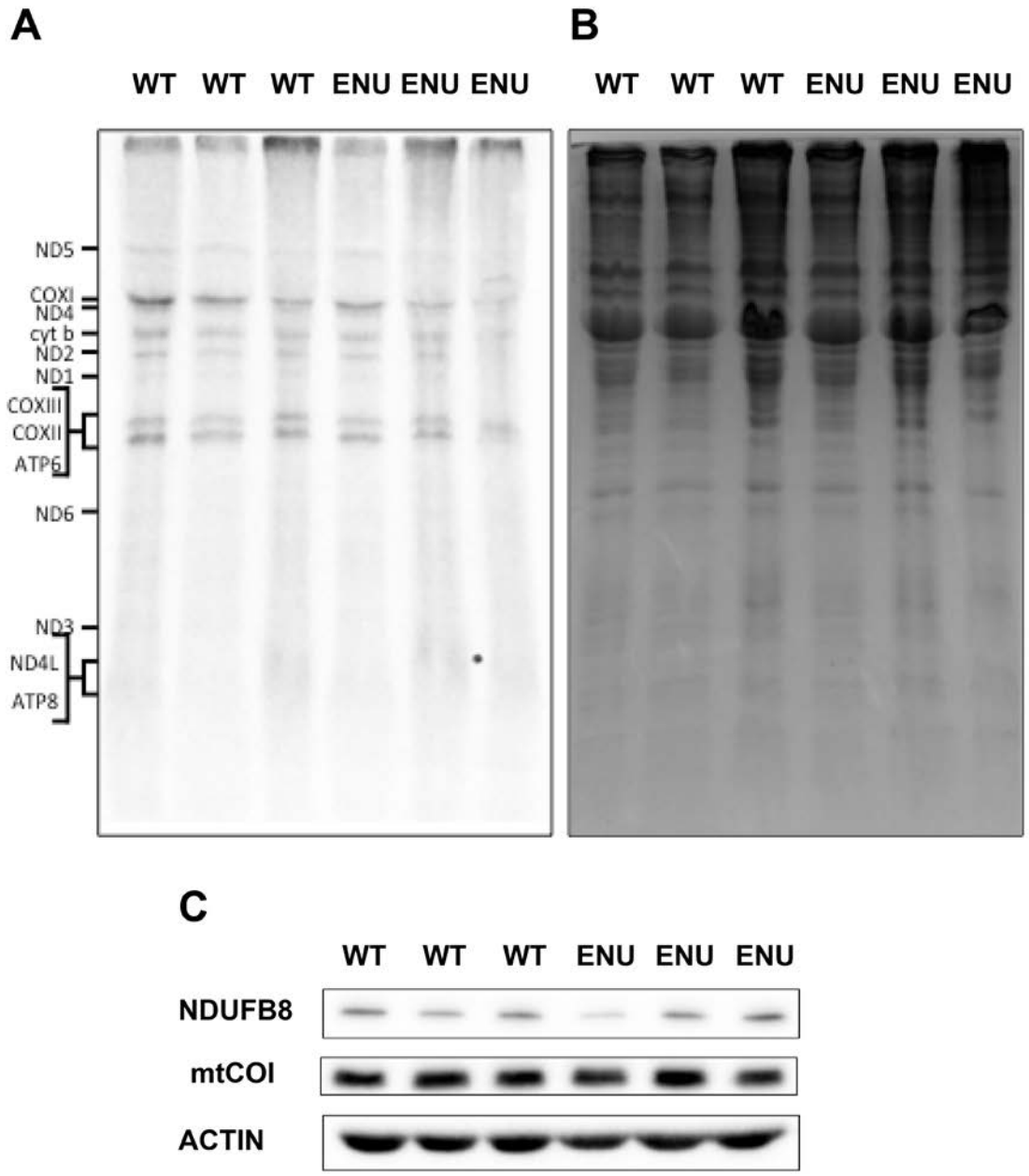

Figure 4.4 – Analysis of mitochondrial translation in *Wars2*$^{V117L/V117L}$ *in vitro*.
A) Mitochondrial translation assay. Electrophoretic patterns of mitochondrial translation products from MEFs labeled with [^{35}S]-Methionine and Cysteine in the presence of emetine. B) [^{35}S]-Methionine and Cysteine control gel stained with coomassie blue. C) Steady state protein levels of CI (NDUFB8), CIV (mtCOI) and actin (control) in MEF. WT = *Wars2*$^{+/+}$, ENU = *Wars2*$^{V117L/V117L}$.

4.2.2.3 Mitochondrial OXPHOS function in *Wars2*$^{V117L/V117L}$ MEFs

In order to determine whether the *Wars2*-V117L allele had a deleterious effect on mitochondrial function in MEFs, mitochondrial stress tests were performed using the

Seahorse XF24 analyser (**Figure 4.5**). The Seahorse XF24 analyser measures oxygen consumption rate (OCR) and extracellular acidification rate (ECAR) in live cultured cells in real-time. The Seahorse XF-24 analyser was used to measure OCR and ECAR in *Wars2*$^{V117L/V117L}$ MEFs under basal conditions and following the administration of mitochondrial OXPHOS inhibitors: Oligomycin (CV inhibitor), FCCP (mitochondrial uncoupler) and Antimycin (CIII inhibitor) / Rotenone (CI inhibitor). Thus, it is possible to evaluate: basal mitochondrial OXPHOS function, mitochondrial proton leak, ATP production, maximal respiration and spare respiratory capacity. Unexpectedly *Wars2*$^{V117L/V117L}$ MEFs had increased basal respiration, proton leak, ATP production, maximal respiration and spare respiratory capacity compared to *Wars2*$^{+/+}$ MEFs (**Figure 4.5A+C**). Basal ECAR was comparable between *Wars2*$^{V117L/V117L}$ and *Wars2*$^{+/+}$ MEFs (**Figure 4.5B**). Contrary to our original hypothesis, these data showed that *Wars2*$^{V117L/V117L}$ MEFs had increased mitochondrial function compared to *Wars2*$^{+/+}$.

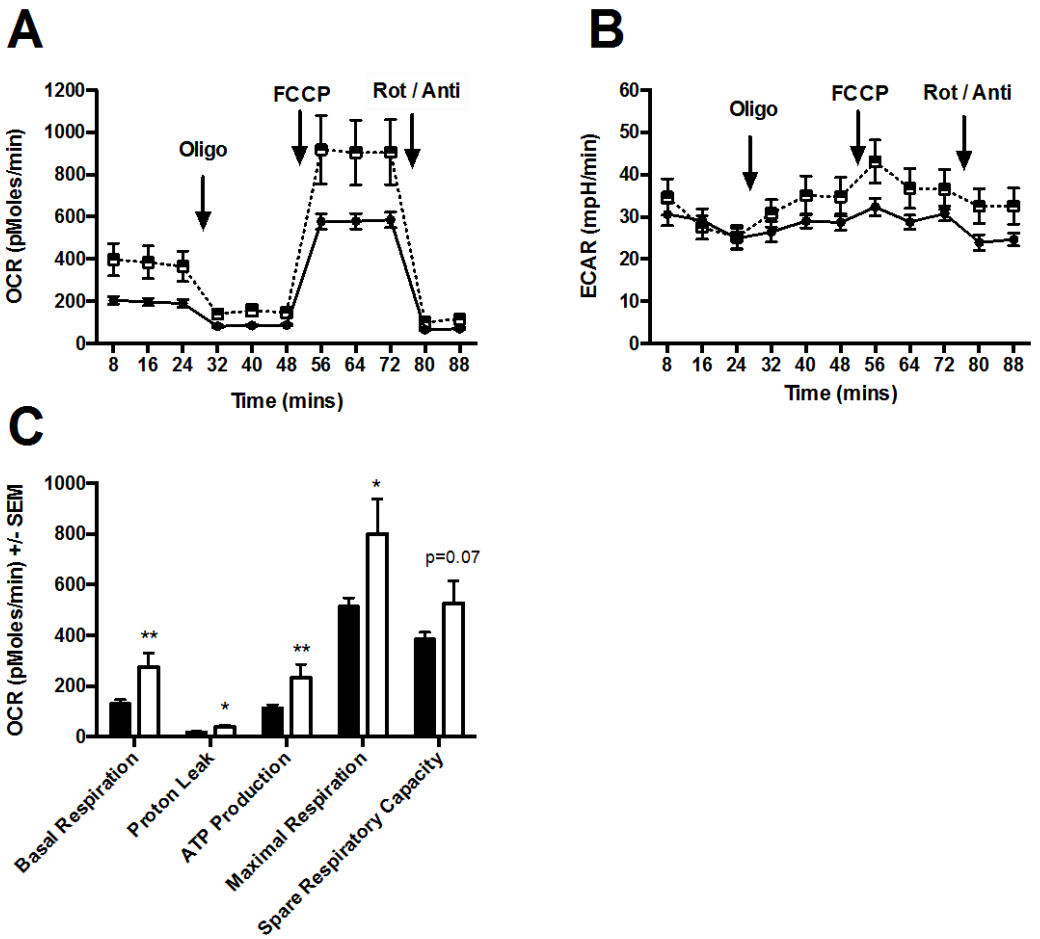

Figure 4.5 – Analysis of mitochondrial function in *Wars2*$^{V117L/V117L}$ MEF.
A) Oxygen consumption rate (OCR) and B) extracellular acidification rate measured in MEF at baseline and after Oligomycin (oligo), FCCP and Rotenone+Antimycin (Rot / Anti) treatment, data normalized to live cell number. C) Relative oxygen consumption rates of: basal respiration, proton leak, ATP production, maximal respiration and spare respiratory capacity in MEFs. Data shown as mean ± SEM. Data analyzed using student's t-test: ***** P<0.05, ****** P<0.01, ******* P<0.001.

We hypothesised that the increase in mitochondrial function observed in *Wars2*$^{V117L/V117L}$ MEFs was due to up-regulation in mitochondrial biogenesis. To test this hypothesis, mitochondrial mass was analysed in *Wars2*$^{V117L/V117L}$ MEFs (**Figure 4.6A**). MEFs were stained with a fluorescent mitochondrial marker MitoTracker Green. MitoTracker staining was quantified using fluorescence-activated cell sorting (FACS). Total fluorescence per cell was measured using 30,000 cells per samples. Average fluorescence per cell was 40% increased in *Wars2*$^{V117L/V117L}$ MEFs compared to *Wars2*$^{+/+}$ controls showing that *Wars2*$^{V117L/V117L}$ MEFs had increased mitochondrial mass compared to *Wars2*$^{+/+}$ (**Figure 4.6A**). These data were consistent with our hypothesis that *Wars2*$^{V117L/V117L}$ MEFs had increased mitochondrial function due to up-regulation of mitochondrial biogenesis.

Peroxisome proliferator-activated receptor gamma coactivator 1-alpha (PGC1A) is often termed the 'master regulator' of mitochondrial biogenesis. PGC1a is a transcriptional coactivator. It has been shown that PGC1a transcriptionally regulates transcription factors for mitochondrial genes such as NRF1 and NRF2. PGC1a also directly binds to and co-activates NRF1 to promote the transcription of mitochondrial transcription factor A (TFAM) which in turn regulates transcription and regulation of the mitochondrial genome (Wu et al., 1999). PGC1A mRNA expression was 70% increased in *Wars2*$^{V117L/V117L}$ MEFs relative to *Wars2*$^{+/+}$ MEFs indicating a transcriptional up-regulation of mitochondrial biogenesis in *Wars2*$^{V117L/V117L}$ MEFs (**Figure 4.6B**). Taken together these data shows that the *Wars2*-V117L ENU-induced mutation causes increased mitochondrial mass and up-regulation of mitochondrial biogenesis in MEFs.

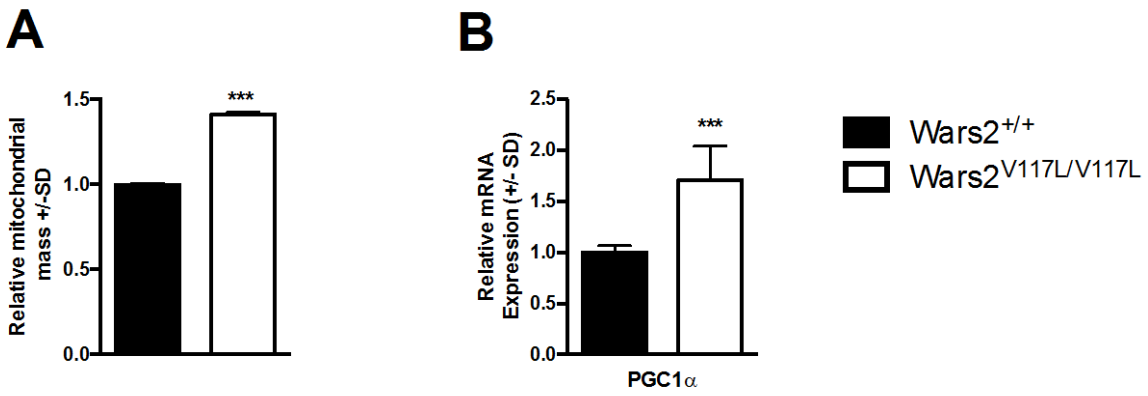

Figure 4.6 – Regulation of mitochondrial mass and biogenesis in *Wars2*$^{V117L/V117L}$ MEF. A) Relative mitochondrial mass in MEF. MEFs were stained with MitoTracker-Green and fluorescence was quantified by FACS. 30,000 cells per sample were used for FACS analysis. *Wars2*$^{+/+}$ (n=3) and *Wars2*$^{V117L/V117L}$ (n=3). Data shown here as relative mean fluorescence per sample ± SD. B) Relative expression levels of PGC1A mRNA in MEF. *Wars2*$^{+/+}$ (n=3) and *Wars2*$^{V117L/V117L}$ (n=3). Data shown as mean 2□ddCT ± SD. Data analyzed using student's t-test: ***** P<0.05, ****** P<0.01, ******* P<0.001.

4.2.2.4 Summary of *in vitro* data

In summary, *in vitro* analysis showed that the *Wars2*-V117L allele disrupts *Wars2* exon-skipping resulting in reduced full-length *Wars2* mRNA. However, despite this, there was no evidence that mitochondrial translation was inhibited in *Wars2*$^{V117L/V117L}$ MEFs. In fact, we went on to show that *Wars2*$^{V117L/V117L}$ MEFs had increased mitochondrial OXPHOS function and mitochondrial mass. Whilst these observations may seem contradictory they were not completely unexpected. Similar observations have been reported in studies of mtRS mutations in humans where mtRS mutations cause OXPHOS deficiencies *in vivo* but not *in vitro*. Our findings suggest that *Wars2*$^{V117L/V117L}$ MEFs up-regulate mitochondrial biogenesis to compensate or prevent the inhibition of mitochondrial translation and mitochondrial dysfunction *in vitro*. The next question we asked was whether similar compensatory pathways can be activated *in vivo*.

4.2.3 Characterization of *Wars2*-V117L ENU-induced mutation *in vivo*

Although *in vitro* data showed that the *Wars2*-V117L mutation does not cause impaired mitochondrial dysfunction, there was phenotypic evidence, present in chapter 3, consistent

with the hypothesis that the *Wars2*-V117L allele does cause mitochondrial dysfunction *in vivo*. *Wars2*$^{V117L/V117L}$ mice had reduced energy expenditure at 22°C and lipid accumulation in BAT, both of which could be caused by impaired mitochondrial OXPHOS function. Additionally, the phenotypes that we identified in *Wars2*$^{V117L/V117L}$ mice (hypertrophic cardiomyopathy, sensorineural hearing loss and reduced adiposity) have also been observed in human patients with loss-of-function mtRS alleles again suggesting that the *Wars2*-V117L allele is a loss of function allele. In this section we tested the hypothesis that the *Wars2*-V117L allele causes dysregulation of *Wars2* mRNA splicing and reduced mt-TrpRS protein levels, ultimately leading to inhibition of mitochondrial translation and mitochondrial OXPHOS deficiencies *in vivo*.

4.2.3.1 *Wars2* mRNA splicing in *Wars2*$^{V117L/V117L}$ tissues

In vitro, we showed that the *Wars2*-V117L ENU-induced mutation disrupts *Wars2* mRNA splicing resulting in reduced full-length *Wars2* mRNA levels in *Wars2*$^{V117L/V117L}$ MEFs compared to wild-type controls. To determine whether the *Wars2*-V117L allele disrupts *Wars2* mRNA splicing *in vivo*, *Wars2*-Total mRNA and *Wars2*-FL mRNA levels were quantified in *Wars2*$^{V117L/V117L}$ heart, liver, kidney and skeletal muscle at 12 months of age (**Figure 4.7A-D**). *Wars2*-Total mRNA (*Wars2*-Exon4/Exon5 and Wars2-Exon5/Exon6) was 40% reduced in *Wars2*$^{V117L/V117L}$ heart relative to *Wars2*$^{+/+}$ controls (**Figure 4.7A**); no significant differences in *Wars2*-Total mRNA were observed in *Wars2*$^{V117L/V117L}$ liver, kidney and skeletal muscle compared *Wars2*$^{+/+}$ (**Figure 4.7B - D**). There was a trend for reduced *Wars2*-Total mRNA in *Wars2*$^{V117L/V117L}$ kidney, however this was not statistically significant due biological variation (**Figure 4.7C**). *Wars2*-FL mRNA was decreased by: 83, 67, 84 and 74% in *Wars2*$^{V117L/V117L}$ heart, liver, kidney and skeletal muscle respectively relative to *Wars2*$^{+/+}$ controls (**Figure 7A-D**). These data showed that the *Wars2*-V117L allele increased *Wars2* Exon 2 and/or Exon 3 skipping in *Wars2*$^{V117L/V117L}$ tissues and caused reduced *Wars2*-FL mRNA.

In order to determine whether there were differences in the amount of *Wars2* exon-skipping the ratio of *Wars2*-FL mRNA: *Wars2*-Total mRNA were analysed in *Wars2*$^{V117L/V117L}$ tissues (**Figure 4.7E**). The ratios of *Wars2*-FL: *Wars2*-Total mRNA were: 0.28, 0.30, 0.30 and 0.24 in *Wars2*$^{V117L/V117L}$ heart, liver, kidney and muscle respectively. If all *Wars2* mRNA were *Wars2*-FL, then the ratio of *Wars2*-FL: *Wars2*-Total mRNA would be 1.0. Here we show that in *Wars2*$^{V117L/V117L}$ tissues the ratio of *Wars2*-FL: *Wars2*-Total mRNA was between 0.24 – 0.30 (**Figure 4.7E**). These data show that the majority, between 76 – 70 %, of *Wars2*-Total mRNA did not contain exon 2 and / or exon 3. 70 – 76% of *Wars2*$^{V117L/V117L}$ mRNA transcripts were therefore either *Wars2*-TR3 and/or *Wars2*-TR2+3 transcripts previously identified in *Wars2*$^{V117L/V117L}$ MEFs. The ratio of *Wars2*-FL: *Wars2*-Total mRNA were comparable between tissues showing that the effect of the *Wars2*-V117L ENU-induced mutation on *Wars2* exon-skipping is not tissue specific (**Figure 4.7E**). Interestingly however, the *Wars2*-FL: *Wars2*-Total mRNA ratio in *Wars2*$^{V117L/V117L}$ MEFs was 0.43, over 10% higher than in any *Wars2*$^{V117L/V117L}$ tissues analyzed. These data indicate that the impact of the *Wars2*-V117L ENU-induced mutation on *Wars2* Exon-skipping is more profound *in vivo* than *in vitro*. Also we observed that *Wars2* total mRNA was significantly reduced in in *Wars2*$^{V117L/V117L}$ heart tissue but no significant differences on Wars2-total mRNA were observed in any other *Wars2*$^{V117L/V117L}$ tissue relative to *Wars2*$^{+/+}$. This observation suggests that there are differences in *Wars2* transcriptional regulation in *Wars2*$^{V117L/V117L}$ tissues *in vivo* and this may contribute to the susceptibility of cardiac tissue to the *Wars2*-V117L allele.

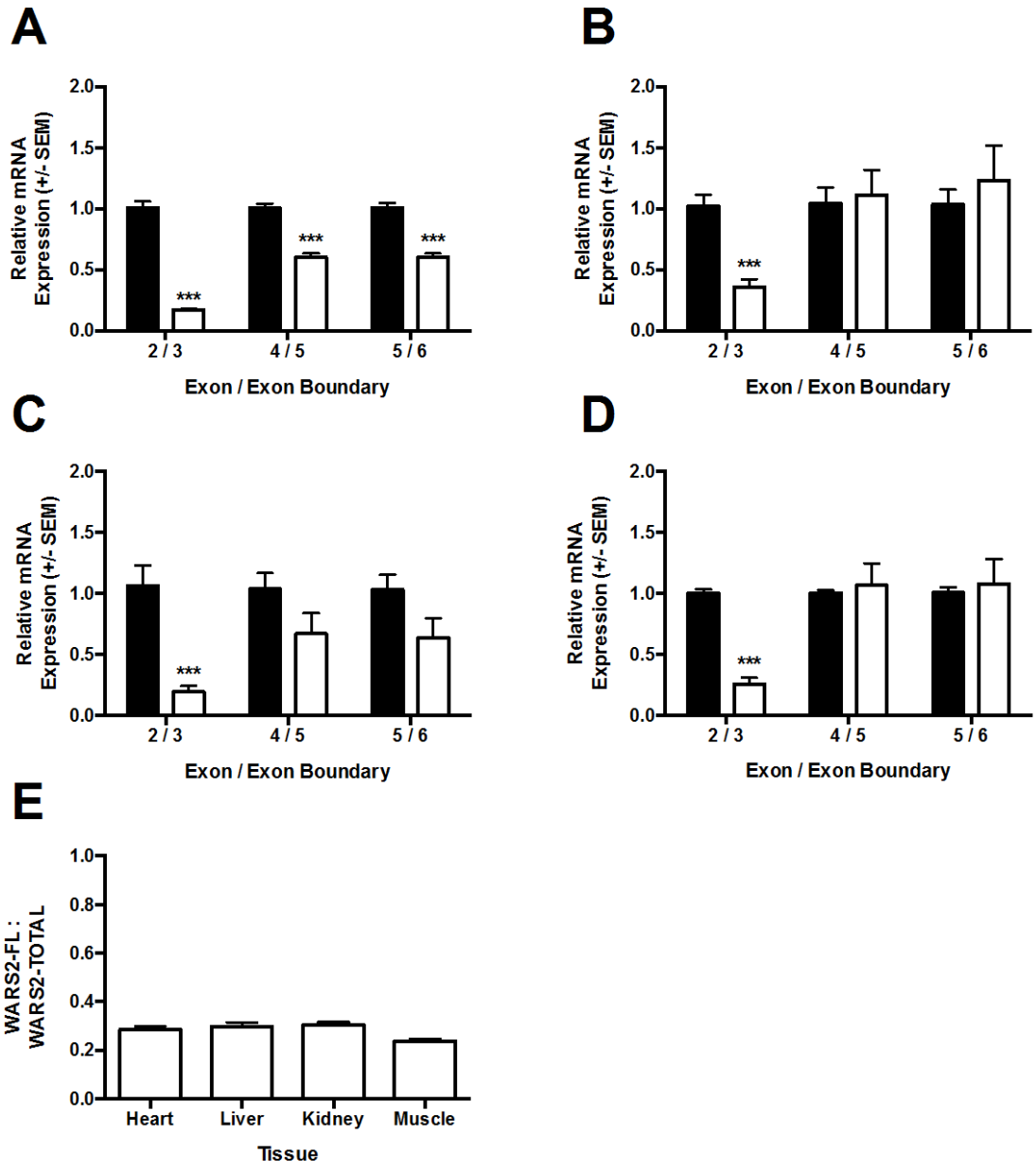

Figure 4.7 – Tissue specific analysis of *Wars2* exon-skipping in *Wars2*$^{V117L/V117L}$ mice. Relative expression levels of *Wars2*-Exon2/3 (*Wars2*-FL), *Wars2*-Exon4/5 (*Wars2*-Total) *Wars2*-Exon5/6 (*Wars2*-Total) mRNA in A) heart, B) liver, C) kidney, D) skeletal muscle. *Wars2*$^{+/+}$ (n=8) and *Wars2*$^{V117L/V117L}$ (n=8). Data shown as mean 2□ddCT ± SEM. E) Quantification of *Wars2*-FL : *Wars2*-Total mRNA in *Wars2*$^{V117L/V117L}$ tissues. Data analyzed using student's t-test: ***** P<0.05, ****** P<0.01, ******* P<0.001.

4.2.3.2 Regulation of mt-TrpRS in *Wars2*$^{V117L/V117L}$ tissues

We showed that the *Wars2*-V117L allele caused increased *Wars2* mRNA exon-skipping *in vitro* and *in vivo* and resulted in reduced levels of *Wars2*-FL, protein coding, mRNA. We

hypothesised that reduced *Wars2*-FL mRNA would cause a reduction in the steady state levels of mt-TrpRS steady state protein levels in *Wars2*$^{V117L/V117L}$ tissues.

We were unable to validate any commercially available mt-TrpRS antibodies. We therefore commissioned the production of a custom mt-TrpRS antibody. To do this two peptides corresponding to amino acid residues C-KGPAATLAPQKESGERVFSGIQ-coNH2 (Exon 1 / Exon 2) and C-KKVKSLRDPSSKMSKSDPDKL-coNH2 (Exon 6) of mouse mt-TrpRS were synthesized and used to immunize rabbits (Covalab). Antiserum was collected from the rabbits and was affinity purified on Sulfolink coupling gels (Pierce).

To validate the custom mt-TrpRS antibody, immunoprecipitation (IP) of mt-TrpRS was performed in *Wars2*$^{V117L/V117L}$ and *Wars2*$^{+/+}$ liver lysates (**Figure 4.8**). A band at ~35kDa was enriched in both *Wars2*$^{+/+}$ and *Wars2*$^{V117L/V117L}$ post-IP fractions compared with the pre-IP lysate (**Figure 4.8A**). The strength of 35kDa band was stronger in *Wars2*$^{+/+}$ preps compared with *Wars2*$^{V117L/V117L}$ preps in both pre-IP and post-IP fractions. A second identical polyacrylamide gel was run and was stained with coomassie brilliant blue protein stain to allow us to identify protein bands (**Figure 4.8B**). Protein bands at ~35kDa were identified in both *Wars2*$^{V117L/V117L}$ and *Wars2*$^{+/+}$ lanes of the coomassie stained polyacrylamide gel. The ~35kDa bands were cut from the gel and were sent for mass-spectrometry analysis (**Figure 4.8C**). Trptophanyl-tRNA ligase, mitochondrial (also known as mt-TrpRS) peptide sequences were identified in both band 1 (*Wars2*$^{+/+}$) and band 2 (*Wars2*$^{V117L/V117L}$) via mass spectrometry. The confidence score for mt-TrpRS in band 1 is 123.97 compared with 27.55 in band 2. The confidence score is based upon the number of unique peptides identified and the overall protein coverage. Both protein coverage and the number of unique peptides identified were greater in band 1 compared with band 2 consistent with greater protein enrichment in the *Wars2*$^{+/+}$ Post-IP fraction compared with *Wars2*$^{V117L/V117L}$ Post-IP fraction (**Figure 8C**). These data show that the custom-made antibody recognizes a band at 35kD corresponding to mt-TrpRS. The predicted size of mt-TrpRS is 40.1kD. The difference in

size between the observed size (35kD) and the predicted size (40.1kD) is consistent with cleavage of the mt-TrpRS mitochondrial signalling peptide upon mitochondrial import as previously observed by Jorgensen R *et al* (Jorgensen et al., 2000).

Immunoblots were performed to assess mt-TrpRS steady state protein levels in *Wars2*$^{V117L/V117L}$ tissues (**Figure 4.8D**). Mt-TrpRS protein levels were substantially reduced in *Wars2*$^{V117L/V117L}$: heart, liver and kidney tissues relative to *Wars2*$^{+/+}$ (**Figure 4.8D**). Unexpectedly, mt-TrpRS levels were in fact higher in *Wars2*$^{V117L/V117L}$ skeletal muscle relative to *Wars*$^{+/+}$ (**Figure 4.8D**). It was not possible to quantify mt-TrpRS protein levels of the mt-TrpRS band due to its low intensity in *Wars2*$^{V117L/V117L}$ samples however as shown from the IP performed using liver lysates, mt-TrpRS was present in both *Wars2*$^{+/+}$ and *Wars2*$^{V117L/V117L}$ preps.

The reduction in mt-TrpRS protein observed in *Wars2*$^{V117L/V117L}$ heart, liver and kidney tissues is consistent with reduced *Wars2*-FL mRNA transcript levels observed in these tissues previously. However, mt-TrpRS protein levels were increased in *Wars2*$^{V117L/V117L}$ skeletal muscle despite reduced *Wars2*-FL mRNA levels suggesting that mt-TrpRS protein levels are not dependant upon Wars2-FL mRNA expression levels in skeletal muscle.

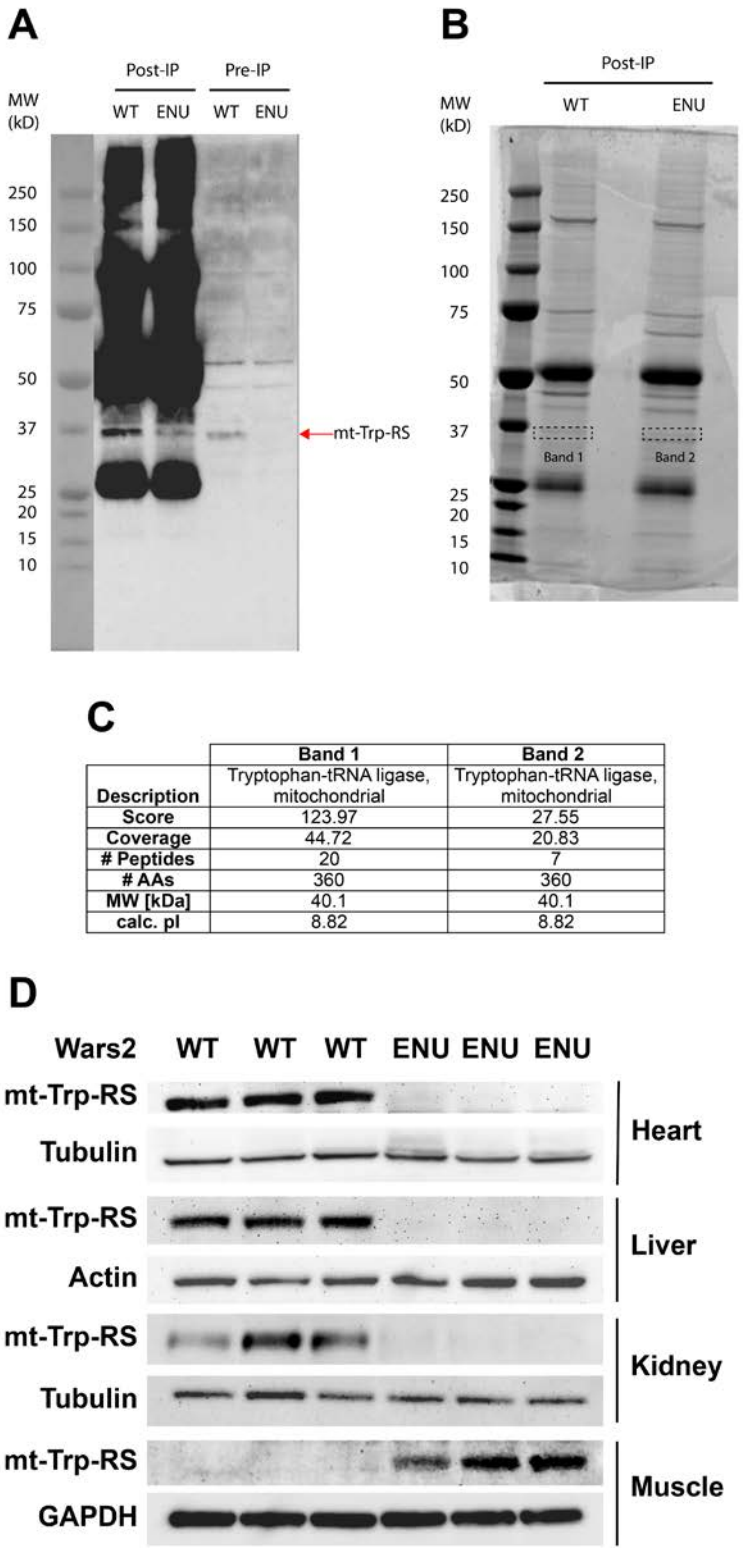

	Band 1	Band 2
Description	Tryptophan-tRNA ligase, mitochondrial	Tryptophan-tRNA ligase, mitochondrial
Score	123.97	27.55
Coverage	44.72	20.83
# Peptides	20	7
# AAs	360	360
MW [kDa]	40.1	40.1
calc. pI	8.82	8.82

Figure 4.8 – Tissue specific differences in mt-TrpRS in *Wars2*$^{V117L/V117L}$ mice.
Validation custom-made mt-TrpRS antibody A) Immunoblot analysis of mt-TrpRS in *Wars2*$^{+/+}$ and *Wars2*$^{V117L/V117L}$ liver lysates pre and post immunoprecipitation. B) Post-IP fractions were separated by polyacrylamide electrophoresis and stained with Coomassi blue. Band 1 and Band 2 were cut from the gel and sent for mass-spectrometry analysis. C) Summary of mt-TrpRS peptides identified by mass-spectrometry in band 1 and band 2. D) Immunoblot analysis

of steady state protein levels of mt-TrpRS in heart, liver, kidney and skeletal muscle. WT = *Wars2*$^{+/+}$, ENU = *Wars2*$^{V117L/V117L}$.

4.2.3.3 Mitochondrial Translation *In Vivo*

As shown above the *Wars2*-V117L ENU-induced mutation causes reduced mt-TrpRS protein levels in heart, liver and kidney tissues. In order to determine whether reduced mt-TrpRS protein had a functional effect on mitochondrial translation *in vivo*, immunoblots were performed to assess the steady state protein levels of mitochondrial OXPHOS complex subunits in *Wars2*$^{V117L/V117L}$ heart (**Figure 4.9A**), liver (**Figure 4.9B**), kidney (**Figure 4.9C**) and skeletal muscle (**Figure 4.9D**) at 12 months of age.

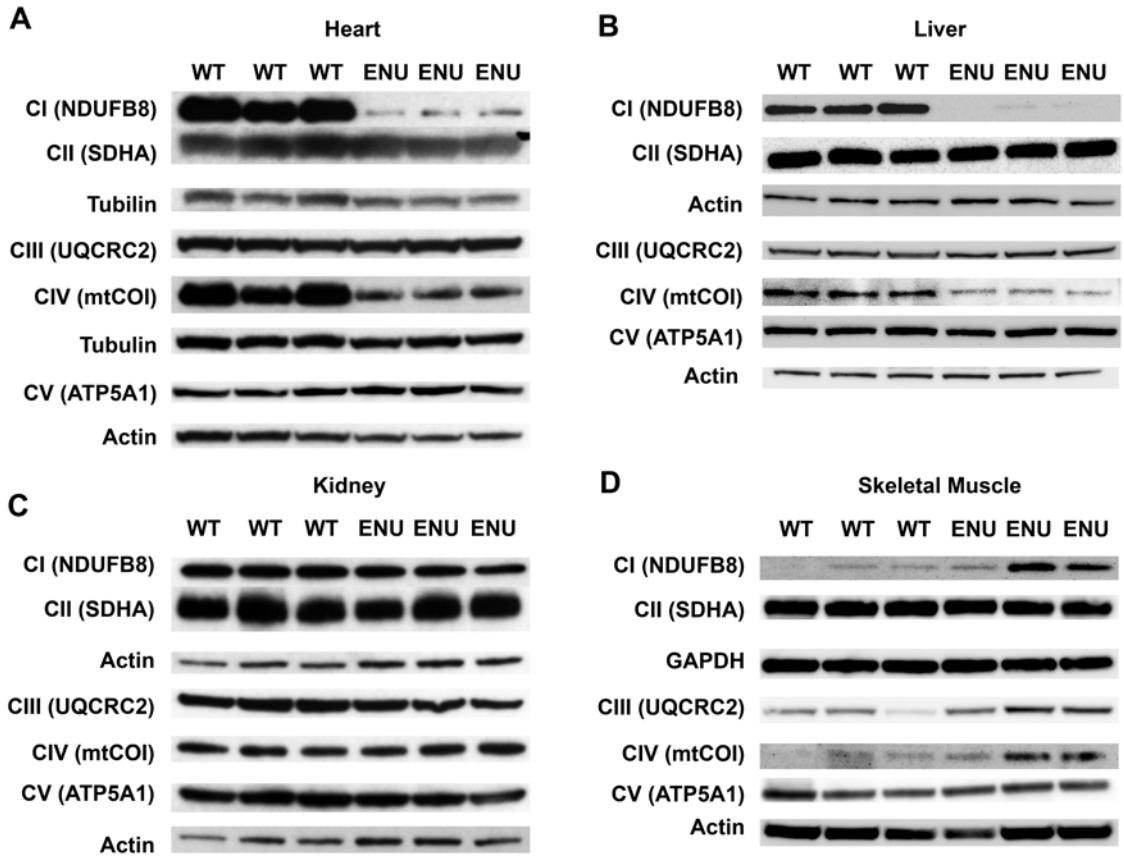

Figure 4.9 – Immunoblot analysis of OXPHOS subunits at 12 months of age.
Immunoblot analysis of steady state protein levels of OXPHOS subunits in A) heart, B) liver, C) kidney and D) skeletal muscle. WT = *Wars2*$^{+/+}$, ENU = *Wars2*$^{V117L/V117L}$. Complex 1 (CI) - NADH:Ubiquinone Oxidoreductase Subunit B8 (NDUFB8); Complex 2 (CII) – Succinate Dehydrogenase Complex Flavoprotein Subunit A (SDHA); Complex 3 (CIII) – Ubiquinol-Cytochrome C Reductase Core Protein II (UQCRC2); Complex 4 (CIV) – Mitochondrially Encoded Cytochrome C Oxidase I (mtCOI); Complex 5 (CV) – ATP Synthase, H+ Transporting, Mitochondrial F1 Complex, Alpha Subunit 1, Cardiac Muscle (ATP5A).

Mitochondrial OXPHOS complex subunit immunoblots were quantified using ImageJ (**Figure 4.10**). NDUFB8 and mtCOI protein levels were significantly reduced in *Wars2*$^{V117L/V117L}$ heart and liver compared to *Wars2*$^{+/+}$ (**Figure 4.10A+B**). No significant differences in SDHA, UQCRC2 and ATP5A1 protein levels were observed in *Wars2*$^{V117L/V117L}$ and *Wars2*$^{+/+}$ heart and liver at 12 months of age (**Figure 4.10A+B**). In kidney, no significant differences in NDUFB8, SDHA, UQCRC2 or ATP5A1 protein levels were observed between genotypes (**Figure 4.10C**). mtCOI protein levels were significantly reduced in *Wars2*$^{V117L/V117L}$ kidney compared with *Wars2*$^{+/+}$ (**Figure 4.10C**). However, the reduction in mtCOI protein levels observed in in *Wars*$^{V117L/V117L}$ kidney was modest (-19%) compared to *Wars2*$^{V117L/V117L}$ heart and liver where mtCOI protein levels were substantially reduced (-61% and -85% respectively). In the *Wars2*$^{V117L/V117L}$ tissues where we have previously shown reduced mt-TrpRS protein levels such as heart, liver and kidney, we have also observed reduced mtCOI protein levels to varying degrees. NDUFB8 was also reduced in *Wars2*$^{V117L/V117L}$ heart and liver, but was not significantly reduced in *Wars2*$^{V117L/V117L}$ kidney.

In contrast with this, there is a trend for increased NDUFB8, UQRC2 and mtCOI levels in *Wars2*$^{V117L/V117L}$ skeletal muscle compared with *Wars2*$^{+/+}$ (**Figure 4.10D**). NDUFB8 and mtCOI protein levels were on average 3.22 and 1.50 fold increased in *Wars2*$^{V117L/V117L}$ skeletal muscle compared with *Wars2*$^{+/+}$ (**Figure 4.10D**). These trends for increased *Wars2*$^{V117L/V117L}$ NDUFB8 and mtCOI protein level were not significantly different due to high variation between biological replicates and low n numbers. The average UQCRC2 protein levels were 2.00 fold increased in *Wars2*$^{V117L/V117L}$ compared with *Wars2*$^{+/+}$ which was statistically significant (**Figure 4.10D**). NDUFB8 and ATP5A protein levels were comparable between *Wars2*$^{V117L/V117L}$ and *Wars2*$^{+/+}$ skeletal muscle (**Figure 4.10D**). These data are consistent with increased mt-TrpRS protein levels observed in *Wars2*$^{V117L/V117L}$ skeletal muscle at the same time point and indicate that mitochondrial translation is not inhibited in skeletal muscle due to the presence of mt-TrpRS protein.

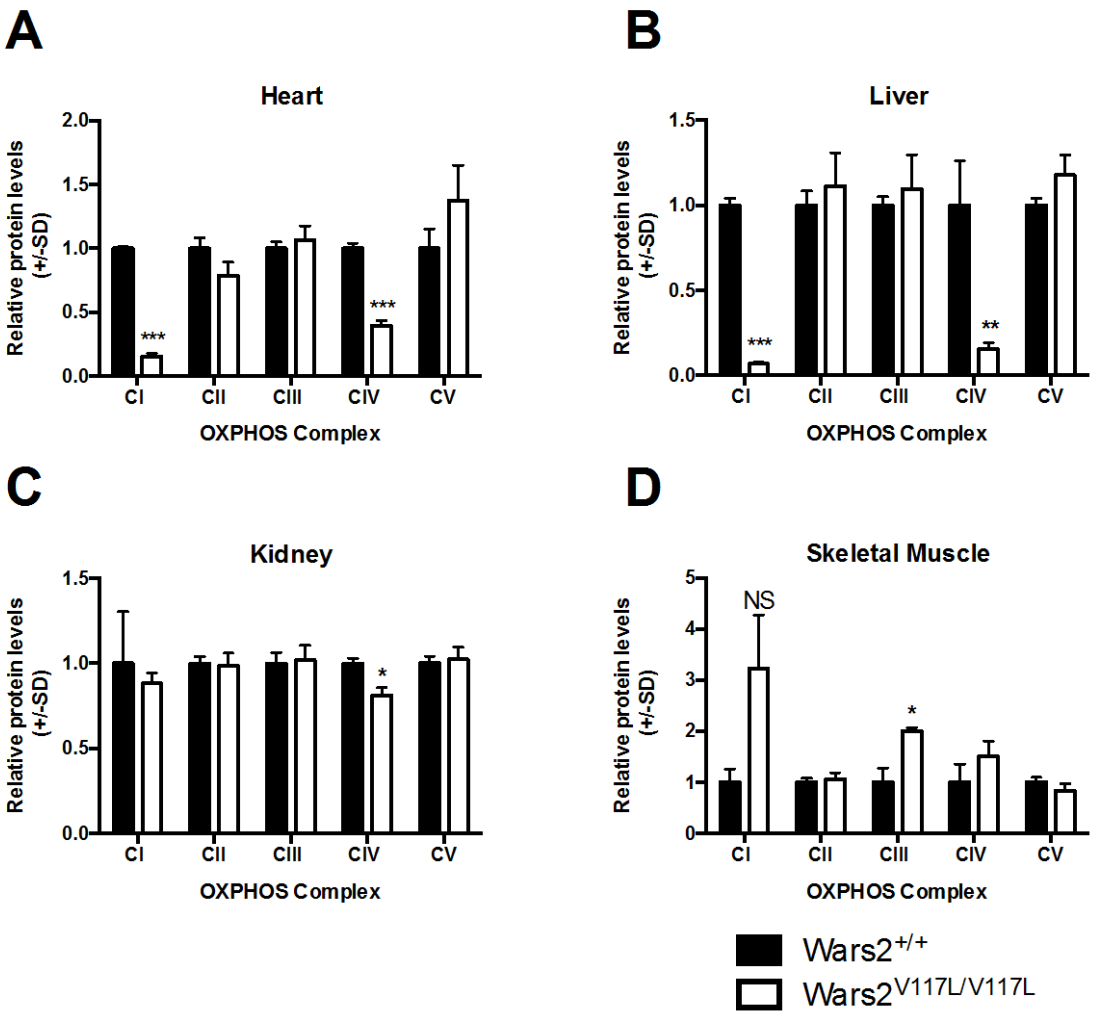

Figure 4.10 – Mitochondrial OXPHOS levels in *Wars2*$^{V117L/V117L}$ tissues.
Immunoblot analysis of mitochondrial OXPHOS complex subunits in A) Heart. B) Liver, C) Kidney, D) Skeletal muscle at 12 months of age. CI – NDUFB8, CII – SDHA, CIII – UQRC2, CIV – mtCOI and CV (ATP5A). Immunoblots were quantified using ImageJ and normalized to loading controls. Data in A-D shown as mean ± SD. Data analyzed using student's t-test: ***** P<0.05, ****** P<0.01, ******* P<0.001.

4.2.3.4 Summary of *In Vivo* Data

In summary, the *Wars2*-V117L allele causes reduced levels of full-length *Wars2* mRNA in all *Wars2*$^{V117L/V117L}$ tissues analysed. There were no tissue specific differences in *Wars2* mRNA splicing in *Wars2*$^{V117L/V117L}$ tissues as the ratio of *Wars2*-Total mRNA to *Wars2*-FL mRNA is comparable between tissues. Reduced *Wars2*-FL mRNA levels resulted in tissue specific reductions in mt-TrpRS protein levels in *Wars2*$^{V117L/V117L}$ tissues. mt-TrpRS steady state protein levels were reduced in *Wars2*$^{V117L/V117L}$ heart, liver and kidney tissue but were increased in *Wars2*$^{V117L/V117L}$ skeletal muscle relative to *Wars2*$^{+/+}$. Reduced mt-TrpRS protein levels caused OXPHOS deficiencies in *Wars2*$^{V117L/V117L}$ tissues to varying degrees.

CI and CIV subunit protein levels were substantially reduced in *Wars2*$^{V117L/V117L}$ heart and liver. Whereas in *Wars2*$^{V117L/V117L}$ kidney, reduced mt-TrpRS caused only mild reductions in CIV. Finally, in *Wars2*$^{V117L/V117L}$ skeletal muscle no OXPHOS complex subunit deficiencies were observed which is explained by the fact that there were increased mt-TrpRS protein levels in this tissue (**Table 4.3**). Overall these data show that the *Wars2*-V117L ENU-induced mutation is a partial loss-of-function allele with tissue specific penetrance. These data also show that the penetrance of the *Wars2*-V117L allele is likely dependent upon tissue specific differences in transcriptional regulation of *Wars2*-Total mRNA and tissue specific differences in the steady state levels of mt-TrpRS protein.

	***Wars2* mRNA**		**Mt-TrpRS**	**OXPHOS**				
	Total	**FL**		**CI**	**CII**	**CIII**	**CIV**	**CV**
Heart	↓	↓	↓	↓	-	-	↓	-
Liver	-	↓	↓	↓	-	-	↓	-
Kidney	-	↓	↓	-	-	-	↓	-
Sk. Muscle	-	↓	↑	↑NS		↑	↑NS	

Table 4.3 – Summary of data characterising the *Wars2*-V117L ENU-induced allele *in vivo*.

4.3 Discussion

The overarching aim of this chapter was to characterise the nature of the *Wars2*-V117L allele. We hypothesised that the *Wars2*-V117L allele would disrupt *Wars2*-mRNA splicing resulting in reduced mt-TrpRS protein levels, inhibition of mitochondrial translation and mitochondrial OXPHOS deficiencies. I will now dissect this hypothesis into three questions: does the *Wars2*-V117L allele disrupt *Wars2* mRNA splicing? Does the *Wars2*-V117L allele

caused reduced levels of mt-TrpRS? Does the *Wars2*-V117L allele cause inhibition of mitochondrial translation? The answers to these questions will now be discussed.

4.3.1 Does the *Wars2*-V117L allele disrupt *Wars2* mRNA splicing?

In this chapter, I showed compelling evidence that the *Wars2*-V117L mutation disrupts *Wars2* mRNA splicing *in vitro* and *in vivo*. First of all, *Wars2* mRNA transcripts were amplified by PCR, separated by size and sequenced in *Wars2*$^{V117L/V117L}$ and *Wars2*$^{+/+}$ MEFs. *Wars2*-FL mRNA transcript was sequenced in both *Wars2*$^{V117L/V117L}$ and *Wars2*$^{+/+}$ MEFs. Unexpectedly additional truncated *Wars2* transcripts were identified in *Wars2*$^{+/+}$ MEFs showing that *Wars2* is post-transcriptionally regulated by splicing in wild-type cells. In *Wars2*$^{+/+}$ MEFs, truncated *Wars2* mRNA transcripts were identified where the second or third exons of *Wars2* had been skipped, in-phase (*Wars2*-TR2 and *Wars2*-TR3 respectively). In *Wars2*$^{V117L/V117L}$ MEFs *Wars2*-TR3 transcript was also observed however an additional truncated transcript was identified where the second and third exons of *Wars2* had been skipped in phase (*Wars2*-2+3). This was the first evidence that *Wars2*-V117L allele disrupts *Wars2* mRNA splicing. Based upon peptide sequence analysis, the mt-TrpRS catalytic core domain forms a Rossman-like fold that requires amino acids from position 36 (exon 2) to 312 (Exon 6). Within this catalytic core domain, exon 2 encodes the HIGH motif conserved in all Class I aminoacyl-tRNA synthetases that is required for ATP binding. Based upon these two observations, it is unlikely that the truncated *Wars2* transcripts that lack the second and / or third exons in *Wars2* would encode a functional truncated protein if translated.

I went onto quantify *Wars2* mRNA splicing *in vitro* and *in vivo* and showed that there was reduced levels of full-length *Wars2* mRNA in *Wars2*$^{V117L/V117L}$ MEFs, heart, kidney, liver and skeletal muscle. To quantify this, a taqman probe spanning the exon 2 / exon 3 boundary was used. The exon 2 / 3 boundary was not present in any of the identified truncated *Wars2* mRNA transcripts but is present in *Wars2*-FL mRNA. To confirm that the reduction in

Wars2-FL mRNA levels observed in *Wars2*$^{V117L/V117L}$ samples was not due to transcriptional down regulation, taqman probes spanning the exon 4 / exon 5 and exon 5 / exon 6 boundaries were used. All identified *Wars2* transcripts, full-length and truncated, retained the fourth, fifth and sixth exons of *Wars2*. Therefore, by using these probes it was possible to quantify total *Wars2* mRNA transcript levels. No significant differences in *Wars2*-total mRNA transcript levels were observed in *Wars2*$^{V117L/V117L}$ liver, kidney and skeletal muscle relative to wild-type controls. This showed that in these tissues the reduction in *Wars2*-FL mRNA was not due to transcriptional down regulation of *Wars2* but due to increased exon-skipping.

Unexpectedly *Wars2*-total mRNA was significantly reduced in *Wars2*$^{V117L/V117L}$ MEFs and heart (-17% and -40% respectively) but not as substantially as *Wars2*-FL mRNA. The reduction in *Wars2*-total mRNA observed in *Wars2*$^{V117L/V117L}$ MEFs and heart could be due to transcriptional down-regulation or non-sense mediated RNA decay of truncated *Wars2* transcripts. The *Wars2* mRNA exon-skipping events identified in *Wars2* truncated transcripts were in-phase and did not create premature stop codons making nonsense mediated RNA decay unlikely. Furthermore, it was possible to amplify truncated transcripts by PCR in *Wars2*$^{V117L/V117L}$ MEFs. This showed that truncated *Wars2* transcripts were, to some extent, present and were are not degraded. Taken together this shows that the reduction in total *Wars2*-mRNA observed in *Wars2*$^{V117L/V117L}$ MEFs and heart is due to transcriptional down regulation. Therefore, in *Wars2*$^{V117L/V117L}$ MEFs and heart, reduced *Wars2*-FL mRNA levels are not only due to increased exon-skipping but also due to transcriptional down-regulation of *Wars2* mRNA. The mechanism through which *Wars2* is transcriptionally down-regulated in *Wars2*$^{V117L/V117L}$ MEFs and heart will be investigated in my next results chapter.

Splice variant mutations in mtRS genes have been shown to cause mitochondrial disorders in human patients. For example, the majority of patients identified with *DARS2* mutations

in humans have at least one mutation in the 3' end of the second intron of *DARS2.* The most common *DARS2* splice variant mutation is the 228-20_-21delTTinsC allele that effects splicing of the third exon of *DARS2*. *DARS2* patients present with highly specific neuropathology: leukoencephalopathy with brainstem and spinal cord involvement and lactate elevation (LBSL) (Scheper et al., 2007). Berge *et al* showed that splice variant *DARS2* mutations were more penetrant in neuronal cell lines compared with non-neuronal cell lines potentially explaining the brain specific pathology associated with *DARS2* patients (van Berge et al., 2012). Based upon these findings we additionally hypothesized that the tissue specific pathology identified in *Wars2*$^{V117L/V117L}$ mice may be caused by tissue specific susceptibility to the *Wars2*-V117L splice variant allele.

In order to determine whether there were differences in *Wars2* mRNA splicing in *Wars2*$^{V117L/V117L}$ tissues and cells, the ratio of *Wars2*-FL: *Wars2*-total mRNA was analyzed. In *Wars2*$^{V117L/V117L}$ tissues the *Wars2*-FL: *Wars2*-total ratio was comparable and ranged from 0.24 – 0.30 indicating that 76 – 70% of total *Wars2* mRNA transcripts are truncated. Furthermore, it showed that the tissue specific pathology observed in the *Wars2*$^{V117L/V117L}$ mice was independent of tissue specific differences in splicing. Therefore, the tissue specific penetrance of the *Wars2*-V117L allele must be due to an alternate mechanism *in vivo*.

There were, however, differences between the effect of the *Wars2*-V117L allele on exon-skipping *in vitro* and *in vivo.* In *Wars2*$^{V117L/V117L}$ MEFs, the ratio of *Wars2*-FL : *Wars2*-total mRNA was 0.43 compared to 0.24 - 0.30 in *Wars2*$^{V117L/V117L}$ tissues. This shows that the *Wars2*-V117L allele caused increased exon-skipping *in vivo* rather than *in vitro.* MEFs were cultured from mouse embryos. The differences in the effect of the *Wars2*-V117L allele observed *in vitro* and *in vivo* may therefore represent differences in the regulation of mRNA splicing during development compared to mature, post-mitotic tissues. Several examples of differential regulation of splicing during development have been documented. Barberan-

Soler *et al*, showed that there was an over 4-fold change in alternate splicing of 18% of 352 confirmed alternate exons in *C. elegans* during development from embryo to adult. They went on to show that one of the most developmentally regulated alternatively spliced genes was in fact the alternative splicing factor *hrpf-1* (Barberan-Soler & Zahler, 2008). Kalsotra *et al* made similar observations within the context of heart development in mouse. They showed that during mouse embryonic heart development, 63 alternative splicing events were coordinated in distinct temporal patterns. They went on to show that CUGBP and ETR-3-like factors (CELF) binding motifs were enriched in alternatively spliced transcripts introns and that CELF proteins were over 10-fold down-regulated during heart development. These data showed that the differential regulation of CELF proteins determined splicing transitions of a subset of alternatively spliced transcripts during mouse embryonic heart development (Kalsotra et al., 2008). It is possible therefore that differential regulation of mRNA splicing during development explains the reduced exon-skipping observed in *Wars2*$^{V117L/V117L}$ MEFs. Consistent with this hypothesis is the observation that the reduced adiposity and sensorineural hearing loss phenotypes observed in *Wars2*$^{V117L/V117L}$ were progressive with age in adult mice with no evidence to show that the *Wars2*-V117L allele impairs embryonic development in these mice. Differential regulation of *Wars2* mRNA splicing in development may therefore explain the adult onset phenotypes observed in *Wars2*$^{V117L/V117L}$ mice.

In conclusion, the *Wars2*-V117L ENU-induced mutation does disrupt *Wars2* mRNA splicing by increasing exon-skipping events. Quantification of this shows that in *Wars2*$^{V117L/V117L}$ cells and tissues, *Wars2*-FL mRNA levels are over 50% reduced. This also indicated that the *Wars2*-V117L allele in its homozygous state causes a greater reduction in *Wars2*-FL mRNA than the *Wars2*-KO allele in its heterozygous state. The *Wars2*-KO allele is haploinsufficient in mice. Our data further suggests that *Wars2* function must be reduced by over 50% to be associated with disease pathology in mice. This is not even taking into account the potential

additional deleterious effects of the mt-TrpRS valine 117 leucine amino acid change. This is will be discussed in the next section.

4.3.2 Does the *Wars2*-V117L allele cause reduced levels of mt-TrpRS?

In order to quantify steady state mt-TrpRS protein levels, a custom-made mt-TrpRS antibody was made and validated. Mt-TrpRS steady state protein levels were significantly reduced in *Wars2*$^{V117L/V117L}$ heart, liver and kidney compared to *Wars2*$^{+/+}$ consistent with the hypothesis that the *Wars2*-V117L allele causes reduced *Wars2*-FL mRNA resulting in reduced mt-TrpRS steady state protein levels. However, the reduction in mt-TrpRS observed in *Wars2*$^{V117L/V117L}$ heart, liver and kidney was greater than the reduction in *Wars2*-FL mRNA also observed in these tissues. This suggests that the reductions in mt-TrpRS protein observed in *Wars2*$^{V117L/V117L}$ heart, liver and kidney are not only caused by reduced *Wars2*-FL mRNA. EASE-MM *in silico* analysis predicted that the mt-TrpRS valine 117 leucine amino acid change would be destabilising. The fact that almost undetectable levels of mt-TrpRS protein were observed in *Wars2*$^{V117L/V117L}$ heart, liver and kidney supports EASE-MM predictions that the valine to leucine amino acid change may also contribute to reduced mt-TrpRS steady state protein levels by reducing the stability or half-life of mt-TrpRS protein in these tissues. That being said, it was possible to immunoprecipitation of mt-TrpRS protein in *Wars2*$^{V117L/V117L}$ liver samples which showed that mt-TrpRS protein is present in *Wars2*$^{V117L/V117L}$ liver, all be it at low levels.

Furthermore, mt-TrpRS steady state protein levels were increased in *Wars2*$^{V117L/V117L}$ skeletal muscle compared to *Wars2*$^{+/+}$ controls. This was unexpected as *Wars2*-FL mRNA was significantly reduced in *Wars2*$^{V117L/V117L}$ skeletal muscle samples. There are two explanations for this observations. The first is that there is an alternate mt-TrpRS isoform expressed in skeletal muscle that is translated from an alternate *Wars2* transcript that does not include the ascribed Wars2-Exon2/Exon3 boundary. This would explain why there is

reduced levels of '*Wars2*-FL' mRNA transcript as this may not be the primary protein coding transcript in skeletal muscle. In order to test this hypothesis, further work must be done such as Northern blot analysis to determine whether there are alternate *Wars2* mRNA transcripts in skeletal muscle or WB blot analysis using a high percentage polyacrylamide gel in order to determine whether the skeletal muscle mt-TrpRS protein band is different in size to that observed in other tissues. The second explanation for this abnormal result is that in skeletal muscle, steady state mtRS protein levels are not dependent upon *Wars2* mRNA gene expression but are instead regulated at a post-translational level. To my knowledge there is no evidence within the literature that mtRS proteins are post-translationally regulated. However, there is evidence that mitochondrial proteins are regulated post-translationally through phosphorylation and acetylation events. For example it has been shown that, the steady state protein levels and activities of OXPHOS subunits NDUFA9, CII SDHA, ATP5A can be regulated through NAD^+-dependant de-acetylation by SIRT3 in mitochondria (Ahn et al., 2008; Finley et al., 2011; Kendrick et al., 2011). Furthermore, large-scale mass-spectrometry based post-translational modification studies have identified multiple phosphorylation and acetylation post-translational events in multiple proteins required for mitochondrial translation particularly mitochondrial ribosomal proteins indicating that mitochondrial translation is post-translationally regulated (Emine C Koc & Koc, 2012). It is possible therefore that mt-TrpRS is post-translationally regulated in *Wars2*$^{V117L/V117L}$ skeletal muscle resulting in increased mt-TrpRS stability or activity, which would explain the increased steady state levels observed in *Wars2*$^{V117L/V117L}$ skeletal muscle. Again further work must be performed to determine whether this is the case such as mass spectrometry analysis to identify skeletal muscle specific mt-TrpRS post-translational modifications or binding partners. Although this results requires further clarification, it does provide an explanation for why no OXPHOS deficiencies or abnormal pathology were observed in the skeletal muscle of *Wars2*$^{V117L/V117L}$ mice.

In summary, the *Wars2*-V117L allele causes tissue specific differences in mt-TrpRS steady state protein levels. mt-TrpRS protein levels were reduced in *Wars2*$^{V117L/V117L}$ heart, liver and kidney. These reductions in mt-TrpRS were not only due to reduced *Wars2*-FL mRNA but may also be due to reduced mt-TrpRS stability due to the valine 117 leucine amino acid substitution. Mt-TrpRS protein levels were increased in skeletal muscle despite reduced *Wars2*-FL mRNA levels indicating that there is either a skeletal muscle specific mt-TrpRS isoform or that mt-TrpRS may be post-translationally regulated in skeletal muscle.

4.3.3 Does the *Wars2*-V117L allele cause inhibition of mitochondrial translation?

The mitochondrial OXPHOS pathway is made up 5 complexes: CI (NADH dehydrogenase-CoQ reductase), CII (succinate dehydrogenase), CIII (ubiquinone-Cyt c oxidoreductase), CIV (Cytochrome C Oxidase) and complex V (ATP synthase). CI, CIII, CIV and CV are made up of multiple subunits encoded by nDNA and mtDNA. CII is assembled from 4 sub-units that are all encoded by nDNA. Mutations that inhibit mitochondrial translation can cause combined deficiencies in CI, CIII, CIV and CV whilst CII remains unaffected. The abundance of tryptophan in mtDNA encoded OXPHOS subunits are summarized in **Table 4.4**.

OXPHOS Complex	Gene	Total Trp	Trp (%)
CI	mtND1	9	2.8
	mtND2	8	2.3
	mtND3	4	3.5
	mtND4	13	2.8
	mtND4L	0	0.0
	mtND5	13	2.1
	mtND6	5	2.9
CIII	mtCytB	11	2.9
CIV	mtCOI	17	3.3
	mtCOII	5	2.2
	mtCOIII	12	4.6
CV	mtATP6	3	1.3
	mtATP8	3	4.5

Table 4.4 – Summary of the total number of tryptophan molecules encoded by mtDNA encoded OXPHOS subunits.

Tryptophan is required for 12 out of 13 of mtDNA encoded OXPHOS subunits; the exception is the CI subunit mtND4L that does not contain tryptophan. Therefore, we hypothesized that in *Wars2*$^{V117L/V117L}$ heart, liver and kidney, where reduced mt-TrpRS steady state protein levels had been observed; would have combined CI, CIII, CIV and CV subunit deficiencies due to inhibition of mitochondrial translation.

In order to indirectly assess mitochondrial translation *in vivo*, the steady state protein levels of mitochondrial OXPHOS subunits were quantified by immunoblot analysis. Tissue specific OXPHOS deficiencies were observed in *Wars2*$^{V117L/V117L}$ mice. CI and CIV subunit levels were substantially reduced in *Wars2*$^{V117L/V117L}$ heart and liver relative to *Wars2*$^{+/+}$ consistent with reduced mt-TrpRS protein observed in these tissues and inhibition of mitochondrial translation. The mitochondrial genome does not encode any protein subunits of CII. Inhibition of mitochondrial translation does not therefore cause CII deficiencies. No significant differences in the steady state protein levels of the CII subunit SDHA were observed in *Wars2*$^{V117L/V117L}$ heart or liver as predicted and consistent with inhibition of mitochondrial translation. No significant differences in the CIII or CV subunits measured in *Wars2*$^{V117L/V117L}$ heart or liver were observed compared to *Wars2*$^{+/+}$ controls. In this study, UQCRC2 and ATP5A subunits were quantified as markers of CIII and CV complex assembly. These subunits are not encoded by the mitochondrial genome and are not directly regulated by mitochondrial translation. However, inhibition of mitochondrial translation has been shown to cause reductions in CIII and CV assembly resulting in degradation of the UQCRC2 and ATP5A subunits respectively. No significant differences in CIII or CV subunits were observed in *Wars2*$^{V117L/V117L}$ heart and liver relative to *Wars2*$^{+/+}$ indicating that CIII and CV assembly is conserved in these tissues. Overall, these data show that reduced mt-TrpRS protein causes CI and CIV deficiencies in the heart and liver of in *Wars2*$^{V117L/V117L}$ mice which is likely explained by inhibition of mitochondrial translation.

In *Wars2*$^{V117L/V117L}$ kidney, mt-TrpRS protein levels were substantially reduced. Despite this only mild reductions in OXPHOS subunits were observed. No significant differences in CI, CII, CIII and CV were observed in *Wars2*$^{V117L/V117L}$ kidney relative to *Wars2*$^{+/+}$. CIV was significantly reduced in *Wars2*$^{V117L/V117L}$ kidney relative to *Wars2*$^{+/+}$. There are two potential explanations for this result. The first is that the rate of mitochondrial translation is low in kidney tissue and that the reduction in mt-TrpRS protein levels are not rate limiting in *Wars2*$^{V117L/V117L}$ kidney but are rate limiting in other tissues such as liver or heart. The second explanation is that there are cell-type specific OXPHOS deficiencies in kidney tissue. There are several different functional structures within the kidney including glomeruli, proximal tubules, distal tubules and collecting ducts, each containing several different cells types. For example, glomeruli are comprised of pariental epithelial cells, podocytes, glycocalyx-coated fenestrated endothelial cells and mesangial cells and collecting ducts are comprised of principal cells and intercalated cells. Given the varied function and cell-type composition of these function structures it is possible that there are OXPHOS deficiencies in certain cell-types within *Wars2*$^{V117L/V117L}$ kidneys and it was not possible to detect these deficiencies by western blot analysis using whole kidney lysates. In order to address this future, COX/SDH staining of kidney sections would enable the identification of COX negative cell types within the kidney of *Wars2*$^{V117L/V117L}$ mice which could then facilitate follow-up analysis to identify phenotypes associated with cell-type specific kidney dysfunction(s).

In *Wars2*$^{V117L/V117L}$ skeletal muscle no OXPHOS deficiencies were observed. In fact, there was a trend for increased CI and CIV OXPHOS subunit steady state protein levels in *Wars2*$^{V117L/V117L}$ skeletal muscle compared to *Wars2*$^{+/+}$. CIII subunit protein levels were significantly increased in *Wars2*$^{V117L/V117L}$ skeletal muscle relative to *Wars2*$^{+/+}$. These observations are consistent with the increase in mt-TrpRS steady state protein levels also observed in *Wars2*$^{V117L/V117L}$ skeletal muscle and suggest that mitochondrial translation is

not inhibited in skeletal muscle because mt-TrpRS protein levels are above wild-type levels. However, given the trend for increased OXPHOS subunit levels in *Wars2*$^{V117L/V117L}$ skeletal muscle it is possible that mitochondrial biogenesis may be up-regulated. Similar observations have been made in patients with mtRS mutations. For instance, Coughlin *et al* identified a patient with *CARS2* mutations associated with epileptic encephalopathy and complex movement disorder. In this patient, CI, CII and CIV OXPHOS deficiencies were observed in patient liver homogenates. However, mtDNA : nDNA copy number was 3-fold increased in patient skeletal muscle and no significant differences in OXPHOS complex activities were observed in skeletal muscle homogenates (Coughlin et al., 2015). It is possible that up-regulation of mitochondrial biogenesis in *Wars2*$^{V117L/V117L}$ skeletal muscle may explain the trend for increased OXPHOS subunit levels.

There was also evidence of up-regulation of mitochondrial biogenesis in *Wars2*$^{V117L/V117L}$ MEFs. In *Wars2*$^{V117L/V117L}$ MEFs, no significant differences in mitochondrial translation or OXPHOS steady state protein levels were observed despite reductions in *Wars2*-FL mRNA. It is not uncommon for mtRS mutations to cause tissue specific OXPHOS deficiencies *in vivo* but not *in vitro*. For example, Gotz *et al* identified 3 patients with *AARS2* mutations associated with hypertrophic cardiomyopathy. Mitochondrial translation assays were performed using cultured primary myoblasts, fibroblasts and myotubules from the *AARS2* mutant patients and showed no evidence of mitochondrial translation defects. By comparison tissue biopsies from the same patients showed tissue specific OXPHOS deficiencies *in vivo*. Steady state protein levels of CI and CIV subunits were undetectable in the mutant *AARS2* patient heart biopsies. Partial CIV deficiencies were observed in patient brain and skeletal muscle biopsies but OXPHOS subunit levels were normal in patient liver biopsies (Götz et al., 2011). Not only were OXPHOS steady state protein levels normal in *Wars2*$^{V117L/V117L}$ MEFs but mitochondrial OXPHOS function was in fact increased. Subsequent analysis showed that the increase in mitochondrial function in *Wars2*$^{V117L/V117L}$ was due to increased mitochondrial mass and up-regulation of mitochondrial biogenesis as

shown by up-regulation of *Pgc1α* mRNA. It is possible therefore that, like in *Wars2*$^{V117L/V117L}$ MEFs, up-regulation of mitochondrial biogenesis protects skeletal muscle and possibly other tissues from OXPHOS deficiency in *Wars2*$^{V117L/V117L}$ mice.

In summary the *Wars2*-V117L allele does cause tissue specific OXPHOS deficiencies *in vivo* which are likely explained by inhibition of mitochondrial translation. mt-TrpRS protein levels were reduced, to variable degrees, in all tissues where OXPHOS deficiencies were observed. CI and CIV deficiencies were observed in *Wars2*$^{V117L/V117L}$ heart and liver and mild reductions in CIV were observed in *Wars2*$^{V117L/V117L}$ kidney. Future work will aim to determine whether there are cell-type specific OXPHOS deficiencies in the kidney which may provide an explanation why only modest reductions were observed in whole-kidney homogenates. By contrast there was no evidence that the *Wars2*-V117L allele causes OXPHOS deficiencies or inhibition of mitochondrial translation in *Wars2*$^{V117L/V117L}$ skeletal muscle. This is explained by the fact that there is no reduction in mt-TrpRS protein in *Wars2*$^{V117L/V117L}$ skeletal muscle despite reduced '*Wars2*-FL' mRNA. Future work is required to clarify whether there is an alternate mt-TrpRS isoform in skeletal muscle which would explain the presence of mt-TrpRS protein despite reduced levels of Wars2-FL mRNA. In *Wars2*$^{V117L/V117L}$ MEFs there was evidence to suggest that up-regulation of mitochondrial biogenesis prevented OXPHOS deficiencies. It is possible that tissue specific differences in the regulation of mitochondrial biogenesis *in vivo* may also explain the tissue-specific penetrance of the *Wars2*-V117L allele. This hypothesis was explored in the next results chapter.

5 Tissue specific mechanisms

5.1 Introduction

5.1.1 The Integrated Stress Response and Mitochondrial Dysfunction

The integrated stress response is activated upon phosphorylation of eukaryotic translation initiation factor 2A (eIF2A) due to cellular stresses. The primary action of the ISR is inhibition of cytoplasmic protein translation. As a consequence of inhibition of cytoplasmic protein translation there is reduced cap-dependent protein translation and preferential translation of specific transcription factors including activating transcription factor 4 (ATF4) which have alternate open reading frames in their 5'UTR (Lu, Harding, & Ron, 2004). ATF4 transcriptionally regulates a range of stress response genes to, in collaboration with reduced rates of cytoplasmic protein synthesis, attenuate cellular stresses and restore normal cell function. ATF4 transcriptionally regulates a wide range of genes including but by no means limited to: *CHOP*, *GADD34*, *ATF3*, *BIP* and *TRIB3* (Quirós, Mottis, & Auwerx, 2016).

There are four known eIF2A-kinases that phosphorylate eIF2a upon sensing different cellular stresses: PKR-like ER kinase (PERK - *EIF2AK3*) activates the ISR upon sensing disrupted proteostasis in the endoplasmic reticulum (UPR^{er}); general control nonderepressible 2 (GCN2 – *EIF2AK4*) activates the ISR upon sensing cytoplasmic amino acid deficiency; double stranded RNA-activated protein kinase (PKR – *EIF2AK2*) senses double-stranded RNA upon viral infection activating the ISR; heme-regulated inhibitor (HRI – *EIF2AK1*) activates the ISR upon sensing cytoplasmic heme deficiencies (**Figure 5.1**).

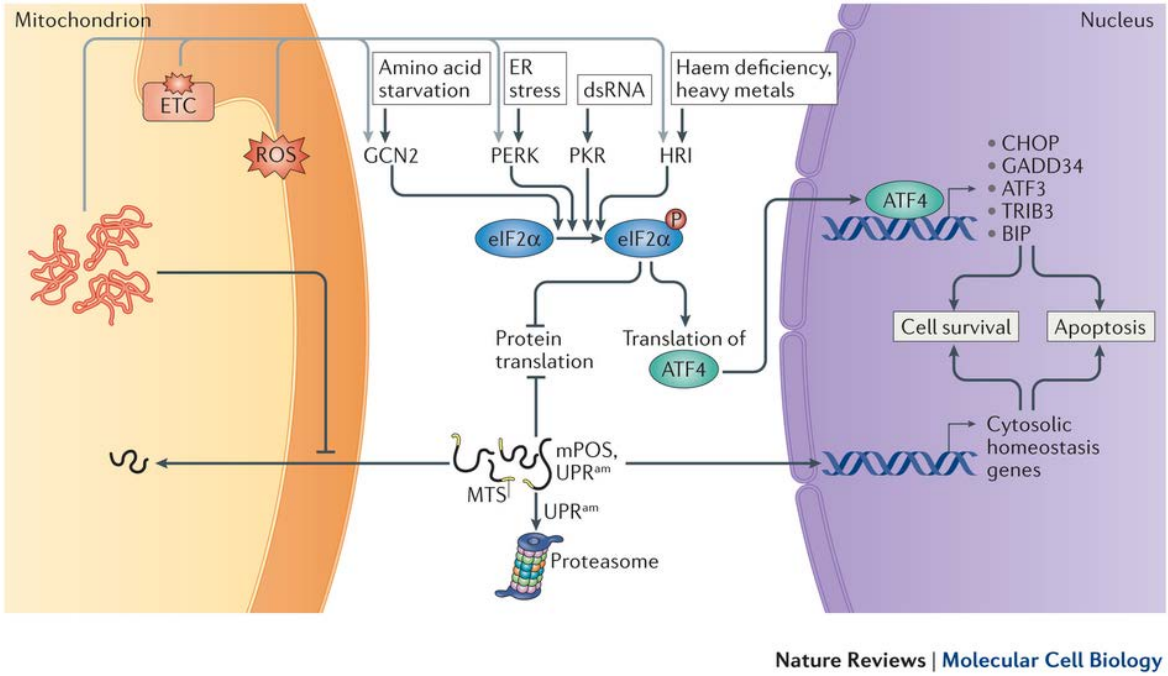

Figure 5.1 – Activation of the integrated stress response.
Figure from (Quirós et al., 2016).

Although the four known eIF2A-kinases have primarily been characterised in association with the aforementioned cellular stresses, there is evidence within the literature that mitochondrial stresses such as disrupted mitochondrial proteostasis (mitochondrial unfolded protein response (UPR^{mt})), oxidative stress / ROS production and mitochondrial OXPHOS dysfunction / inhibition of mitochondrial translation can also activate the ISR.

In 2012 Kim *et al* demonstrated that autophagy deficiency caused ATF4 activation in mice. They went on to show ATF4 activation in autophagy deficient mice is dependent upon mitochondrial OXPHOS deficiency and results in transcriptional up-regulation of FGF21 in mouse skeletal muscle (Kim et al., 2013). Kim *et al* did not determine which of the four eIF2A-kinases activated the ISR in this context but they do show that *Fgf21* is transcriptionally regulated by ATF4. This possibly explains how plasma FGF21 is a biomarker of mitochondrial disorders in humans (Davis et al., 2013).

In 2012, Baker *et al* showed that mitochondrial ROS production caused GCN2 dependant phosphorylation of eIF2a in *C. elegans*. In this study *clk-1(qm30)* mutant *C. elegans* were used. *clk-1* (mammalian homolog – *COQ7*) encodes a mitochondrial protein required for ubiquinone synthesis and acts as a lipid antioxidant throughout the cell and an electron transporter within the electron transport chain. *clk-1(qm30)* worms display reduced respiration and impaired development. Baker *et al* identified two complementary, but independent, pathways activated in *clk-1(qm30)* worms due to mitochondrial stress. These were induction of mitochondrial chaperone proteins through ATFS-1 and inhibition of global protein translation due to phosphorylation of eIF2a. *clk-1(qm30)* worms had increased p-eIF2a levels compared to wildtype controls. Phosphorylation of eIF2a was ameliorated upon RNAi knockdown of GCN2 in *clk-1(qm30)* worms. They then crossed *gcn-2*-deletion worms *(gcn-2(ok871))* with *clk-1(qm30)* worms showing that *gcn-2(ok871);clk-1(qm30)* worms had further reduced oxygen consumption and increased oxidative damage compared to *clk-1(qm30)* worms indicating that *gcn-2* promotes mitochondrial function in response to mitochondrial stress. Finally, they treated *clk-1(qm30)* worms with the mitochondrial ROS scavenger ascorbate showing that, like *gcn-2* knockdown, ascorbate treatment ameliorated eIF2a phosphorylation. Overall they showed that mitochondrial oxidative stress activates the ISR in *clk-1(qm30)* worms dependent upon *gcn-2*.

Michel *et al* showed that in mammalian cells inhibition of mitochondrial translation can activate the ISR dependent upon GCN2. In this study they inhibited mitochondrial translation in Hep3B cells through doxycycline-treatment treatment. Doxycycline-treatment caused OXPHOS deficiencies and GCN2-dependant activation of the ISR independent of the UPR^{mt} in Hep3B cells. Overall they showed that in mammalian cells inhibition of mitochondrial translation can activate the ISR dependent upon GCN2.

There is also evidence to suggest that the UPR^{mt} can activate the ISR through PKR. Rath *et al* showed that activation of the UPR^{mt}, through transfection of truncated ornithine

transcarbamylase, triggered phosphorylation of eIF2a and cJun dependent upon PKR recruitment in intestinal epithelial cells. In this paper they demonstrated that upon UPR^{mt} induction, PKR mRNA and protein expression were increased and that PKR coimmunoprecipitated with eIF2a showing direct interaction (Rath, Balzola, Bernstein, Ho, & Russell, 2012).

Differing models have been presented demonstrating that the ISR can be activated by different mitochondrial stresses including oxidative stress, inhibition of mitochondrial translation and mitochondrial proteolytic stress. There is also evidence to suggest that different eIF2a-kinases sense different mitochondrial stresses to activate the ISR.

5.1.2 *Dars2*-KO mouse model

More recently and most relevant to this study, Dogan *et al* published data characterizing a heart and skeletal-muscle specific *Dars2* knock-out mouse model and presented evidence that disrupted mitochondrial proteostasis / UPR^{mt}, rather than OXPHOS dysfunction or mitochondrial translation inhibition, lead to activation of the ISR in *Dars2*-KO heart. *Dars2* encodes mitochondrial aspartyl-tRNA synthetase (mt-AspRS). In this study they generated a tissue specific *Dars2* knockout mouse by crossing *Dars2*$^{loxp/loxp}$ mice with mice expressing cre-recombinase under the muscle creatine kinase promotor (Ckmm-cre). The resultant *Dars2*$^{loxP/loxP,+/Ckmm\text{-}cre}$ mice (*Dars2*-KO) had complete loss of *Dars2* / mt-AspRS activity in heart and muscle by 6 weeks of age resulting in OXPHOS deficiencies in both heart and muscle at the same time point. Phenotypically the *Dars2*-KO mice developed cardiomyopathy and had reduced maximal life-span. *Dars2*-KO mice died at to 6-7 weeks of age due to severe hypertrophic cardiomyopathy. Additional phenotypes included reduced adiposity and changes in circulating metabolite levels including lower blood glucose and increased circulating free fatty acids. In this study Dogan *et al*, made several intriguing observations. Specifically, in the heart, they showed that *Dars2* knock-out resulted in up-regulation of mitochondrial biogenesis, activation of the mitochondrial

unfolded protein response (UPR^{mt}), reduced autophagy and activation of genes associated with the integrated stress response at 6 weeks of age. They then performed the same analysis at 1 and 3 weeks of age where OXPHOS deficiencies were either not observed or were mildly reduced respectively. At 3 weeks of age, mild CIV subunit deficiencies were observed in *Dars2*-KO heart. At the same time point they showed up-regulation of UPR^{mt} proteins, mild up-regulation of PGC1a, autophagy inhibition and transcriptional changes associated with activation of the ISR such as increased *Atf4*, *Atf5*, *Chop* and *Fgf21* mRNA levels. Finally, at 1 week of age they showed that *Atf5* and *Fgf21* were transcriptionally up-regulated despite no OXPHOS deficiencies being observed. Furthermore, at 1 week of age no changes in PGC1a, UPR^{mt} proteins or autophagy markers were observed. Dogan *et al* concluded that inhibition of mitochondrial translation caused disrupted mitochondrial proteostasis and that proteostatic stress, rather than OXPHOS deficiency, was the primary stimulus responsible for activating down-stream signalling pathways through *Atf4*, and Chop such as: increased mitochondrial biogenesis, autophagy inhibition, UPR^{mt} activation and systemic metabolic changes caused by *Fgf21* up-regulation. It is worth noting at this point that whilst Dogan *et al* show transcriptional up-regulation of genes associated with the ISR such as *Atf4*, *Atf5* and *Chop*, they did not show the primary marker of activation of the ISR namely the phosphorylation status of eIF2a or ATF4 protein levels **(Figure 5.2)** (Dogan et al., 2014).

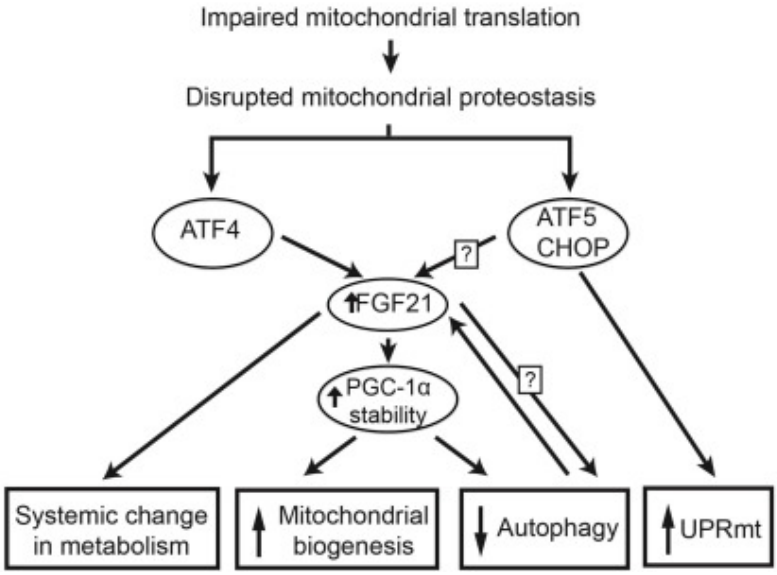

Figure 5.2 - Proposed model for the heart-mediated stress responses to perturbed protein homeostasis caused by DARS2 deficiency.
(Dogan et al., 2014)

5.1.3 Chapter Aims

In this chapter we characterised the tissue specific mechanisms activated in the *Wars2*$^{V117L/V117L}$ mice. To do this we performed a comparative study of the *Wars2*$^{V117L/V117L}$ mouse model and the *Dars2*-KO mouse model. We focused on three main pathways that were reported to be dysregulated in the *Dars2*-KO mouse model:

1. The integrated stress response
2. PGC1a / mitochondrial biogenesis
3. Autophagy

In each case we asked two questions. Do we observe the same mechanistic changes in the *Wars2*$^{V117L/V117L}$ mice as reported in *Dars2*-KO mice? Are these pathways differentially regulated in a tissue specific manner in *Wars2*$^{V117L/V117L}$ mice? Our overall aim was to mechanistically explain the tissue specific penetrance and pathology associated with the *Wars2*-V117L allele in *Wars2*$^{V117L/V117L}$ mice.

5.2 Results

5.2.1 The integrated stress response & FGF21

5.2.1.1 Tissue specific activation of the ISR

Currently there is evidence within the literature that mitochondrial stresses such as ROS production, OXPHOS deficiency and the UPR^{mt}, can lead to activation of the ISR *in vivo*. Based on these observations we sought to determine whether the *Wars2*-V117L ENU-induced mutation activates the ISR in *Wars2*$^{V117L/V117L}$ mice. To do this, immunoblot analysis of the steady state levels of phosphorylated eIF2a (p-eIF2a) was performed in *Wars2*$^{V117L/V117L}$ heart, liver, kidney and skeletal muscle at 12 months of age (**Figure 5.3A**). p-eIF2a protein levels were quantified and normalised to (Total) eIF12a (**Figure 5.3B**). At 12 months of age the p-eIF2a levels were approximately 6 and 2 fold increased in *Wars2*$^{V117L/V117L}$ heart and liver respectively compared with *Wars2*$^{+/+}$ littermate controls. There were no differences in p-eIF2a:total-eIF2A levels between *Wars2*$^{V117L/V117L}$ and *Wars2*$^{+/+}$ kidney or skeletal muscle samples at 12 months of age **(Figure 5.3B)**. These data show that the ISR is activated in *Wars2*$^{V117L/V117L}$ heart and liver but not in *Wars2*$^{V117L/V117L}$ kidney or skeletal muscle.

Consistent with this, ATF4 protein levels were on average 4 fold increased in *Wars2*$^{V117L/V117L}$ heart samples compared to *Wars2*$^{+/+}$, indicating increased cap-dependent protein synthesis in *Wars2*$^{V117L/V117L}$ heart **(Figure 5.3C)**. *Atf4* and *Atf5* mRNA levels were significantly elevated in *Wars2*$^{V117L/V117L}$ heart compared to *Wars2*$^{+/+}$ at 12 months of age. *Atf4* and *Atf5* mRNA levels were not significantly different in *Wars2*$^{V117L/V117L}$ and *Wars2*$^{+/+}$ liver, kidney or skeletal muscle samples compared to *Wars2*$^{+/+}$ (**Figure 5.3D&E**). *Atf5* mRNA levels were on average higher in *Wars2*$^{V117L/V117L}$ skeletal muscle however this was due to one anomalous result where *Atf5* mRNA levels were 9 fold increased compared to *Wars2*$^{+/+}$ **(Figure 5.3E)**. If this anomalous result was excluded from our analysis, *Atf5* mRNA

expression levels are on average 1.3-fold increased (p=0.088) in *Wars2*$^{V117L/V117L}$ skeletal muscle compared to Wars2$^{+/+}$. Downstream targets of AFT4 such as *Chop*, *Mthfd2* and *Fgf21* (Teske et al, 2013) were on average 1.9, 40.4 and 53.7 fold increased in *Wars2*$^{V117L/V117L}$ heart compared to *Wars2*$^{+/+}$ respectively, further evidence of increased ATF4 activity in the heart **(Figure 5.3F)**.

Taken together these results show that activation of the ISR occurs in *Wars2*$^{V117L/V117L}$ tissues where substantial OXPHOS deficiencies were observed previously such as the heart and, to a lesser extent, the liver. However, in *Wars2*$^{V117L/V117L}$ kidney where only mild reductions in CIV were observed there was no evidence of ISR activation. Equally, there was no evidence that the ISR is activated in Wars2$^{V117L/V117L}$ skeletal muscle again where no OXPHOS subunit deficiencies were observed. Overall these data show that there is tissue-specific activation of the ISR in *Wars2*$^{V117L/V117L}$ mice dependent upon OXPHOS deficiency.

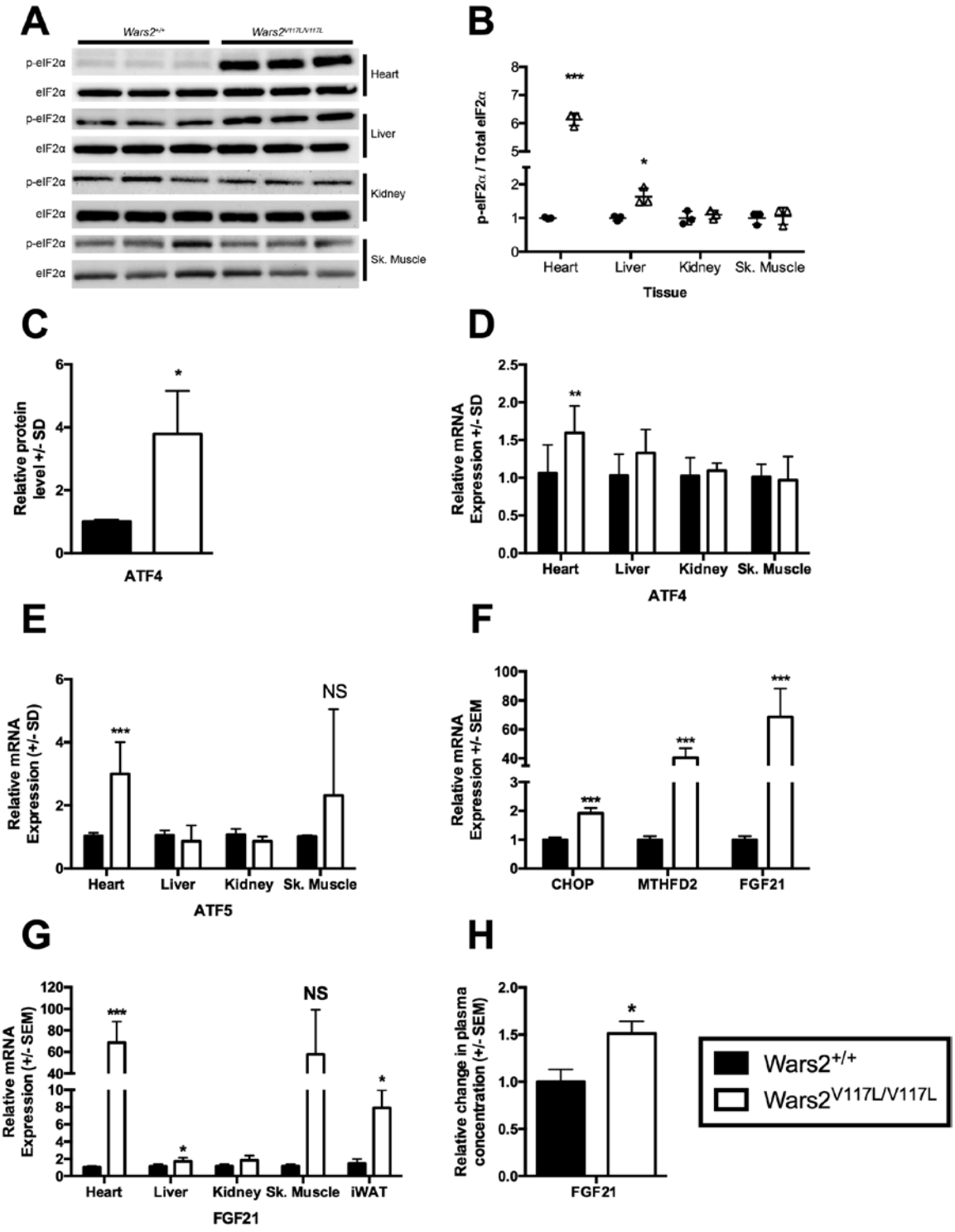

Figure 5.3 – Tissue specific activation of the ISR and FGF21.
A) Immunoblot analysis of p-eIF2A and (Total) eIF2a protein levels in heart, liver, kidney and skeletal muscle at 12 months of age. B) Quantification of p-eIF2a steady state protein levels normalized to (Total) eIF2a at 12 months of age. C) Immunoblot analysis of ATF4 protein levels in heart. Relative mRNA expression levels of D) *Atf4* and E) *Atf5* in heart, liver, kidney and skeletal muscle. F) Relative mRNA expression levels of *Chop*, *Mthfd2* and *Fgf21* in heart. G) Relative mRNA expression levels of *Fgf21* in heart, liver, kidney, skeletal muscle and iWAT. H) Relative FGF21 plasma concentration. Immunoblots (A&B) were quantified using ImageJ and normalized to loading controls. Data in B&C shown as mean ± SD; *Wars2*$^{+/+}$ (n=3) and *Wars2*$^{V117L/V117L}$ (n=3). mRNA gene expression analysis (D – G) data shown as mean 2□ddCT

± SEM; *Wars2*$^{+/+}$ (n=6-8) and *Wars2*$^{V117L/V117L}$ (n=6-8). Plasma FGF21 concentrations (H) shown as mean ± SEM; *Wars2*$^{+/+}$ (n=12) and *Wars2*$^{V117L/V117L}$ (n=12). Analysis shown in A – H was performed using tissues / plasma collected from mice at 12 months of age. Data were analyzed using student's t-test: ***** P<0.05, ****** P<0.01, ******* P<0.001.

5.2.1.2 Tissue specific regulation of FGF21

Dogan *et al* reported increased FGF21 expression in *Dars2*-KO heart and increased plasma FGF21 suggesting that elevated circulating FGF21 is causal for systemic changes in metabolism, reduced body mass and increased glucose tolerance. Similar phenotypic observations were made in *Wars2*$^{V117L/V117L}$ mice as previously mentioned.

In order to determine whether plasma FGF21 was increased in *Wars2*$^{V117L/V117L}$ mice, plasma was collected at 12 months of age and FGF21 ELISA assays were performed. We also observed significantly elevated plasma FGF21 concentrations in *Wars2*$^{V117L/V117L}$ mice compared to *Wars2*$^{+/+}$ **(Figure 5.3H)**. Given that the *Wars2*-V117L allele is not tissue specific we sought to determine whether *Fgf21* is transcriptionally up-regulated in tissues other than the heart. *Fgf21* mRNA expression was on average 68.6, 1.7 and 7.9 fold increased in Heart, Liver and iWAT of *Wars2*$^{V117L/V117L}$ mice at 12 months of age relative to *Wars2*$^{+/+}$. There was a trend for increased *Fgf21* mRNA expression in *Wars2*$^{V117L/V117L}$ skeletal muscle however this was not significant due to high degrees in biological variance ranging from a 2.6 to 344.5-fold increase in *Fgf21* mRNA expression in *Wars2*$^{V117L/V117L}$ skeletal muscle compared to *Wars2*$^{+/+}$. Kidney *Fgf21* mRNA was not significantly different in *Wars2*$^{V117L/V117L}$ and *Wars2*$^{+/+}$ mice **(Figure 5.3G)**.

These data show that tissues other than the heart, such as liver, skeletal muscle and iWAT, also transcriptionally up-regulate Fgf21 mRNA in *Wars2*$^{V117L/V117L}$ mice and that this response is not specific to the heart alone. However, *Fgf21* mRNA is up-regulated most profoundly and most significantly in the *Wars2*$^{V117L/V117L}$ heart compared to other tissues and, taken together with comparable observations from the *Dars2*-KO mouse, suggest that the heart is the primary source of elevated plasma FGF21 in *Wars2*$^{V117L/V117L}$ mice.

5.2.1.3 Activation of the ISR is coincident with OXPHOS deficiency in *Wars2*$^{V117L/V117L}$ heart

In order to better characterize the observed relationship between OXPHOS deficiency and activation of the ISR in *Wars2*$^{V117L/V117L}$ mice, immunoblot analysis of OXPHOS subunits and p-eIF2a:total-eIF2A levels was performed at 1 (**Figure 5.4A**), 3 (**Figure 5.4B**) and 12 (**Figure 5.4C**) months of age in *Wars2*$^{V117L/V117L}$ heart. Mt-TrpRS steady state protein levels were also analysed in all tissues at 1, 3 and 12 months of age and were consistently reduced at each time point in *Wars2*$^{V117L/V117L}$ heart compared to *Wars2*$^{+/+}$ (**Figure 5.4**).

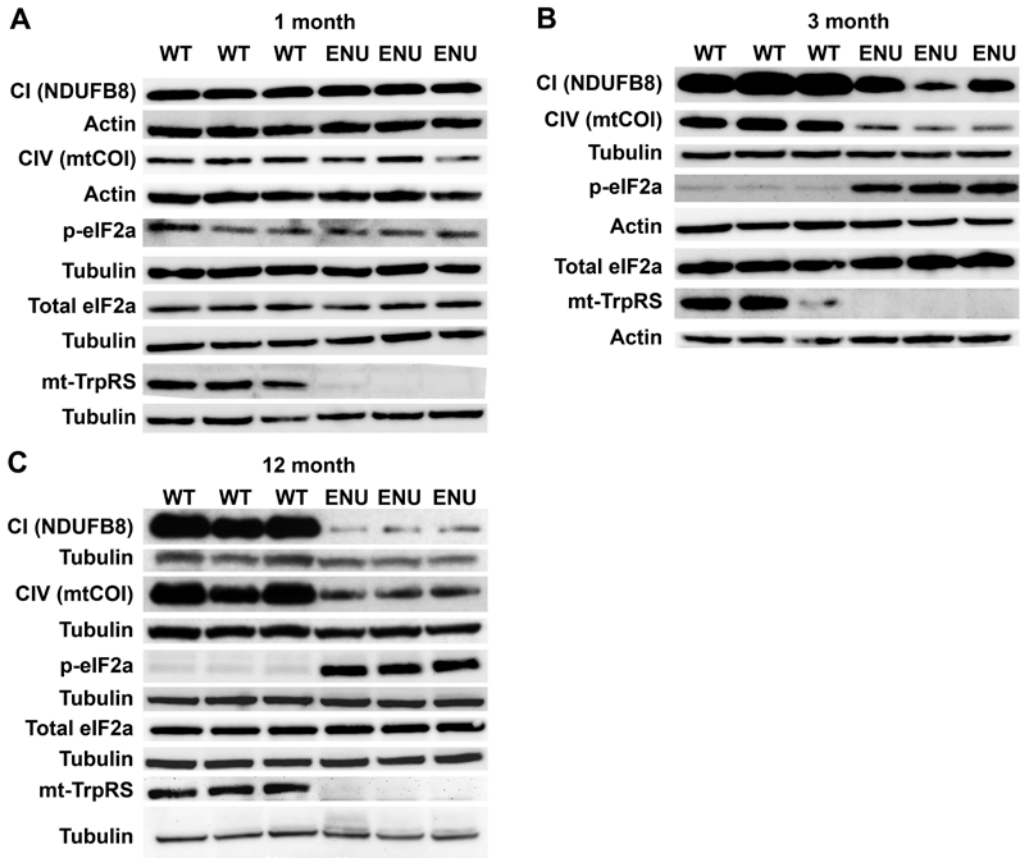

Figure 5.4 – Time-course immunoblot analysis of OXPHOS subunits and p-eIF2a steady protein in *Wars2*$^{V117L/V117L}$ heart.
Immunoblot analysis of CI and CIV OXPHOS subunits, p-eIF2a, (total) eIF2a and mt-TrpRS steady state protein levels in heart tissue at A) 1 month of age, B) 3 months of age and C) 12 months of age. WT – *Wars2*$^{+/+}$ (n=3), ENU - *Wars2*$^{V117L/V117L}$ (n=3).

Immunoblots were quantified and analysed using ImageJ (**Figure 5.5**). CI subunit protein levels were significantly decreased at 1 month of age and were on average 15% reduced in *Wars2*$^{V117L/V117L}$ heart samples compared to *Wars2*$^{+/+}$ (**Figure 5.5A)**. CI (NDUFB8) protein

levels were progressively reduced with increased age in *Wars2*$^{V117L/V117L}$ heart samples and were on average 59 and 87 % reduced at 3 and 12 months respectively compared to *Wars2*$^{+/+}$ (**Figure 5.5A**).

At 1 month of age, CIV (mtCOI) protein levels were comparable between *Wars2*$^{V117L/V117L}$ and *Wars2*$^{+/+}$ heart samples (**Figure 5.5B**). CIV (mtCOI) protein levels were on average 69 and 62 % decreased at 3 and 12 months respectively in *Wars2*$^{V117/V117L}$ hearts samples compared to *Wars2*$^{+/+}$ showing no age related progression in CIV deficiency between 3 and 12 months of age **(Figure 5.5B)**. At 1 month of age, p-eIF2a:total-eIF2A were comparable between *Wars2*$^{V117L/V117L}$ and *Wars2*$^{+/+}$ heart samples (**Figure 5.5C**). However, p-eIF2a:total-eIF2A levels were on average 4 and 6 fold increased in *Wars2*$^{V117L/V117L}$ heart samples compared to *Wars2*$^{+/+}$ at 3 and 12 months of age respectively showing that activation of the ISR is progressive with age in *Wars2*$^{V117L/V117L}$ heart **(Figure 5.5B)**.

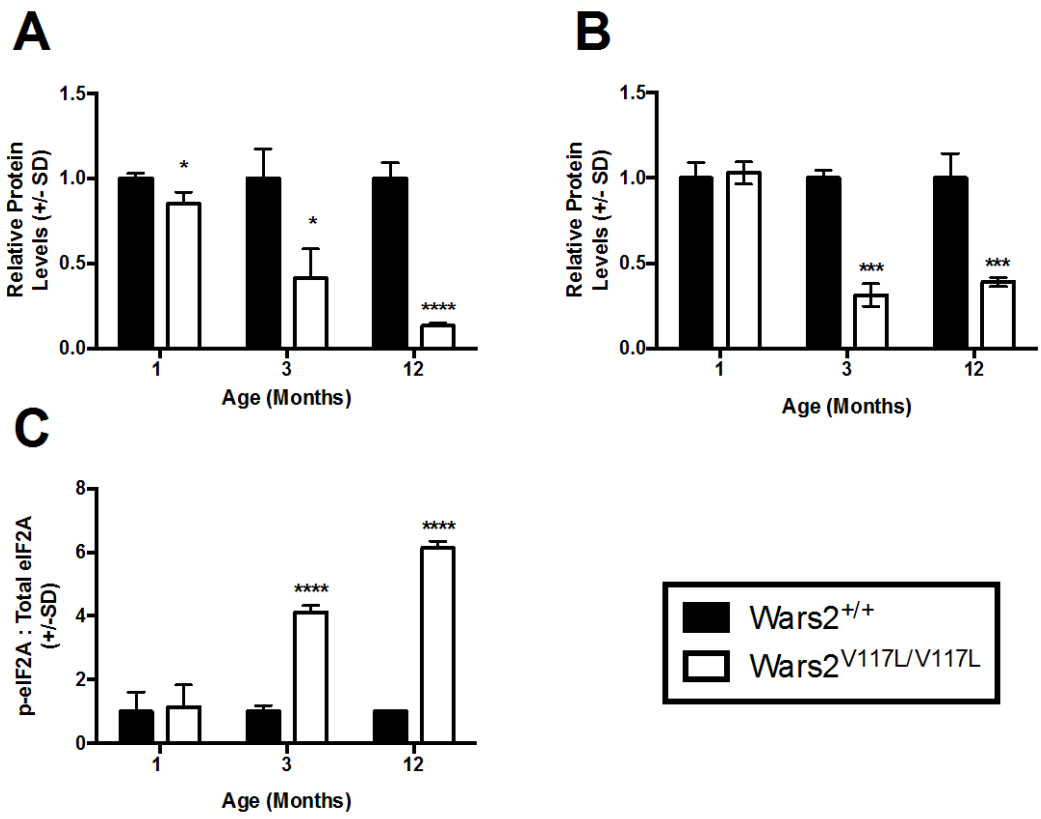

Figure 5.5 – Time line of activation of the ISR and OXPHOS deficiencies in *Wars2*$^{V117L/V117L}$ heart.

Immunoblot analysis of A) NDUFB8 – CI, B) mtCOI – CIV and C) p-eIF2A protein levels at 1, 3 and 12 months of age. Immunoblots were quantified using ImageJ and normalized to loading controls. Data shown as mean ± SD; *Wars2*$^{+/+}$ (n=3) and *Wars2*$^{V117L/V117L}$ (n=3). Data were analyzed using student's t-test: ***** P<0.05, ****** P<0.01, ******* P<0.001.

Taken together these data show two things. Firstly, that CI deficiency occurs prior to activation of the ISR in *Wars2*$^{V117L/V117L}$ heart in contrast with previous data from Dogan *et al*. Secondly, these data show that activation of the ISR is progressive with age and co-incident with progressive CI deficiency.

5.2.1.4 Activation of the ISR is independent of the UPR^{mt} in *Wars2*$^{V117L/V117L}$ heart

The next question we addressed was whether the *Wars2*-V117L ENU-induced mutation causes disrupted mitochondrial proteostasis in the heart leading to activation of the mitochondrial unfolded protein response (UPR^{mt}) as reported by Dogan *et al* in *Dars2*-KO heart. To assess mitochondrial proteostasis the steady state protein levels of two mitochondrial proteases, CLPP and LONP1, and two mitochondrial protein chaperones, HSP60 and HSP70 were quantified by immunoblot analysis at 1, 3 and 12 months of age. There was no difference in the steady state protein levels of LONP1, CLPP, HSP60 or HSP70 in *Wars2*$^{V117L/V117L}$ and *Wars2*$^{+/+}$ heart samples at 1, 3 or 12 months of age **(Figure 5.6A-D)**. The only statistically significant result was a 17% reduction in LONP1 in *Wars2*$^{V117L/V117L}$ heart at 1 month of age. HSP60 protein levels were not measured in the heart at 1 month of age.

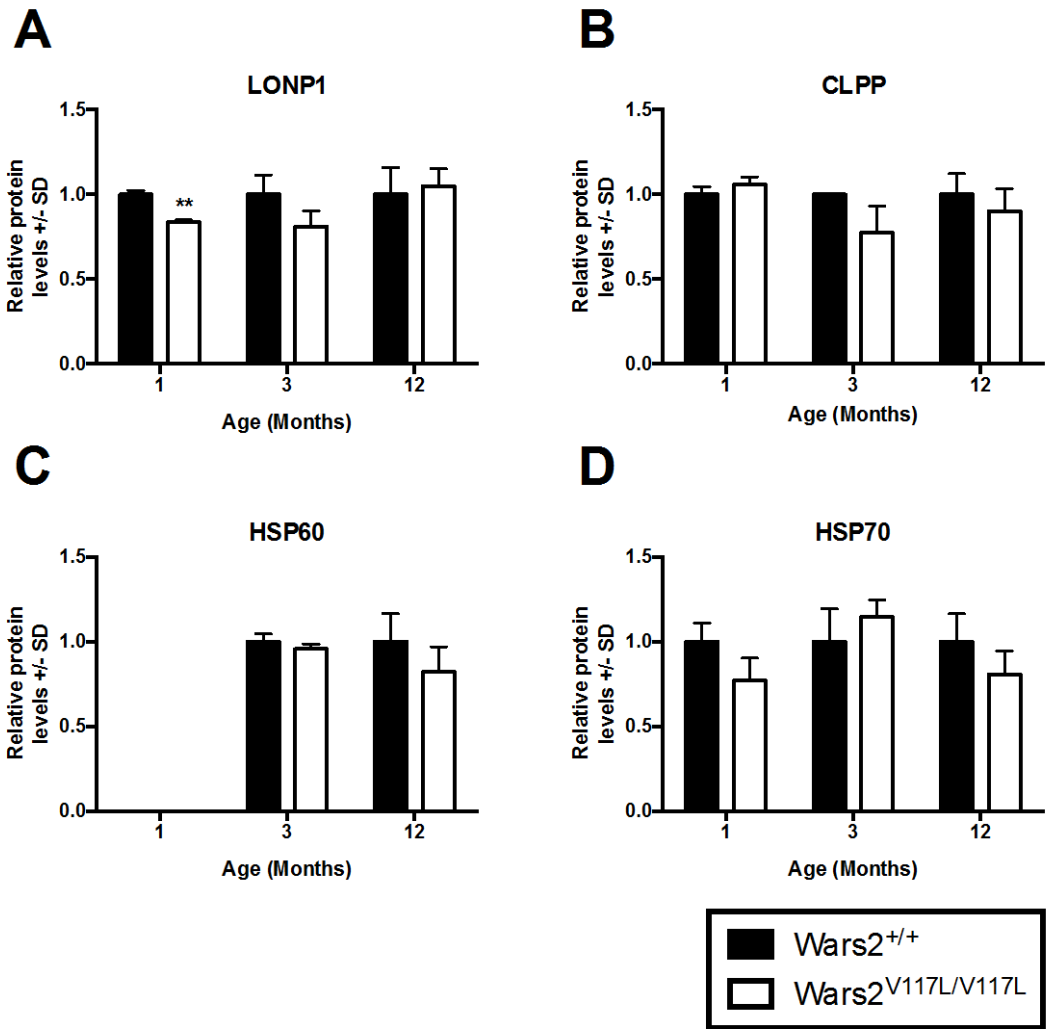

Figure 5.6 – Time line of activation of the UPR^{mt} in *Wars2$^{V117L/V117L}$* heart.
Immunoblot analysis of A) LONP1, B) CLPP, C) HSP60 and D) HSP70 protein levels in heart whole lysates at 1, 3 and 12 months of age. Immunoblots were quantified using ImageJ and normalized to loading controls. Data shown as mean ± SD; *Wars2$^{+/+}$* (n=3) and *Wars2$^{V117L/V117L}$* (n=3). Data were analyzed using student's t-test: ***** P<0.05, ****** P<0.01, ******* P<0.001.

In contrast with data from Dogan *et al*, we show no evidence of up-regulation of mitochondrial protease or chaperone proteins associated with activation of the UPR^{mt} at any time point in the *Wars2$^{V117L/V117L}$* heart. This data shows that in the *Wars2$^{V117L/V117L}$* heart activation of the ISR is independent of the UPR^{mt} and occurs via an alternate mechanism.

5.2.1.5 Activation of the ISR is independent of ER stress and ROS production in *Wars2$^{V117L/V117L}$* heart

Dogan *et al* reported that in their model, activation of the ISR was likely due to disrupted mitochondrial proteostasis. However, in the *Wars2$^{V117/V117L}$* heart we observed progressive

activation of the ISR that this was co-incident with CI deficiency and independent of any measured marker of disrupted proteostasis. This lead us to ask the question: what links inhibition of mitochondrial translation with activation of the ISR?

There are four known eIF2a kinases EIF2AK1 (HRI), EIF2K2 (PKR) EIF2AK3 (PERK) and EIF2AK4 (GCN2). Each of the four-eIF2A kinases sense different cellular stresses: heme deficiency, double stranded RNA, UPR^{er} and amino acid starvation respectively. Upon cellular stress eIF2A kinases autophosphorylate and activate leading to phosphorylation of eIF2A and activation of the ISR. Due to the fact that there are no commercially available antibodies for phosphorylated HRI, PKR or GCN2 in mouse we were unable to assess activation of these eIF2a kinases directly.

PERK has been shown to sense ER stress. ER stress can occur when there is high protein demand, viral infection, heat stress, inflammatory cytokines or accumulation of unfolded proteins in the ER lumen. PERK has also been shown to be required at ER-mitochondrial contact sites to convey apoptosis following ROS mediated ER stress (Verfaillie et al., 2012). Also ROS production has also been linked with mitochondrial dysfunction (C.-H. Wang, Wu, Wu, & Wei, 2013). We therefore hypothesized that in *Wars2*$^{V117/V117L}$ heart the ISR is activated through PERK upon ROS-mediated ER stress as a result of OXPHOS deficiency.

To test this hypothesis, we first looked at PERK activation using an antibody raised to p(T980)-PERK. PERK-T980 is a residue found in the kinase activation loop, the phosphorylation of which is essential for autocatalytic activity of this kinase (Kusio-Kobialka et al., 2012). No band was detected in *Wars2*$^{V117L/V117L}$ or *Wars2*$^{+/+}$ heart using the p(T980)-PERK antibody, potentially indicating that PERK is not activated in either context **(Figure 5.7A)**. However, without a positive control we are unable to confirm this result as this may be a false negative. We also quantified total-PERK showing a trend for increased total PERK in *Wars2*$^{V117L/V117L}$ heart samples compared to *Wars2*$^{+/+}$. The meaning of this result

is unclear as there is no evidence in the literature that up-regulation of PERK is indicative of PERK activation.

As well as PERK there are two more master sensors of ER stress IRE1α and ATF6. Upon ER stress IRE1α dimerizes and autophosphorylates becoming active. Active IRE1α has been shown to splice X-box binding protein 1 (XBP1) mRNA, spliced XBP1 mRNA encodes a transcription factor that upregulates UPR^{er} target genes (Calfon et al., 2002). To measure IRE1α activation total, unspliced and spliced XBP1 mRNA were quantified in *Wars2*$^{V117L/V117L}$ heart samples. There was no significant difference in the amount of spliced-XBP1 mRNA in *Wars2*$^{V117L/V117L}$ and *Wars2*$^{+/+}$ heart samples **(Figure 5.7B)**. Total-X*bp1* and unspliced *Xbp1* mRNA were on average 22 and 21% reduced in *Wars2*$^{V117L/V117L}$ heart samples compared to *Wars2*$^{+/+}$ respectively. These results indicate that there is no difference in IRE1α activity in *Wars2*$^{V117L/V117L}$ heart.

The final ER stress sensor is ATF6α, a type II ER transmembrane transcription factor. Upon ER stress ATF6α (75kDa) transits to the Golgi where is cleaved generating an active 50kDa ATF6α isoform that translocates to the nucleus and transcriptionally regulates UPR^{er} genes (Ye et al., 2000). There was no difference in the levels of cleaved or uncleaved ATF6α in *Wars2*$^{V117L/V117L}$ and *Wars2*$^{+/+}$ heart samples **(Figure 5.7C)**. This is further evidence that there is no dysregulation of ER proteostasis in *Wars2*$^{V117L/V117L}$ heart.

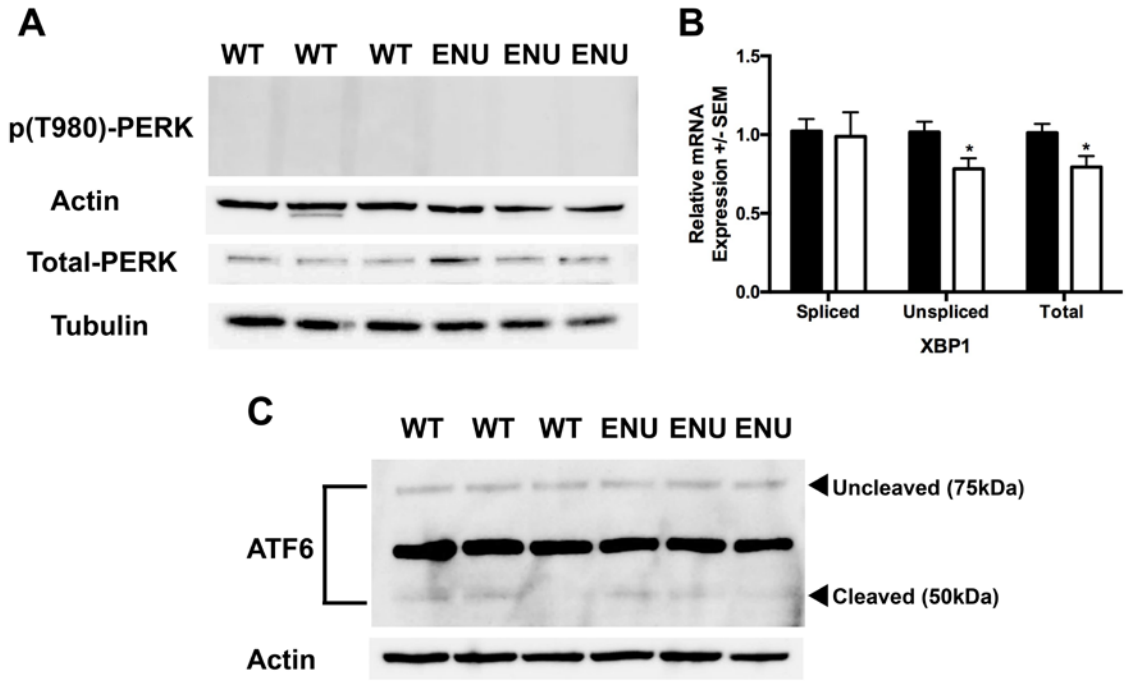

Figure 5.7 – Analysis of ER stress response pathways in *Wars2*$^{V117L/V117L}$ heart.
A) Immunoblot analysis of p(T980)-PERK, total-PERK and actin/tubulin (loading controls) in whole heart lysates. B) Relative mRNA expression analysis of spliced, unspliced and total *Xbp1* in heart. C) Immunoblot analysis of uncleaved & uncleaved ATF6 and actin (loading control) in whole heart lysates. WT = *Wars2*$^{+/+}$, ENU = *Wars2*$^{V117L/V117L}$. mRNA expression analysis(B) data shown as mean 2□ddCT ± SEM; *Wars2*$^{+/+}$ (n=8) and *Wars2*$^{V117L/V117L}$ (n=8). Analysis shown in A - C was performed using tissues collected from mice at 12 months of age. Data were analyzed using student's t-test: ***** P<0.05, ****** P<0.01, ******* P<0.001.

Finally, we assessed ROS production in *Wars2*$^{V117L/V117L}$ heart. Imbalances in ROS production can cause damage to DNA, protein and lipid through non-reversible modifications. In the context of proteins, increased ROS damage can be measured by the presence of carbonyl groups (Berlett & Stadtman, 1997). The OxyBlot system (Chemicon/Millipore) was used to quantify the proportion of proteins modified with carbonyl groups in total *Wars2*$^{V117L/V117L}$ heart lysates. There was no difference in the amount of carbonylated proteins in *Wars2*$^{V117L/V117L}$ heart lysates compared with *Wars2*$^{+/+}$ at 12 months of age **(Figure 5.8A)**. As a second measure of ROS production the steady state levels of mitochondrial superoxide dismutase 2 (SOD2) protein were quantified in heart lysates. SOD2 functions as a mitochondrial ROS scavenger and is up-regulated in response to increased mitochondrial ROS production (Ho & Crapo, 1988). There was no difference in the steady state protein levels of SOD2 in *Wars2*$^{V117L/V117L}$ compared to *Wars2*$^{+/+}$ controls **(Figure 8B)**.

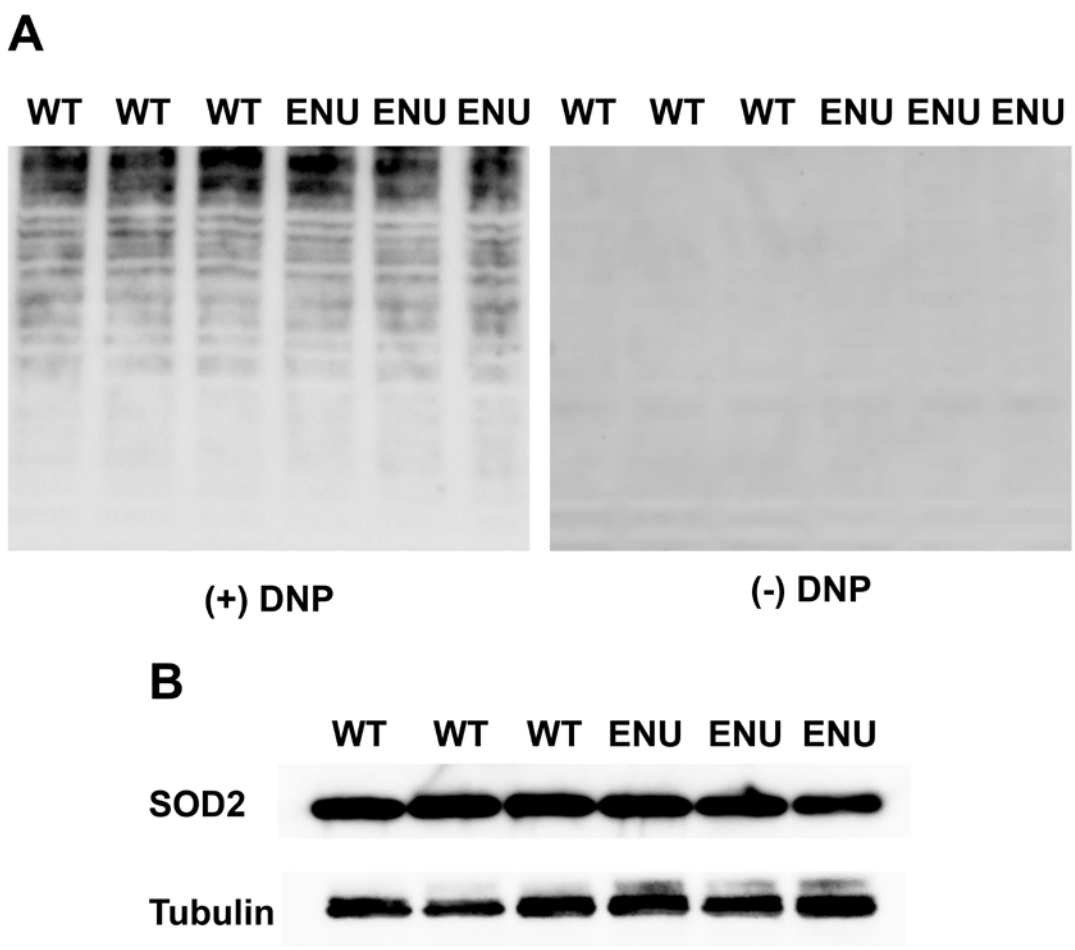

Figure 5.8 – Analysis of oxidative stress in *Wars2*$^{V117L/V117L}$ heart.
A) OxyBLOT analysis of protein carbonylation levels in whole heart lysates. (+) DNP = DNP labeled carbonylated proteins, (-DNP) = non-DNP labeled carbonylated proteins. B) Immunoblot analysis of SOD2 and tubulin (loading control) in whole heart lysates. Analysis shown in A & B was performed using tissues collected from mice at 12 months of age.

Whilst these data do not rule out PERK as the kinase that phosphorylated eIF2a in the *Wars2*$^{V117L/V117L}$ heart, it does rule out disrupted ER proteostasis or increased ROS production as the link between inhibition of mitochondrial translation and activation of the ISR in the *Wars2*$^{V117L/V117L}$ heart. Further work is required to identify the mechanism and eIF2a kinase linking the *Wars2*-V117L allele and activation of the ISR in *Wars2*$^{V117L/V117L}$ heart.

5.2.2 Tissue specific regulation of mitochondrial biogenesis

As stated previously, Dogan *et al* reported that *Dars2* deficiency in the heart causes increased PGC1a stability resulting in up-regulation of mitochondrial biogenesis. Similarly, up-regulation of *Pgc1a* mRNA was observed in *Wars2*$^{V117L/V117L}$ MEFs. Therefore, we examined the effect of the *Wars2*-V117L ENU-induced mutation on the tissue specific regulation of mitochondrial biogenesis in *Wars2*$^{V117L/V117L}$ mice.

5.2.2.1 Regulation of PGC1a in *Wars2*$^{V117L/V117L}$ heart

First of all, regulation of mitochondrial biogenesis was assessed in *Wars2*$^{V117L/V117L}$ heart. To do this we first looked at the steady state protein levels of PGC1a in *Wars2*$^{V117L/V117L}$ heart lysates. The PGC1A predicted size is 92kDa. We did not observe a band at 92kDa in heart samples using two different PGC1a antibodies. However, a band at approximately 70kDa was observed using both PGC1a antibodies. Both of these antibodies were raised in different host species using different epitopes. Based upon this we have concluded that the band observed at 70kDa is likely PGC1a and that it is migrating faster than predicted in

our system. Using both antibodies, the 70kDa PGC1a band was drastically reduced in *Wars2*$^{V117L/V117L}$ heart samples compared to *Wars2*$^{+/+}$ **(Figure 5.9A)**. This result was highly unexpected given that *Dars2* deficiency caused increased PGC1a as reported by Dogan *et al*.

We therefore sought to confirm this result by measuring the mRNA expression of *Pgc1a*, genes known to regulate PGC1a and genes transcriptionally regulated by PGC1a. Firstly there was no difference in the mRNA expression levels of *Pgc1a* in *Wars2*$^{V117L/V117L}$ and *Wars2*$^{+/+}$ heart samples. There was a trend for increased *Pgc1a* mRNA expression levels however this was not statistically significant (p=0.09) **(Figure 5.9B)**. However, *Sirt1* mRNA was 31% reduced in *Wars2*$^{V117L/V117L}$ heart samples compared to *Wars2*$^{+/+}$. SIRT1 has previously been shown to deacetylate PGC1a leading to increased activation and transcriptional activity (Rodgers et al., 2005). Reduced *Sirt1* expression in consistent with reduced PGC1a activity **(Figure 5.9B)**.

PGC1a is a transcriptional coactivator with many down-stream targets including genes involved in mitochondrial biogenesis, such as TFAM, as well as genes involved in fatty acid oxidation regulation, such as *Ppara* (Scarpulla, 2002; Vega, Huss, & Kelly, 2000). *Tfam* mRNA expression levels were on average 31% reduced in *Wars2*$^{V117L/V117L}$ heart compared with *Wars2*$^{+/+}$ consistent with reduced PGC1a activity and reduced mitochondrial biogenesis **(Figure 5.9B)**. This is consistent with previous data shown in chapter 4 where *Wars2*-total mRNA is down-regulated in *Wars2*$^{V117L/V117L}$ heart samples. Furthermore, FAO genes *Ppara*, *Acacb*, *Acadm*, *Acadl*, *Cpt1a* and Cpt1b were all significantly down regulated in *Wars2*$^{V117L/V117L}$ compared to *Wars2*$^{+/+}$ **(Figure 5.9C)**. In contrast with this the expression of *Acaca* that is required for lipogenesis was non-significantly different between samples. Again this data is consistent with reduced PGC1a activity. Finally, mtDNA:nDNA ratio was quantified in *Wars2*$^{V117L/V117L}$ heart. No significant differences in mtDNA:nDNA were observed in *Wars2*$^{V117L/V117L}$ and *Wars2*$^{+/+}$ heart samples. These data indicate that

transcriptional down-regulation of mitochondrial biogenesis in *Wars2*$^{V117L/V117L}$ heart did not cause reduced mitochondrial DNA replication **(Figure 5.9D)**. Taken together these results indicate that the *Wars2*-V117L ENU-induced mutation results in reduced PGC1a activity in the heart of *Wars2*$^{V117L/V117L}$ mice resulting in reduced transcriptional regulation of mitochondrial biogenesis and fatty acid oxidation genes. Again this data demonstrates clearly contrasting data to that reported by Dogan *et al*.

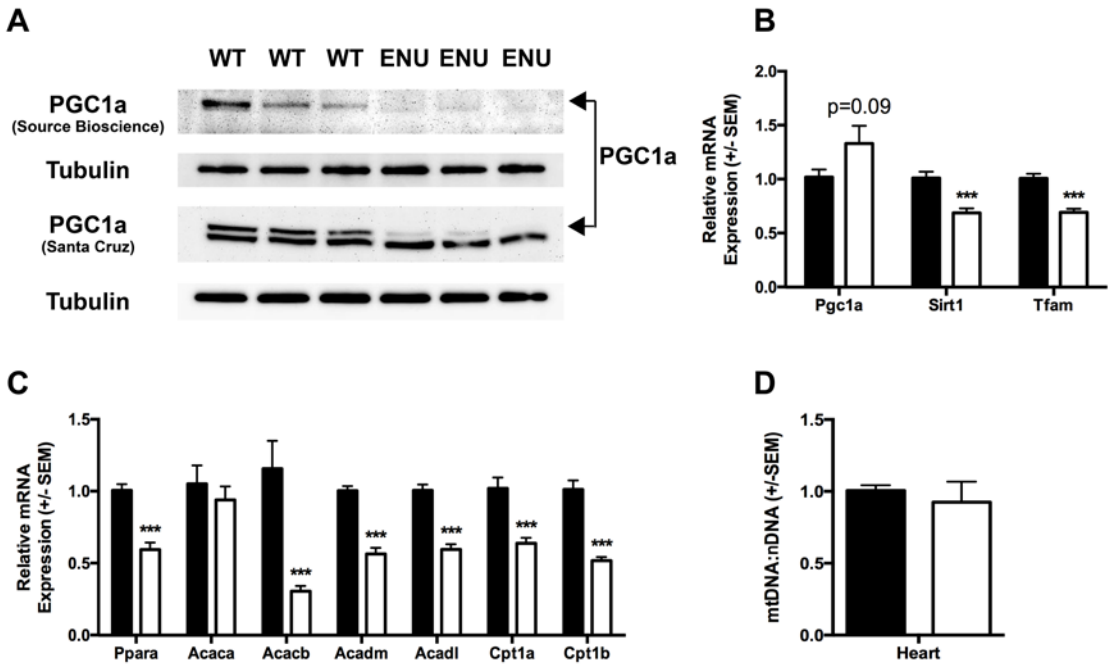

Figure 5.9 – PGC1a regulation in *Wars2*$^{V117L/V117L}$ heart.
A) Immunoblot analysis of PGC1a and tubulin (loading control) protein levels in whole heart lysates using two PGC1a antibodies. mRNA expression analysis of B) *Pgc1a*, *Sirt1* & *Tfam* and C) *Ppara*, *Acaca*, *Acacb*, *Acadm*, *Acadl*, *Cpt1a* & *Cpt1b* in heart. D) Relative mtDNA copy number normalized to nDNA content in whole heart DNA preparations. Data in B – D shown as mean 2□ddCT ± SEM; *Wars2*$^{+/+}$ (n=8) and *Wars2*$^{V117L/V117L}$ (n=8). Analysis shown in A - D was performed using tissues collected from mice at 12 months of age. Data were analyzed using student's t-test: ***** P<0.05, ****** P<0.01, ******* P<0.001.

5.2.2.2 Regulation of PGC1a in *Wars2*$^{V117L/V117L}$ Liver, Kidney and Skeletal Muscle

It was clear that in *Wars2*$^{V117L/V117L}$ heart, PGC1a activity was reduced. This was in contrast with observations reported by Dogan *et al* where PGC1a was up-regulated in *Dars2*-KO heart and our previously observation that *Pgc1a* mRNA was increased in *Wars2*$^{V117L/V117L}$ MEFs. We then sought to determine whether mitochondrial biogenesis was up-regulated in

other *Wars2*$^{V117L/V117L}$ tissue. First we looked at PGC1a protein levels in *Wars2*$^{V117L/V117L}$ liver, kidney and skeletal muscle at 12 months of age. Again in all tissues, no band was observed at 92kDa, the predicted size of PGC1a. However, we consistently observed a double band at 70kDa in liver, kidney and skeletal muscle. There was no clearly consistent difference in the steady state levels of PGC1a protein in *Wars2*$^{V117L/V117L}$ and *Wars2*$^{+/+}$ liver, kidney and skeletal muscle at 12 months of age **(Figure 5.10A)**. Therefore, we performed mRNA expression analysis in *Wars2*$^{V117L/V117L}$ tissues to determine whether *Pgc1a*, genes known to regulate PGC1a and genes transcriptionally regulated by PGC1a were differentially regulated. In *Wars2*$^{V117L/V117L}$ liver there was a non-significant trend for increased *Pgc1a* mRNA expression (p=0.29) compared to *Wars2*$^{+/+}$ similar to observations in *Wars2*$^{V117L/V117L}$ heart. However, in contrast to *Wars2*$^{V117L/V117L}$ heart, there was no significant difference the mRNA expression levels of *Sirt1*, *Tfam* or fatty acid oxidation genes in *Wars2*$^{V117L/V117L}$ liver compared to *Wars2*$^{+/+}$ **(Figure 5.10B)**. Equally no significant difference in mRNA expression of *Pgc1a* or associated genes were observed in *Wars2*$^{V117L/V117L}$ kidney compared to *Wars2*$^{+/+}$ at 12 months of age **(Figure 5.10C)**. Interestingly *Pgc1a* mRNA expression was on average 4 fold increased in *Wars2*$^{V117L/V117L}$ skeletal muscle compared to *Wars2*$^{+/+}$ at 12 months of age **(Figure 5.10D)**. There was also a trend for increased mRNA expression of genes down-stream of PGC1a in *Wars2*$^{V117L/V117L}$ skeletal muscle compared to *Wars2*$^{+/+}$ however these differences were not statistically different. Taken together these data show that whilst *Pgc1a* may be transcriptionally up-regulated, there is no evidence of increased PGC1a transcription factor activity or up-regulation of mitochondrial biogenesis in *Wars2*$^{V117L/V117L}$ skeletal muscle. **(Figure 5.10D)**.

Finally, we quantified mtDNA copy number in *Wars2*$^{V117L/V117L}$ liver, kidney and skeletal muscle at 12 months of age. There was no significant difference between *Wars2*$^{V117L/V117L}$ and *Wars2*$^{+/+}$ mtDNA:nDNA in liver or skeletal muscle at 12 months of age consistent with the conclusion that mitochondrial biogenesis is not up-regulated in these tissues.

Unexpectedly mtDNA:nDNA was on average a 59 % reduced in *Wars2*$^{V117L/V117L}$ kidney at 12 months of age compared to *Wars2*$^{+/+}$ **(Figure 5.10E)**.

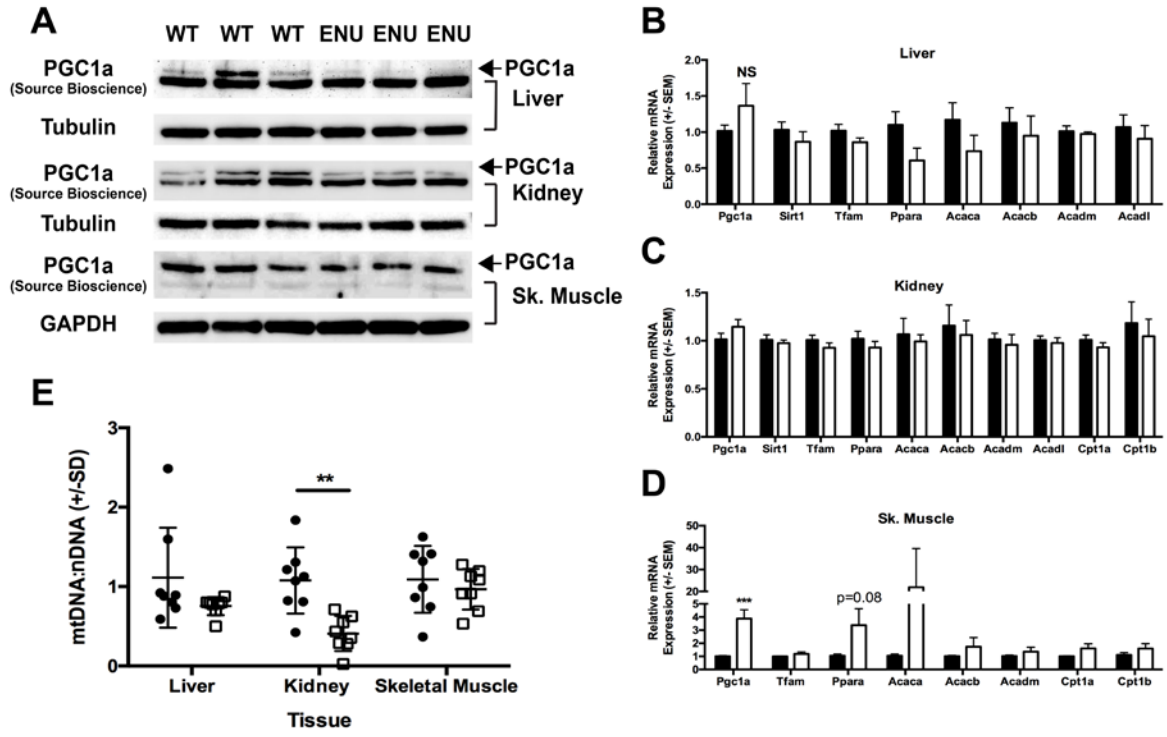

Figure 5.10 - PGC1a regulation in *Wars2*$^{V117L/V117L}$ liver, kidney and skeletal muscle.
A) Immunoblot analysis of PGC1a (arrow) and tubulin / GAPDH (loading control) protein levels in whole liver, kidney & skeletal muscle lysates. mRNA expression analysis of Pgc1a and associated genes in B) liver, C) kidney and D) skeletal muscle. E) Relative mtDNA copy number normalized to nDNA content in whole liver, kidney and skeletal muscle DNA preparations. Data in B – E shown as mean 2□ddCT ± SEM / SD; *Wars2*$^{+/+}$ (n=6-8) and *Wars2*$^{V117L/V117L}$ (n=6-8). Analysis shown in A - E was performed using tissues collected from mice at 12 months of age. Data were analyzed using student's t-test: ***** P<0.05, ****** P<0.01, ******* P<0.001.

5.2.2.3 Regulation of PGC1a and 'browning pathways' in *Wars2*$^{V117L/V117L}$ White Adipose Tissue

As mentioned previously, abnormal pathology was observed in *Wars2*$^{V117L/V117L}$ WAT. Reduced adipocyte size and the presence of multilocular lipid droplet formation were observed in *Wars2*$^{V117L/V117L}$ iWAT and gWAT indicating an increase in WAT 'browning'. 'Browning' of WAT has been shown to occur due to two key mechanisms: up-regulation of UCP1 and up-regulation of mitochondrial biogenesis. We sought to determine the mechanistic underpinning of the abnormal WAT pathology observed in *Wars2*$^{V117L/V117L}$ mice.

First we checked *Wars2* exon splicing in iWAT. *Wars2*-FL mRNA was on average 75% reduced in *Wars2*$^{V117L/V117L}$ iWAT relative to *Wars2*$^{+/+}$ consistent with previous findings from other tissues and cells **(Figure 5.11A)**. There was no difference in the amount of *Wars2*-Total mRNA in *Wars2*$^{V117L/V117L}$ and *Wars2*$^{+/+}$ iWAT (measured by exon 4/5 and 5/6 boundaries). Immunoblot analysis of UCP1 steady protein levels in *Wars2*$^{V117L/V117L}$ iWAT were performed (**Figure 5.11B**) and were quantified by ImageJ (**Figure 5.11C**). UCP1 protein and *Ucp1* mRNA were on average 1.7 and 93.7 fold increased respectively in *Wars2*$^{V117L/V117L}$ iWAT relative to *Wars2*$^{+/+}$ consistent with the observed 'browning' pathology **(Figure 5.11C&D)**. Equally additional genes associated with 'browning' such as *Dio2* and *Cidea* were significantly elevated in *Wars2*$^{V117L/V117L}$ iWAT compared to *Wars2*$^{+/+}$. Consistent with observations in *Wars2*$^{V117L/V117L}$ MEFs and skeletal muscle, *Pgc1a* mRNA expression was on average 5.7 fold increased in in *Wars2*$^{V117L/V117L}$ iWAT relative to *Wars2*$^{+/+}$ **(Figure 5.11C)**. As mentioned previously PGC1a regulates mitochondrial biogenesis and fatty acid oxidation. To determine whether mitochondrial biogenesis is up-regulated we quantified the mRNA expression level of nDNA genes encoding OXPHOS subunits. *Cox7a* and *Cox8b* were on average 21.2 and 10.9 fold increased in *Wars2*$^{V117L/V117L}$ iWAT relative to *Wars2*$^{+/+}$ indicative of transcriptional up-regulation of mitochondrial biogenesis and iWAT browning pathways **(Figure 5.11C)**. Finally, fatty acid oxidation genes such as *Cpt1b* and *Acacb* were also transcriptionally up-regulated in *Wars2*$^{V117L/V117L}$ iWAT relative to *Wars2*$^{+/+}$ **(Figure 5.11C)**.

There data show that the 'browning' pathology observed in *Wars2*$^{V117L/V117L}$ iWAT is caused by transcriptional up-regulation of genes associated with brown adipocytes, mitochondrial biogenesis and fatty acid oxidation.

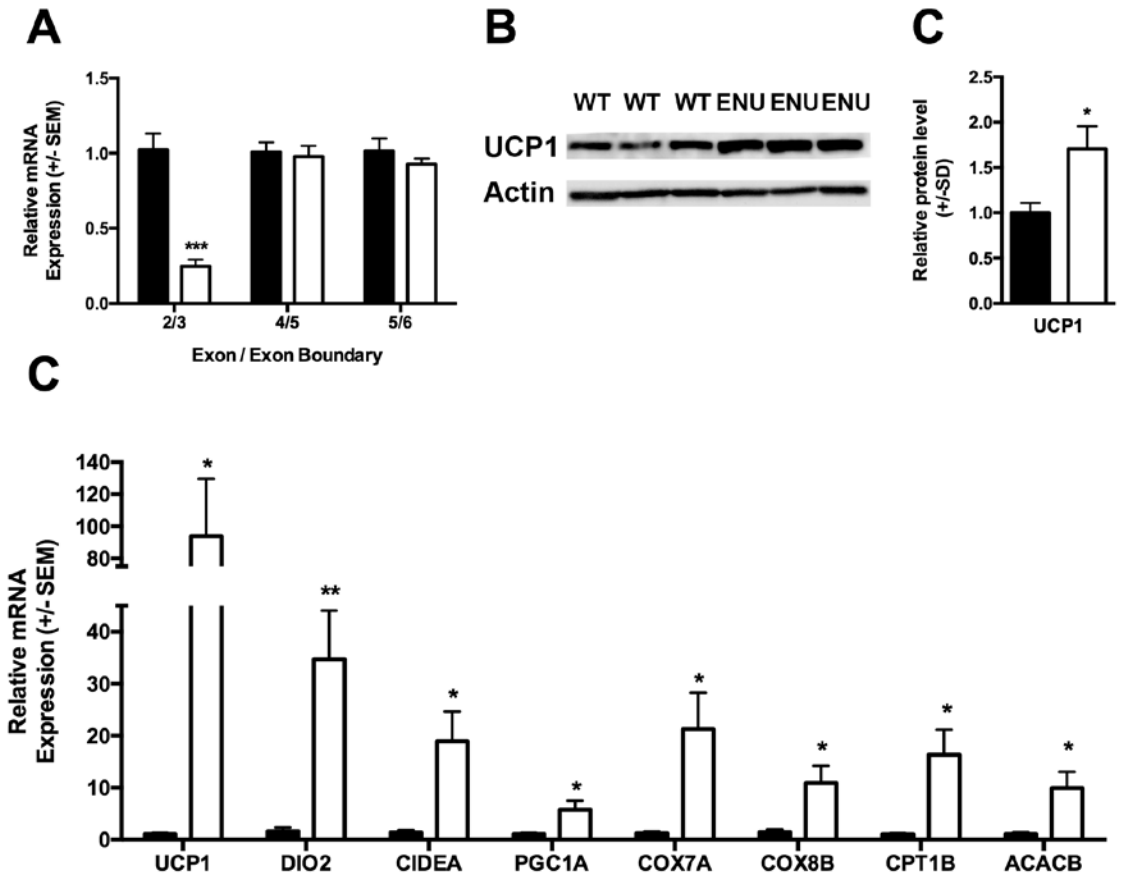

Figure 5.11 – PGC1a and 'browning' regulation in *Wars2*$^{V117L/V117L}$ iWAT.
A) Relative mRNA expression levels of *Wars2*-Exon2/3 (*Wars2*-FL), *Wars2*-Exon4/5 (*Wars2*-Total) *Wars2*-Exon5/6 (*Wars2*-Total) in iWAT. B) Immunoblot analysis of UCP1 protein levels in whole iWAT lysates. C) Quantification of UCP1 steady state protein levels. D) mRNA gene expression analysis of 'browning' and *Pgc1a* associated genes in iWAT. Data in A & C shown as mean 2□ddCT ± SEM; *Wars2*$^{+/+}$ (n=8) and *Wars2*$^{V117L/V117L}$ (n=8). Immunoblots were quantified using ImageJ and normalized to loading controls. Data in B shown as mean ± SD; *Wars2*$^{+/+}$ (n=3) and *Wars2*$^{V117L/V117L}$ (n=3). Analysis shown in A - C was performed using tissues collected from mice at 12 months of age. Data were analyzed using student's t-test: ***** P<0.05, ****** P<0.01, ******* P<0.001.

5.2.2.4 Summary

Taken together these results indicated that PGC1a activity and expression are differentially regulated in a tissue specific manner in *Wars2*$^{V117L/V117L}$ mice. In *Wars2*$^{V117L/V117L}$ heart reduced PGC1a protein levels and down-regulation of genes up and down-stream of PGC1a indicate reduced PGC1a activity and transcriptional down-regulation of mitochondrial biogenesis and fatty acid oxidation in *Wars2*$^{V117L/V117L}$ heart at 12 months of age. This is in direct contrast with observations by Dogan *et al* where increased PGC1a stability and activity was observed in *Dars2*-KO heart.

The observed reduction in PGC1a activity observed in *Wars2*$^{V117L/V117L}$ heart was not observed in *Wars2*$^{V117L/V117L}$ liver, kidney, skeletal muscle or iWAT. In fact, in *Wars2*$^{V117L/V117L}$ skeletal muscle and iWAT *Pgc1a* was transcriptionally up-regulated. The increase in *Pgc1a* mRNA expression in *Wars2*$^{V117L/V117L}$ skeletal muscle is consistent with previous observations such as increased mt-TrpRS protein and increased OXPHOS subunit protein levels in *Wars2*$^{V117L/V117L}$ skeletal muscle at the same time point. However, there was no statistically significant change in genes transcriptionally regulated by PGC1a. Taken together this indicates that whilst *Pgc1a* mRNA is transcriptionally up-regulated, there is no evidence that there is increased transcription factor activity of PGC1a protein or up-regulation of mitochondrial biogenesis in skeletal muscle. In contrast with this, not only in *Pgc1a* mRNA transcriptionally upregulated in *Wars2*$^{V117L/V117L}$ iWAT but genes downstream of PGC1a, such *Cpt1b* and *Acacb*, and mitochondrial subunit genes, such *Cox7a* and *Cox8b*, are also up-regulated. Taken together these data show that *Pgc1a* and mitochondrial biogenesis are up-regulated in *Wars2*$^{V117L/V117L}$ iWAT consistent with increased 'browning'. Overall these data show that whilst there are tissue specific differences in the expression of *Pgc1a* in *Wars2*$^{V117L/V117L}$ mice, iWAT is the only tissue tested where there is evidence of up-regulation of mitochondrial biogenesis.

Possibly the most intriguing result was observed in *Wars2*$^{V117L/V117L}$ kidney where reduced mtDNA:nDNA was observed at 12 months of age. Up until this point we had thought that the *Wars2*-V117L ENU-induced mutation had very little effect on mitochondrial function in the kidney despite reductions in *Wars2*-FL mRNA and mt-TrpRS protein. However, mtDNA:nDNA is significantly reduced in *Wars*$^{V117L/V117L}$ kidney independent of transcriptional changes in mitochondrial biogenesis, fatty acid oxidation, ISR or UPR^{mt}. Equally only a mild reduction in CIV was observed in *Wars2*$^{V117L/V117L}$ kidney at the same time point. These data require further evaluation validation in order to determine their significance.

5.2.3 Tissue specific regulation of autophagy

Also reported by Dogan *et al* was inhibition of autophagy in *Dars2*-KO hearts as shown through an increase in LC3I and a decrease in LCII in *Dars2*-KO hearts. We sought to determine whether the *Wars2*-V117L allele disrupted autophagy in the heart of *Wars2*$^{V117L/V117L}$ mice. To do this LC3 immunoblots were performed at 12 months in *Wars2*$^{V117L/V117L}$ heart, liver and kidney. There was no obvious difference in the amount of LC3I or LC3II in *Wars2*$^{V117L/V117L}$ heart and liver at 12 months of age compared to *Wars2*$^{+/+}$ **(Figure 5.12A)**. In fact, if anything the amount of LC3II was increased in *Wars2*$^{V117L/V117L}$ heart compared to *Wars2*$^{+/+}$ indicating increased autophagy and again is counter to observations from Dogan *et al*. Most intriguingly however was the observed increased in LC3II in *Wars2*$^{V117L/V117L}$ kidney at 12 months of age compared to *Wars*$^{+/+}$ indicating an increase in active autophagosomes **(Figure 5.12A)**. These results along with the reduction in mtDNA:nDNA observed in *Wars2*$^{V117L/V117L}$ kidney at 12 months may indicate increased mitophagy.

In order to determine a time line for activation of mito/autophagy in *Wars2*$^{V117/V117L}$ kidney we repeated the same analysis at an earlier time point. At 9 months of age there was no difference in the amount of LC3II or mtDNA:nDNA in *Wars2*$^{V117L/V117L}$ kidney compared to *Wars2*$^{+/+}$ **(Figure 5.12B&C)**. There results suggested that activation of mito/autophagy in the *Wars2*$^{V117/V117L}$ kidney is progressive with age. Further analysis is required to determine whether the increase in LC3II observed in *Wars2*$^{V117L/V117L}$ kidney represents an increase in (mito)autophagic flux as well determining the stimulus triggering the formation of active autophagosomes in the kidney.

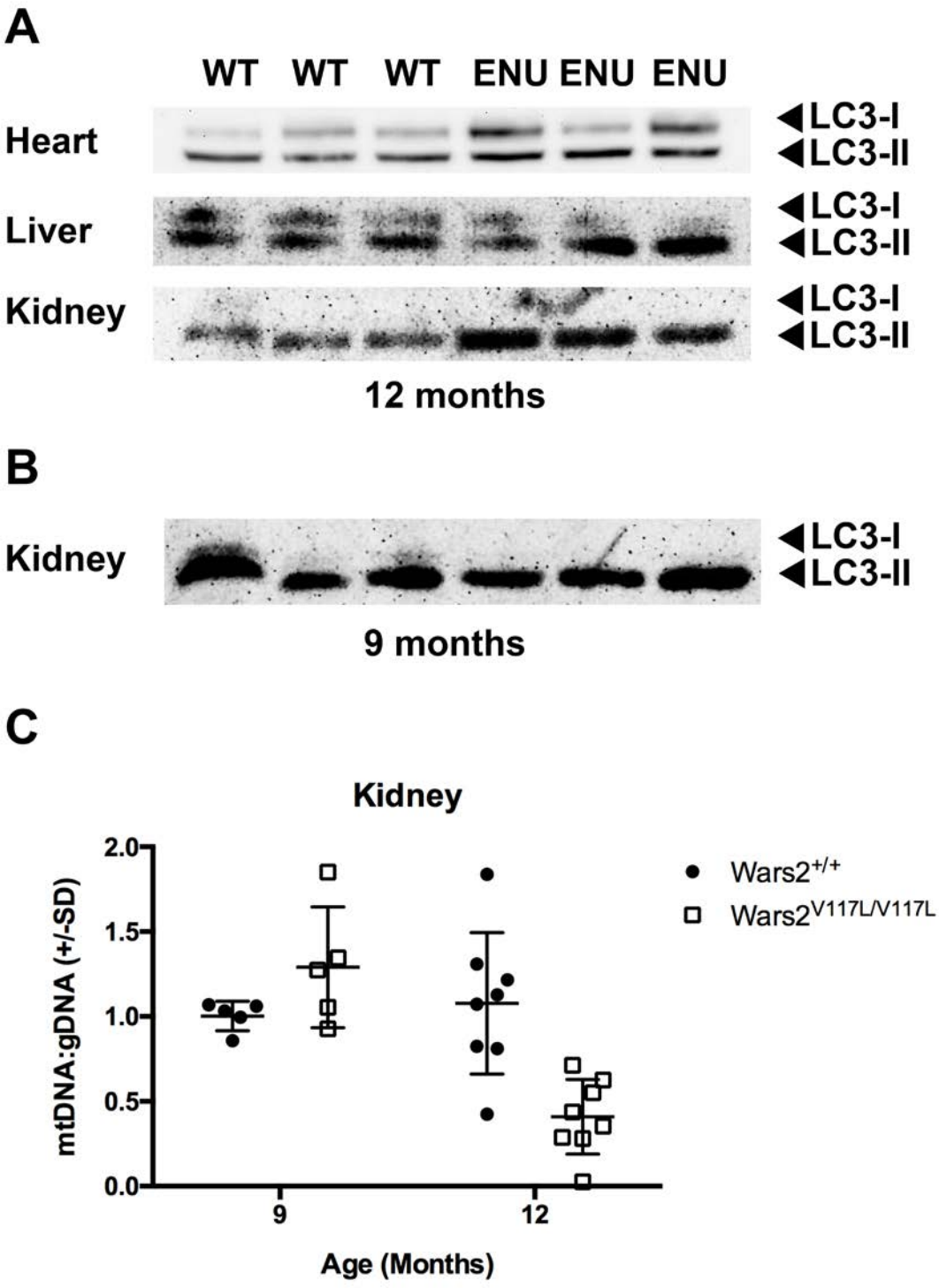

Figure 5.12 – Tissue specific differences in LC3 isoforms in *Wars2$^{V117L/V117L}$* mice. Immunoblot analysis of LC3 protein isoforms in A) heart liver & kidney at 12 months of age and in B) kidney at 9 months of age. C) Relative mtDNA copy number normalized to nDNA content in whole kidney DNA preparations at 9 and 12 months of age. Data in C shown as mean 2□ddCT ± SD; *Wars2$^{+/+}$* (n=5-8) and *Wars2$^{V117L/V117L}$* (n=5-8). WT = *Wars2$^{+/+}$*, ENU = *Wars2$^{V117L/V117L}$*. Data were analyzed using student's t-test: ***** P<0.05, ****** P<0.01, ******* P<0.001.

5.3 Discussion

In this chapter we investigated whether the *Wars2*-V117L allele caused activation of mechanisms associated with mitochondrial dysfunction in a tissue specific manner in *Wars2*$^{V117L/V117L}$ mice. The overarching aim of this study was to determine tissues-specific mechanisms that may explain the tissue specific penetrance and pathology associated with the *Wars2*-V117L allele. To do this we focused on three main pathways, the integrated stress response (ISR), mitochondrial biogenesis and autophagy. We also investigated the mechanism through which the ISR is activated in *Wars2*$^{V117L/V117L}$ heart. I will now discuss each of these pathways individually.

5.3.1 *Wars2*-V117L allele causes tissue-specific activation of the ISR in *Wars2*$^{V117L/V117L}$ mice

In this chapter I presented convincing evidence that the ISR was activated in a tissue specific manner in *Wars2*$^{V117L/V117L}$ mice. The definitive measure of activation of the ISR is phosphorylation of eIF2a. In *Wars2*$^{V117L/V117L}$ mice, p-eIF2a levels were significantly increased in heart and liver tissue but no significant differences were observed in *Wars2*$^{V117L/V117L}$ kidney or skeletal muscle. This showed that the ISR was activated in *Wars2*$^{V117L/V117L}$ heart and, to a lesser extent, liver but not in *Wars2*$^{V117L/V117L}$ kidney or skeletal muscle. p-eIF2a causes inhibition of cytoplasmic protein synthesis allows cap-independent translation of ATF4. ATF4 protein was increased in *Wars2*$^{V117L/V117L}$ heart further showing activation of the ISR and cap-independent protein synthesis. Genes previously associated with activation of the ISR such as *Atf4*, *Atf5*, *Chop* and *Mthfd2* were transcriptionally up-regulated in *Wars2*$^{V117L/V117L}$ heart further evidence of activation of the ISR. However, in *Wars2*$^{V117L/V117L}$ liver, no significant differences in *Atf4* or *Atf5* mRNA expression were observed. These data showed that the ISR may only be partially active in *Wars2*$^{V117L/V117L}$ liver. Furthermore, there was no evidence that the ISR was active in *Wars2*$^{V117L/V117L}$ kidney as *Atf4, Atf5* mRNA expression levels were comparable to wild-type.

Atf5 mRNA levels were on average increased in *Wars2*$^{V117L/V117L}$ skeletal muscle however due to high biological variability this trend was not significant. Overall these data show that the ISR is activated in a tissue specific manner in *Wars2*$^{V117L/V117L}$ mice and was only activated in tissues with OXPHOS deficiencies such as the heart and liver suggesting that inhibition of mitochondrial translation is linked with activation of the ISR.

These data also showed that activation of the ISR caused up-regulation of *Fgf21* mRNA resulting in increased plasma FGF21. *Fgf21* has been shown to be transcriptionally regulated by ATF4 in autophagy deficient mice (Kim et al., 2013). mRNA analysis showed that Fgf21 mRNA levels were greatly increased in *Wars2*$^{V117L/V117L}$ heart and, to a lesser extent, liver and iWAT. FGF21 was also observed to be increased in *Dars2*-KO plasma and *Fgf21* mRNA expression was also increased in *Dars2*-KO heart. Taken together these data show that the increase in plasma FGF21 observed in *Wars2*$^{V117L/V117L}$ mice is primarily produced by the heart due to activation of the ISR and increased ATF4 activity. Increased plasma FGF21 may also explain the systemic changes in metabolism observed in *Wars2*$^{V117L/V117L}$ mice. In addition to this,

FGF21 is an endocrine hormone and has been shown to be an important regulator of systemic metabolism in mouse and humans. For example, in mice plasma FGF21 has been shown to cause increased insulin independent glucose-uptake in adipose tissue and skeletal muscle (Kharitonenkov et al., 2005; Mashili, 2014). Furthermore, in *ob/ob* and *db/db* mice therapeutic administration of FGF21 caused reduced plasma glucose and triglyceride levels (Kharitonenkov et al., 2005). The increase in plasma FGF21 therefore explains the reduced plasma glucose levels and increased glucose tolerance observed in *Wars2*$^{V117L/V117L}$ mice. FGF21 has also been shown to have beneficial effects on body weight and WAT morphology in mice models. Fisher et al used FGF21-KO mice to show that FGF21 regulates PGC1a and 'browning' of WAT in response to adaptive thermogenesis (F. F. Fisher et al., 2012). Veniant *et al* performed follow-up studies. Lean and obese mice

were treated with an FGF21 agonist and housed mice at 21°C and 30°C. They showed that the FGF21 stimulation caused increased glucose tolerance, and reduced body weight in both lean and obese mice at both temperatures. They went on to show that FGF21 also caused temperature dependant browning of WAT. Finally, they showed that the beneficially effects of FGF21 on weight loss were independent of UCP1 expression and browning pathways. Based upon these data, FGF21 is also the cause of reduced total body weight and WAT 'browning' in *Wars2*$^{V117L/V117L}$ mice. However, it also suggests that the FGF21 induced weight loss observed in *Wars2*$^{V117L/V117L}$ may not dependent upon WAT 'browning'. Finally, FGF21 has also been implicated in ketogenesis. Inagaki *et al* generated liver specific FGF21 overexpression mice. They showed that, in fed mice, hepatic overexpression of FGF21 caused increased WAT lipolysis and liver ketogenesis resulting in elevated plasma ketone bodies and reduced plasma triglycerides. Therefore, FGF21 may also the cause of increased plasma ketone bodies and reduced TAG levels observed in *Wars2*$^{V117L/V117L}$ mice. Overall we conclude that activation of the ISR in *Wars2*$^{V117L/V117L}$ heart caused systemic changes in metabolism including changes in glucose, lipid and ketone homeostasis in *Wars2*$^{V117L/V117L}$ mice mediated by cardiac-derived FGF21.

Next we examined the mechanism activating the ISR in *Wars2*$^{V117L/V117L}$ heart. Previously we had observed that the ISR was only activated in tissues with substantial OXPHOS deficiencies such as the heart and liver. To investigate this observed relationship further OXPHOS subunits and p-eIF2a protein levels were analysed at 1, 3, and 12 months of age in *Wars2*$^{V117L/V117L}$ heart. We showed that CI deficiency occurred before activation of the ISR in *Wars2*$^{V117L/V117L}$ heart. Furthermore, we showed that CI deficiency was progressive with age and co-incident with progressive activation of the ISR in *Wars2*$^{V117L/V117L}$ heart. Taken together these data suggested that activation of the ISR was secondary to OXPHOS deficiency in *Wars2*$^{V117L/V117L}$ heart and dependent upon OXPHOS levels.

However, this contradicted findings from Dogan *et al* who showed that activation of the ISR in the *Dars2*-KO heart occurred after OXPHOS deficiency and that the primary stimulus for activation of the ISR was disrupted mitochondrial proteostasis (Dogan et al., 2014). We went on to show that activation of the ISR in *Wars2*$^{V117L/V117L}$ heart was independent of activation of the UPR^{mt}. No significant differences LONP1, CLPP, mtHSP60 or mtHSP70 were observed in *Wars2*$^{V117L/V117L}$ heart compared to wild-type controls at 1, 3 or 12 months of age. Whereas all four of the aforementioned UPR^{mt} associated proteins were up-regulated in the *Dars2*-KO heart. Taken together these data showed that activation of the ISR in *Wars2*$^{V117L/V117L}$ heart was not due to disrupted mitochondrial proteostasis and was therefore via an alternate mechanism.

We hypothesised that the OXPHOS deficiencies observed in *Wars2*$^{V117L/V117L}$ heart could lead to ROS induced ER stress and that ER stress could cause activation of the ISR through PERK. However, no differences in markers of ER stress or oxidative stress were observed in *Wars2*$^{V117L/V117L}$ heart showing that activation of the ISR was independent of ER stress and oxidative stress in *Wars2*$^{V117L/V117L}$ heart. Overall these data show that activation of the ISR in *Wars2*$^{V117L/V117L}$ heart was co-incident with progressive CI deficiency and independent of UPR^{mt}, UPR^{er} or oxidative stress.

However, there are still questions that remain to be answered. Such as: Why is the UPR^{mt} activated in the *Dars2*-KO heart but not in the *Wars2*$^{V117L/V117L}$ heart? What is the mechanism of ISR activation in *Wars2*$^{V117L/V117L}$ heart? I will now discuss these questions individually.

5.3.1.1 Why is the UPR^{mt} activated in the *Dars2*-KO heart but not in the *Wars2*$^{V117L/V117L}$ heart?

I postulate that the reason why the UPR^{mt} is active in the *Dars2*-KO heart but not in the *Wars2*$^{V117L/V117L}$ heart is due to differences in the nature of the alleles. The *Wars2*-V117L allele is hypomorphic whereas the *Dars2*-KO allele is a null allele. This means that in *Dars2*-KO heart there is no mt-AspRS activity causing complete inhibition of mitochondrial translation. Whereas in the *Wars2*$^{V117L/V117L}$ heart, although there is reduced mt-TrpRS protein, mitochondrial translation is not completely inhibited. This is evident as OXPHOS subunit protein levels were comparatively normal to wild-type controls in *Wars2*$^{V117L/V117L}$ heart at 1 month of age.

The UPR^{mt} is activated by disrupted mitochondrial proteostasis caused by accumulation of unfolded or unassembled proteins in the mitochondrial matrix. The UPR^{mt} upregulates mitochondrial proteases and protein chaperones to degrade unfolded proteins and to aid correct protein assembly to alleviate mitochondrial proteostatic stress (Pellegrino, Nargund, & Haynes, 2013). It is logical therefore, that inhibition of mitochondrial translation causes disrupted mitochondrial proteostasis and activation of the UPR^{mt}. If mitochondrial translation is inhibited, OXPHOS complexes CI, CIII, CIV or CV may not assemble because there are deficiencies in core subunits of these complexes that are encoded by the mtDNA. Therefore, nDNA encoded OXPHOS subunits imported into the mitochondria and accumulate leading to disrupted mitochondrial proteostasis and activation of the UPR^{mt}. However, in both *Wars2*$^{V117L/V117L}$ and *Dars2*-KO heart, activation of the ISR was observed. Activation of the ISR causes inhibition of cytoplasmic protein translation. Therefore, activation of the ISR therefore should attenuate mitochondrial proteostatic stress by reducing the amount of nDNA encoded mitochondrial OXPHOS subunits being synthesised in the cytoplasm and therefore accumulating in the mitochondrial matrix. In *Wars2*$^{V117L/V117L}$ heart, the reduction in the rate of cytoplasmic translation caused by activation of the ISR,

matches the reduced rate of mitochondrial protein synthesis allowing OXPHOS complexes to be assembled all be it at a reduced rate and preventing mitochondrial proteolytic stress. However, in *Dars2*-KO heart, despite the reduced rate of cytoplasmic protein synthesis, nDNA encoded OXPHOS subunits still accumulate in the mitochondrial matrix because the is no mt-AspRS activity and there is complete inhibition of mitochondrial protein synthesis. Therefore, the ISR can successfully attenuate mitochondrial proteostatic stress in the *Wars2*$^{V117L/V117L}$ heart but not in *Dars2*-KO heart.

This idea may also explain the differences in the severity of the cardiac phenotypes observed in the two mouse models. The *Dars2*-KO mice died at 6 weeks of age due to severe hypertrophic cardiomyopathy whereas the *Wars2*$^{V117L/V117L}$ mice were able to survive beyond 12 months of age. Activation of the ISR may therefore play a protective role to prevent disrupted mitochondrial proteostasis and activation of the UPR^{mt} in the *Wars2*$^{V117L/V117L}$ heart to slow the progression and severity of the hypertrophic cardiomyopathy also observed in these mice. It is possible that regulation of mitochondrial proteostatic stress may explain the variability in the age of onset and severity of phenotypes observed in mtRS patients. In mtRS mutant patient with early onset, severe phenotypes resulting in premature death, the ISR or alternate compensatory mechanisms cannot sufficiently attenuate mitochondrial proteostatic stress caused by inhibition of mitochondrial translation resulting in acute disease progression. However, in mtRS mutant patients with later onset phenotypes, the ISR and / or additional compensatory mechanisms attenuates mitochondrial proteostatic stress resulting in a chronic / slower disease progression. It is possible therefore that therapeutic strategies aiming to attenuate proteostatic stress in mtRS patients may slow disease progression and prolong life in mtRS patients.

5.3.1.2 What is the mechanism of ISR activation in *Wars2*$^{V117L/V117L}$ heart?

The ISR is activated through phosphorylation of eIF2a by one of four kinases PKR, HRI, PERK and GCN2. One of these four kinases must therefore activate the ISR in the

Wars2$^{V117L/V117L}$ heart. There is evidence within the literature that inhibition of mitochondrial translation causes GCN2 dependant activation of the ISR *in vitro*. Michel *et al* treated mammalian cells with doxycycline to inhibit mitochondrial translation. They showed that doxycycline treated caused OXPHOS deficiencies and GCN2-dependant activation of the ISR. We hypothesise that the ISR is activated through GCN2 in *Wars2*$^{V117L/V117L}$ heart by sensing inhibition of mitochondrial translation directly. I will now explore this hypothesis.

GCN2 has most extensively been investigated and described within the context of amino acid deprivation and the amino acid response pathway (AAR). The AAR is essentially activation of the ISR through GCN2 due to amino acid deprivation. However, GCN2 does not directly sense amino acid levels. GCN2 has a histidyl-tRNA synthetase (HisRS)-related domain that binds uncharged cytoplasmic tRNAs. When cells are starved of essential amino acids or when synthesis of non-essential amino acids are inhibited there are reduced levels of charged tRNAs in the cytoplasm. GCN2 directly but non-specifically binds uncharged tRNAs and is activated through dimerization and autophosphorylation resulting in phosphorylation of the eIF2a. The fact that GCN2 is described as an amino acid sensor is misleading because what it actually senses is uncharged tRNA levels that could result from not only amino acid deprivation but also inhibition of cytoplasmic aminoacyl-tRNA synthetases. More importantly, GCN2 is activated non-specifically by uncharged tRNA binding. Is it possible that GCN2 can sense inhibition of mitochondrial translation through direct binding with uncharged mt-tRNAs?

For this hypothesis to be true, mt-tRNAs must be present in the cytoplasm where GCN2 resides. There are examples within the literature demonstrating that mt-tRNAs regulate cytoplasmic proteins through direct binding in the cytoplasm. Maniataki and Mourelatos *et al* showed that human mt tRNA^{Met} is exported to the cytoplasm where is associates with Argonaute 2 (Alerting, 2005). More importantly they showed that as well as mt-tRNA^{Met}; mt-tRNA^{Ile}, mt-tRNA^{Lys} and mt tRNA^{Glu} were also present in the cytoplasmic fraction of 293

cells indicating that mt-tRNAs are present in the cytoplasm. Furthermore, Marnef *et al* showed that human polypyrimidine tract-binding protein (PTB) directly binds with mt-tRNA^{Thr}. In this study they used *in vivo* RNA-protein cross-linking to show that mt-tRNA^{Thr} binds PTB in the cytoplasm and to exclude the possibility that PTB binds mt-tRNA^{Thr} released from mitochondria damaged through the process of sub-cellular fractionation (Marnef, Jády, & Kiss, 2015). Taken together these studies demonstrate that mt-tRNAs are present in the cytoplasm and bind cytoplasmic proteins in certain circumstances. It is possible therefore that in *Wars2*$^{V117L/V117L}$ heart and liver, that uncharged mt-tRNA^{Trp} may be present in cytoplasm and activates the ISR through direct binding with GCN2.

However, for this hypothesis to be true why isn't the ISR activated in *Wars2*$^{V117L/V117L}$ kidney where mt-TrpRS protein levels were substantially reduced? There are two possible explanations for this. First of all, OXPHOS subunit steady state protein levels were overall largely unchanged in *Wars2*$^{V117L/V117L}$ kidney. This suggests that mitochondrial translation was only partially inhibited in the *Wars2*$^{V117L/V117L}$ kidney and that there is sufficient residual mt-TrpRS activity to meet the requirement for charged mt-tRNA^{Trp} in mitochondrial translation. Therefore, the ISR is not activated in *Wars2*$^{V117L/V117L}$ kidney because the levels of uncharged mt-tRNA^{Trp} are low. The second explanation is that mt-tRNA^{Trp} export / transport to the cytoplasm is dependent upon OXPHOS deficiency. In *Wars2*$^{V117L/V117L}$ heart, activation of the ISR was progressive with age and co-incident OXPHOS deficiencies. This suggests that the stress activating the ISR in *Wars2*$^{V117L/V117L}$ heart increases as CI levels decrease. I postulate that as OXPHOS / CI levels decrease; the permeability of the inner mitochondrial membrane increases allowing mt-tRNAs to diffuse into the cytoplasm. In the cytoplasm uncharged mt-tRNA^{Trp} binds GCN2, activating the ISR. The hypothesis would explain why activation of the ISR was proportional to CI deficiency in *Wars2*$^{V117L/V117L}$ heart. It would also explain why the ISR is not activated in the *Wars2*$^{V117L/V117L}$ kidney. OXPHOS subunits were overall largely unchanged in the *Wars2*$^{V117L/V117L}$ kidney. Therefore, there is no increase in inner mitochondrial membrane permeability, preventing diffusion of mt-

$tRNA^{Trp}$ into the cytoplasm and preventing activation of the ISR despite reduced levels of mt-TrpRS protein.

5.3.2 Tissue specific regulation of mitochondrial biogenesis in *Wars2*$^{V117L/V117L}$ mice

In the previous chapter, we showed that *Wars2*$^{V117L/V117L}$ MEFs had increased mitochondrial function, increased mitochondrial mass and transcriptional up-regulation of *Pgc1a* mRNA. In this chapter we investigated whether the *Wars2*-V117L allele caused up-regulation of mitochondrial biogenesis in *in vivo* and hypothesised that altered regulation of mitochondrial biogenesis may explain the tissue specific penetrance of the *Wars2*-V117L allele.

There is evidence that *Pgc1a* and mitochondrial biogenesis are differentially regulated in a tissue specific manner in *Wars2*$^{V117L/V117L}$ mice. In *Wars2*$^{V117L/V117L}$ heart, immunoblot analysis showed that steady state protein levels of PGC1a were reduced in the heart. Consistent with this result, we also showed that genes that regulate PGC1a, such as *Sirt1*, and genes downstream of PGC1a such as *Tfam*, *Ppara* and FAO genes, were transcriptionally down regulated in *Wars2*$^{V117L/V117L}$ heart. Overall these data showed that PGC1a activity was reduced in *Wars2*$^{V117L/V117L}$ heart. In *Wars2*$^{V117L/V117L}$ kidney and liver there was no evidence that PCG1a activity was altered. However, in *Wars2*$^{V117L/V117L}$ skeletal muscle and iWAT there was evidence to suggest that *Pgc1a* and mitochondrial biogenesis, respectively, were transcriptionally up-regulated.

Pgc1a mRNA levels were significantly increased in *Wars2*$^{V117L/V117L}$ skeletal muscle and there was also a trend for up-regulation of genes down-stream of PGC1a however these trends were not statistically significant. This data shows that whilst *Pgc1a* is transcriptionally up-regulated in *Wars2*$^{V117L/V117L}$ skeletal muscle, mitochondrial biogenesis is not up-

regulated. Therefore, up-regulation of mitochondrial biogenesis does not explain the increase in mt-TrpRS protein and OXPHOS proteins previously observed in *Wars2*$^{V117L/V117L}$ skeletal muscle.

In *Wars2*$^{V117L/V117L}$ iWAT, not only was *Pgc1a* transcriptionally upregulated, but also genes associated with 'browning' pathways (*Ucp1*, *Dio2*), mitochondrial biogenesis (*Cox7a*, *Cox8b*) and fatty acid oxidation (*Cpt1b*, *Acacb*) were also transcriptionally up-regulated. Furthermore, UCP1 steady state protein levels were also increased in *Wars2*$^{V117L/V117L}$ iWAT. These data are consistent with observations in *Wars2*$^{V117L/V117L}$ MEFs, which showed that up-regulation of *Pgc1a* and mitochondrial biogenesis prevented OXPHOS deficiency and inhibition of mitochondrial translation resulting in increased mitochondrial OXPHOS function and mitochondrial mass. Future work is required to determine whether mt-TrpRS and OXPHOS protein levels are increased in *Wars2*$^{V117L/V117L}$ iWAT and to confirm that up-regulation of mitochondrial biogenesis has a protective effect in this tissue.

Overall these data showed that whilst *Pgc1a* is differentially up-regulated in *Wars2*$^{V117L/V117L}$ tissues, iWAT was the only tissue where up-regulation of mitochondrial biogenesis was observed *in vivo*. These data explain the 'browning' observed in *Wars2*$^{V117L/V117L}$ WAT but do not provide an explanation for increased mt-TrpRS or OXPHOS protein levels in *Wars2*$^{V117L/V117L}$ skeletal muscle.

5.3.3 Tissue specific regulation of (mito)autophagy in *Wars2*$^{V117L/117L}$ mice

Dogan *et al* reported observed autophagy deficiency in *Dars2*-KO heart. In this chapter, we investigated whether the *Wars2*-V117L allele caused autophagy deficiency in *Wars2*$^{V117L/V117L}$ mice *in vivo*. To date, we have collected limited evidence to investigate

regulation of autophagy in *Wars2*$^{V117L/V117L}$ mice. However, from the evidence that we have collected there are some potentially very interesting inferences.

In order to assess regulation of autophagy, immunoblot analysis of LC3 isoforms was performed in *Wars2*$^{V117L/V117L}$ heart, liver and kidney at 12 months of age. In *Dars2*-KO heart, there was increase in the ratio of LC3I:LC3II isoforms indicative reduced levels of active autophagosomes and inhibition of autophagy. However, in *Wars2*$^{V117L/V117L}$ heart and liver there was no substantial difference in the LCI:LCII ratio compared to *Wars2*$^{+/+}$. These data indicate that autophagy may not be inhibited in *Wars2*$^{V117L/V117L}$ heart and liver.

Most unexpectedly, we observed a decrease in LC3I:LC3II ratio and a loss of mtDNA:nDNA in *Wars2*$^{V117L/V117L}$ kidney tissue between 9 and 12 months of age. Taken together these results may be interpreted as an age related increase in mitophagic flux, as mitophagy is the selective removal of mitochondria via autophagy. However western blot analysis of LC3 isoforms are difficult to interpret. Conversion of LC3I to LC3II does correlate with activation of autophagosomes. On the other hand, during autophagy LC3II is degraded. Therefore, increased LCII may not necessarily indicate an increase in autophagic flux but rather a build-up of active autophagosomes due to autophagy inhibition. In order to address this, future work must be performed to determine the significance of these results. Primarily, western blot analysis of P62 protein levels could be performed as P62 has been shown to bind LC3 and is degraded during autophagy acting as a secondary marker of autophagy activation. Furthermore, a 59% reduction in mtDNA:nDNA was observed in *Wars2*$^{V117L/V117L}$ kidney at 12 months of age whilst only a small reduction in CIV steady state protein levels were observed at the same time point. These two results are somewhat contradictory. As previously mentioned, it is possible that there may be a cell-type specific effect of the *Wars2*-V117L mutation in kidney tissue. It is also possible therefore mtDNA depletion may occur in a cell-type specific manner in *Wars2*$^{V117L/V117L}$ kidney tissue. To investigate this possibility, laser dissection could be used to isolate different kidney structures and/or cell

types in *Wars2*$^{V117L/V117L}$ kidney sections which would allow follow-up cell-type specific mtDNA:nDNA copy number and OXPHOS enzyme activity analysis as well as assessment of autophagic flux markers LC3 and P62.

5.4 Conclusions

In this chapter the overall aim was to determine the tissue specific penetrance of the *Wars2*-V117L allele through mechanistic analysis. The overarching goal was to mechanistically explain the tissue specific pathology observed in *Wars2*$^{V117L/V117L}$ mice. To some extent, we have achieved this aim by identifying disease causing mechanisms, such as the ISR, as well as protective / compensatory mechanisms, such as up-regulation of mitochondrial biogenesis. I will now summarise our findings and outline hypotheses for unexplained results (**Figure 5.13)**.

In Wars2$^{V117L/V117L}$ heart and liver we showed that reduced *Wars2*-FL mRNA caused reduced mt-TrpRS protein and OXPHOS deficiencies likely caused by inhibition of mitochondrial translation. OXPHOS deficiencies activated the ISR (primarily in the heart) leading to inhibition of global cytoplasmic protein synthesis (not yet shown) and increased ATF4. ATF4 transcriptionally up-regulated down-stream targets including *Chop*, *Mthfd2* and *Fgf21*. Increased *Fgf21* expression in the heart and possibly the liver resulted in increased plasma FGF21 causing systemic changes in metabolism including reduced plasma glucose, reduced TAG, increased FFA and increased KB (**Figure 5.13A**).

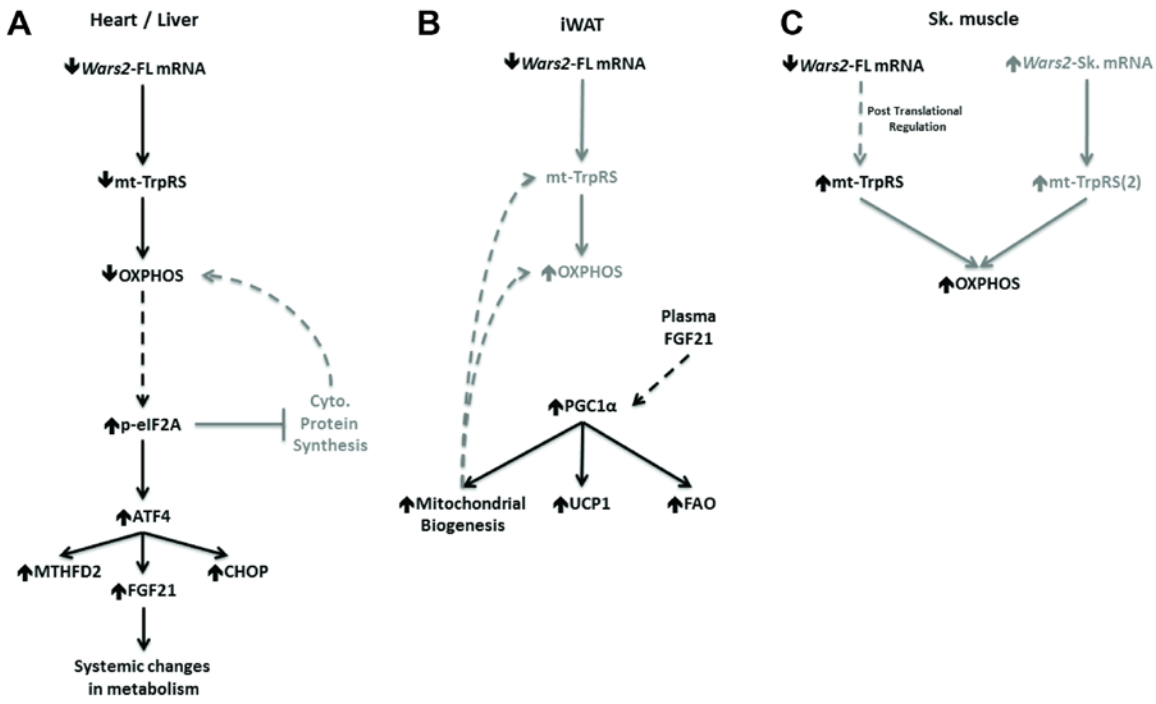

Figure 5.13 – Summary of tissue specific mechanisms and hypotheses in *Wars2*$^{V117L/V117L}$ mice.
A) In *Wars2*$^{V117L/V117L}$ heart and liver, reduced *Wars2*-FL mRNA caused reduced mt-TrpRS protein and progressive OXPHOS deficiencies. Either directly or indirectly, OXPHOS deficiencies resulted in activation of the ISR as shown by increased p-eIF2a and activation of the ISR. It is possible that activation of the ISR contributes to further OXPHOS deficiency by cytoplasmic protein synthesis inhibition. Increased ATF4 caused up-regulation of known target genes such as *Chop*, *Mthfd2* and *Fgf21*. Up-regulation of *Fgf21*, in heart and possibly liver, was responsible for increased plasma FGF21. Increased plasma FGF21 caused systemic changes in metabolism such as increased insulin-independent glucose uptake (increased glucose tolerance), ketogenesis (increased plasma KB) and increased lipolysis (increased plasma FFA). B) In *Wars2*$^{V117L/V117L}$ iWAT, either due to exogenous FGF21 or via an alternate mechanism, *Pgc1a* was up-regulated causing increased 'browning' (multilocular lipid droplet formation, increased UPC1 protein and up-regulation browning genes *Ucp1*, *Dio2* and *Cidea*), increased fatty acid oxidation (upregulation of FAO genes *Cpt1b* and *Acacb*, reduced iWAT weight and increased plasma FFAs) and up-regulation of mitochondrial biogenesis (upregulation of nDNA encoded OXPHOS genes *Cox7a* and *Cox8b*). We hypothesise that up-regulation of mitochondrial biogenesis causes up-regulation of mitochondrial translation preventing OXPHOS deficiency, however this has not yet been shown. C) In *Wars2*$^{V117L/V117L}$ skeletal muscle increased mt-TrpRS prevented OXPHOS deficiencies despite reduced levels of *Wars2*-FL mRNA. There are two explanations for this. mt-TrpRS may be post-translationally regulated, leading to increased stability or reduced turnover, preventing OXPHOS deficiency. Alternatively, there may be a skeletal muscle specific *Wars2* mRNA transcript (Wars2-Sk. mRNA) encoding an alternate mt-TrpRS isoform (mt-TrpRS(2)) that retains aminoacylation activity and prevents OXPHOS deficiency. (Black text and lines = data presented in this thesis, grey text and lines = hypothesized mechanisms).

In *Wars2*$^{V117L/V117L}$ iWAT, either due to exogenous FGF21 or via an alternate mechanism, *Pgc1a* and downstream pathways were upregulated including 'browning', FAO and mitochondrial biogenesis pathways. We speculate that up-regulation of mitochondrial

biogenesis prevents OXPHOS deficiency and dysfunction in *Wars2*$^{V117L/V117L}$ iWAT in keeping with results observed in *Wars2*$^{V117L/V117L}$ MEFs, however this has not yet been shown (**Figure 5.13B**).

In *Wars2*$^{V117L/V117L}$ skeletal muscle there was increased mt-TrpRS and OXPHOS subunits levels independent of reduced *Wars2*-FL mRNA expression levels. We propose two possible explanations for these results. First, mt-TrpRS may be post-translationally regulated in skeletal muscle, either through protein-protein interaction or post-translational modification, thereby increasing protein stability or reducing protein turnover and preventing OXPHOS deficiency. Second, there may be a skeletal muscle specific *Wars2* mRNA transcript encoding an alternate mt-TrpRS isoform that retains aminoacylation activity and prevents OXPHOS deficiency (**Figure 5.13C**).

In *Wars2*$^{V117L/V117L}$ kidney, modest OXPHOS deficiencies were observed despite reduced *Wars2*-FL mRNA, reduced mt-TrpRS and mtDNA depletion. We hypothesise that there are cell-types within *Wars2*$^{V117L/V117L}$ kidney that harbour OXPHOS deficiencies but these deficiencies are not fully detectable by western blot analysis using whole kidney lysates.

6 General Discussion

6.1 Achievement of the Aims and Objectives

The aims of this this thesis were:

- To determine the tissue specific pathology associated with the *Wars2*-V117L allele in mouse (Chapter 3)
- To determine the nature of the *Wars2*-V117L allele *in situ*, *in vitro* and *in vivo* (Chapter 4)
- To investigate tissue specific response mechanisms in *Wars2*$^{V117L/17L}$ mice (Chapter 5)

Overall we have achieved the primary aims of this project. We showed that the *Wars2*-V117L allele causes tissue-specific pathology in mice including: hypertrophic cardiomyopathy, sensorineural hearing loss, reduced adiposity and systemic changes in metabolism (**Figure 6.1**).

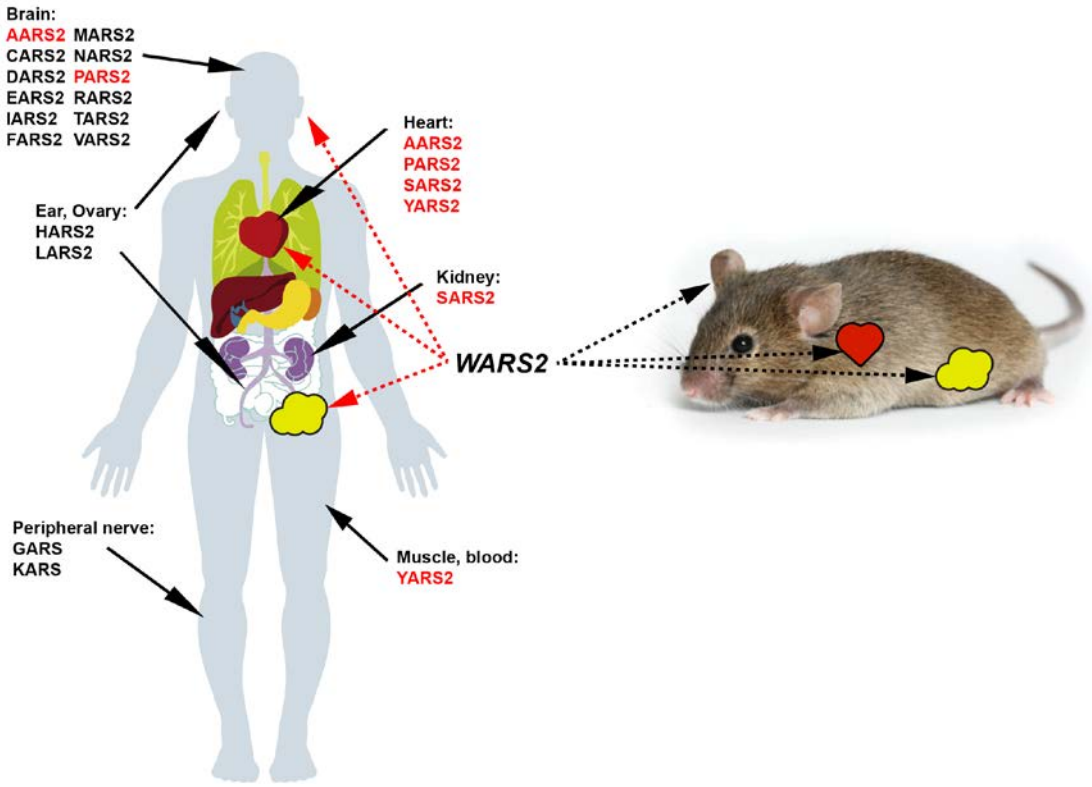

Figure 6.1 – Tissue-specific pathology associated with *Wars2* mutations.

Furthermore, we showed that the *Wars2*-V117L allele is a loss-of-function allele that disrupts *Wars2* mRNA splicing and causes a reduction in the amount of *Wars2*-FL mRNA *in vitro* and *in vivo*. We went on to show that this resulted in tissue-specific reductions in mt-TrpRS protein and OXPHOS deficiencies. Finally, we identified tissue specific stress response mechanisms that explain the tissue-specific pathology observed in the *Wars2*$^{V117L/V117L}$ mice. In particular, we showed that the *Wars2*-V117L allele activates the ISR in *Wars2*$^{V117L/V117L}$ heart causing hypertrophic cardiomyopathy. Activation of the ISR also resulted in increased plasma FGF21 explaining the systemic changes in metabolism observed in *Wars2*$^{V117L/V117L}$ mice. We also identified potential protective mechanisms and showed that increased *Pgc1a* mRNA expression may prevent OXPHOS deficiencies and inhibition of mitochondrial translation in *Wars2*$^{V117L/V117L}$ MEFs and iWAT.

6.2 Key future experiments

6.2.1 Why are the *Wars2*$^{V117L/V117L}$ mice lean?

Wars2$^{V117L/V117L}$ mice had substantially reduced body weight due to reduced adiposity as shown by reduced fat mass, reduced WAT adipocyte size and increased WAT browning. However, CLAMS analysis provided no real evidence that the *Wars2*$^{V117L/V117L}$ mice have increased energy expenditure or reduced energy intake compared to littermate controls. In fact, the *Wars2*$^{V117L/V117L}$ mice had reduced energy expenditure compared to wild type controls when housed at home cage temperature. Reduced energy expenditure is explained in part by OXPHOS deficiencies in *Wars2*$^{V117L/V117L}$ tissues but it doesn't explain why the mice are lean. In order to address this question further work must be done to address whether *Wars2*$^{V117L/V117L}$ mice have reduced energy intake. Several gastrointestinal phenotypes have been found in humans with mitochondrial disease including gastroesophageal sphincter dysfunction, constipation, dysphagia, vomiting, gastroparesis and diarrhoea (Finsterer & Frank, 2017). It is possible that *Wars2*$^{V117L/V117L}$ mice have

reduced body mass due to a, yet to be identified, gastrointestinal phenotype resulting in reduced calorific uptake. To access this, paired feeding studies should be performed to determine whether *Wars2*$^{V117L/V117L}$ mice have the reduced calorific intake. In addition to this, faecal calorific content should be analysed using bomb calorimetry to measure intestinal calorific absorption. Through doing so it will be possible to say whether reduced energy uptake in the cause of the reduced body mass phenotype observed in *Wars2*$^{V117L/V117L}$ mice. Furthermore, this may provide an explanation for low BMI in human patients with mitochondrial disease (Wolny et al., 2009).

6.2.2 OXPHOS deficiencies in *Wars2*$^{V117L/V117L}$ kidney

Only mild OPXHOS deficiencies were observed in *Wars2*$^{V117L/V117L}$ whole kidney homogenates despite reduced levels of mt-TrpRS protein. Whilst it is possible that there is still sufficient mt-TrpRS activity within the kidney to sustain mitochondrial translation it is also possible that there are cell-type specific effects within the kidney that were not detectable by western blot analysis using whole kidney homogenates. To address this possibility, COX/SDH staining of kidney tissue sections must be performed to identify whether there are cell types within the kidney of *Wars2*$^{V117L/V117L}$ mice with OXPHOS deficiencies. Although no abnormal pathology was observed histologically in *Wars2*$^{V117L/V117L}$ kidney, very little work has been done to test kidney function. In order to compliment the COX/SDH staining, additional phenotyping tests should be performed to ascertain whether kidney function is affected in these mice, for example albuminuria assays should be performed to assess functionality of the renal glomerular filtration permeability barrier.

6.2.3 Additional liver phenotyping

Liver pathology and function was not extensively tested in *Wars2*$^{V117L/V117L}$ mice. Histological analysis did show inflammatory cell foci in *Wars2*$^{V117L/V117L}$ mice however the presence of this abnormal pathology was comparable to littermate controls and deemed to be in accordance with expected levels for the mouse strain used in this study. However, substantial OXPHOS deficiencies were observed in the liver of *Wars2*$^{V117L/V117L}$ mice and plasma biochemistry showed increased KB likely due to increased hepatic ketogenesis and elevated plasma FGF21 levels. Furthermore, *Wars2*$^{V117L/V117L}$ mice had lower fasted plasma glucose levels which could be caused by impaired gluconeogenesis in the liver. Therefore, despite the fact that we did not observe any outstanding liver pathology via histology, there is certainly evidence to suggest that liver function is effected in the *Wars2*$^{V117L/V117L}$ mic. In human studies it has been shown that patients with NAFLD, and more specifically NASH, have reduced mitochondrial OXPHOS enzyme activities in liver which likely contributes for hepatic lipid accumulation and inflammation (Pérez-Carreras et al., 2003). NASH is characterised by hepatic inflammation, cell damage and fat accumulation. Future work should therefore aim to assess whether features of NASH, as well as other potential liver phenotypes, are observed in *Wars2*$^{V117L/V117L}$ mice. This should include measuring plasma ALT and AST levels. Plasma ALT and AST levels are increased by hepatic inflammation. Also additional histopathology should be performed to detect hepatic fibrosis such as Picrosirius red and TUNEL staining. Furthermore, liver lipid levels should be assessed using triglyceride and cholesterol assays to determine whether the OXPHOS deficiencies observed in *Wars2*$^{V117L/V117L}$ cause fatty liver. Through doing so, it will be possible to better characterise liver function in *Wars2*$^{V117L/V117L}$ mice and it may also provide insight as to whether hepatic mitochondrial dysfunction is a cause or consequence of NAFLD.

6.2.4 Mt-TrpRS in skeletal muscle

Mitochondrial OXPHOS deficiencies were not observed in *Wars2*$^{V117L/V117L}$ skeletal muscle which is explained by the presence of mt-TrpRS protein. However, mRNA levels of *Wars2*-FL transcripts were reduced in skeletal muscle. Future experiments are required to explain these contradictory results. There are two potential explanations. Firstly, there could be a skeletal specific mt-TrpRS isoform. To test this hypothesis, WB analysis should be performed using a high percentage polyacrylamide gel electrophoresis to determine whether the size of mt-TrpRS protein is different in skeletal muscle compared to other tissues. Additionally, northern blot analysis should be performed to determine whether there are alternate *Wars2* mRNA transcripts in skeletal muscle. The second explanation is that mt-TrpRS protein is post-translationally regulated in skeletal muscle by either protein-protein interaction or post-translational modification. To test this hypothesis, mt-TrpRS pull-down followed by mass-spectrometry analysis should be performed to identify potential mt-TrpRS binding partners and post-translational modification in skeletal muscle. Furthermore, in order to confirm that there is in fact no OXPHOS dysfunction in *Wars2*$^{V117L/V117L}$ skeletal muscle, COX/SDH staining and OXPHOS enzyme activity assays should be performed to compliment OXPHOS steady state protein analysis shown in this thesis.

6.2.5 Does the *Wars2-V117L* mutation cause inhibition of mitochondrial translation *in vivo?*

Throughout this study, western blot analysis of nDNA and mtDNA encoded OXPHOS proteins has been used as an indicator of mt-TrpRS activity and mitochondrial translation. However, we did not show that reduced mt-TrpRS steady state protein levels caused reduced mt-TrpRS activity or inhibition of mitochondrial translation *in vivo*. To test mt-TrpRS aminoacylation activity, northern blot analysis should be performed to quantify the levels of aminoacylated mt-tRNA^{Trp} in in *Wars2*$^{V117L/V117L}$ tissues. To assess mitochondrial translation *in vivo,* mitochondria should be isolated from *Wars2*$^{V117L/V117L}$ tissues and incubated with

^{35}S-Methionine and ^{35}S-cysteine to label *de novo* products of mitochondrial translation which can then be quantified. Through doing so we will be able to determine whether reduced mt-TrpRS protein causes inhibition of mitochondrial translation and whether this occurs is a tissue specific manner.

6.2.6 Does the *Wars2*-V117L mutation effect angiogenesis?

Recently, Wang *et al* published data indicating that *Wars2* function is a determinant of angiogenesis in rat and zebra fish (M. Wang et al., 2016). They showed that low coronary flow, as observed in spontaneously hypertensive rat (SHR) model, mapped to a L53F missense mutation in the rat *Wars2* gene. Coronary flow correlates with capillary density which is dependent upon angiogenic vessel formation. The identified *Wars2*-L53F mutation was located within the highly conserved ATP-binding 'HXGH' motif in WARS2 protein and caused a 40% reduction in WARS2 protein ATP hydrolysis enzyme activity. Following on from this, they showed that the *Wars2* knockdown caused impaired proliferation, increased cell death, abnormal cell morphology, reduced mitochondrial OXPHOS function and reduced angiogenic potential in a human endothelial cell immortalised line. Furthermore, they showed that that *Wars2* knock-down caused pericardial oedema, cardia contractile failure and early death in zebrafish. They characterised the cardiac phenotype in zebrafish further and showed that *Wars2* knockdown caused impaired angiogenesis outside the heart and caused separation of the endocardial and myocardial cell layer within the heart(M. Wang et al., 2016). Together these findings show that reduced *Wars2* impairs angiogenesis in *in vitro* and *in vivo* models.

In this thesis, the effect of the *Wars2*-V117L mutation on angiogenesis has not been examined. However, future experiments must focus on determining whether the *Wars2*-V117L mutation causes similar reductions in endothelial cell angiogenic potential as reported in this study to firstly validate these findings but also to determine whether impaired angiogenesis contributes to phenotypes identified in the *Wars2*$^{V117L/V117L}$ mice. A study from

Sano et al showed that impaired angiogenesis, through p53 induction, is critical in the transition of hypertrophic cardiomyopathy into heart failure (Sano et al., 2007). Together with finding that *Wars2* knock-down caused a fatal cardiac phenotype in zebrafish, these data implicate impaired angiogenesis as a potential contributing factor to the hypertrophic cardiomyopathy phenotype observed in *Wars2*$^{V117L/V117L}$ mice. Furthermore, adipose tissue mass and development is highly dependent upon on angiogenesis. For example, administration of antiangiogenic agents caused dose dependant weight loss and reduced adipose tissue mass in the ob/ob mice. As well as reduced adipose tissue mass, administration of antiangiogenic agents caused marked remodelling of adipose tissue vasculature and reduced proliferation of adipose tissue endothelial cells (Rupnick et al., 2002). Reduced angiogenesis could certainly contribute to the reduced adiposity phenotype observed in *Wars2*$^{V117L/V117L}$ mice. In order to assess whether the *Wars2*-V117L mutation causes impaired angiogenesis *in vivo*, additional histochemical analysis could be performed. For example, immunohistochemical analysis of endothelial cell number in heart and adipose tissue could be quantified using endothelial cell markers such as von Willebrand factor (VWF) antibodies to stain endothelial cells and blood vessel morphology could be assessed by staining blood vessels using a blood vessel staining kit (ECM590, Merck Millipore). Additionally, endothelial cells could be isolated from *Wars2*$^{V117L/V117L}$ cardiac tissue and cultured *in vitro* which would allow subsequent analysis of the cell intrinsic effects of the *Wars2*-V117L mutation on endothelial cell proliferation and angiogenic potential (Marelli-Berg, Peek, Lidington, Stauss, & Lechler, 2000).

6.3 Translational implications

There are several translational implications of the work presented in this thesis. The first translational implication of this study is that it may now be possible to identify human patients with *WARS2* mutations based upon this phenotype profile. In this study we showed that loss-of-function *Wars2* alleles caused hypertrophic cardiomyopathy, sensorineural

hearing loss and reduced adiposity in mice. Individually each of these phenotypes have been observed in human patients with mtRS mutations, but not in combination. By identifying human patients with *WARS2* alleles associated with hypertrophic cardiomyopathy, sensorineural hearing loss and reduced adiposity would confirm that the mouse can model human mtRS patients and would expand the scope for future mouse studies in the future. Furthermore, it would expand the clinical criteria associated with mtRS mutations in the future that could lead to correct diagnosis.

Currently the main treatments for patients with mitochondrial diseases aim to alleviate symptoms rather than prevent disease-causing mechanisms. We have evidence to suggest that up-regulation of PGC1a and mitochondrial biogenesis prevented / protected against mitochondrial dysfunction in *Wars2*$^{V117L/V117L}$ iWAT, MEFs and possibly skeletal muscle. This is also consistent with observations on increased mtDNA:nDNA copy number observed in the skeletal muscle of some patients with mtRS mutations. Although this mechanism requires further validation and examination, it suggests that stimulation of PGC1a activity and mitochondrial biogenesis could be a viable therapeutic strategy to treat patients with mtRS mutations.

The concept of up-regulating mitochondrial biogenesis in order to treat mitochondrial diseases is not a new one. Bastin *el al* have shown that treatment of patient cells with OXPHOS deficiencies with the PPAR agonist bezafibrate, increased PGC1a mRNA expression and resulted in increased OXPHOS enzyme activities (Bastin, Aubey, Rötig, Munnich, & Djouadi, 2008). Dietary supplementation with the NAD^+ precursor nicotinamide riboside (NR) has also been shown to be a successful alternate strategy of stimulating PGC1a activity and mitochondrial biogenesis via SIRT activation in mice. Cerutti *et al* showed that dietary supplementation with NR stimulated mitochondrial biogenesis and attenuated CIV deficiencies in the *Sco2* knockout/knockin mouse model of mitochondrial myopathy, resulting in increased exercise tolerance (Cerutti et al., 2014). Similarly, Khan *et*

al showed that dietary supplementation with NR stimulated mitochondrial biogenesis and increased OXPHOS steady state protein levels in the *Deletor* mouse model of mitochondrial myopathy that carry a dominant patient mutation in the mitochondrial replicative helicase Twinkle, to ameliorate phenotypic markers of mitochondrial myopathy (Khan et al., 2014). Interestingly in both studies, NR treatment also stimulated activation of the UPR^{mt} suggesting that activation of the UPR^{mt} contributes to therapeutic benefit of NR treatment. In this study we compared the disease causing mechanisms active in the *Dars2*-KO heart with the *Wars2*$^{V117L/V117L}$ heart. Our data suggests that the reason for the increased severity of the cardiac phenotype observed in the *Dars2*-KO model compared to the *Wars2*$^{V117L/V117L}$ model is because of disrupted mitochondrial proteostasis. If this is indeed true, then dietary supplementation with NR could be a viable therapeutic strategy for mtRS patients with acute phenotypes as it could not only stimulate mitochondrial biogenesis but alleviate mitochondrial proteostatic stress through UPR^{mt} activation.

I propose that in the future, therapeutic administration of benzafibrate and / or NR dietary supplementation should be used to test the hypothesis that up-regulation of mitochondrial biogenesis can prevent OXPHOS deficiencies and disease pathology in *Wars2*$^{V117L/V117L}$ and Wars2$^{V117L/-}$ mice. If this is indeed true, then stimulation of mitochondrial biogenesis may be a viable therapeutic strategy for patients with mtRS mutations.

6.4 What determines the tissue-specific pathology observed in patients with mtRS mutations?

In the *Wars2*$^{V117L/V117L}$ mice we observed tissue specific mechanisms that are associated with disease pathology such as the ISR. We also identified pathways that compensated or protected tissues from the deleterious effects of the *Wars2*-V117L allele such up-regulation of the *Pgc1a*. Whilst this may explain why there is tissue specific pathology in

Wars2$^{V117L/V117L}$ mouse model it doesn't explain why mutations in different mtRS genes cause different clinical pathologies in humans. A possible explanation for this phenomenon is that different mtRS genes are differentially regulated in a tissue specific manner and that regulation of the mtRS genes / proteins is more complex than is currently acknowledged.

To my knowledge, very little is known about how mtRS genes are transcriptionally, post-transcriptionally or post-translationally regulated. Given the 'house-keeping' nature of mtRS proteins and the fact that they are all required for the same process, mitochondrial translation, one might expect that all mtRS genes are co-operatively regulated and that the mechanism(s) through which they are regulated are conserved in all tissues. However, I believe that there is evidence to suggest that this is not the case.

In my introduction, I presented RNseq expression data showing the median expression of mtRS mRNA transcripts in human tissues. The pattern of expression for each mtRS gene across all tissues was distinct. If mtRS genes were transcriptionally co-regulated, then the pattern of expression across all tissues would be the same for all mtRS genes irrespective of actual transcript levels. The fact that this is not the case suggests that mtRS genes are not transcriptionally co-regulated and that different transcription factors govern the expression of different mtRS genes in different tissues. If this indeed the case, then it is also likely that mtRS genes are differentially regulated down-stream of stress response mechanisms such as the ISR, mitochondrial biogenesis or UPR^{mt}.

There is also evidence that mtRS genes are regulated post-transcriptionally by alternate splicing. In this study we showed that wild-type *Wars2* mRNA is post-transcriptionally regulated through splicing. This was shown by the fact that additional *Wars2* mRNA transcripts were identified in *Wars2*$^{+/+}$ MEFs. There is also evidence that other aminoacyl-tRNA synthetases are regulated through splicing such as *KARS*. *KARS* is alternatively spliced to produce two isoforms, a cytoplasmic isoform that requires splicing from exon 1

to exon 3 and a mitochondrial isoform that includes exons 1, 2 and 3 (Tolkunova, Park, Xia, King, & Davidson, 2000). These data indicate that mtRS genes may also be post-transcriptionally regulated by splicing adding another levels of complexity to their modes of regulation.

Finally, we have presented evidence to suggest that mtRS proteins may also be post-translationally regulated. In *Wars2*$^{V117L/V117L}$ skeletal muscle, there was increased mt-TrpRS protein despite reduced *Wars2*-FL mRNA. This showed that the expression levels of mt-TrpRS in *Wars2*$^{V117L/V117L}$ skeletal muscle were independent of *Wars2* mRNA and therefore possibly regulated post-translationally. If this hypothesis is true, then it likely that other mtRS proteins may also be regulated post-translationally. In order to confirm this hypothesis, co-immunoprecipitation of mt-TrpRS protein in *Wars2*$^{V117L/V117L}$ skeletal muscle could be performed to identify potential protein binding partners and mass-spectrometry analysis could be used to identify post-translational modifications.

Overall I believe that there is evidence that the regulation of mtRS genes / proteins is more complex than one would predict. If this is indeed true, then it is also likely that different mtRS genes are differentially regulated in response to different stress response mechanisms in different tissues. I believe that until we have a comprehensive understanding of how mtRS genes are transcriptionally, post-transcriptionally and post-translationally regulated in a ‘stressed’ and ‘non-stressed’ cellular environment, that the relationship between mtRS mutations and tissue specific pathology will remain ‘unexplained’.

Bibliography

Ahn, B. H., Kim, H. S., Song, S., Lee, I. H., Liu, J., Vassilopoulos, A., … Finkel, T. (2008). A role for the mitochondrial deacetylase Sirt3 in regulating energy homeostasis. *Proc Natl Acad Sci U S A*, *105*(38), 14447–14452. https://doi.org/10.1073/pnas.0803790105

Alerting, E. (2005). Human mitochondrial tRNA Met is exported to the cytoplasm and associates with the Argonaute 2 protein Human mitochondrial tRNA Met is exported to the cytoplasm and associates with the Argonaute 2 protein. *Rna*, 849–852. https://doi.org/10.1261/rna.2210805.To

Almalki, A., Alston, C. L., Parker, A., Simonic, I., Mehta, S. G., He, L., … Chrzanowska-Lightowlers, Z. M. A. (2014). Mutation of the human mitochondrial phenylalanine-tRNA synthetase causes infantile-onset epilepsy and cytochrome c oxidase deficiency. *Biochimica et Biophysica Acta - Molecular Basis of Disease*, *1842*(1), 56–64. https://doi.org/10.1016/j.bbadis.2013.10.008

Anderson, S., Bankier, A. T., Barrell, B. G., de Bruijn, M. H., Coulson, A. R., Drouin, J., … Young, I. G. (1981). Sequence and organization of the human mitochondrial genome. *Nature*, *290*(5806), 457–465. https://doi.org/10.1038/290457a0

Anitori, R., Manning, K., Quan, F., Weleber, R. G., Buist, N. R. M., Shoubridge, E. A., & Kennaway, N. G. (2005). Contrasting phenotypes in three patients with novel mutations in mitochondrial tRNA genes. *Molecular Genetics and Metabolism*, *84*(2), 176–188. https://doi.org/10.1016/j.ymgme.2004.10.003

Barberan-Soler, S., & Zahler, A. M. (2008). Alternative splicing regulation during C. elegans development: Splicing factors as regulated targets. *PLoS Genetics*, *4*(2). https://doi.org/10.1371/journal.pgen.1000001

Bartelt, A., Bruns, O. T., Reimer, R., Hohenberg, H., Ittrich, H., Peldschus, K., … Heeren, J. (2011). Brown adipose tissue activity controls triglyceride clearance. *Nat Med*, *17*(2), 200–205. https://doi.org/10.1038/nm.2297

Baruffini, E., Dallabona, C., Invernizzi, F., Yarham, J. W., Melchionda, L., Blakely, E. L., … Ghezzi, D. (2013). MTO1 mutations are associated with hypertrophic cardiomyopathy and lactic acidosis and cause respiratory chain deficiency in humans and yeast. *Human Mutation*, *34*(11), 1501–1509. https://doi.org/10.1002/humu.22393

Bastin, J., Aubey, F., Rötig, A., Munnich, A., & Djouadi, F. (2008). Activation of peroxisome proliferator-activated receptor pathway stimulates the mitochondrial respiratory chain and can correct deficiencies in patients' cells lacking its components. *Journal of Clinical Endocrinology and Metabolism*, *93*(4), 1433–1441. https://doi.org/10.1210/jc.2007-1701

Bayat, V., Thiffault, I., Jaiswal, M., Tétreault, M., Donti, T., Sasarman, F., … Bellen, H. J. (2012). Mutations in the mitochondrial methionyl-tRNA synthetase cause a neurodegenerative phenotype in flies and a recessive ataxia (ARSAL) in humans. *PLoS Biology*, *10*(3). https://doi.org/10.1371/journal.pbio.1001288

Belostotsky, R., Ben-Shalom, E., Rinat, C., Becker-Cohen, R., Feinstein, S., Zeligson, S., … Frishberg, Y. (2011). Mutations in the mitochondrial Seryl-tRNA synthetase cause hyperuricemia, pulmonary hypertension, renal failure in infancy and alkalosis, HUPRA syndrome. *American Journal of Human Genetics*, *88*(2), 193–200. https://doi.org/10.1016/j.ajhg.2010.12.010

Berlett, B. S., & Stadtman, E. R. (1997). Protein oxidation in aging, disease, and oxidative stress. *The Journal of Biological Chemistry*, *272*(33), 20313–20316. https://doi.org/10.1074/jbc.272.33.20313

Berson, A., De Beco, V., Letteron, P., Robin, M. A., Moreau, C., El Kahwaji, J., … Pessayre, D. (1998). Steatohepatitis-inducing drugs cause mitochondrial dysfunction and lipid peroxidation in rat hepatocytes. *Gastroenterology*, *114*(4 I), 764–774. https://doi.org/10.1016/S0016-5085(98)70590-6

Bhargava, K., Templeton, P., & Spremulli, L. L. (2004). Expression and characterization of isoform 1 of human mitochondrial elongation factor G. *Protein Expression and Purification*, *37*(2), 368–376. https://doi.org/10.1016/j.pep.2004.06.030

Bibb, M. J., Van Etten, R. A., Wright, C. T., Walberg, M. W., & Clayton, D. A. (1981). Sequence and gene organization of mouse mitochondrial DNA. *Cell*, *26*(2 PART 2), 167–180. https://doi.org/10.1016/0092-8674(81)90300-7

Blakely, E. L., Yarham, J. W., Alston, C. L., Craig, K., Poulton, J., Brierley, C., … Taylor, R. W. (2013). Pathogenic mitochondrial tRNA point mutations: Nine novel mutations affirm their importance as a cause of mitochondrial disease. *Human Mutation*, *34*(9), 1260–1268. https://doi.org/10.1002/humu.22358

Borglum, A. D., Flint, T., Tommerup, N., Fleckner, J., Justesen, J., & Kruse, T. A. (1996). Assignment of the human tryptophanyl-{tRNA} synthetase gene ({WARS}) to chromosome 14q32.2-{>}q32.32. *CYTOGENETICS AND CELL GENETICS*, *73*(1–2), 99–103. https://doi.org/10.1159/000134317

Brandon, M. C., Lott, M. T., Nguyen, K. C., Spolim, S., Navathe, S. B., Baldi, P., & Wallace, D. C. (2005). MITOMAP: a human mitochondrial genome database--2004 update. *Nucleic Acids Research*, *33*(Database issue), D611-3. https://doi.org/10.1093/nar/gki079

Bromberg, Y., & Rost, B. (2007). SNAP: Predict effect of non-synonymous polymorphisms on function. *Nucleic Acids Research*, *35*(11), 3823–3835. https://doi.org/10.1093/nar/gkm238

Brown, W. M., George, M., & Wilson, a C. (1979). Rapid evolution of animal mitochondrial DNA. *Proceedings of the National Academy of Sciences of the United States of America*, *76*(4), 1967–71. https://doi.org/10.1098/rspb.2007.0169

Bykhovskaya, Y., Casas, K., Mengesha, E., Inbal, A., & Fischel-Ghodsian, N. (2004). Missense mutation in pseudouridine synthase 1 (PUS1) causes mitochondrial myopathy and sideroblastic anemia (MLASA). *American Journal of Human Genetics*, *74*(6), 1303–8. https://doi.org/10.1086/421530

Caldwell, S. H., Swerdlow, R. H., Khan, E. M., Iezzoni, J. C., Hespenheide, E. E., Parks, J. K., & Parker, W. D. (1999). Mitochondrial abnormalities in non-alcoholic steatohepatitis. *Journal of Hepatology*, *31*(3), 430–434. https://doi.org/10.1016/S0168-8278(99)80033-6

Calfon, M., Zeng, H., Urano, F., Till, J. H., Hubbard, S. R., Harding, H. P., … Ron, D. (2002). IRE1 couples endoplasmic reticulum load to secretory capacity by processing the XBP-1 mRNA. *Nature*, *415*(6867), 92–96. https://doi.org/10.1038/nature01193

Cassandrini, D., Cilio, M. R., Bianchi, M., Doimo, M., Balestri, M., Tessa, A., … Bertini, E. (2013). Pontocerebellar hypoplasia type 6 caused by mutations in RARS2: Definition of the clinical spectrum and molecular findings in five patients. *Journal of Inherited Metabolic Disease*, *36*(1), 43–53. https://doi.org/10.1007/s10545-012-9487-9

Cerutti, R., Pirinen, E., Lamperti, C., Marchet, S., Sauve, A. A., Li, W., … Zeviani, M. (2014). NAD+-dependent activation of Sirt1 corrects the phenotype in a mouse model of mitochondrial disease. *Cell Metabolism*, *19*(6), 1042–1049. https://doi.org/10.1016/j.cmet.2014.04.001

Chang, D. D., Hixson, J. E., & Clayton, D. A. (1986). Minor transcription initiation events indicate that both human mitochondrial promoters function bidirectionally. *Molecular and Cellular Biology*, *6*(1), 294–301. Retrieved from http://eutils.ncbi.nlm.nih.gov/entrez/eutils/elink.fcgi?dbfrom=pubmed&id=3785149&retmode=ref&cmd=prlinks

Chinnery, P. F., Johnson, M. A., Wardell, T. M., Singh-Kler, R., Hayes, C., Brown, D. T., … Turnbull, D. M. (2000). The epidemiology of pathogenic mitochondrial DNA mutations. *Annals of Neurology*, *48*(2), 188–193. https://doi.org/10.1002/1531-8249(200008)48:2<188::AID-ANA8>3.0.CO;2-P

Corral-Debrinski, M., Shoffner, J. M., Lott, M. T., & Wallace, D. C. (1992). Association of mitochondrial DNA damage with aging and coronary atherosclerotic heart disease. *Mutation Research DNAging*, *275*(3–6), 169–180. https://doi.org/10.1016/0921-8734(92)90021-G

Corral-Debrinski, M., Stepien, G., Shoffner, J. M., Lott, M. T., Kanter, K., & Wallace, D. C. (1991). Hypoxemia is associated with mitochondrial DNA damage and gene induction.

Implications for cardiac disease. *JAMA : The Journal of the American Medical Association*, *266*(13), 1812–6. Retrieved from http://www.ncbi.nlm.nih.gov/pubmed/1890710

Coughlin, C. R., Scharer, G. H., Friederich, M. W., Yu, H.-C., Geiger, E. A., Creadon-Swindell, G., … Shaikh, T. H. (2015). Mutations in the mitochondrial cysteinyl-tRNA synthase gene, CARS2, lead to a severe epileptic encephalopathy and complex movement disorder. *Journal of Medical Genetics*, *52*(8), 532–40. https://doi.org/10.1136/jmedgenet-2015-103049

Curbo, S., Lagier-Tourenne, C., Carrozzo, R., Palenzuela, L., Lucioli, S., Hirano, M., … Johansson, M. (2006). Human mitochondrial pyrophosphatase: cDNA cloning and analysis of the gene in patients with mtDNA depletion syndromes. *Genomics*, *87*(3), 410–416. https://doi.org/10.1016/j.ygeno.2005.09.017

Cypess, A. M., Lehman, S., Williams, G., Tal, I., Rodman, D., Goldfine, A. B., … Kahn, C. R. (2009). Identification and Importance of Brown Adipose Tissue in Adult Humans. *New England Journal of Medicine*, *360*(15), 1509–1517. https://doi.org/10.1056/NEJMoa0810780

Dallabona, C., Diodato, D., Kevelam, S. H., Haack, T. B., Wong, L. J., Salomons, G. S., … Van Der Knaap, M. S. (2014). Novel (ovario) leukodystrophy related to AARS2 mutations. *Neurology*, *82*(23), 2063–2071. https://doi.org/10.1212/WNL.0000000000000497

Davis, R. L., Liang, C., Edema-Hildebrand, F., Riley, C., Needham, M., & Sue, C. M. (2013). Fibroblast growth factor 21 is a sensitive biomarker of mitochondrial disease. *Neurology*, *81*(21), 1819–1826. https://doi.org/10.1212/01.wnl.0000436068.43384.ef

Del Mar O'Callaghan, M., Emperador, S., López-Gallardo, E., Jou, C., Buján, N., Montero, R., … Montoya, J. (2012). New mitochondrial DNA mutations in tRNA associated with three severe encephalopamyopathic phenotypes: Neonatal, infantile, and childhood onset. *Neurogenetics*, *13*(3), 245–250. https://doi.org/10.1007/s10048-012-0322-0

Dennerlein, S., Rozanska, A., Wydro, M., Chrzanowska-Lightowlers, Z. M. A., & Lightowlers, R. N. (2010). Human ERAL1 is a mitochondrial RNA chaperone involved in the assembly of the 28S small mitochondrial ribosomal subunit. *The Biochemical Journal*, *430*(3), 551–558. https://doi.org/10.1042/BJ20100757

DiMauro, S., & Schon, E. A. (2003). Mitochondrial Respiratory-Chain Diseases. *New England Journal of Medicine*, *348*(26), 2656–2668. https://doi.org/10.1056/NEJMra022567

Diodato, D., Melchionda, L., Haack, T. B., Dallabona, C., Baruffini, E., Donnini, C., … Ghezzi, D. (2014). VARS2 and TARS2 Mutations in Patients with Mitochondrial Encephalomyopathies. *Human Mutation*, *35*(8), 983–989.

https://doi.org/10.1002/humu.22590

Dogan, S. A., Pujol, C., Maiti, P., Kukat, A., Wang, S., Hermans, S., … Trifunovic, A. (2014). Tissue-specific loss of DARS2 activates stress responses independently of respiratory chain deficiency in the heart. *Cell Metabolism*, *19*(3), 458–469. https://doi.org/10.1016/j.cmet.2014.02.004

Dubrovsky, E. B., Dubrovskaya, V. A., Levinger, L., Schiffer, S., & Marchfelder, A. (2004). Drosophila Rnase Z processes mitochondrial and nuclear pre-tRNA 3' ends in vivo. *Nucleic Acids Research*, *32*(1), 255–262. https://doi.org/10.1093/nar/gkh182

Edvardson, S., Shaag, A., Kolesnikova, O., Gomori, J. M., Tarassov, I., Einbinder, T., … Elpeleg, O. (2007). Deleterious mutation in the mitochondrial arginyl-transfer RNA synthetase gene is associated with pontocerebellar hypoplasia. *American Journal of Human Genetics*, *81*(4), 857–62. https://doi.org/10.1086/521227

Ekstrand, M. I., Falkenberg, M., Rantanen, A., Park, C. B., Gaspari, M., Hultenby, K., … Larsson, N. G. (2004). Mitochondrial transcription factor A regulates mtDNA copy number in mammals. *Human Molecular Genetics*, *13*(9), 935–944. https://doi.org/10.1093/hmg/ddh109

Elliott, H. R., Samuels, D. C., Eden, J. A., Relton, C. L., & Chinnery, P. F. (2008). Pathogenic Mitochondrial DNA Mutations Are Common in the General Population. *American Journal of Human Genetics*, *83*(2), 254–260. https://doi.org/10.1016/j.ajhg.2008.07.004

Elo, J. M., Yadavalli, S. S., Euro, L., Isohanni, P., Götz, A., Carroll, C. J., … Suomalainen, A. (2012). Mitochondrial phenylalanyl-trna synthetase mutations underlie fatal infantile alpers encephalopathy. *Human Molecular Genetics*, *21*(20), 4521–4529. https://doi.org/10.1093/hmg/dds294

Eriani, G., Delarue, M., Poch, O., Gangloff, J., & Moras, D. (1990). Partition of tRNA synthetases into two classes based on mutually exclusive sets of sequence motifs. *Letters to Nature*, *347*, 203–206. https://doi.org/10.1038/346183a0

Falkenberg, M., Gaspari, M., Rantanen, A., Trifunovic, A., Larsson, N.-G., & Gustafsson, C. M. (2002). Mitochondrial transcription factors B1 and B2 activate transcription of human mtDNA. *Nat. Genet*, *31*(3), 289–294. https://doi.org/10.1038/ng909

Fedorenko, A., Lishko, P. V., & Kirichok, Y. (2012). Mechanism of fatty-acid-dependent UCP1 uncoupling in brown fat mitochondria. *Cell*, *151*(2), 400–413. https://doi.org/10.1016/j.cell.2012.09.010

Finley, L. W. S., Haas, W., Desquiret-Dumas, V., Wallace, D. C., Procaccio, V., Gygi, S. P., & Haigis, M. C. (2011). Succinate dehydrogenase is a direct target of sirtuin 3 deacetylase activity. *PLoS ONE*, *6*(8), 4–9. https://doi.org/10.1371/journal.pone.0023295

Finsterer, J., & Frank, M. (2017). Gastrointestinal manifestations of mitochondrial disorders: a systematic review. *Therapeutic Advances in Gastroenterology*, *10*(1), 142–154. https://doi.org/10.1177/1756283X16666806

Fisher, F. F., Kleiner, S., Douris, N., Fox, E. C., Mepani, R. J., Verdeguer, F., … Spiegelman, B. M. (2012). FGF21 regulates PGC-1α and browning of white adipose tissues in adaptive thermogenesis. *Genes and Development*, *26*(3), 271–281. https://doi.org/10.1101/gad.177857.111

Fisher, R. P., & Clayton, D. A. (1985). A transcription factor required for promoter recognition by human mitochondrial RNA polymerase. Accurate initiation at the heavy- and light-strand promoters dissected and reconstituted in vitro. *Journal of Biological Chemistry*, *260*(20), 11330–11338.

Fisher, R. P., Topper, J. N., & Clayton, D. A. (1987). Promoter selection in human mitochondria involves binding of a transcription factor to orientation-independent upstream regulatory elements. *Cell*, *50*(2), 247–258. https://doi.org/10.1016/0092-8674(87)90220-0

Fleischman, A., Kron, M., Systrom, D. M., Hrovat, M., & Grinspoon, S. K. (2009). Mitochondrial function and insulin resistance in overweight and normal-weight children. *Journal of Clinical Endocrinology and Metabolism*, *94*(12), 4923–4930. https://doi.org/10.1210/jc.2009-1590

Folkman, L., Stantic, B., Sattar, A., & Zhou, Y. (2016). EASE-MM: Sequence-Based Prediction of Mutation-Induced Stability Changes with Feature-Based Multiple Models. *Journal of Molecular Biology*, *428*(6), 1394–1405. https://doi.org/10.1016/j.jmb.2016.01.012

Galmiche, L., Serre, V., Beinat, M., Assouline, Z., Lebre, A. S., Chretien, D., … Rötig, A. (2011). Exome sequencing identifies MRPL3 mutation in mitochondrial cardiomyopathy. *Human Mutation*, *32*(11), 1225–1231. https://doi.org/10.1002/humu.21562

Glamuzina, E., Brown, R., Hogarth, K., Saunders, D., Russell-Eggitt, I., Pitt, M., … Grunewald, S. (2012). Further delineation of pontocerebellar hypoplasia type 6 due to mutations in the gene encoding mitochondrial arginyl-tRNA synthetase, RARS2. *Journal of Inherited Metabolic Disease*, *35*(3), 459–467. https://doi.org/10.1007/s10545-011-9413-6

Götz, A., Tyynismaa, H., Euro, L., Ellonen, P., Hyötyläinen, T., Ojala, T., … Suomalainen, A. (2011). Exome sequencing identifies mitochondrial alanyl-tRNA synthetase mutations in infantile mitochondrial cardiomyopathy. *American Journal of Human Genetics*, *88*(5), 635–642. https://doi.org/10.1016/j.ajhg.2011.04.006

Guo, M., Chong, Y. E., Shapiro, R., Beebe, K., Yang, X.-L., & Schimmel, P. (2009). Paradox

of mistranslation of serine for alanine caused by AlaRS recognition dilemma. *Nature*, *462*(7274), 808–812. https://doi.org/10.1038/nature08612

Hallmann, K., Zsurka, G., Moskau-Hartmann, S., Kirschner, J., Korinthenberg, R., Ruppert, A. K., … Kunz, W. S. (2014). A homozygous splice-site mutation in CARS2 is associated with progressive myoclonic epilepsy. *Neurology*, *83*(23), 2183–2187. https://doi.org/10.1212/WNL.0000000000001055

Hammen, P. K., & Weiner, H. (1998). Mitochondrial leader sequences: structural similarities and sequence differences. *The Journal of Experimental Zoology*, *282*(March), 280–283. https://doi.org/10.1002/(SICI)1097-010X(199809/10)282:1/2<280::AID-JEZ30>3.0.CO;2-V [pii]

Haque, M. E., Grasso, D., & Spremulli, L. L. (2008). The interaction of mammalian mitochondrial translational initiation factor 3 with ribosomes: Evolution of terminal extensions in IF3mt. *Nucleic Acids Research*, *36*(2), 589–597. https://doi.org/10.1093/nar/gkm1072

Hardisty-Hughes, R. E., Parker, A., & Brown, S. D. M. (2010). A hearing and vestibular phenotyping pipeline to identify mouse mutants with hearing impairment. *Nature Protocols*, *5*(1), 177–90. https://doi.org/10.1038/nprot.2009.204

Harms, M., & Seale, P. (2013). Brown and beige fat: development, function and therapeutic potential. *Nat Med*, *19*(10), 1252–1263. https://doi.org/10.1038/nm.3361

He, J., Cooper, H. M., Reyes, A., Di Re, M., Kazak, L., Wood, S. R., … Holt, I. J. (2012). Human C4orf14 interacts with the mitochondrial nucleoid and is involved in the biogenesis of the small mitochondrial ribosomal subunit. *Nucleic Acids Research*, *40*(13), 6097–6108. https://doi.org/10.1093/nar/gks257

Herrero, J., Muffato, M., Beal, K., Fitzgerald, S., Gordon, L., Pignatelli, M., … Flicek, P. (2016). Ensembl comparative genomics resources. *Database*, *2016*. https://doi.org/10.1093/database/bav096

Herrmann, J. M., & Neupert, W. (2004). Protein Import into Mitochondria. *Encyclopedia of Biological Chemistry*, (Figure 2), 510–515. https://doi.org/10.1016/B0-12-443710-9/00545-7

Heuvel, L. P. Van Den, Ph, D., Shoubridge, E. A., & Ph, D. (2004). Mutant Mitochondrial Elongation Factor G1 and Combined Oxidative Phosphorylation Deficiency, 2080–2086.

Ho, Y. S., & Crapo, J. D. (1988). Isolation and characterization of complementary DNAs encoding human manganese-containing superoxide dismutase. *FEBS Letters*, *229*(2), 256–260. https://doi.org/10.1016/0014-5793(88)81136-0

Holt, I. J., Harding, a E., Petty, R. K., & Morgan-Hughes, J. a. (1990). A new mitochondrial disease associated with mitochondrial DNA heteroplasmy. *American Journal of*

Human Genetics, *46*(3), 428–33. Retrieved from http://www.pubmedcentral.nih.gov/articlerender.fcgi?artid=1683641&tool=pmcentrez&rendertype=abstract

Inagaki, T., Dutchak, P., Zhao, G., Ding, X., Gautron, L., Parameswara, V., … Kliewer, S. A. (2007). Endocrine Regulation of the Fasting Response by PPARα-Mediated Induction of Fibroblast Growth Factor 21. *Cell Metabolism*, *5*(6), 415–425. https://doi.org/10.1016/j.cmet.2007.05.003

Isohanni, P., Linnankivi, T., Buzkova, J., Lönnqvist, T., Pihko, H., Valanne, L., … Suomalainen, a. (2010). DARS2 mutations in mitochondrial leucoencephalopathy and multiple sclerosis. *Journal of Medical Genetics*, *47*(1), 66–70. https://doi.org/10.1136/jmg.2009.068221

Jacobs, H. T., Hutchin, T. P., Käppi, T., Gillies, G., Minkkinen, K., Walker, J., … Mueller, R. F. (2005). Mitochondrial DNA mutations in patients with postlingual, nonsyndromic hearing impairment. *European Journal of Human Genetics : EJHG*, *13*(1), 26–33. https://doi.org/10.1038/sj.ejhg.5201250

Jenkinson, E. M., Rehman, A. U., Walsh, T., Clayton-Smith, J., Lee, K., Morell, R. J., … Newman, W. G. (2013). Perrault syndrome is caused by recessive mutations in CLPP, encoding a mitochondrial ATP-dependent chambered protease. *American Journal of Human Genetics*, *92*(4), 605–613. https://doi.org/10.1016/j.ajhg.2013.02.013

Jorgensen, R., Søgaard, T. M., Rossing, a B., Martensen, P. M., & Justesen, J. (2000). Identification and characterization of human mitochondrial tryptophanyl-tRNA synthetase. *The Journal of Biological Chemistry*, *275*(22), 16820–6. Retrieved from http://www.ncbi.nlm.nih.gov/pubmed/10828066

Köhler, C., Heyer, C., Hoffjan, S., Stemmler, S., Löcke, T., Thiels, C., … Abicht, A. (2015). Early-onset leukoencephalopathy due to a homozygous missense mutation in the DARS2 gene. *Molecular and Cellular Probes*, *29*(5), 319–322. https://doi.org/10.1016/j.mcp.2015.06.005

K. Grohmann, F. Amalric, S. Crews, and G. A. (2013). Failure to detect “cap” structures in mitochondrial DNA-coded poly(A)-containing RNA from He La cells. *Journal of Chemical Information and Modeling*, *53*(9), 1689–1699. https://doi.org/10.1017/CBO9781107415324.004

Kalsotra, A., Xiao, X., Ward, A. J., Castle, J. C., Johnson, J. M., Burge, C. B., & Cooper, T. A. (2008). A postnatal switch of CELF and MBNL proteins reprograms alternative splicing in the developing heart BIOLOGY, *41*, 1–6.

Kastrissianakis, K., Anand, G., Quaghebeur, G., Price, S., Prabhakar, P., Marinova, J., … McShane, T. (2013). Subdural effusions and lack of early pontocerebellar hypoplasia in siblings with RARS2 mutations. *Archives of Disease in Childhood*, *98*(12), 1004–7.

https://doi.org/10.1136/archdischild-2013-304308

Keane, T. M., Goodstadt, L., Danecek, P., White, M. A., Wong, K., Yalcin, B., … Adams, D. J. (2011). Mouse genomic variation and its effect on phenotypes and gene regulation. *Nature*, *477*(7364), 289–94. https://doi.org/10.1038/nature10413

Kelley, D. E., He, J., Menshikova, E. V., & Ritov, V. B. (2002). Dysfunction of mitochondria in human skeletal muscle in type 2 diabetes. *Diabetes*, *51*(10), 2944–2950. https://doi.org/10.2337/diabetes.51.10.2944

Kendrick, A. A., Choudhury, M., Rahman, S. M., McCurdy, C. E., Friederich, M., Van Hove, J. L. K., … Jonscher, K. R. (2011). Fatty liver is associated with reduced SIRT3 activity and mitochondrial protein hyperacetylation. *The Biochemical Journal*, *433*(3), 505–14. https://doi.org/10.1042/BJ20100791

Khan, N. A., Auranen, M., Paetau, I., Pirinen, E., Euro, L., Forsström, S., … Suomalainen, A. (2014). Effective treatment of mitochondrial myopathy by nicotinamide riboside, a vitamin B3. *EMBO Molecular Medicine*, *6*(6), 721–731. https://doi.org/10.1002/emmm.201403943

Kharitonenkov, A., Shiyanova, T. L., Koester, A., Ford, A. M., Micanovic, R., Galbreath, E. J., … Shanafelt, A. B. (2005). FGF-21 as a novel metabolic regulator. *Journal of Clinical Investigation*, *115*(6), 1627–1635. https://doi.org/10.1172/JCI23606

Kim, K. H., Jeong, Y. T., Oh, H., Kim, S. H., Cho, J. M., Kim, Y.-N., … Lee, M.-S. (2013). Autophagy deficiency leads to protection from obesity and insulin resistance by inducing Fgf21 as a mitokine. *Nature Medicine*, *19*(December), 83–92. https://doi.org/10.1038/nm.3014

Koc, E. C., Burkhart, W., Blackburn, K., Moseley, a, Koc, H., & Spremulli, L. L. (2000). A proteomics approach to the identification of mammalian mitochondrial small subunit ribosomal proteins. *The Journal of Biological Chemistry*, *275*(42), 32585–91. https://doi.org/10.1074/jbc.M003596200

Koc, E. C., Burkhart, W., Blackburn, K., Moyer, M. B., Schlatzer, D. M., Moseley, A., & Spremulli, L. L. (2001). The large subunit of the mammalian mitochondrial ribosome: Analysis of the complement of ribosomal proteins present. *Journal of Biological Chemistry*, *276*(47), 43958–43969. https://doi.org/10.1074/jbc.M106510200

Koc, E. C., & Koc, H. (2012). Regulation of mammalian mitochondrial translation by post-translational modifications. *Biochimica et Biophysica Acta*, *1819*(9–10), 1055–66. https://doi.org/10.1016/j.bbagrm.2012.03.003

Koc, E. C., & Spremulli, L. L. (2003). RNA-binding proteins of mammalian mitochondria. *Mitochondrion*, *2*(4), 277–291. https://doi.org/S1567-7249(03)00005-9 [pii]\r10.1016/S1567-7249(03)00005-9

Konovalova, S., & Tyynismaa, H. (2013). Mitochondrial aminoacyl-tRNA synthetases in

human disease. *Molecular Genetics and Metabolism*. https://doi.org/10.1016/j.ymgme.2013.01.010

Kotani, T., Akabane, S., Takeyasu, K., Ueda, T., & Takeuchi, N. (2013). Human G-proteins, ObgH1 and Mtg1, associate with the large mitochondrial ribosome subunit and are involved in translation and assembly of respiratory complexes. *Nucleic Acids Research*, *41*(6), 3713–3722. https://doi.org/10.1093/nar/gkt079

Kumar, P., Henikoff, S., & Ng, P. C. (2009). Predicting the effects of coding non-synonymous variants on protein function using the SIFT algorithm. *Nature Protocols*, *4*(7), 1073–1081. https://doi.org/10.1038/nprot.2009.86

Kusio-Kobialka, M., Podszywalow-Bartnicka, P., Peidis, P., Glodkowska-Mrowka, E., Wolanin, K., Leszak, G., … Piwocka, K. (2012). The PERK-eIF2α phosphorylation arm is a pro-survival pathway of BCR-ABL signaling and confers resistance to imatinib treatment in chronic myeloid leukemia cells. *Cell Cycle*, *11*(21), 4069–4078. https://doi.org/10.4161/cc.22387

Labauge, P., Dorboz, I., Eymard-Pierre, E., Dereeper, O., & Boespflug-Tanguy, O. (2011). Clinically asymptomatic adult patient with extensive LBSL MRI pattern and DARS2 mutations. *Journal of Neurology*, *258*(2), 335–337. https://doi.org/10.1007/s00415-010-5755-5

Li, Z., Schonberg, R., Guidugli, L., Johnson, A. K., Arnovitz, S., Yang, S., … del Gaudio, D. (2015). A novel mutation in the promoter of RARS2 causes pontocerebellar hypoplasia in two siblings. *Journal of Human Genetics*, *60*(7), 363–369. https://doi.org/10.1038/jhg.2015.31

Liao, H. X., & Spremulli, L. L. (1989). Interaction of bovine mitochondrial ribosomes with messenger RNA. *Journal of Biological Chemistry*, *264*(13), 7518–7522.

Liao, H. X., & Spremulli, L. L. (1990). Identification and initial characterization of translational initiation factor 2 from bovine mitochondria. *Journal of Biological Chemistry*, *265*(23), 13618–13622.

Lim, S. C., Friemel, M., Marum, J. E., Tucker, E. J., Bruno, D. L., Riley, L. G., … Compton, A. G. (2013). Mutations in LYRM4, encoding iron-sulfur cluster biogenesis factor ISD11, cause deficiency of multiple respiratory chain complexes. *Human Molecular Genetics*, *22*(22), 4460–4473. https://doi.org/10.1093/hmg/ddt295

Lin, J., Chiconelli Faria, E., Da Rocha, A. J., Rodrigues Masruha, M., Pereira Vilanova, L. C., Scheper, G. C., & Van der Knaap, M. S. (2010). Leukoencephalopathy With Brainstem and Spinal Cord Involvement and Normal Lactate: A New Mutation in the DARS2 Gene. *Journal of Child Neurology*, *25*(11), 1425–1428. https://doi.org/10.1177/0883073810370897

Lu, P. D., Harding, H. P., & Ron, D. (2004). Translation reinitiation at alternative open

reading frames regulates gene expression in an integrated stress response, *167*(1), 27–33. https://doi.org/10.1083/jcb.200408003

Lundin, M., Baltscheffsky, H., & Ronne, H. (1991). Yeast PPA2 gene encodes a mitochondrial inorganic pyrophosphatase that is essential for mitochondrial function. *Journal of Biological Chemistry*, *266*(19), 12168–12172. https://doi.org/10.1177/019263650008462009

Ma, L., & Spremulli, L. L. (1995). Cloning and sequence analysis of the human mitochondrial translational initiation factor 2 cDNA. *J Biol Chem*, *270*(4), 1859–1865. Retrieved from http://www.ncbi.nlm.nih.gov/pubmed/7829522

Maassen, J. A., Hart, L. M., Essen, E. Van, Heine, R. J., Nijpels, G., Roshan, S., … Lemkes, H. H. P. J. (2004). Mitochondrial Diabetes, 103–109.

Maniura-Weber, K., Taylor, R. W., Johnson, M. a, Chrzanowska-Lightowlers, Z. M., Morris, A. a M., Charlton, C. P. J., … Bindoff, L. a. (2004). A novel point mutation in the mitochondrial tRNA(Trp) gene produces a neurogastrointestinal syndrome. *European Journal of Human Genetics : EJHG*, *12*(6), 509–12. https://doi.org/10.1038/sj.ejhg.5201185

Marelli-Berg, F. M., Peek, E., Lidington, E. A., Stauss, H. J., & Lechler, R. I. (2000). Isolation of endothelial cells from murine tissue. *Journal of Immunological Methods*, *244*(1–2), 205–215. https://doi.org/10.1016/S0022-1759(00)00258-1

Marnef, A., Jády, B. E., & Kiss, T. (2015). Human polypyrimidine tract-binding protein interacts with mitochondrial tRNAThr in the cytosol. *Nucleic Acids Research*, *44*(3), 1342–1353. https://doi.org/10.1093/nar/gkv1355

Martikainen, M. H., Ellfolk, U., & Majamaa, K. (2013). Impaired information-processing speed and working memory in leukoencephalopathy with brainstem and spinal cord involvement and elevated lactate (LBSL) and DARS2 mutations: A report of three adult patients. *Journal of Neurology*, *260*(8), 2078–2083. https://doi.org/10.1007/s00415-013-6940-0

Mashili, F. (2014). Direct effects of FGF21 on glucose uptake in human skeletal muscle: implications for type 2 diabetes and obesity. *Diabetes/Metabolism Research and Reviews*, *32*(30), 96–102. https://doi.org/10.1002/dmrr

McMurray, F., Church, C. D., Larder, R., Nicholson, G., Wells, S., Teboul, L., … Cox, R. D. (2013). Adult Onset Global Loss of the Fto Gene Alters Body Composition and Metabolism in the Mouse. *PLoS Genetics*, *9*(1). https://doi.org/10.1371/journal.pgen.1003166

Mita, S., Schmidt, B., Schon, E. A., DiMauro, S., & Bonilla, E. (1989). Detection of “deleted” mitochondrial genomes in cytochrome-c oxidase-deficient muscle fibers of a patient with Kearns-Sayre syndrome. *Proceedings of the National Academy of Sciences of*

the United States of America, *86*(23), 9509–13. https://doi.org/10.1073/pnas.86.23.9509

Miyake, N., Yamashita, S., Kurosawa, K., Miyatake, S., Tsurusaki, Y., Doi, H., … Matsumoto, N. (2011). A novel homozygous mutation of DARS2 may cause a severe LBSL variant. *Clinical Genetics*, *80*(3), 293–296. https://doi.org/10.1111/j.1399-0004.2011.01644.x

Mkaouar-Rebai, E., Chamkha, I., Kammoun, F., Kammoun, T., Aloulou, H., Hachicha, M., … Fakhfakh, F. (2009). Two new mutations in the MT-TW gene leading to the disruption of the secondary structure of the tRNATrp in patients with Leigh syndrome. *Molecular Genetics and Metabolism*, *97*(3), 179–184. https://doi.org/10.1016/j.ymgme.2009.03.003

Montoya, J., Ojala, D., & Attardi, G. (1981). Distinctive features of the 5' terminal sequences of the human mitochondrial mRNAs. *Nature*, *290*, 465–470.

Mootha, V. K., Lindgren, C. M., & Eriksson, K. F. (2003). PGC-1α-responsive genes involved in oxidative phosphorylation are coordinately downregulated in human diabetes. *… Genetics*, *34*(3), 267–273. https://doi.org/10.1038/ng1180

Murano, I., Barbatelli, G., Giordano, A., & Cinti, S. (2009). Noradrenergic parenchymal nerve fiber branching after cold acclimatisation correlates with brown adipocyte density in mouse adipose organ. *Journal of Anatomy*, *214*(1), 171–178. https://doi.org/10.1111/j.1469-7580.2008.01001.x

N.Z., L., C.L., A., K., S., S.-M., P., D., K., L., H., … R.W., T. (2015). Neuropathologic Characterization of Pontocerebellar Hypoplasia Type 6 Associated With Cardiomyopathy and Hydrops Fetalis and Severe Multisystem Respiratory Chain Deficiency due to Novel RARS2 Mutations. *Journal of Neuropathology and Experimental Neurology*, *74*(7), 688–703. https://doi.org/10.1097/NEN.0000000000000209

Nagaike, T., Suzuki, T., Katoh, T., & Ueda, T. (2005). Human mitochondrial mRNAs are stabilized with polyadenylation regulated by mitochondria-specific poly(A) polymerase and polynucleotide phosphorylase. *Journal of Biological Chemistry*, *280*(20), 19721–19727. https://doi.org/10.1074/jbc.M500804200

Nagao, A., Suzuki, T., Katoh, T., Sakaguchi, Y., & Suzuki, T. (2009). Biogenesis of glutaminyl-mt tRNAGln in human mitochondria. *Proceedings of the National Academy of Sciences of the United States of America*, *106*(38), 16209–16214. https://doi.org/10.1073/pnas.0907602106

Nagao, A., Suzuki, T., & Suzuki, T. (2007). Aminoacyl-tRNA surveillance by EF-Tu in mammalian mitochondria. *Nucleic Acids Symposium Series (2004)*, (51), 41–2. https://doi.org/10.1093/nass/nrm021

Nakajima, J., Eminoglu, T. F., Vatansever, G., Nakashima, M., Tsurusaki, Y., Saitsu, H., … Miyake, N. (2014). A novel homozygous YARS2 mutation causes severe myopathy, lactic acidosis, and sideroblastic anemia 2. *Journal of Human Genetics*, *59*(4), 229–32. https://doi.org/10.1038/jhg.2013.143

Nelson, I., Hanna, M. G., Alsanjari, N., Scaravilli, F., Morgan-Hughes, J. A., & Harding, A. E. (1995). A new mitochondrial DNA mutation associated with progressive dementia and chorea: A clinical, pathological, and molecular genetic study. *Annals of Neurology*, *37*(3), 400–403. https://doi.org/10.1002/ana.410370317

Newman, J. C., & Verdin, E. (2014). Ketone bodies as signaling metabolites. *Trends in Endocrinology and Metabolism*. https://doi.org/10.1016/j.tem.2013.09.002

Niccoli, T., & Partridge, L. (2012). Ageing as a risk factor for disease. *Current Biology*. https://doi.org/10.1016/j.cub.2012.07.024

Nishri, D., Goldberg-Stern, H., Noyman, I., Blumkin, L., Kivity, S., Saitsu, H., … Lev, D. (2016). RARS2 mutations cause early onset epileptic encephalopathy without ponto-cerebellar hypoplasia. *European Journal of Paediatric Neurology*, *20*(3), 412–417. https://doi.org/10.1016/j.ejpn.2016.02.012

O'Keefe, E. J., Hamilton, E. H., Lee, S. C., & Steinert, P. (1993). Trichohyalin: a structural protein of hair, tongue, nail, and epidermis. *J Invest Dermatol*, *101*(1 Suppl), 65S–71S. Retrieved from http://www.ncbi.nlm.nih.gov/pubmed/7686953

Osawa, S., Jukes, T. H., Watanabe, K., & Muto, a. (1992). Recent evidence for evolution of the genetic code. *Microbiological Reviews*, *56*(1), 229–264.

Oslowski, C. M., & Urano, F. (2011). Chapter Four - Measuring ER Stress and the Unfolded Protein Response Using Mammalian Tissue Culture System. In *The Unfolded Protein Response and Cellular Stress, Part B* (Vol. Volume 490, pp. 71–92). https://doi.org/http://dx.doi.org/10.1016/B978-0-12-385114-7.00004-0

Pellegrino, M. W., Nargund, A. M., & Haynes, C. M. (2013). Signaling the mitochondrial unfolded protein response. *Biochimica et Biophysica Acta - Molecular Cell Research*, *1833*(2), 410–416. https://doi.org/10.1016/j.bbamcr.2012.02.019

Pérez-Carreras, M., Del Hoyo, P., Martín, M. a, Rubio, J. C., Martín, A., Castellano, G., … Solis-Herruzo, J. a. (2003). Defective hepatic mitochondrial respiratory chain in patients with nonalcoholic steatohepatitis. *Hepatology (Baltimore, Md.)*, *38*(4), 999–1007. https://doi.org/10.1053/jhep.2003.50398

Perilli, G., Saraceni, C., Daniels, M. N., & Ahmad, A. (2013). Diabetic Ketoacidosis: A Review and Update. *Current Emergency and Hospital Medicine Reports*, *1*(1), 10–17. https://doi.org/10.1007/s40138-012-0001-3

Pierce, S. B., Chisholm, K. M., Lynch, E. D., Lee, M. K., Walsh, T., Opitz, J. M., … King, M. C. (2011). Mutations in mitochondrial histidyl tRNA synthetase HARS2 cause ovarian

dysgenesis and sensorineural hearing loss of Perrault syndrome. *Proc Natl Acad Sci U S A*, *108*(16), 6543–6548. https://doi.org/10.1073/pnas.1103471108

Pierce, S. B., Gersak, K., Michaelson-Cohen, R., Walsh, T., Lee, M. K., Malach, D., … Levy-Lahad, E. (2013). Mutations in LARS2, encoding mitochondrial leucyl-tRNA synthetase, lead to premature ovarian failure and hearing loss in Perrault syndrome. *American Journal of Human Genetics*, *92*(4), 614–620. https://doi.org/10.1016/j.ajhg.2013.03.007

Pierce, S. B., Walsh, T., Chisholm, K. M., Lee, M. K., Thornton, A. M., Fiumara, A., … King, M. C. (2010). Mutations in the DBP-deficiency protein HSD17B4 cause ovarian dysgenesis, hearing loss, and ataxia of perrault syndrome. *American Journal of Human Genetics*, *87*(2), 282–288. https://doi.org/10.1016/j.ajhg.2010.07.007

Potter, P. K., Bowl, M. R., Jeyarajan, P., Wisby, L., Blease, A., Goldsworthy, M. E., … Brown, S. D. M. (2016). Novel gene function revealed by mouse mutagenesis screens for models of age-related disease. *Nature Communications*, *7*, 12444. https://doi.org/10.1038/ncomms12444

Pütz, J., Dupuis, B., Sissler, M., & Florentz, C. (2007). Mamit-tRNA, a database of mammalian mitochondrial tRNA primary and secondary structures. *RNA (New York, N.Y.)*, *13*(8), 1184–90. https://doi.org/10.1261/rna.588407

Quirós, P. M., Mottis, A., & Auwerx, J. (2016). Mitonuclear communication in homeostasis and stress. *Nature Reviews. Molecular Cell Biology*, *17*(4), 213–226. https://doi.org/10.1038/nrm.2016.23

Rankin, J., Brown, R., Dobyns, W. B., Harington, J., Patel, J., Quinn, M., & Brown, G. (2010). Pontocerebellar hypoplasia type 6: A British case with PEHO-like features. *American Journal of Medical Genetics, Part A*, *152*(8), 2079–2084. https://doi.org/10.1002/ajmg.a.33531

Rath, E., Balzola, F., Bernstein, C., Ho, G. T., & Russell, R. K. (2012). Induction of dsRNA-activated protein kinase links mitochondrial unfolded protein response to the pathogenesis of intestinal inflammation: Commentary. *Inflammatory Bowel Disease Monitor*, *12*(3), 133–134. https://doi.org/10.1136/gutjnl-2011-300767

Riley, L. G., Cooper, S., Hickey, P., Rudinger-Thirion, J., McKenzie, M., Compton, A., … Christodoulou, J. (2010). Mutation of the mitochondrial tyrosyl-tRNA synthetase gene, YARS2, causes myopathy, lactic acidosis, and sideroblastic anemia - MLASA syndrome. *American Journal of Human Genetics*, *87*(1), 52–59. https://doi.org/10.1016/j.ajhg.2010.06.001

Riley, L. G., Menezes, M. J., Rudinger-Thirion, J., Duff, R., de Lonlay, P., Rotig, A., … Christodoulou, J. (2013). Phenotypic variability and identification of novel YARS2 mutations in YARS2 mitochondrial myopathy, lactic acidosis and sideroblastic

anaemia. *Orphanet Journal of Rare Diseases*, *8*, 193. https://doi.org/10.1186/1750-1172-8-193

Ritov, V. B., Menshikova, E. V., He, J., Ferrell, R. E., Goodpaster, B. H., & Kelley, D. E. (2005). Deficiency of subsarcolemmal mitochondria in obesity and type 2 diabetes. *Diabetes*, *54*(1), 8–14. https://doi.org/10.2337/diabetes.54.1.8

Rivera, H., Martín-Hernández, E., Delmiro, A., García-Silva, M. T., Quijada-Fraile, P., Muley, R., … Martínez-Azorín, F. (2013). A new mutation in the gene encoding mitochondrial seryl-tRNA synthetase as a cause of HUPRA syndrome. *BMC Nephrology*, *14*(1), 195. https://doi.org/10.1186/1471-2369-14-195

Rodgers, J. T., Lerin, C., Haas, W., Gygi, S. P., Spiegelman, B. M., & Puigserver, P. (2005). Nutrient control of glucose homeostasis through a complex of PGC-1a and SIRT1. *Nature*, *434*(7029), 113–118. https://doi.org/10.1038/nature03314.1.

Rorbach, J., Gammage, P. A., & Minczuk, M. (2012). C7orf30 is necessary for biogenesis of the large subunit of the mitochondrial ribosome. *Nucleic Acids Research*, *40*(9), 4097–4109. https://doi.org/10.1093/nar/gkr1282

Rupnick, M. A., Panigrahy, D., Zhang, C.-Y., Dallabrida, S. M., Lowell, B. B., Langer, R., & Folkman, M. J. (2002). Adipose tissue mass can be regulated through the vasculature. *Proceedings of the National Academy of Sciences of the United States of America*, *99*(16), 10730–5. https://doi.org/10.1073/pnas.162349799

Saada, a, Shaag, a, Arnon, S., Dolfin, T., Miller, C., Fuchs-Telem, D., … Elpeleg, O. (2007). Antenatal mitochondrial disease caused by mitochondrial ribosomal protein (MRPS22) mutation. *Journal of Medical Genetics*, *44*(12), 784–786. https://doi.org/10.1136/jmg.2007.053116

Sacconi, S., Salviati, L., Nishigaki, Y., Walker, W. F., Hernandez-Rosa, E., Trevisson, E., … Davidson, M. M. (2008). A functionally dominant mitochondrial DNA mutation. *Human Molecular Genetics*, *17*(12), 1814–1820. https://doi.org/10.1093/hmg/ddn073

Şahin, S., Cansu, A., Kalay, E., Dinçer, T., Kul, S., Çakır, İ. M., … Budak, G. Y. (2016). Leukoencephalopathy with thalamus and brainstem involvement and high lactate caused by novel mutations in the EARS2 gene in two siblings. *Journal of the Neurological Sciences*, *365*, 54–58. https://doi.org/10.1016/j.jns.2016.04.008

Saito, M., Okamatsu-Ogura, Y., Matsushita, M., Watanabe, K., Yoneshiro, T., Nio-Kobayashi, J., … Tsujisaki, M. (2009). High incidence of metabolically active brown adipose tissue in healthy adult humans: Effects of cold exposure and adiposity. *Diabetes*, *58*(7), 1526–1531. https://doi.org/10.2337/db09-0530

Sanaker, P. S., Nakkestad, H. L., Downham, E., & Bindoff, L. A. (2010). A novel mutation in the mitochondrial tRNA for tryptophan causing a late-onset mitochondrial encephalomyopathy. *Acta Neurologica Scandinavica*, *121*(2), 109–113.

https://doi.org/10.1111/j.1600-0404.2009.01243.x

Sano, M., Minamino, T., Toko, H., Miyauchi, H., Orimo, M., Qin, Y., … Komuro, I. (2007). p53-induced inhibition of Hif-1 causes cardiac dysfunction during pressure overload. *Nature*, *446*(7134), 444–448. https://doi.org/10.1038/nature05602

Santorelli, F. M., Shanske, S., Macaya, a, DeVivo, D. C., & DiMauro, S. (1993). The mutation at nt 8993 of mitochondrial DNA is a common cause of Leigh's syndrome. *Annals of Neurology*, *34*(6), 827–34. https://doi.org/10.1002/ana.410340612

Santorelli, F. M., Tanji, K., Sano, M., Shanske, S., El-Shahawi, M., Kranz-Eble, P., … De Vivo, D. C. (1997). Maternally inherited encephalopathy associated with a single-base insertion in the mitochondrial tRNA(Trp) gene. *Annals of Neurology*, *42*(2), 256–260. https://doi.org/10.1002/ana.410420220

Sanyal, A. J., Campbell-Sargent, C., Mirshahi, F., Rizzo, W. B., Contos, M. J., Sterling, R. K., … Clore, J. N. (2001). Nonalcoholic steatohepatitis: association of insulin resistance and mitochondrial abnormalities. *Gastroenterology*, *120*(5), 1183–92. https://doi.org/10.1053/gast.2001.23256

Sasarman, F., Antonicka, H., Horvath, R., & Shoubridge, E. A. (2011). The 2-thiouridylase function of the human MTU1 (TRMU) enzyme is dispensable for mitochondrial translation. *Human Molecular Genetics*, *20*(23), 4634–4643. https://doi.org/10.1093/hmg/ddr397

Sasarman, F., Nishimura, T., Thiffault, I., & Shoubridge, E. A. (2012). A novel mutation in YARS2 causes myopathy with lactic acidosis and sideroblastic anemia. *Human Mutation*, *33*(8), 1201–1206. https://doi.org/10.1002/humu.22098

Scarpulla, R. C. (2002). Nuclear activators and coactivators in mammalian mitochondrial biogenesis. *Biochimica et Biophysica Acta - Gene Structure and Expression*. https://doi.org/10.1016/S0167-4781(02)00343-3

Schaefer, A. M., McFarland, R., Blakely, E. L., He, L., Whittaker, R. G., Taylor, R. W., … Turnbull, D. M. (2008). Prevalence of mitochondrial DNA disease in adults. *Annals of Neurology*, *63*(1), 35–39. https://doi.org/10.1002/ana.21217

Scheper, G. C., van der Klok, T., van Andel, R. J., van Berkel, C. G. M., Sissler, M., Smet, J., … van der Knaap, M. S. (2007). Mitochondrial aspartyl-tRNA synthetase deficiency causes leukoencephalopathy with brain stem and spinal cord involvement and lactate elevation. *Nature Genetics*, *39*(4), 534–539. https://doi.org/10.1038/ng2013

Schmitt, E., Panvert, M., Blanquet, S., & Mechulam, Y. (1995). Transition state stabilization by the â€™ high â€™ motif of class I aminoacyl-tRNA synthetases : the case of Escherichia coli methionyl-tRNA synthetase, *23*(23), 4793–4798.

Schon, E. A., DiMauro, S., & Hirano, M. (2012). Human mitochondrial DNA: roles of inherited and somatic mutations. *Nat Rev Genet*, *13*(12), 878–890.

https://doi.org/10.1038/nrg3275

Schwartzentruber, J., Buhas, D., Majewski, J., Sasarman, F., Papillon-Cavanagh, S., Thiffaut, I., … Samuels, M. E. (2014). Mutation in the nuclear-encoded mitochondrial isoleucyl-tRNA synthetase IARS2 in patients with cataracts, growth hormone deficiency with short stature, partial sensorineural deafness, and peripheral neuropathy or with leigh syndrome. *Human Mutation*, *35*(11), 1285–1289. https://doi.org/10.1002/humu.22629

Shahni, R., Wedatilake, Y., Cleary, M. A., Lindley, K. J., Sibson, K. R., & Rahman, S. (2013). A distinct mitochondrial myopathy, lactic acidosis and sideroblastic anemia (MLASA) phenotype associates with YARS2 mutations. *American Journal of Medical Genetics, Part A*, *161*(9), 2334–2338. https://doi.org/10.1002/ajmg.a.36065

Shamseldin, H. E., Alshammari, M., Al-Sheddi, T., Salih, M. a, Alkhalidi, H., Kentab, A., … Alkuraya, F. S. (2012). Genomic analysis of mitochondrial diseases in a consanguineous population reveals novel candidate disease genes. *Journal of Medical Genetics*, *49*(4), 234–41. https://doi.org/10.1136/jmedgenet-2012-100836

Silvestri, G., Mongini, T., Odoardi, F., Modoni, a, deRosa, G., Doriguzzi, C., … Servidei, S. (2000). A new mtDNA mutation associated with a progressive encephalopathy and cytochrome c oxidase deficiency. *Neurology*, *54*(8), 1693–6. Retrieved from http://www.ncbi.nlm.nih.gov/pubmed/10762520

Silvestri, G., Rana, M., DiMuzio, A., Uncini, A., Tonali, P., & Servidei, S. (1998). A late-onset mitochondrial myopathy is associated with a novel mitochondrial DNA (mtDNA) point mutation in the tRNA(Trp) gene. *Neuromuscular Disorders*, *8*(5), 291–295. https://doi.org/10.1016/S0960-8966(98)00037-6

Simon, M., Richard, E. M., Wang, X., Shahzad, M., Huang, V. H., Qaiser, T. A., … Riazuddin, S. (2015). Mutations of Human NARS2, Encoding the Mitochondrial Asparaginyl-tRNA Synthetase, Cause Nonsyndromic Deafness and Leigh Syndrome. *PLoS Genetics*, *11*(3), 1–26. https://doi.org/10.1371/journal.pgen.1005097

Smits, P., Mattijssen, S., Morava, E., van den Brand, M., van den Brandt, F., Wijburg, F., … van den Heuvel, L. (2010). Functional consequences of mitochondrial tRNA Trp and tRNA Arg mutations causing combined OXPHOS defects. *European Journal of Human Genetics : EJHG*, *18*(August 2009), 324–329. https://doi.org/10.1038/ejhg.2009.169

Smits, P., Saada, A., Wortmann, S. B., Heister, A. J., Brink, M., Pfundt, R., … van den Heuvel, L. P. (2011). Mutation in mitochondrial ribosomal protein MRPS22 leads to Cornelia de Lange-like phenotype, brain abnormalities and hypertrophic cardiomyopathy. *European Journal of Human Genetics : EJHG*, *19*(4), 394–399. https://doi.org/10.1038/ejhg.2010.214

Sofou, K., Kollberg, G., Holmström, M., Dávila, M., Darin, N., Gustafsson, C. M., … Asin-Cayuela, J. (2015). Whole exome sequencing reveals mutations in NARS2 and PARS2 , encoding the mitochondrial asparaginyl-tRNA synthetase and prolyl-tRNA synthetase, in patients with Alpers syndrome. *Molecular Genetics & Genomic Medicine*, *3*(1), 59–68. https://doi.org/10.1002/mgg3.115

Solda, G., Caccia, S., Robusto, M., Chiereghin, C., Castorina, P., Ambrosetti, U., … Asselta, R. (2015). First independent replication of the involvement of LARS2 in Perrault syndrome by whole-exome sequencing of an Italian family. *J Hum Genet*, (November 2015), 295–300. https://doi.org/10.1038/jhg.2015.149

Steenweg, M. E., Ghezzi, D., Haack, T., Abbink, T. E. M., Martinelli, D., Van Berkel, C. G. M., … Zeviani, M. (2012). Leukoencephalopathy with thalamus and brainstem involvement and high lactate “LTBL” caused by EARS2 mutations. *Brain*, *135*(5), 1387–1394. https://doi.org/10.1093/brain/aws070

Synofzik, M., Schicks, J., Lindig, T., Biskup, S., Schmidt, T., Hansel, J., … Schols, L. (2011). Acetazolamide-responsive exercise-induced episodic ataxia associated with a novel homozygous DARS2 mutation. *Journal of Medical Genetics*, *48*(10), 713–715. https://doi.org/10.1136/jmg.2011.090282

Talim, B., Pyle, A., Griffin, H., Topaloglu, H., Tokatli, A., Keogh, M. J., … Horvath, R. (2013). Multisystem fatal infantile disease caused by a novel homozygous EARS2 mutation. *Brain*, *136*(2), 2012–2014. https://doi.org/10.1093/brain/aws197

Taskin, B. D., Karalok, Z. S., Gurkas, E., Aydin, K., Aydogmus, U., Ceylaner, S., … Pearl, P. L. (2016). Early-Onset Mild Type Leukoencephalopathy Caused by a Homozygous EARS2 Mutation. *Journal of Child Neurology*, *31*(7), 1–4. https://doi.org/10.1177/0883073816630087

Taylor, R. W., Pyle, A., Griffin, H., Blakely, E. L., Duff, J., He, L., … Chinnery, P. F. (2014). Use of Whole-Exome Sequencing to Determine the Genetic Basis of Multiple Mitochondrial Respiratory Chain Complex Deficiencies. *Jama*, *312*(1), 68. https://doi.org/10.1001/jama.2014.7184

Taylor, R. W., & Turnbull, D. M. (2005). Mitochondrial DNA mutations in human disease. *Nature Reviews. Genetics*, *6*(5), 389–402. https://doi.org/10.1038/nrg1606

Thiffault, I., Rioux, M. F., Tetreault, M., Jarry, J., Loiselle, L., Poirier, J., … Brais, B. (2006). A new autosomal recessive spastic ataxia associated with frequent white matter changes maps to 2q33-34. *Brain*, *129*(9), 2332–2340. https://doi.org/10.1093/brain/awl110

Tischner, C., Hofer, A., Wulff, V., Stepek, J., Dumitru, I., Becker, L., … Wenz, T. (2015). MTO1 mediates tissue specificity of OXPHOS defects via tRNA modification and translation optimization, which can be bypassed by dietary intervention. *Human*

Molecular Genetics, *24*(8), 2247–2266. https://doi.org/10.1093/hmg/ddu743

Tolkunova, E., Park, H., Xia, J., King, M. P., & Davidson, E. (2000). The human lysyl-tRNA synthetase gene encodes both the cytoplasmic and mitochondrial enzymes by means of an unusual: Alternative splicing of the primary transcript. *Journal of Biological Chemistry*, *275*(45), 35063–35069. https://doi.org/10.1074/jbc.M006265200

Tucker, E. J., Hershman, S. G., Köhrer, C., Belcher-Timme, C. A., Patel, J., Goldberger, O. A., … Mootha, V. K. (2011). Mutations in MTFMT underlie a human disorder of formylation causing impaired mitochondrial translation. *Cell Metabolism*, *14*(3), 428–434. https://doi.org/10.1016/j.cmet.2011.07.010

Tyynismaa, H. (2013). Mitochondrial aminoacyl-tRNA synthetases. In *Mitochondrial Disorders Caused by Nuclear Genes* (Vol. 9781461437, pp. 263–276). https://doi.org/10.1007/978-1-4614-3722-2_16

Tzoulis, C., Tran, G. T., Gjerde, I. O., Aasly, J., Neckelmann, G., Rydland, J., … Bindoff, L. A. (2012). Leukoencephalopathy with brainstem and spinal cord involvement caused by a novel mutation in the DARS2 gene. *Journal of Neurology*, *259*(2), 292–296. https://doi.org/10.1007/s00415-011-6176-9

Valente, L., Piga, D., Lamantea, E., Carrara, F., Uziel, G., Cudia, P., … Tiranti, V. (2009). Identification of novel mutations in five patients with mitochondrial encephalomyopathy. *Biochimica et Biophysica Acta*, *1787*, 491–501. https://doi.org/10.1016/j.bbabio.2008.10.001

van Berge, L., Dooves, S., van Berkel, C. G. M., Polder, E., van der Knaap, M. S., Scheper, G. C., … Scheper, G. C. (2012). Leukoencephalopathy with brain stem and spinal cord involvement and lactate elevation is associated with cell-type-dependent splicing of mtAspRS mRNA. *The Biochemical Journal*, *441*(3), 955–62. https://doi.org/10.1042/BJ20110795

Van Den Heuvel, L., Smits, P., & Smeitink, J. (2010). Mitochondrial translation and beyond: Processes implicated in combined oxidative phosphorylation deficiencies. *Journal of Biomedicine and Biotechnology*. https://doi.org/10.1155/2010/737385

van den Ouweland, J. M., Lemkes, H. H., Ruitenbeek, W., Sandkuijl, L. A., de Vijlder, M. F., Struyvenberg, P. A., … Maassen, J. A. (1992). Mutation in mitochondrial tRNA(Leu)(UUR) gene in a large pedigree with maternally transmitted type II diabetes mellitus and deafness. *Nature Genetics*, *1*(5), 368–71. https://doi.org/10.1038/ng0892-368

Vanlander, A. V., Menten, B., Smet, J., De Meirleir, L., Sante, T., De Paepe, B., … Van Coster, R. (2015). Two siblings with homozygous pathogenic splice-site variant in mitochondrial asparaginyl-tRNA synthetase (NARS2). *Human Mutation*, *36*(2), 222–231. https://doi.org/10.1002/humu.22728

Vega, R. B., Huss, J. M., & Kelly, D. P. (2000). The coactivator PGC-1 cooperates with peroxisome proliferator-activated receptor alpha in transcriptional control of nuclear genes encoding mitochondrial fatty acid oxidation enzymes. *Molecular and Cellular Biology*, *20*(5), 1868–76. https://doi.org/10.1128/MCB.20.5.1868-1876.2000

Verfaillie, T., Rubio, N., Garg, A., Bultynck, G., Rizzuto, R., Decuypere, J.-P., … Agostinis, P. (2012). PERK is required at the ER-mitochondrial contact sites to convey apoptosis after ROS-based ER stress. *Cell Death and Differentiation*, *19*(10), 1880–1891. https://doi.org/10.1038/cdd.2012.74

Vilardo, E., Nachbagauer, C., Buzet, A., Taschner, A., Holzmann, J., & Rossmanith, W. (2012). A subcomplex of human mitochondrial RNase P is a bifunctional methyltransferase-extensive moonlighting in mitochondrial tRNA biogenesis. *Nucleic Acids Research*, *40*(22), 11583–11593. https://doi.org/10.1093/nar/gks910

Virtanen, K. a, Lidell, M. E., Orava, J., Heglind, M., Westergren, R., Niemi, T., … Nuutila, P. (2009). Functional brown adipose tissue in healthy adults. *The New England Journal of Medicine*, *360*, 1518–1525. https://doi.org/10.1056/NEJMoa0808949

Walker, M. A., Mohler, K. P., Hopkins, K. W., Oakley, D. H., Sweetser, D. A., Ibba, M., … Thibert, R. L. (2016). Novel Compound Heterozygous Mutations Expand the Recognized Phenotypes of FARS2-Linked Disease. *Journal of Child Neurology*, *31*(9), 1–11. https://doi.org/10.1177/0883073816643402

Wang, C.-H., Wu, S.-B., Wu, Y.-T., & Wei, Y.-H. (2013). Oxidative stress response elicited by mitochondrial dysfunction: implication in the pathophysiology of aging. *Experimental Biology and Medicine (Maywood, N.J.)*, *238*(5), 450–60. https://doi.org/10.1177/1535370213493069

Wang, M., Sips, P., Khin, E., Rotival, M., Sun, X., Ahmed, R., … Cook, S. A. (2016). Wars2 is a determinant of angiogenesis. *Nat Commun*, *7*, 12061. https://doi.org/10.1038/ncomms12061

Webb, B. D., Wheeler, P. G., Hagen, J. J., Cohen, N., Linderman, M. D., Diaz, G. A., … Schadt, E. E. (2015). Novel, Compound Heterozygous, Single-Nucleotide Variants in MARS2 Associated with Developmental Delay, Poor Growth, and Sensorineural Hearing Loss. *Human Mutation*, *36*(6), 587–592. https://doi.org/10.1002/humu.22781

Wolny, S., McFarland, R., Chinnery, P., & Cheetham, T. (2009). Abnormal growth in mitochondrial disease. *Acta Paediatrica, International Journal of Paediatrics*, *98*(3), 553–554. https://doi.org/10.1111/j.1651-2227.2008.01148.x

Wu, Z., Puigserver, P., Andersson, U., Zhang, C., Adelmant, G., Mootha, V., … Spiegelman, B. M. (1999). Mechanisms controlling mitochondrial biogenesis and respiration through the thermogenic coactivator PGC-1. *Cell*, *98*(1), 115–124. https://doi.org/10.1016/S0092-8674(00)80611-X

Yang, Y., Liu, W., Fang, Z., Shi, J., Che, F., He, C., … Wu, Y. (2016). A Newly Identified Missense Mutation in FARS2 Causes Autosomal-Recessive Spastic Paraplegia. *Human Mutation*, *37*(2), 165–9. https://doi.org/10.1002/humu.22930

Ye, J., Rawson, R. B., Komuro, R., Chen, X., Davé, U. P., Prywes, R., … Goldstein, J. L. (2000). ER stress induces cleavage of membrane-bound ATF6 by the same proteases that process SREBPs. *Molecular Cell*, *6*(6), 1355–1364. https://doi.org/10.1016/S1097-2765(00)00133-7

7 Appendix

		Genotype (*Wars2*)								
Tissue	**Pathology**	**WT**	**WT**	**WT**	**HET**	**HET**	**HET**	**HOM**	**HOM**	**HOM**
Liver	Inflammatory cell foci	1	1	1	1	1	1	1	1	1
	Single cell necrosis, centrilobular	0	0	0	0	0	0	0	0	0
	Hepatocellular adenoma	0	P	0	0	P	P	0	0	P
Kidney	Tubular basophilia	0	0	1	1	1	2	0	0	0
	Cortical tubular vacuolation	2	1	1	2	2	2	2	2	1
	Inflammatory cell foci, cortex	1	0	0	0	0	0	0	0	0
	Inflammation, pelvis	0	0	0	0	0	0	1	0	0
	Cortical mineralisation	1	0	0	1	1	0	1	0	0
	pelvic dilatation, unilateral	0	0	0	2	0	0	0	0	1
	Mineralisation, papilla	0	0	1	0	0	0	0	0	0

Table 7.1 – Histological analysis of *Wars2*$^{V117L/V117L}$ liver and kidney tissue.
Liver and kidney H&E stained sections from *Wars2*$^{+/+}$ (n=3), *Wars2*$^{+/V117L}$ (n=3) and *Wars2*$^{V117L/V117L}$ (n=3) mice were scored for the presence of abnormal pathology. Sections were scored blinded by genotype using a non-linear semi-quantitative grading system from 0 – 5. 0 = no change recorded, 1 = minimal (the least change that is visible on light microscopy at x 20, small, focal or affecting <10% of tissue), 2 = Mild (slight) (change is readily detected but not a major feature, may be multifocal small lesions or affect <20% of tissue, may still be within background appearance for the species), 3 = Moderate (change is more extensive or is comprised of more foci, may be seen in every field of view at x 20, beyond the usual background for the lesion in the species and may start to have relevance for organ function and correlate with other changes such as organ weight for example), 4 = Moderately severe (same as 3 but more of the tissue is affected for example up to 75% and likely to have relevance for organ function), 5 = Severe / Marked (Virtually the whole tissue is affected by the change and likely to be functionally relevant and detrimental). Hepatocellular adenoma was scored using a binary scoring system where P = present and 0 = absent.